Conodont (U-Th)/He thermochronology of the Mormon Mountains, Tule Spring Hills, and Beaver Dam Mountains, southeastern Nevada and southwestern Utah

By

James P. Tyrrell

B.S., Washington and Lee University, 2014

Submitted to the graduate degree program in Geology and the Graduate Faculty of the University of Kansas in partial fulfillment of the requirements for the degree of Master of Science.

_____

Co-Chairperson, Dr. Tandis S. Bidgoli

_____

Co-Chairperson, Dr. J. Douglas Walker

_____

Dr. Andreas Möller

Date defended: 12/6/2016

The Thesis Committee for James P. Tyrrell
certifies that this is the approved version of the following thesis:

Conodont (U-Th)/He thermochronology of the Mormon Mountains, Tule Spring Hills, and Beaver Dam Mountains, southeastern Nevada and southwestern Utah

_____
Co-Chairperson, Dr. Tandis S. Bidgoli

_____
Co-Chairperson, Dr. J. Douglas Walker

Date approved: 12/6/2016

ABSTRACT

(U-Th)/He thermochronology is a well-established dating technique used to understand the temperature-time histories of rocks in a wide range of geologic settings. The technique is presently restricted to rocks that contain specific accessory minerals like apatite or zircon. Marine carbonates and shales typically lack these accessory phases, and thus present a challenge for application of the method. Here, we explore the utility of biogenic apatite from conodonts as a (U-Th)/He thermochronometer at a well-studied calibration site located in eastern Nevada and southwestern Utah.

We perform (U-Th)/He thermochronometry, laser ablation inductively coupled plasma mass spectrometry, X-ray micro-computed tomography, and scanning electron microscopy on specimens with conodont color alteration indices (CAI) of 1.5 – 3 extracted from carbonate rocks in the footwalls of low-angle normal faults in the Mormon Mountains, Tule Spring Hills, and Beaver Dam Mountains. Conodont (U-Th)/He (CHe) dates have high scatter; dates are commonly reproducible to 20% of sample means, but can deviate up to 150%. All CAI 1.5 – 2.5 conodonts produce CHe dates younger than 193 Ma, consistent with thermal resetting of samples; however, most CAI 3 conodonts give ages 2 – 3x older than Mississippian and Permian deposition. Average U, Th, and rare earth element (REE) concentrations depend on porosity and permeability differences between albid and hyaline conodont tissue and range from <10 to 100s of ppm in concentration. Parent isotope concentrations are especially low in CAI 3 conodonts, commonly <1 ppm, and there is an inverse relationship between these concentrations and CHe dates. The majority of parent U, Th, and Sm, and REEs are concentrated within the outer 5 μm of the conodont elements and consistently show 5 – 10x enrichment relative to cores. Margin enrichment is also depressed with increasing CAI. SEM imaging shows a shift in the orientation of apatite

microcrystallites from perpendicular to parallel to the major axis of the conodont elements at CAI 3, and corrosion and recrystallization features on the surfaces of some CAI 2.5 and 3 conodonts.

We propose these microstructural changes associated with increasing CAI influence CHe dates. Parent isotope loss occurs during the post-cooling stage, either in the outcrop or in the laboratory. Our hypothesis is that the double-buffered formic acid procedure for dissolving dolomitized carbonates may accelerate this loss in higher CAI conodonts.

ACKNOWLEDGEMENTS

I want to thank my advisors, Dr. Tandis Bidgoli, Dr. Doug Walker, and Dr. Andreas Möller, for all their help throughout this exciting, challenging, and formative experience in my life. Your guidance has allowed me to persevere through this project and feel confident that I can overcome any difficulty and achieve any goal I set in the future.

I also want to thank my parents, Maureen and Jeff, my siblings, Kate and Jack, my friends, and my entire extended family in the Kansas City area for their unconditional love and support throughout this process. Without each and every one of you I would not be where I am today.

TABLE OF CONTENTS

LIST OF FIGURES

LIST OF TABLES

INTRODUCTION

(U-Th)/He thermochonology is a geologic tool based on the radioactive decay of isotopes of U, Th, and Sm to daughter ^{4}He. Helium retention in apatite is temperature dependent and transitions from near complete preservation below 40 °C to complete expulsion by thermally activated volume diffusion above 80 °C (Wolf et al., 1996, 1998; House et al., 1999; Stockli et al., 2000). These temperatures define the apatite helium (AHe) partial retention zone (PRZ; Wolf et al., 1998) and represent the lowest temperature sensitivity of commonly utilized thermochronometers, making (U-Th)/He thermochronology a widely applicable technique and valuable to researchers with a variety of goals and interests (e.g., House et al., 1998; Spotila et al., 1998; Brady, 2002; Crowhurst et al., 2002; Lorencak et al., 2004; Stock et al., 2006; Flowers et al., 2008; Clark et al., 2010; Gavillot et al., 2010; Cogné et al., 2011). In tectonics, the technique can be used to establish the timing of fault initiation and rate of footwall exhumation (e.g., Stockli et al., 2001; Stockli et. al., 2002), and to estimate the magnitude of deformation, admissible fault geometries, and paleo-geothermal gradients (e.g., Crowley et al., 2002; Söderlund et al., 2005; Bidgoli et al., 2015). For sedimentary basin analysis and hydrocarbon systems modeling, (U-Th)/He data can be tied to other burial and temperature history data (e.g., stratigraphic thicknesses, biostratigraphic constraints, paleothermometry data, etc.) to evaluate such things as trap development, seal integrity, rock quality and diagenesis, oil and gas generation and migration patterns, and expected resource volumes (see summary in Armstrong, 2005 and references therein).

Although the (U-Th)/He method is useful for studying a range of near-surface processes, application of the method is currently restricted to igneous, metamorphic, and siliciclastic rocks with specific minerals such as apatite or zircon present. Marine carbonates and shales typically

lack these accessory phases in sizes practical for (U-Th)/He dating; thus, identifying datable material in carbonates and shales presents a significant opportunity to expand the method and enhance our understanding of the thermal history of rocks from these settings.

Conodonts may offer a way for using the (U-Th)/He method in carbonate successions (Peppe and Reiners, 2007; Flowers et al., 2014; Powell et al., 2014). These tooth-like microfossils are common in Cambrian through Triassic carbonates and shales, and are preserved as biomineralized apatite with U and Th in concentrations that are comparable to magmatic sources of apatite (Trotter and Eggins, 2006; Peppe and Reiners, 2007). The microfossils are referred to as elements, which were apparently part of the feeding apparatus of the host animal. Conodonts are already routinely collected and used as biostratigraphic markers (e.g., Bergström, 1970; Sweet et al., 1970; Behnken, 1975; Over, 2007; Hogancamp et al., 2016) and as maximum temperature indicators via the conodont color alteration index (CAI; Epstein et al., 1977; Rejebian et al., 1987). Thus, conodonts are particularly attractive because successful use as a (U-Th)/He thermochronometer means that a single conodont element, when paired with other geologic data, could provide three independent time and temperature constraints – cooling age, biostratigraphic age, and maximum temperature.

Peppe and Reiners (2007) is the only published study to date that has explored the utility of conodonts as (U-Th)/He thermochronometers. Successful aspects of their study included determining that the closure temperature for conodonts is similar to magmatic apatite (60 – 67 °C), and that the diffusion domain likely corresponds to the whole of the conodont element. Several of the samples in their study also yielded (U-Th)/He (CHe) dates consistent with regional thermal histories for the sample locales. Other samples, however, showed a wide spread in dates and an inverse correlation with parent isotope concentrations, pointing to possible open-system behavior

at some point late in the history of the samples (i.e. post-cooling).

Some of the challenges associated with conodonts as potential thermochronometers may relate to their inherent variability. They are found in a variety of shapes and sizes; morphologies include bar, blade, cone, and platform elements. Although Peppe and Reiners (2007) confirmed that the diffusion domain size was likely the conodont element, conodont biogenic apatite is composed of two structural components (crown and basal body) and three primary tissue types (albid, hyaline, and basal tissues). Each of these tissue types varies in microcrystalline size and arrangement, elemental composition, porosity and permeability, and relative percentage within a single conodont element (Pietzner et al., 1968; Wright et al., 1990; Trotter and Eggins, 2006). These variations can influence primary isotope distributions within individual conodonts and the potential for isotope and elemental mobility. Similarly, temperature changes, as documented by CAI, can alter the microstructures of the conodonts, which may also impact isotope distributions, He diffusivity, and CHe ages (Burnett, 1988; Fuchs, 1989; Königshof, 1992; Nöth, 1998). These challenges have yet to be resolved in the emerging CHe method.

Here, we evaluate the suitability of biogenic apatite from conodonts for (U-Th)/He thermochronology by dating material extracted from surface outcrops located in the footwalls of three well-studied low-angle normal faults (LANFs) in eastern Nevada and western Utah (Figures 1, 2, and 3). These faults are among the best cited examples of low-angle normal faults, and have been the focus of detailed geologic and structural investigations (Wernicke et al., 1985; Axen et al., 1990; Axen, 1993). They have also been the focus of recent zircon and apatite (U-Th)/He study (Bidgoli et. al., 2015) and earlier fission-track studies (O'Sullivan, 1994; Stockli, 1999). These studies along with published thermochronology data from the region (Fitzgerald et al., 1991, 2009;

Reiners et al., 2000; Quigley et al., 2010) provide relatively tight constraints on the thermal history of the study area, and allow direct comparisons with CHe results.

In this paper, we report CHe dates as well as trace and REE isotope concentrations from laser ablation inductively coupled plasma mass spectrometry (LA-ICPMS) depth profiles to better characterize the potential of conodonts as thermochronometers. We show that while some dates are consistent with the known thermal history of the region, most of our samples have dates that are older than the expected Miocene age and show significant scatter. Additionally, many CAI 3 conodonts dated older than deposition, a clear indication of open-system behavior during the low temperature history of our samples. Although our results do not allow us to conclusively determine the cause for open-system behavior, we show that microstructural changes associated with increasing CAI may be a contributing factor for parent isotope mobility and the limited reproducibility of our CHe dates.

BACKGROUND

Study area background

Overview

The study area is located in a part of the Basin and Range province that experienced significant extension during the Miocene (Wernicke et al., 1985; Hintze, 1986; Figures 1 and 2). Extension was accommodated by three LANFs in the area: the Mormon Peak Detachment (MPD) in the Mormon Mountains, the Tule Springs Detachment (TSD) in the Tule Springs Hills, and Castle Cliffs Detachment (CCD) in the Beaver Dam Mountains (Wernicke et al., 1985; Hintze, 1986; Axen et al., 1990; Axen, 1993; Figure 3). These LANFs are well studied in terms of their geometries and kinematics (Wernicke, 1982; Wernicke et al., 1985; Axen et al., 1990; Axen, 1993; Swanson and Wernicke, 2015). Additionally, new apatite and zircon (U-Th)/He thermochronology data from the area (Bidgoli et. al., 2015) and published fission-track data (O'Sullivan, 1994; Stockli, 1999) provide constraints on the thermal histories of the footwalls of these detachment faults in non-carbonate intervals, and suggest that extension-related cooling occurred between 17 and 14 Ma (Figure 4). However, much of the exposed outcrop in this region is carbonate rock lacking thermochronological data. Thus, the study area is ideal as a calibration site for testing the (U-Th)/He method on conodonts in that the CHe results can be directly compared to other datasets.

Structural and tectonic history

Two major phases of deformation occurred in the study area. Mesozoic contractional structures are part of a mid-Cretaceous to early Cenozoic belt of deformation associated with the Sevier orogeny (Longwell, 1949; Armstrong, 1968, Fleck, 1970, Bohannon, 1983; Heller et al., 1986; Carpenter, 1989; Axen et al., 1990; Carpenter and Carpenter, 1994). Contraction was principally facilitated through the Mormon-Tule Springs thrust, an east-vergent decollément-style

thrust with approximately 30 km of shortening across it (Wernicke, 1982; Wernicke et al., 1984; 1985). Miocene extension via three major low-angle normal faults (LANFs) later gave the region its current tectonic expression.

The CCD is the major extensional structure in the Beaver Dam Mountains and likely initiated with a low dip of up to 32 degrees, but is currently exposed with dips of 10 to 20 degrees in outcrop (Axen et al., 1990; Axen, 1993). The CCD extends from the eastern Beaver Dam Mountains to beneath the Tule Spring Hills where propagation likely terminates. The Beaver Dam anticline (monocline) is preserved in the footwall of the detachment and is variously interpreted as being related to Miocene flexural unloading (Axen and Wernicke, 1989; Axen, 2004) or Laramide-age contraction (Hintze, 1986; Carpenter and Carpenter, 1994; Christie-Blick et al., 2007).

Extension in the Tule Spring Hills and Mormon Mountains initiated also in the Miocene along the structurally shallower TSD and MPD, respectively. The TSD resides in the hanging wall of the CCD and has a ramp-flat geometry, with the detachment's flat initiating at a low angle, between 3-15 degrees, and reactivating part of the Tule Springs thrust (Axen, 1993). The TSD has accommodated 5.5-7 km of middle to late Miocene extension. Pliocene north-trending normal and strike slip faults, which cut and offset the TSD between 6 and 8 km left-laterally, dominate the low-relief exposed ridges and valleys that make up the modern Tule Spring Hills. The MPD, located west of the TSD, also initiated at a low dip. Current exposures of the fault dip 5-10 degrees, but palinspastic reconstructions of the MPD suggest an original dip of 20-28 degrees and that it likely accommodated 12 to 13 km of extension (Wernicke et al., 1985; Swanson and Wernicke, 2015).

Not all researchers concur that low-angle normal faulting created the modern structural expression of the Mormon Mountains, Tule Spring Hills, and Beaver Dam Mountains. Some

workers theorize that low-angle features in these ranges are the result of gravity slides, and that Miocene extension was minor and accommodated through high-angle range-bounding normal faults (Carpenter and Carpenter, 1994; Anders et al., 2006). Basal gravity slides are capable of producing structures that look similar to LANFs (e.g. Pierce, 1957, 1975; Anders et al., 2010). Anders et al. (2006) argued for a reinterpretation of the MPD based on the presence of basal conglomerates and related clastic dikes, the limited deformation in the footwall beneath the MPD, and multidirectional kinematic indicators. None of these aspects violate the LANF interpretation.

Although debate exists on the origin of these structures, results from a recent thermochronology study suggest a low-angle normal fault interpretation is more likely. Zircon and apatite (U-Th)/He thermochronology, along with fission-track dating show that protracted cooling associated with footwall exhumation initiated at around 17 Ma in the Beaver Dam Mountains (O'Sullivan, 1994; Stockli, 1999; Bidgoli et al., 2015). Extension then propagated westward to the Tule Spring Hills and Mormon Mountains by about 13-14 Ma (Bidgoli et al., 2015). Not only are the westward faults younger, but ages within each fault block are also systematically younger in the direction of slip on the fault and show no relationship with elevation, consistent with a LANF interpretation (Bidgoli et al., 2015). A maximum of 40 km of extension is permitted across the three detachments in the study area based on the (U-Th)/He data (Bidgoli et al., 2015), which is substantial but lower than previous estimates of 54 +/- 10 km (Wernicke and Axen, 1988; Axen et al., 1990).

Stratigraphy

The Mormon Mountains, Tule Spring Hills, and Beaver Dam Mountains expose Precambrian crystalline basement overlain by Cambrian sandstone and shale and thick successions of Cambrian through Permian shallow-water marine carbonates (Wernicke, 1985; Hintze, 1986).

Above these units lie Triassic carbonates, Jurassic and Cretaceous siliciclastics, and Tertiary ash-flow tuffs (Hintze, 1986). Previous thermochronology studies dated apatites and zircons extracted from Precambrian basement gneisses and granites, Cambrian sandstones, and Permian through Jurassic sandstones and conglomerates (O'Sullivan, 1994; Stockli et al., 1999; Bidgoli et al., 2015). Carbonate-dominated intervals were chosen for this study and have not been previously dated. Units sampled in this study include the Cambrian Bright Angle Shale and Bonanza King Formations, Devonian Muddy Peak Dolomite, Mississippian Redwall Limestone/Monte Cristo Limestone, Pennsylvanian Callville Limestone, and Permian Pakoon Dolomite (Hintze, 1986). Sampled intervals were predominantly medium-to-coarse grained, light-to-dark gray dolomitized packestones to grainstones.

Conodont background

Overview

Conodont apatite begins uptake of U, Th, and REE during deposition, and concentrations are thought to be preserved through burial and diagenesis at low temperatures, making them potential candidates for (U-Th)/He analysis (Bernat, 1975; Wright et al., 1984; Shaw and Wasserberg, 1985; Trueman and Tuross, 2002, Trotter and Eggins, 2006). Conodonts are made of hyaline, albid, and basal tissue, each of which varies microstructurally and in uptake of trace elements, which is a potential complication to dating (see following section; Trotter and Eggins, 2006; Trotter et al., 2007; Sanz-Lopez et al., 2012). Other challenges associated with dating conodonts include the impact of burial and diagenesis on conodont microstructure (documented through CAI), which may ultimately influence parent isotope distributions, He diffusivity, and CHe ages. These factors, along with the complex morphologies of the conodont elements, also make it hard to accurately estimate the alpha ejection correction, a necessary morphometrically-

based age correction that is applied to (U-Th)/He dates (Farley et al., 1996).

Mineralogy, microstructure, and color alteration index (CAI)

Conodonts are made of biogenic carbonate fluorapatite that is compositionally similar to francolite ($Ca_5Na_{0.14}(PO_4)_{3.01}(CO_3)_{0.016}F_{0.73}(H_2O)_{0.85}$), and are composed of three basic histologic types that differ in the size and connectivity of microcrystallites, which can affect porosity and permeability of conodonts, and ultimately, their compositions (Pietzner et al., 1968; Wright et al., 1990; Trotter and Eggins, 2006; Trotter et al., 2007; Sanz-Lopez et al., 2012). Albid tissue is composed of both fine and very large microcrystals (up to 100s of μm) but has the lowest porosity and permeability due to unconnected intracrystalline pores (Trotter et al., 2007, Sanz-Lopez et al., 2012). Hyaline tissue is made up of medium-sized microcrystals (up to 30 μm) with higher (up to 10 nm) lamellar porosity (Pietzner et al., 1968; Trotter and Eggins, 2006; Trotter et al., 2007; Sanz-Lopez et al., 2012). Basal bodies are a third histologic type, and they have a very fine polycrystalline matrix with high intercrystalline porosity and permeability (Trotter et al., 2007). Microcrystalline structures can vary within each tissue type, and tissue types also differ in their average concentrations of radiogenic parent isotopes, trace elements, and REEs. Albid tissue produces the lowest concentrations, commonly less than 10 ppm U, hyaline tissue generally possesses moderate concentrations, between 10 and 100 U ppm, and basal bodies contain the highest concentrations, commonly >100 ppm U. Recent studies have shown that REE patterns in conodonts are controlled largely by diagenetic uptake (Bright et al., 2009; Zhao et al., 2013; Chen et al., 2015); thus concentrations within individual conodonts can be heavily influenced by their specific post-mortem histories.

In 1977, A.G. Epstein created the conodont color alteration index (CAI), a scale from 1 – 8 that describes color changes that occur to conodonts that experience different temperatures. From

1 to 8, colors shift from light brown to dark brown to gray to black to white at temperatures ranging from <50 to >600 degrees Celsius (Epstein, 1977; Rejebian et al., 1987). These color changes correspond to microstructural alterations that occur within conodonts at increasing burial temperatures. Surficial microstructural orientation shifts commonly begin at lower levels of CAI (Königshof, 1992; Nöth, 1998). From CAI 1 to 3, a preferential rotation of microcrystals from perpendicular to parallel to the largest axis of the conodont has been observed (Nöth, 1998). Microcrystalline orientation shifts may impact porosity and permeability within conodonts, and may affect diffusion pathways and chemical exchange near the exterior of grains (Burnett, 1988; Sanz-Lopez et al., 2012).

In addition to microstructural shifts, surface textures can change with increasing CAI. Typical surficial microtextures include large (~2 μm) blocky crystals, columnar crystals, crystal fans, and denticular crystals (Blanco-Ferrera et al., 2010, Sanz-Lopez et al., 2012). All microtextures are seen in conodonts above CAI 1. Additionally, at higher temperatures, conodonts may experience hydrothermal alteration by dissolution and/or recrystallization (Burnett, 1988; Fuchs, 1989; Königshof, 2003). Surface texture patterns in chemically corroded conodonts are described as pocked, frosted, or pitted surfaces (Nöth, 1998). Dolomite rhombs from the host rock and large apatite crystallites can be embedded into corroded surfaces in higher CAI conodonts, indicating acidic fluids can substantially alter surficial microtextures (Königshof, 2003; Sanz-Lopez et al., 2012). While more common in conodonts that have experienced contact metamorphism (CAI 4), recrystallization features can begin in conodonts with CAI as low as 1.5, depending on depositional environment and post-depositional conditions (Ebneth et al., 1997; Nöth, 1998). Surface microtextures are different from internal conodont microstructural patterns (i.e. lamellar tissue structure; Sanz-Lopez et al., 2012), and the effect of increasing CAI on

potential microstructural changes at depth remains unclear for conodonts with lower CAIs.

Geo- and thermochronometer studies

A small number of studies have used conodonts as geo- and thermochronometers (e.g., Turekian et al., 1970; Sachs et al., 1980; Kovach and Zartman, 1981; Ueki and Sano, 2001; Elrick et al., 2002; Peppe and Reiners, 2007; Flowers et al., 2014; Powell et al., 2014). Early studies by Turekian et al. (1970) and Sachs et al. (1980) found major problems in that conodonts and other fossil bones were susceptible to He loss and/or had low parent isotope concentrations. Several subsequent studies tested the potential of conodonts as U/Pb geochronometers and determined that conodonts typically generated U/Pb ages close to their depositional or early diagenetic age, but had large scatter (Kovach and Zartman, 1981; Ueki and Sano, 2001; Elrick et al., 2002).

Peppe and Reiners (2007) was the first published study to test the potential of conodonts as (U-Th)/He thermochronometers. They analyzed CAI 1-5 conodonts from seven localities around North America and concluded that three or potentially four of their seven samples yielded reproducible ages that correspond to known regional cooling ages. Uncertainties within 2σ for samples they considered acceptable range from 3.3% to 15%. He diffusion experiments showed that conodont apatite has a closure temperature of 60-70 °C, consistent with the window for magmatic apatite. Their study also showed that among the samples that did not yield reproducible CHe dates, many showed inverse correlations between parent isotope concentrations and CHe date, indicating conodonts may have experienced a period of open-system behavior. Overall, their work suggests that conodonts have potential as thermochronometers, but more robust analysis is required to evaluate CHe ages with respect to specific regional geologic cooling histories, and extrapolate how characteristics of conodonts such as CAI, microstructure, apatite tissue type, and species morphology and evolution patterns impact CHe dating potential.

METHODS

Sample collection

We collected samples from three transects across exposed carbonate footwall blocks in the Mormon Mountains, Tule Spring Hills, and Beaver Dam Mountains (Figure 2). We sampled each transect along the structural dip, perpendicular to the strike of the faults following methods of Stockli (2005), so that thermal profiles of extension-related exhumation would be captured. We collected roughly 5 kilograms of carbonate material per sample, at 200 to 300 m horizontal spacing between samples, depending on outcrop availability. In total 43 samples were collected: 14 samples in the Mormon Mountains, 8 samples in the Tule Spring Hills, and 20 samples in the Beaver Dam Mountains. Sampled intervals were dominantly medium to coarse-grained dolomitic packestones to grainstones.

Sample dissolution and conodont separation

Carbonate samples were dissolved using double-buffered formic acid following the methods described by Jeppson and Anehus (1995). Formic acid is preferred to other common carbonate dissolution techniques (i.e. acetic acid) because it is quick, effective on dolomites, and less prone to etching or destroying conodonts during extraction (Jeppson and Anehus, 1995). Conodonts are susceptible to damage if the pH of the acid used during dissolution is outside the optimal range, which can vary based on taxonomy and locale (Jeppson and Anehus, 1995; Jeppson et al., 1999). For dolomitized carbonates processed using buffered formic acid, an initial pH of as low as 2.43 is safe, although a higher pH may be required to preserve certain specimens (Jeppson and Anehus, 1995). Therefore, careful monitoring of pH and potential damage to specimens is of paramount importance while processing samples.

Our samples were dissolved in a 10.6% formic acid solution, with 20 g of calcium carbonate and 1.2 g of tricalcium phosphate added as buffering agents. Dolomite material was weighed and 11 ml of the solution was added per gram of dolomite. The solution was mixed regularly to prevent density segregation. Following dissolution, lithium metatungstate (2.83 – 2.84 g/cm^3) was used for heavy liquid separation (Hanan and Totten, 1996). Conodonts were then separated from residues, dry picked under a binocular scope, and evaluated for species identification and CAI. CAI values ranged from 1.5 to 3 using the criteria originally defined by Epstein (1977). In total, 15 of the 43 samples dissolved yielded conodonts. The number of conodont elements extracted per sample was variable and ranged from <10 to >150 elements, for a total of 568 elements. Sample dissolution and CAI analyses were performed at the University of Iowa's Micropaleontology Laboratory.

Laser ablation ICPMS

We performed laser ablation-inductively coupled plasma mass spectrometry (LA-ICPMS) to generate depth profiles of trace elements (^{137}Ba, ^{206}Pb, ^{207}Pb, ^{208}Pb, ^{232}Th, and ^{238}U) and specific rare earth elements (^{139}La, ^{140}Ce, ^{141}Pr, ^{146}Nd, ^{147}Sm, ^{153}Eu, ^{158}Gd, ^{163}Dy, ^{166}Er, and ^{172}Yb, as well as ^{89}Y which behaves similarly) within conodonts. ^{43}Ca was measured as an internal standard. U, Th, Sm, Nd, and Pb isotopes were measured to determine concentration distributions with respect to datable isotopic systems. Low, middle, and high REEs were selected to obtain a holistic data set across a spectrum of atomic masses, to determine if isotopic concentration and distribution patterns were element-specific. LA-ICPMS analyses were made using a Thermo Scientific Element-2 high resolution ICPMS coupled with a Photon Machines excimer laser with a 193 nm wavelength and 5 ns pulse width at The University of Kansas Isotope Geochemistry Laboratories (Table 1).

We generated 512 ablation pits in 400 conodont elements using a procedure modified from Trotter and Eggins (2006). Conodont elements were picked and mounted onto epoxy pucks using a clear double-sided tape. The puck was then inserted into the sample cell of the laser and between 1 and 5 ablation pits were shot into each conodont element during 2 experimental runs. We attempted to ablate the flattest surfaces on conodont exteriors, but finding completely flat surfaces was impossible. Ablating oblique surfaces required consideration that rim and depth zoning patterns may exist in different positions and to smaller spatial extents than they appear to in our spots. We adjusted the laser fluence, spot size, and ablation time between runs to reduce the likelihood that small and/or thin conodont elements would break in the ablation process. The first run included Mormon Mountains and Tule Spring Hills conodonts. We used a 3 J/cm^{-2} laser fluence, 10 Hz pulse rate, 50 μm spot size, and total ablation time of 35 seconds. Beaver Dam Mountains conodonts were analyzed in the second trial, where we used 2.5 J/cm^{-2} laser fluence, 10 Hz pulse rate, 35 μm spot sizing, and total ablation time of 30 seconds. The ablation rate was estimated at ~1 μm per second, based on a measured ablation depth of 0.2 μm per laser pulse in Durango apatite from Trotter and Eggins (2006). We used half the fluence but twice the pulse rate compared to that study and estimate that the ablation rate is roughly equivalent. Total method time per spot was 50 seconds in both trials including background measurement, and individual mass cycle times were roughly 0.6 seconds. All conodont elements were photographed before and after analysis for documentation.

Data reduction was completed using the Trace_Element_IS data reduction scheme in Iolite V2.5 (Paton et al., 2011). The Iolite software generates spot data (depth profiles) in terms of elemental counts per second (cps) versus time in seconds. We used the Longerich et al. (1996) data reduction method to calculate concentrations, dividing the count rate by the normalized sensitivity

after correcting for volume of sample ablated using a calibration standard. Our internal calibration standard was 37.88 weight percent Ca for conodont apatite (see Table 1 for summary of input parameters). NIST 612 glass, Durango apatite, and Fish Canyon Tuff apatite were also ablated for comparison as external standards (see Table 2 for summary of measured values). Trotter and Eggins (2006) measured an average U concentration in Durango apatite at 8.88 ppm via LA-ICPMS, we measured 7.19 ppm U in our Durango standard via LA-ICPMS. In terms of compositional similarity between spots, the Durango apatite has shown measured isotopic concentrations to be reproducible to between 1% and 5% (Eggins et al., 1998), and the dates obtained in this study fall within this range. Fish Canyon Tuff apatite has been more variable in previous studies depending on specific sample locations (Farley, 2002; Gleadow et al., 2015). FCT average U concentration obtained here is 11.99 ppm, while Gleadow et al. (2015) found an average FCT apatite U concentration of 13.72 ppm. No substantial inter-element fractionation was witnessed from the change in spot size and depth between trials; average Durango apatite Ca concentrations between trials were within 2.4% and average BD and MMTS Ca concentrations between trials were within 1.7%.

X-ray micro-computed tomography (MicroCT)

We re-picked conodont elements from the previous laser-ablation epoxy pucks onto hole-punch sized disks (7.9 mm diameter) of sticky tape for X-ray micro-computed tomography (MicroCT) lab work. Disks were photographed on customized Nikon SMZ-U/100 stereomicroscopes for documentation prior to mounting. Up to five disks were then stacked on top of a standard thumbtack and taped together to create a single mount. The thumbtack mount is the ideal size and shape to insert into a holder, resting as close to the energy source as possible, maximizing image quality. The conodont mount was then bombarded with X-rays to generate

grayscale images of the individual conodont elements. In total 4 scans were performed imaging roughly 400 conodont elements at 5 μm resolution between image slices, with 500 to 600 slices per scan. MicroCT analyses were completed using an Xradia microXCT 400 Scanner at the University of Texas at Austin High-Resolution X-ray Computed Tomography Facility.

Image analyses were performed in ImageJ (Schneider et al., 2012) and BLOB3D (Ketcham, 2005). ImageJ was used to visualize the CT scans and BLOB3D was used for voxel-based quantitative analysis of all conodonts selected for (U-Th)/He dating. The procedure for calculating conodont size parameters followed the segmentation, separation, and extraction method described in Ketcham (2005). Segmentation in ImageJ began by identifying in which scans an individual conodont first appeared and ultimately disappeared. Conodonts were isolated by cropping images to the maximum two-dimensional horizontal slice area of the desired conodont element. The cropped scans were then modeled through a grayscale analysis using an 8-bit, 256-level color scale in BLOB3D. This was accomplished by first determining average grayscale values for conodont apatite and background air in each scan. The midpoint between these values was used as a threshold to separate conodont material from air. Voxels with grayscale values above the threshold were grouped as the conodont. We then extracted three-dimensional measurements from the scans and calculated surface area, volume, surface to volume ratio, and minimum and maximum axial dimensions and orientations (Ketcham, 2005). These calculations were made to better understand the impact of grain size and morphological variability on (U-Th)/He dates, and for future work on determining a morphology-independent alpha-ejection correction (see next section; Farley et al., 1996; Farley, 2002; Evans et al., 2008).

(U-Th)/He thermochronology

The (U-Th)/He method is based on the production of ^{4}He during radioactive decay of isotopes of U, Th, and Sm. Helium is mobilized by thermally activated volume diffusion; thus, temperature is the main factor in determining whether ^{4}He is retained or expelled during radioactive decay of parent isotopes. In apatite, helium is completely expelled above 80 °C and mostly retained below 40 °C (Wolf et al., 1996, 1998; House et al., 1999; Stockli et al., 2000). The AHe PRZ is an intermediary temperature range where He is neither entirely retained nor entirely expelled (Wolf et al., 1998). (U-Th)/He dates from samples in the PRZ are heavily influenced by slight differences in temperature at depth, which can help explain scatter in certain sample populations (e.g., House et al., 2001; Stockli et al., 2002). Additional factors that impact ^{4}He retention include grain size (e.g., Farley, 2000; Reiners and Farley, 2001), cooling rate (e.g., Dodson, 1973), and crystal lattice damage (e.g., Nasdala et al., 2001; Shuster et al., 2006).

We performed (U-Th)/He thermochronometry on 69 conodont elements from 15 samples. Up to 6 conodont aliquots were analyzed per sample. Conodont elements were first picked under customized Nikon SMZ-U/100 stereomicroscopes and placed into platinum tubes with the ends crimped to seal the grains within. Conodonts with distinct, identifiable morphologies such as blade denticles or cone elements of various sizes and without large fractures were selected for dating. We hoped to avoid selecting fragments with no discernable morphology, which was not possible in many samples, especially the Tule Spring Hills conodonts. Following picking, conodont elements were degassed using a Photon Machines diode and U.S. Laser Nd:YAG laser to 1070°C for five minutes. Aliquots were reheated until the re-extracts were <1% of the previous total. The gas released was spiked with ^{3}He for isotope dilution, purified using a gettering and cryogenic trapping system, and measured using a Blazers Prisma QMS-200 quadrupole mass spectrometer. Conodonts were then dissolved using 30% HNO_3 and spiked with U^{235}, Th^{230}, and Sm^{149}. The

resulting solution was measured for parent isotopes on a Thermo Scientific Element-2 high resolution ICPMS with CETAC micro-concentric nebulizer and ESI autosampler.

The alpha ejection correction (Ft) is a morphometry-based age correction applied to grains with non-ideal geometries to calculate for the effect of alpha particle ejection on (U-Th)/He ages. Alpha particles can eject from grains if they are near their surfaces, which can alter parent/daughter ratios and affect (U-Th)/He dates (Ziegler, 1977; Farley et al., 1996). The proximity to surface at risk for alpha ejection varies by parent isotope and ranges from 11 to 34 micrometers, and U-series parent isotopes are at risk up to 20 micrometers (Farley et al., 1996). Conodonts have highly variable, irregular shapes that are more susceptible to alpha ejection compared to grains with conventional morphologies. This issue could result in substantial parent/daughter fractionation at conodont margins where the morphology is thin, jagged, or pointy (e.g. near serrated tooth edges of blade conodont elements), and lead to CHe dates that are too young.

Standard Ft corrections are two-dimensional, calculated using length and width of grains with simple geometries. 2D corrections are not ideal for highly complex conodonts. Evans et al. (2008) first attempted 3D alpha ejection corrections using an erosional procedure to remove the outer 20 micrometers of grains. Our 3D Ft calculations were performed in BLOB3D, and CHe dates were reported with and without the Ft corrections in Table 5. All laboratory and analytical work was performed at the (U-Th)/He and U-Pb Geo-Thermochronometry Lab at the University of Texas at Austin. Data reduction was performed using the laboratory's in-house Excel-based software packages.

Scanning Electron Microscopy

Scanning electron microscopy was performed at the University of Kansas Microscopy & Analytical Imaging Lab. We attempted secondary electron (SE) and backscattered electron (BSE)

imaging, and energy dispersive X-ray spectroscopy (EDS) using a FEI Versa 3D Dual Beam with multiple detectors. Both SE and BSE techniques are useful for very high-resolution imaging of grain surfaces for a variety of materials, including fossil bones: SE imaging is ideal for detecting low-energy electrons emitted from light isotopes, while BSE imaging is better suited for detecting high-energy electrons from heavier isotopes (Hay and Sandberg, 1967; Bell, 1990; Joy, 1991; Turner-Walker and Syversen, 2002). EDS maps can be used to understand isotope distribution patterns at depth within grains at up to atomic-level resolution (Allen et al., 2012). Together, we hoped these techniques would produce a comprehensive data set of images that could aid in our interpretations of isotope distributions within conodonts and our understanding of the CHe data.

Sample preparation for imaging conodont surfaces was minimal. Conodont disks used for microCT scans were placed onto metal posts with double-sided black reflective tape and inserted into the SEM. Two polished epoxy pucks were also prepared with the goal of analyzing the internal structure of conodont elements from samples MM08 and BD16.

All conodont surfaces were imaged using the SE method, and several were imaged using BSE and EDS methods using the FEI Versa 3D Dual Beam microscope (Figures 12, 13, 14, 15). EDS test maps were generated in the AZtecEnergy EDS data reduction software program. Concentrations measured in the EDS program were too low to produce images that provided meaningful information to help with our interpretation of parent isotope distributions within conodonts, and further analysis was abandoned.

RESULTS

LA-ICPMS depth profiles

LA-ICPMS depth profiles reveal that trace and REEs are heterogeneously distributed within conodonts in a variety of patterns and with a range of concentrations. All measured trace and REE concentrations are consistently highest near conodont margins and decrease with depth. Significant intra- and inter-sample variability in trace element and REE concentrations was also observed. Concentrations and trends and their relationship with conodont histologies and CAI are described herein. Examples of LA-ICPMS depth profiles are presented in Figure 5. LA-ICPMS input specifications and a summary of external standard measured values are presented in Tables 1 and 2. A summary of elemental concentrations calculated from conodonts in each mountain range is presented in Table 3, and graphs of parent isotope concentrations measured from LA-ICPMS depth profiles in all grains that were dated are presented in Appendix A. The full calculated LA-ICPMS data set is is available through the IEDA (Interdisciplinary Earth Data Alliance) EarthChem (www.earthchem.org) at http://dx.doi.org/10.1594/IEDA/100631.

Compositional patterns

Most of the conodont elements analyzed possess a narrow rim at their margin that is heavily enriched in U, Th, Sm, and REEs. Rim enrichment is commonly 10x the concentration at depth and U and Th concentrations can exceed 100 ppm and 50 ppm, respectively. These rims can be up to 5 micrometer (μm) thick, but are commonly thinner than two mass cycles or <1.2 μm. Thicker rims may be artifacts of ablating at angles oblique to the conodont surface (see following sections and discussion).

Compositional patterns at depth are variable, with ~70% of conodont elements showing a relatively flat or homogeneous distribution pattern beyond their enriched margins and ~30%

showing a humped or U-shaped trace and REE distribution patterns that may be evidence of zoning (enrichment or depletion) within conodont elements. Zones of enrichment/depletion typically occur between 10 and 30 μm from the surface. We are unable to determine if these are concentric bands or axial zones because the irregular morphology of the individual conodont elements means that the laser ablation profiles were not always acquired perpendicular to the major growth axes. The distribution patterns are consistent for all measured elements, with the exceptions of Pb^{206}, Pb^{207}, and Pb^{208}, for which 10% of conodonts show isolated enrichments of up to 5x at depths between 10 and 30 μm.

We also observe different compositional patterns between light, middle, and heavy REEs. All REEs tend to be distributed in patterns similar to the radiogenic parent isotopes, meaning they consistently show enriched rims of 5 μm or less and relatively depleted cores with local zoning. Although distribution patterns are similar, measured concentrations differ between REEs. Conodonts commonly contain higher concentrations of LREEs compared to MREEs and HREEs. These distributional trends are seen in both the higher concentration margins and lower concentration cores. Margin La/Dy ratios are typically 2:1 to 10:1, and La/Yb ratios are typically 20:1 to 100:1. At the margins in Beaver Dam conodonts, LREE concentrations are often in the 5-10 ppm range, while MREE concentrations are in the 1-5 ppm range, and HREE concentrations are in the <1 ppm range. REE ratios remain similar at depth; La/Dy ratios are typically between 2:1 and 10:1, and La/Yb ratios are between 20:1 and 100:1. At depth in Beaver Dam conodonts, LREE concentrations range from 1-5 ppm, and MREE and HREE concentrations are consistently <1 ppm. Concentrations vary by sample; LREE concentrations are in the 10-100 ppm range in Mormon Mountains conodonts and >100 ppm in Tule Spring Hills conodonts, but the REE ratios are consistent.

Radioactive parent concentrations

Although LA-ICPMS depth profiles exhibit a wide range of element concentrations, these can be summarized into consistent concentration patterns. Concentrations at rims are substantially higher than at depth across the full data set: average U rim concentrations range from <1 ppm to 345 ppm, while average depth U concentrations range from <1 ppm to 41 ppm (where profiles are homogeneous). A summary of parent isotope concentrations is presented in Table 3. Concentrations vary widely between samples, for example rims of BD17 conodont elements mostly exceed 100 ppm U, while rims of BD16 conodont elements commonly contain less than 1 ppm U. These concentrations are also correlated with conodont tissue type and thermal alteration related to CAI. Average U, Th, and Sm concentrations measured through laser ablation ICPMS depth profiling were comparable to (U-Th)/He-based solution ICPMS measurements reported in Table 5.

Beaver Dam conodonts produced relatively consistent parent concentration data. Relative enriched rim concentrations range from 1 ppm to 345 ppm U, <1 ppm to 78 ppm Th, and <1 ppm to 72 ppm Sm (Table 3). At depth within Beaver Dam Mountains conodonts, average U concentrations range from <1 ppm to 25 ppm, average Th concentrations range from <1 ppm to 12 ppm, and average Sm concentrations range from <1 ppm to 46 ppm (Table 3). Rim enrichments of 5x to 10x depth concentration, and stable depth concentration profiles are consistent across all BD samples. Zoning at depth is typically consistent across all measured trace and REE isotopes in BD conodonts. Parent concentrations are extremely high in sample BD17, both at rims and at depth. BD17 conodonts consistently have rim U concentrations in excess of 100 ppm. Concentrations are lowest in samples BD15 and BD16, consistently lower than 7 ppm U at depth in both samples and in some instances lower than 1 ppm (Figure 5).

Conodonts from the Mormon Mountains have similar trace and REE concentrations to the Beaver Dam Mountains conodonts (Figure 5). Rim concentrations in Mormon Mountains conodonts range from 1 ppm to 109 ppm U, <1 ppm to 28 ppm Th, and 2 ppm to 96 ppm Sm (Table 3). At depth in the Mormon Mountains samples, average U concentrations range from 1 ppm to 10 ppm, average Th concentrations ranged from <1 ppm to 3 ppm, and average Sm concentrations range from 1 ppm to 8 ppm (Table 3). Concentrations in MM08 conodonts are typically 3 – 4 ppm higher at depth than in the other three Mormon Mountains samples. Depth zoning is consistent across all trace and REEs in the Mormon Mountains conodonts.

The Tule Spring Hills samples had the most variable concentration data. Trace element and REE concentrations at depth were typically high, while rim enrichments were the most variable (Figure 5). Rim concentrations ranged from 9 ppm to 207 ppm U, 23 ppm to 265 ppm Th, and 33 ppm to 331 ppm Sm (Table 3). At depth in Tule Springs samples average U concentrations ranged from 4 ppm to 41 ppm, average Th concentrations ranged from 18 ppm to 85 ppm, and average Sm concentrations ranged from 2 ppm to 83 ppm (Table 3). Many rims exceeded 10x concentrations at depth, but some rims actually had lower concentrations than at depth. Many conodonts produced depth profiles similar to Mormon and Beaver Dam conodonts, but some conodonts produced more variable profiles, while others broke during analysis. Tule Spring samples were the smallest and most fragmented conodonts, increasing likelihood for breakage, oblique ablation, and potential bias within the dataset.

Tissue type and CAI effects

The patterns of relative rim concentration enrichments and homogeneous depletion or zoning at depth correlate with conodont tissue type. Roughly 70% of the LA-ICPMS spots targeted hyaline crown tissue, which comprises the bulk of conodont structural assemblage. The remaining

30% of spots were ablated into albid crown tissue on the fringes of what were commonly blade and platform elements. Depth profiles in albid tissue produced U-shaped chemical isotope distribution patterns and lower heavy REE concentrations than hyaline tissue, which has gradual chemical isotope depletion patterns and higher trace element and REE concentrations (Figure 6). Large depletion zones, with average concentrations of <10 ppm, were seen deep in ablation pits within albid tissue. Hyaline tissue corresponded with higher concentrations; spot analyses produced concentrations in the 10 – 100 ppm range, sometimes exceeding 100 ppm. The character of laser ablation depth profiles with regard to albid and hyaline tissue is also similar to observations made by Trotter and Eggins, 2006.

We also see consistent relationships between measured concentrations and CAI. Average measured isotope concentrations inversely correlate with CAI across all trace and REE elements. In Beaver Dam Mountains samples average concentrations are substantially higher in CAI 2 conodonts (commonly >10 ppm U, and >100 ppm U in BD17) than CAI 3 conodonts (commonly <5 ppm U), in Mormon Mountains samples concentrations are slightly higher concentrations in CAI 2 conodonts (commonly >10 ppm U) than CAI 2.5 conodonts (commonly <10 ppm U), and in Tule Spring Hills samples concentrations are also higher in CAI 1.5 conodonts (commonly >20 ppm U) than CAI 2 conodonts (commonly <20 ppm U). With respect to rim enrichments, we see decreasing enrichment in trace and REEs near conodont surfaces with increasing CAI. This trend is evident in conodonts from all three mountain ranges. Rim enrichments are still typically 5x to 10x the concentration at depth in higher CAI conodonts in each mountain range. These two major trends (inverse correlation between concentrations and CAI, decreasing rim enrichment with increasing CAI) are consistent across the entire data set when all the LA-ICPMS data is evaluated

together. Tissue type differences may help explain some of the variability in concentrations between conodonts from the same samples that possess identical CAI.

CHe thermochronology

The CHe data show two distinct populations among our samples: the majority of conodonts (58 of 69) date younger than deposition, but a small portion (11 of 69) date older than deposition (Figure 7; Tables 4 and 5). CHe dates have substantial scatter within and between samples. Variation of uncorrected dates within each sample is commonly 20% but up to 150% about the mean. This is due to several factors (e.g., microstructural changes at increasing CAI; see following sections and discussion) that are as yet only loosely controlled or quantified. For this reason, we do not exclude any analyses in computing the final mean age for each sample. This is in contrast to typical practice for magmatic or detrital apatite mineral grains. For these, analytical errors are typically low, on the order of a percent or less, while within sample variation (e.g., repeated analyses on a single standard, are commonly about 5%). This means that aliquots are routinely excluded from final age interpretations. The discussion of CHe results in this section excludes the 3D Ft corrections, which range from 0.248 to 0.910 and are reported in Table 5.

CHe dates from each of the ranges studied are highly scattered in comparison to previous studies of the geologic and thermal history of the region (Hintze, 1986; Wernicke et al., 1985; Axen et al., 1990; Axen, 1993; Stockli, 1999; Bidgoli et al, 2015). The conodont apatite CHe dates are older than expected in all three mountain ranges and have considerably more variability. In comparison, traditional apatite (U-Th)/He samples from Bidgoli et al. (2015) consistently produced dates that were clustered and Miocene in age, and in agreement with AFT.

The six Beaver Dam Mountains (BD) samples produced the oldest CHe dates and are the most scattered. Paleodepth reconstruction of our samples following the strategy outlined in Bidgoli

et al. (2015) show that five of the seven BD samples reside near the apatite fission track partial annealing zone (PAZ; 60-110 °C; Stockli, 1999), while the other two samples (BD15 and BD16) date substantially older than depositional ages (Figure 4). Mean ages from BD samples near the PAZ range from 23.2 +/- 11.6 Ma to 72.4 +/- 21.7 Ma, but individual dates range from 0.7 +/- 0.01 Ma to 110.0 +/- 0.75 Ma (Tables 4 and 5). In contrast, samples BD15 and BD16 produce mean dates that are much older than the Mississippian depositional ages of the rocks themselves (Hintze, 1986), 883 +/- 49 Ma and 1282 +/- 560 Ma respectively (see timescale of Walker et al., 2013). Individual BD15 and BD16 dates range from 138 +/- 21 Ma to 1737 +/- 3.01 Ma. Samples BD02 and BD06 were partially destroyed during laboratory work; however, BD02 produces one CHe date (1.1 +/- 0.01 Ma) and BD06 produces three CHe dates (0.7 +/- 0.01 Ma, 59.2 +/- 0.4 Ma, and 62.5 +/- 0.6 Ma), all of which are younger than deposition.

The four Mormon Mountains (MM) samples in this study produce mean dates from 55.4 +/- 30 Ma to 94.0 +/- 49 Ma (Table 4). Individual dates from MM samples range from 14.8 +/- 0.14 Ma to 192.4 +/- 0.79 Ma, and all are younger than deposition (Table 5). In comparison, Bidgoli et al. (2015) found Mormon Mountains apatite produced average (U-Th)/He dates that ranged from 7.6 +/- 2.5 Ma to 14.6 +/- 0.5 Ma. In the restored-state cross section and paleodepth reconstruction in Figure 4, the Mormon Mountains conodonts plot at similar paleodepths to the respective Mormon Mountains apatite samples. Thus we expect the conodonts to produce similar CHe dates, but instead the conodonts produced older CHe dates with wider scatter. Assuming the closure temperature for conodont apatite is similar to magmatic apatite, these older CHe dates may be pointing to loss of parent elements.

The three Tule Spring Hills (TS) conodont samples produce the youngest trend in mean dates, ranging from 35.9 +/- 4.3 Ma to 68 +/- 41.4 Ma, and are the most reproducible cluster (Table

4). Individual Tule Spring dates range from 20.7 +/- 0.33 Ma to 98.4 +/- 0.90 Ma (Table 5). All Tule Spring CHe dates are also younger than the depositional age. Bidgoli et al. (2015) found Tule Spring Hills apatite samples produced average CHe dates that ranged from 16.0 +/- 3.7 Ma to 27.6 +/- 6.2 Ma. The TS conodonts plot 1-2 km shallower than their corresponding apatite samples in the paleodepth reconstruction in Figure 4, but produce mostly older CHe dates. It is not clear from the reconstructions if the samples from this study define a paleo-partial retention zone, as might be expected for samples at shallower paleodepths, or if these old dates indicate open-system behavior and possible parent isotope loss.

Grain size and effective U

As part of our analysis, we evaluate the CHe data for typical trends. Although no relationship between conodont mass and CHe date is evident (Figure 8), there is a strong inverse relationship between parent isotopes and CHe dates (Figures 9 and 10). The relationship can be represented by the effective U concentration (e[U]), the U concentration equivalent to the alpha productivity of the measured U and Th concentrations in a grain, given by [U] + 0.235x[Th] (Flowers et al., 2009). We exclude Sm due to its low contribution to total alpha particles. Across the full data set, e[U] ranges from 0.2 to 185.8 ppm, with high e[U] samples (>40 ppm) producing young CHe dates of less than 50 Ma. But perhaps the most interesting observation is that CAI 3 conodonts with ages older than deposition (samples BD15 and BD16) all have very low e[U] (<10 ppm). In total, 10 of 13 samples from the three mountain ranges have strong inverse relationships between e[U] and CHe date. The remaining three samples had dates that are either uncorrelated with e[U] (BD06 and TS04) or have positive correlations (BD18).

Conodont tissue type and CAI effects

There appears to be no correlation between tissue type and cooling age. Conodonts with predominantly albid tissue do not produce CHe dates that are quantifiably different from conodonts with predominantly hyaline. Albid tissue does, generally, have lower trace element and REE concentrations than hyaline tissue, but these lower concentrations do not appear to impact CHe dates. The most significant trend in the CHe age data is the strong correlation between CAI and CHe date. Conodonts with higher CAI values consistently have older CHe dates and substantially more scatter in individual dates. Most CAI 3 conodonts produced dates older than depositional age of the rocks themselves. In addition, the Tule Spring Hills samples had the lowest CAI values (1.5 and 2) and produced the youngest mean cooling dates.

The CHe dates from all three ranges produce a consistent trend with CAI (Figure 11). The Beaver Dam Mountains samples contain the highest CAI conodonts; BD15, BD16, and BD20 are CAI 3 while BD02, BD06, BD17, and BD18 are CAI 2. CAI 3 Beaver Dam conodonts produce older CHe dates than CAI 2 conodonts, most of which are older than deposition and have higher scatter (BD15 and BD16 date older than deposition, BD20 dates younger). The Mormon Mountains conodonts are in the middle of the CAI range in this study. Sample MM08 is CAI 2, and samples MM06, MM09, and MM14 are CAI 2.5. MM08 conodonts produce the youngest CHe dates of the four Mormon Mountains samples. The Tule Spring Hills samples yield the lowest CAI conodonts. Samples TS01 and TS08 are CAI 1.5, and TS04 is CAI 2. CAI 2 Tule Spring conodonts produce older CHe dates with higher scatter than CAI 1.5 conodonts. Thus the direct relationship between CAI and CHe age is evident in each of the three mountain ranges.

Scanning electron microscopy

Conodont surface microstructural characteristics are identified through SE and BSE imaging[1] (Figure 12). The images show overgrowth patterns and crystallographic orientations that, when used in conjunction with existing information about conodont CAI and tissue types, allow us to make a qualitative assessment of microstructural changes associated with degree of thermal alteration. Crystallographic orientations roughly correlate with CAI-related observations from Nöth (1998). In Figure 13, conodonts with a range of CAIs can be observed. The CAI 1.5 and 2 conodonts clearly show that the microcrystallites are oriented nearly perpendicular to the major axis of the conodont element. By comparison, the CAI 2.5 conodonts show a shift in the orientation of microcrystals, to nearly 45 degrees. In CAI 3 conodonts, microcrystals become oriented closer to parallel to the major axis of the conodont.

In addition to the change in orientation of microcrystallites, evidence of surface corrosion is apparent in some of the CAI 2.5 and 3 conodonts. Corrosion features include pocked, pitted, and/or frosted surfaces that indicate textural alteration may have occurred (Nöth, 1998; Konigshof, 2003). Conodonts from samples BD15, BD16, and BD20 samples show smaller pocked and pitted apatite crystallites less than 10 μm in diameter, as well as larger dolomite rhombs that cover conodont exteriors. In Figure 14a, a CAI 2.5 MM06 conodont has a surface pattern that appears pocked and pitted, as well as several fractures in the upper-right corner of the SE image. A similar pocked and pitted texture is seen on the surface of a CAI 3 BD20 conodont in Figure 14b. These corrosion features are less common in CAI 1.5 and 2 conodonts, where mineral overgrowth patterns are more random.

[1] [1] The full suite of SEM images is available through the IEDA (Interdisciplinary Earth Data Alliance) EarthChem Library (www.earthchem.org) at http://dx.doi.org/10.1594/IEDA/100632.

Scans of the sidewalls of laser ablation pits show that microstructural heterogeneities within individual conodont elements are both real and visible. The conodont elements were tilted and reimaged at various angles to confirm that the appearance of microstructural changes, represented as different shades of gray, are not artifacts of the imaging process (Figure 15). At near-surface level, tilted scans show that the margins of the conodont grains, which vary in thickness from 1 to 5 μm, appear darker than the interior of the laser ablation pit. At depth, SE imaging uncovers dark gray sections within the sidewalls of laser ablation pits that typically correlate with zoning in the laser ablation data.

We were unable to obtain much information from EDS maps to aid in the analysis of internal composition of conodont elements. Count rates were very low for REEs and heavy nuclides on conodont surfaces and in polished slabs, which made the maps not particularly useful. Although the EDS technique was abandoned, EDS mapping did initially show surface counts of U and Th elements appear lower in samples that dated older than deposition than samples that dated younger.

DISCUSSION

CHe data from this study show that a majority of the samples were thermally reset in the Cenozoic. These conodonts range in CAI from 1.5 to 3 and likely experienced maximum burial temperatures of ≤200 °C (Harris, 1979; Crafford and Harris, 2005) during Cretaceous to early Cenozoic thrusting (Wernicke et al., 1985; Axen et al., 1990; Axen, 1993). Thermal resetting of CAI 1.5 (50-90 °C; Epstein et al., 1977) suggests conodonts have a closure temperature of <90 °C and probably close to 60-70 °C, confirming the results of Peppe and Reiners (2007).

Although many of the conodont samples studied here are thermally reset and show promise for the CHe method, paleodepth reconstructions of the samples show that most of the dates do not align well with ages from previous thermochronology studies in the region (Stockli, 1999; Bidgoli et al., 2015) and are generally too old (Figure 4). Additionally, an inverse relationship between e[U] and CHe date is evident in 10 out of 13 of the samples (Figure 10). Most of the CAI 3 Beaver Dam Mountains conodonts (11 out of 18) produced CHe dates much older than the depositional ages of the samples (Figure 11) and had exceptionally low e[U]. Many samples also have high Th contents relative to U (e.g., Tule Spring Hills samples typically have Th/U ratios >4; Table 5), suggesting preferential loss of U in these samples. Collectively, these observations confirm an imbalance between daughter He and parent U, Th, and Sm isotopes. Several questions arise from these observations. What is causing open-system behavior? What factors influence parent isotope mobility post-exhumation?

Possible causes of open-system behavior

Incomplete dissolution of the conodonts in the (U-Th)/He laboratory is a possible cause of the anomalously old CHe dates and large scatter in the data, and could be a particular concern with

dissolution of large grains (Reiners, 2005). However, no trend was observed between CHe date and grain size (mass) (Figure 7). Similarly, several individual conodonts in certain samples (BD02, BD06, BD17) produced dates that are younger than expected, which is contrary to incomplete recovery of parent isotopes. Although we cannot entirely rule out the possibility of incomplete grain (conodont element) dissolution, based on the above observations and discussion to follow, we believe this is an unlikely cause.

The imbalance between parent and daughter isotopes indicates the He was already generated, so parent isotope loss had to occur below the closure temperature, post-exhumation and cooling of our samples. It is possible that a naturally occurring acid leeching process in the host rock is the underlying cause, but we believe element loss in the laboratory is more likely. Whole-rock carbonate dissolution procedures using dilute acids, usually formic or acetic, are known to impact the number of conodonts that a sample yields (e.g. Harris and Sweet, 1989; Jeppsson and Anehus, 1995; Jeppsson et al., 1999; Jeppsson, 2005), so it follows that these procedures could also impact geochemical data derived from them.

Results from a limited number of studies evaluating the impact laboratory dissolution procedures on light isotopes are conflicting (e.g., Wheeley et al. 2012; Quinton et al., 2016), and highlight the need for robust assessments of the impact of these procedures on geochemical data. Relationships between light oxygen isotopes in conodonts and CAI, tissue type, and carbonate dissolution techniques have been documented in previous paleoclimate and seawater chemistry studies (Wenzel et al., 2000; Trotter et al., 2008; Quinton et al., 2016; Wheeley et al., 2012). Some researchers found no significant difference in light isotopes concentrations between CAI 1 conodonts extracted using different dissolution techniques, as well as no difference in oxygen concentrations between tissue types (Trotter et al., 2008; Quinton et al., 2016). By contrast, other

studies (Wenzel et al., 2000; Wheeley et al., 2012) showed that oxygen isotope ratios in conodonts are statistically variable at CAI 1 and increasingly so at higher CAIs, and also variable between tissue types. The degree of variability in oxygen isotope ratios may also be impacted by the dissolution procedure. Wheeley et al. (2012) demonstrated that the traditional double-buffered formic acid dissolution procedure yielded more variable oxygen isotope data compared to acetic acid and other extraction methods in otherwise identical conodonts.

Although we cannot confidently determine where or when our samples experience open-system behavior, our results suggest that susceptibility to parent isotope loss is variable in conodonts and influenced by a range of factors including heterogeneous parent isotope distributions and thermal alteration (CAI) of our conodonts. Other factors may include conodont histology and possible differences between conodont genera and/or species.

Non-uniform parent isotope distributions

From the LA-ICPMS data, we know that parent isotopes are distributed heterogeneously within conodonts, with the majority of parent isotopes concentrated near the outer margins (Figures 5 and 6). But comparing our work to previous LA-ICPMS studies is complicated by how LA-ICPMS data is typically treated; some researchers ignore the outer margin of conodonts and focus on interior profiles with lower concentrations (Trotter and Eggins, 2006), which best reflect the primary biomineral composition (Millard and Hedges, 1996; Eggins et al., 2003; Trotter and Eggins, 2006). Compositional differences on conodont surfaces are usually interpreted to be the result of contamination or external debris and not reported (Trotter and Eggins, 2006). Relative rim enrichments observed in this study are most likely the result of diagenesis. Studies have shown that trace and REEs are strongly absorbed postmortem in biogenic apatite (Bernat, 1975; Wright et al., 1984; Millard and Hedges, 1996; Eggins et al., 2003; Trotter and Eggins, 2006). Uranium

and REE uptake is fast and may reflect groundwater geochemistry during early burial and diagenesis (Wright et al., 1984; Millard and Hedges, 1996; Eggins et al., 2003; Trotter and Eggins, 2006; Bright et al., 2009). But the low porosity and permeability of conodonts means that trace and REEs cannot diffuse deep into the tissue; thus, they become concentrated near conodont surfaces (Pietzner et al., 1968; Wright et al., 1984; Wright et al., 1990; Trotter and Eggins, 2006; Bright et al., 2009).

For CHe dates, the non-uniform parent isotope distributions affect both the propensity for parent isotope loss and alpha ejection, which greatly complicates the potential for the method and resulting dates. Enrichment of parent isotopes near the element surface means that grain edges may be more prone and sensitive to parent loss. Similarly, this enrichment means that daughter production and ejection at conodont margins is greater than is being accounted for in our uncorrected and Ft-corrected CHe dates (Table 5).

Conodont CAI impacts

The pattern of increasingly old and scattered CHe dates and depressed rim and depth concentrations of our LA-ICPMS depth profiles, both with increasing CAI, suggests that thermal alteration of conodont surfaces is a major contributing factor for parent mobility (Figures 5 and 11). Microstructural changes that commonly occur between CAI 1 and 3 are surface recrystallization, including changes in grain size and orientation, and corrosion (Nöth, 1998; Königshof, 2003; Ebneth et al., 1997; Figure 13). Each of these processes may influence the susceptibility for parent loss in the low temperature history of our conodonts and our resulting CHe dates.

It is possible that both corrosion and recrystallization impact the rim concentrations of the studied conodonts. Corrosion, evidenced by frosted, pocked, and pitted textures, may increase

near-surface porosity and permeability with increasing CAI (Nöth, 1998; Königshof, 2003; Figure 14). Diagenetic processes have been shown to decrease internal surface area and increase porosity of bone structures (Hedges and Millard, 1995; Millard and Hedges, 1996), which may make some samples more prone to geochemical alteration by fluids during the dissolution procedure. Changes in apatite crystal size, habit, and orientation with CAI may also influence chemical stability. For example, larger numbers of crystal dislocations/defects and subgrain boundaries may be present in higher CAI conodonts (Trotter et al., 2007. Additionally, previous studies have shown conodonts to be increasingly brittle at higher CAI (Garcia-Lopez et al., 1997; Nöth, 1998; Königshof, 2003), promoting development of fractures and cleavages (Rejebian et al. 1987; Garcia-Lopez et al., 1997; Nöth, 1998; Königshof, 2003). Such effects may increase the surface area and contact with dilute acids during rock digestion and increase the potential for parent loss in conodonts.

Conodont tissue type and other effects

While notable differences in trace and REE concentrations exist, no trends were identified between tissue type and cooling age. Because all conodonts in this study are comprised of multiple tissue types, their solution ICPMS concentrations and CHe dates represent averages of all the different apatite tissue types present. Thus isolating tissue type as an independent variable to evaluate against CHe dates was not possible with the existing method. Conodont porosity and permeability impacts parent isotope and REE distributions, in theory it is possible that tissue type plays a minor role in influencing the CHe results. In-situ laser spot dating using a method similar to that proposed by Evans et al. (2015) may permit a more quantitative analysis of the effect of conodont tissue type on CHe dating in the future.

Genera- and species-specific differences between conodonts may also factor into susceptibility to surface alteration and parent isotope mobility. Rejebian et al. (1987) demonstrated that platform conodonts reach higher CAI values more quickly during artificial maturation experiments than other morphologies. Evolutionary changes over time and morphology differences between bar, blade, cone, and platform elements and their respective surface ornamentations could also impact how conodonts respond to dissolution techniques. Different species of conodonts have different shapes and sizes that may have different microstructural characteristics, such as size of dental elements, enamel thickness, internal and surface lamellae development patterns, etc. (Burnett and Hall, 1992; Donoghue, 2001). These differences may affect their structural integrity and geochemical composition, which impacts (U-Th)/He dating potential.

Future of the CHe method

Several key challenges remain in advancing the emerging CHe method. Based on the evidence of open system behavior, additional study is needed to evaluate the potential impacts of laboratory dissolution procedures on geochemical data derived from conodonts. LA-ICPMS and CHe data could be acquired from conodonts processed using different digestion solutions and procedures, similar to the experimental setup in Quinton et al. (2016). Sample splits could be dissolved using unbuffered and buffered solutions of formic and acetic acid, of varying strengths. Such experiments could also evaluate the potential effects of prolonged exposure to weak acids, by varying acid processing times on sample splits. These controlled experiments could provide a quantitative assessment of the magnitude of impact that dissolution prcedures have on conodonts of different CAIs, sizes, morphologies, and genera/species, which would speak to the overall utility of conodonts as (U-Th)/He thermochronometers.

Heterogeneous elemental distributions within conodonts also pose a challenge for conodont CHe dating, and methods will need to be developed to properly incorporate such data into an accurate 3D Ft correction. Recent work has focused on improving Ft corrections for grains with non-spherical shapes and heterogeneous isotope distributions. Hourigan et al. (2005) demonstrated that assuming homogeneous isotope distribution can result in up to 30% error in zircon (U-Th)/He ages. Evans et al. (2008) showed that a 3D erosion procedure removing the outer 20 μm of a grain can improve correction accuracy and reduce the Ft by up to 6%, given that alpha particle stopping distances are roughly 20 μm in apatite. Bargnesi et al. (2016) developed a custom alpha-ejection correction for zircons that extrapolates data from LA-ICPMS depth profiles and adjusted (U-Th)/He ages up to 39%. Although successful in many regards, these studies are deficient for our purposes because their work applies to grains with much simpler geometries and parent isotope distribution patterns than conodonts. Future 3D Ft corrections for conodonts will have to account for the exceptionally complicated morphologies and isotope distributions, and for potential issues related to differences in apatite tissue type and CAI.

CONCLUSIONS

This study evaluates the suitability of biogenic apatite from conodonts as a (U-Th)/He thermochronometer by dating conodonts extracted from surface outcrops located in the footwalls of three well-studied low-angle normal faults (LANFs) in eastern Nevada and western Utah. New data provided here shows promise for the emerging CHe method. Thermally reset samples confirm a closure temperature for conodont apatite of <90 °C. Although the majority of the samples are thermally reset, most of the CHe dates are older than anticipated, with some conodonts producing dates older than the depositional age of the samples, a clear indication of open system behavior during the post-cooling, low temperature history of the samples.

Our results do not allow us to conclusively determine the cause for open-system behavior; however, the data acquired by this study show that CHe dates are influenced by a number of factors. The most significant factor is parent loss during conodont extraction, and another key factor is heterogeneous parent distribution. LA-ICPMS depth profiles show that conodont margins have thin rims (1-5 μm) that are typically highly enriched (5x-10x) in trace and REEs that probably reflects uptake during early diagenesis; whereas, concentrations at depth are lower and reflective of primary compositions. Apatite grain morphologies and tissue type (albid or hyaline) also play a fundamental role in isotope concentrations and distribution patterns, likely based on differences in microcrystalline structure, porosity, and permeability, but do not appear to have a quantifiable impact on CHe dates in this study.

Our results also show that microstructural changes associated with increasing CAI may be a contributing factor for anomalously old CHe dates and scatter in the data. Thermal alteration by way of surface recrystallization and corrosion may make sample more susceptible to parent isotope loss. Although a naturally occurring acid leeching process in the host rock cannot be rule out, we

suspect that whole-rock carbonate dissolution procedures using dilute formic acid is a more likely cause. Future work will focus on evaluating the impact of dissolution procedures on geochemical data and CHe dates from conodonts of different CAIs, sizes, morphologies, and genera/species.

REFERENCES

Allen L.J., D'Alfonso, A.J., Freitag, B., and Klenov, D.O., 2012, Chemical mapping at atomic resolution using energy-dispersive x-ray spectroscopy: Materials Research Society Bulletin, v. 37, p. 47-52.

Anders, M.H., Christie-Blick, N., and Walker, C.D., 2006, Distinguishing between rooted and rootless detachments, a case from the Mormon Mountains of southeastern Nevada: Journal of Geology, v. 114, p. 645– 664.

Anders, M.H., Fouke, B.W., Zerkle, A.L., Tavarnelli, E., Alvarez, W., and Harlow, G.E., 2010, The role of calcining and basal fluidization in the long runout of carbonate slides: an example from the Heart Mountain slide block, Wyoming and Montana, USA: The Journal of Geology, v. 118, no 6, p. 577-599.

Armstrong, P.A., 2005, Thermochronometers in Sedimentary Basins: Reviews in Mineralogy & Geochemistry, v. 58, p. 499-525.

Armstrong, R.L., 1968, Sevier Orogenic Belt in Nevada and Utah: Geological Society of America Bulletin, v. 79, p. 429-458.

Axen, G.J., Wernicke, B.P., Carpenter, D.G., Carpenter, J.A., Bradley, M.D., Franz, U.A., and Reber, S.J., 1989, Comment and Reply "On the role of isostasy in the evolution of normal fault systems": GEOLOGY, v. 17, no. 8, p. 774-776.

Axen, G.J., Wernicke, B., and Snow, J.K., 1990, Basin and Range extensional tectonics at the latitude of Las Vegas, Nevada: Geological Society of America Bulletin, v. 100, p. 1738-1757.

Axen, G.J., 1993, Ramp-flat detachment faulting and low- angle normal reactivation of the Tule Springs thrust, southern Nevada: Geological Society of America Bulletin, v. 105, p. 1076–1090.

Axen, G.J., 2004, Mechanics of low-angle normal faults: Rheology and Deformation of the Lithosphere at Continental Margins, p. 46-91.

Bargnesi, E.A., Stockli, D.F., Hourigan, J.K., and Hager, C., 2016, Improved accuracy of zircon (U-Th)/He ages by rectifying parent nuclide zonation with practical methods: Chemical Geology, v. 426, p. 158-169.

Behnken, F.H., 1975, Leonardian and Guadalupian (Permian) conodont biostratigraphy in western and southwestern United States: Journal of Paleontology, v. 49, p. 284-315.

Bell, L.S., 1990, Palaeopathology and diagenesis: an SEM evaluation of structural changes using backscattered electron imaging: Journal of Archaeological Science, v. 17, no. 1, p. 85-102.

Bergström, S.M., 1970, Conodont biostratigraphy of the Middle and Upper Ordovician of Europe and eastern North America: Geological Society of America Memoirs, v. 127, p. 83-162.

Bernat, M., 1975, Les isotopes de l'uranium et du thorium et les terres rares dans l'environment marin: Cah. OSTROM Ser. Geol., v. 7, p. 68-83.

Bidgoli, T.S., Stockli, D.F., and Walker, J.D., 2015, Low temperature thermochronologic constraints on the kinematic histories of the Castle Cliffs, Tule Spring, and Mormon Peak

detachments, southwestern Utah and southeastern Nevada: Geosphere, v. 11, no. 3, p. 850-867.

Blanco-Ferrera, S., Sanz-López, J., García-López, S., Bastida, F., and Luz Valín, M., 2010, Conodont alteration and tectonothermal evolution of a diagenetic unit in the Iberian Variscan belt (Ponga-Cuera unit, NW Spain): Geol. Mag., p. 1-15.

Bohannon, R.G., 1983, Mesozoic and Cenozoic tectonic development of the Muddy, North Muddy, and northern Black Mountains, Clark County, Nevada: The Geological Society of America Memoirs, v. 157, p. 125-148.

Brady, R.J., 2002, Very high slip rates on continental extensional faults: new evidence from (U-Th)/He thermochronometry of the Buckskin Mountains, Arizona: Earth and Planetary Science Letters, v. 197, p. 95-104.

Bright, C.A., Cruse, A.M., Lyons, T.W., MacLeod, K.G., Glascock, M.D., and Ethington, R.L., 2009, Seawater rare-earth element patterns preserved in apatite of Pennsylvanian conodonts?: Geochimica et Cosmochimica Acta, v. 73, p. 1609-1624.

Burnett, R.D., 1988, Physical and chemical changes in conodonts from contact-metamorphosed limestones: Irish Journal of Earth Sciences, v. 9, p. 79-119.

Burnett, R.D., and Hall, J.C., 1992, Significance of ultrastructural features in etched conodonts: Journal of Paleontology, v. 66, no. 2, p. 266-276.

Carpenter, D.G., 1989, Geology of the North Muddy Mountains, Clark County, Nevada and regional structural synthesis: fold-thrust and basin-range structure in southern Nevada, southwest Utah, and northwest Arizona [M.S. Thesis]: Corvallis, Oregon, Oregon State University, p. 1-154.

Carpenter, J.A., and Carpenter, D.G., 1994, Analysis of basin-range and fold-thrust structure, and reinterpretation of the Mormon Peak detachment and similar features as gravity slide systems, southern Nevada, southwest Utah and northwest Arizona, *in* Dobbs, S.W., and Taylor, W.J., eds., Structural and stratigraphic investigations and petroleum potential of the Nevada, with special emphasis south of Railroad Valley producing trend, Volume 2: Nevada Petroleum and Geothermal Society Publication 9, p. 15–52.

Chen, J., Algeo, T.J., Zhao, L., Chen, Z., Cao, L., Zhang, L., and Li, Y., 2015, Diagenetic uptake of rare earth elements by bioapatite, with an example form Lower Triassic conodonts of South China: Earth-Science Reviews, p. 1-22.

Christie-Blick, N., Anders, M.H., Wills, S., Walker, C.D., and Renik, B., 2007, Observations from the Basin and Range Province (western United States) pertinent to the interpretation of regional detachment faults: Geological Society, London, Special Publications, v. 282, p. 421-441.

Clark, M.K., Farley, K.A., Zheng, D., Wang, Z, and Duvall, A.R., Early Cenozoic faulting of the northern Tibetan Plateau margin from apatite (U-Th)/He ages: Earth and Planetary Science Letters, v. 296, p. 78-88.

Cogné, N., Gallagher, K., and Cobbold, P.R., 2011, Post-rift reactivation of the onshore margin of southeast Brazil: Evidence from apatite (U-Th)/He and fission-track data: Earth and Planetary Science Letters, v. 209, p. 118-130.

Crafford, E.J., and Harris, A.G., 2005, New digital conodont color alteration index (CAI) maps of Nevada: The Geological Society of America Abstracts with Programs, v. 37, no. 7, p. 379.

Crowhurst, P.V., Green, P.F., and Kamp, P.J., 2002, Appraisal of (U-Th)/He apatite thermochronology as a thermal history tool for hydrocarbon exploration: An example from the Taranaki Basin, New Zealand: AAPG Bulletin, v. 86, no. 10, p. 1801-1819.

Crowley, P.D., Reiners, P.W., Reuter, J.M., Kaye, and G.D., Laramide exhumation of the Bighorn Mountains, Wyoming: An apatite (U-Th)/He thermochronology study: GEOLOGY, v. 30, no. 1, p. 27-30.

Dodson, M.H., 1972, Closure Temperature in Cooling Geochronological and Petrological Systems: Contr. Mineral. and Petrol., v. 40, p. 259-274.

Donoghue, P.C., 2001, Microstructural variation in conodont enamel is a functional adaptation: Proc. R. Soc. Lond., v. 268, p. 1691-1698.

Ebneth, S., Diener, A., Buhl, D., and Veizer, J., 1997, Strontium isotope systematics of conodonts: Middle Devonian, Eifel Mountains, Germany: Palaeogeography, Palaeoclimatology, Palaeoecology, v. 132, p. 79-96.

Eggins, S., Grün, R., Pike, A., Shelley, M., Taylor, L., 2003, ^{238}U, ^{232}Th profiling and U-series isotope analysis of fossil teeth by laser ablation-ICPMS: Quaternary Science Reviews, v. 22, p. 1373-1382.

Eggins, S.M., Kinsley, L.P.J., and Shelley, J.M.G., 1998, Deposition and element fractionation processes during atmospheric pressure laser sampling for analysis by ICP-MS: Applied Surface Science, v. 127-129, p. 278-286.

Elrick, M.B., 2002, U-Pb isotopic age dating of Devonian conodonts: a new method for dating Paleozoic marine sedimentary deposits?: The Geological Society of America Rocky Mountain 54th Annual Meeting Abstracts with Programs, v. 34, no. 4, p. 52.

Epstein, Anita G., 1977, Conodont color alteration—an index to organism metamorphism: Geological Survery Professional Paper 995, p. 1-31.

Evans, N.J., McInnes, B.I., McDonald, B., Danišík, M., Becker, T., Vermeesch, P., Shelley, M., Marillo-Sialer, E., Patterson, D.B., 2015, An in situ technique for (U-Th-Sm)/He and U-Pb double dating: J. Anal. At. Spectrom, v. 30, p. 1636-1645.

Evans N.J., McInnes, B.I., Squelch, A.P., Austin, P.J., McDonald, B.J., and Wu, Q., 2008, Application of X-ray micro-computed tomography in (U-Th)/He thermochronology: Chemical Geology, v. 257, p. 101-113.

Farley, K.A., 2000, Helium diffusion from apatite: General behavior as illustrated by Durango fluorapatite: Journal of Geophysical Research, v. 105, p. 2903–2914.

Farley, K.A., and Stockli, D.F., 2002, (U-Th)/He dating of phosphates: Apatite, monazite, and xenotime, *in* Kohn, M.J., et al., eds., Phosphates: Geochemical, geobiological, and materials importance: Reviews in Mineralogy and Geochemistry, v. 48, p. 559–578.

Farley, K.A., Wolf, R.A., and Silver, L.T., 1996, The effects of long alpha-stopping distances on (U-Th)/He ages: Geochimica et Cosmochimica Acta, v. 60, p. 4223– 4229.

Felger, T.J., and Beard, L.S., 2010, Geologic map of Lake Mead and surrounding regions, southern Nevada, southwestern Utah, and northwestern Arizona, *in* Umhoefer, P.J., et al., eds., Miocene tectonics of the Lake Mead region, Central Basin and Range: Geological Society of America Special Paper 463, p. 29–38.

Fitzgerald, P.G., Duebendorfer, E.M., Faulds, J.E., and O'Sullivan, P., 2009, South Virgin-White Hills detachment fault system of SE Nevada and NW Arizona: Applying apatite fission track thermochronology to constrain the tectonic evolution of a major continental detachment fault: Tectonics, v. 28, p. 1-31.

Fitzgerald, P.G., Fryxell, J.E., and Wernicke, B.P., 1991, Miocene crustal extension and uplift in southeastern Nevada:Constraints from fission track analysis: GEOLOGY, v. 19, no. 10, p. 1013-1016.

Flowers, R.M., 2014, Quantitative Constraints on Thermal Histories in Carbonates and Marine Shales: Conodont (U-Th)/He Thermochronology: 59th Annual Report on Research 2014 Under Sponsorship of the ACS Petroleum Research Fund, p. 1-6.

Flowers, R.M., Ketcham, R.A., Shuster, D.L., and Farley, K.A., 2009, Apatite (U-Th)/He thermochronometry using a radiation damage accumulation and annealing model: Geochimica et Cosmochimica Acta, v. 73, p. 2347–2365.

Flowers, R.M., Wernicke, B.P., and Farley, K.A., 2008, Unroofing, incision, and uplift history of the southwestern Colorado Plateau from apatite (U-Th)/He thermochronometry: GSA Bulletin, v. 120, no. 5/6, p. 571-587.

Fuchs, A., 1989, Determination of the burial temperature in the Ordovician of Thuringia and Scandinavia by means of conodont color: Neues Jahrbuch fur Geologie und Palaontologie. Monatshefte, v. 7, p. 390-399.

Garcia-López, S., Brime, C., Bastida, F., and Sarmiento, G.N., 1997, Simultaneous use of thermal indicators to analyse the transition from diagenesis to metamorphism: an example from the Variscan Belt of northwest Spain: Geological Magazine, v. 194, p. 323-334.

Gavillot, Y., Axen, G.J., Stockli, D.F., Horton, B.K., and Fakhari, M.D., 2010, Timing of thrust activity in the High Zagros fold-thrust belt, Iran, from (U-Th)/He thermochronometry: Tectonics, v. 29, p. 1-25.

Gleadow, A., Harrison, M., Kohn, B., Lugo-Zazueto, R., and Phillips, D., 2015, The Fish Canyon Tuff: A new look at an old low-temperature thermochronology standard: Earth and Planetary Science Letters, v. 424, p. 95-108.

Hanan, M.A., and Totten, M.W., 1996, Analytical techniques for the separation and SEM identification of heavy minerals in mudrocks: Journal of Sedimentary Research, p. 1027-1030.

Harris, A.G., and Sweet, W.C., 1989, Mechanical and chemical techniques for separating microfossils from rock, sediment, and residue matrix: Paleotechniques, v. 4, p. 70-86.

Harris, A.G., 1979, Conodont color alteration, an organo-mineral metamorphic index, and its application to Appalachian basin geology: SEPM Special Publication No. 26, p. 3-16.

Hay, W.M., and Sandberg, P.A., 1967, The scanning electron microscope, a major break-through

for micropaleontology: Micropaleontology, v. 13, no. 4, p. 407-418.

Hedges, R.E., and Millard, A.R., 1995, Bones and Groundwater: Towards the Modeling of Diagenetic Processes: Journal of Archaeological Science, v. 22, p. 155-164.

Heller, P.L., Bowdler, S.S., Chambers, H.P., Coogan, J.C., Hagen, E.S., Shuster, M.W., and Windslow, N.S., 1986, Time of intial thrusting in the Sevier orogenic belt, Idaho-Wyoming and Utah: GEOLOGY, v. 14, p. 388-391.

Hintze, L.F., 1986, Stratigraphy and structure of the Beaver Dam Mountains, Utah, *in* Griffin, D.T., and Phillips, W.R., eds., Thrusting and extensional structures and mineralization in the Beaver Dam Mountains, southwestern Utah: Utah Geological Association Special Publication 15, p. 1–36.

Hogancamp N.J., Barrick, J.E., and Strauss, R.E., 2016, Geometric morphometric analysis and taxonomic revision of Gzhelian (Late Pennsylvanian) conodont *Idiognathodus simulator* from North America: Acta Palaeontologica Polonica, v. 61, p. 477-502.

Hourigan, J.K., Reiners, P.W., and Brandon, M.T., 2005, U-Th zonation-dependent alpha-ejection in (U-Th)/He chronometry: Geochimica et Cosmochimica Acta, v. 69, no. 13, p. 3349-3365.

House, M.A., Farley, K.A., and Kohn, B.P., 1999, An empirical test of helium diffusion in apatite: borehole data from Otway basin, Australia: Earth and Planetary Science Letters, v. 17, p. 463-474.

House, M.A., Wernicke, B.P., and Farley, K.A., 1998, Dating topography of the Sierra Nevada, California, using apatite (U-Th)/He ages: Nature, v. 396, p. 66-69.

House, M.A., Wernicke, B.P., and Farley, K.A., 2001, Paleo-geomorphology of the Sierra Nevada, California, from (U-Th)/He ages in apatite: American Journal of Science, v. 301, p. 77-102.

Jeppsson, L., 2005, Biases in the recovery and interpretation of micropaleontological data: Symposium on Bias and Completeness in the Conodont Fossil Record held at the 8th International Conodont Symposium, Paleontological Association, no. 73, p. 57-71.

Jeppsson, L., and Anehus, R., 1995, A buffered formic acid technique for conodont extraction: Journal of Paleontology, v. 69, no. 4, p. 790-794.

Jeppsson, L., Anehus, R., and Fredholm, D., 1999, The optimal acetate bufferec acetic acid technique for extracting phosphatic fossils: Journal of Paleontology, v. 73, p. 964-972.

Joy, D.C., 1991, The theory and practice of high-resolution scanning electron microscopy: Ultramicroscopy, v. 37, p. 216-233.

Ketcham, R.A., 2005, Computational methods for quantitative analysis of three-dimensional features in geological specimens: Geosphere, v. 1, no. 1, p. 32-41.

Königshof, P., 1992, Der Farbänderungsindex von Conodonten (CAI) in paläozoischen Gesteinen (Mitteldevon bis Unterkarbon) des Rheinischen Schiefergebirges – eine Ergänzung zur Vitrinitreflexion: Courier Forschungsinstitut Senckenberg, v. 146, p. 1-115.

Königshof, P., 2003, Conodont deformation patterns and textural alteration in Paleozoic conodonts: examples from Germany and France: Senckenbergiana lethaea, v. 83, p. 149-156.

Kovach, J., and Zartman, R.W., 1981, U-Th-Pb dating of conodonts: Geological Society of America Abstract with Programs, v. 13, p. 285.

Longerich, H.P., Jackson, S.E., Günther, D., 1996, Laser ablation inductively coupled plasma mass spectrometric transient signal data acquisition and analyte concentration calculation: Journal of Analytical Atomic Spectrometry, v. 11, p. 889-904.

Longwell, C.R., 1949, Structure of the Northern Muddy Mountain area, Nevada: The Geological Society of America Bulletin, v. 60, no. 5, p. 923-968.

Lorencak, M., Kohn, B.P., Osadetz, K.G., and Gleadow, A.J., 2004, Combined apatite fission track and (U-Th)/He thermochronometry in a slowly cooled terrane: results from a 3440-m-deep drill hole in the southern Canadian Shield: Earth and Planetary Science Letters, v. 227, p. 87-104.

Millard, A.R., and Hedges, R.E., 1996, A diffusion-adsorption model of uranium uptake by archaeological bone: Geochemica et Cosmochimica Acta, v. 60, no. 12, p. 2139-2152.

Nasdala, L., Wenzel, M., Vavra, G., Irmer, G., Wenzel, T., Kober, B., 2001, Metamictisation of natural zircon: accumulation versus thermal annealing of radioactivity-induced damage: Contrib Mineral Petrol, v. 141, p. 125-144.

Nöth, S., 1998, Conodont color (CAI) versus microcrystalline and textural changes in upper Triassic conodonts from northwest Germany: Facies, v. 38, p. 165-174.

O'Sullivan, P., Carpenter, D.G., and Carpenter, J.A., 1994, Cooling history of the Beaver Dam Mountains, Utah: Determined by apatite fission track analysis, in Dobbs, S.W., and Taylor, W.J., eds., Structural and stratigraphic investigations and petroleum potential of Nevada, with special emphasis south of the Railroad Valley producing trend: Nevada Petroleum Society Publication 9, p. 53–64.

Over, D.J., 2007, Conodont biostratigraphy of the Chattanooga Shale, Middle and Upper Devonian, southern Appalachian Basin, eastern United States: Journal of Paleontology, v. 81, p. 1194-1217.

Paton, C., Hellstrom, J., Paul, B., Woodhead, J., and Hergt, J., 2011, Iolite: Freeware for the visualization and processing of mass spectrometric data: J. Anal. At. Spectrom, v. 26, p. 2508-2518.

Peppe, D.J., and Reiners, P.W., 2007, Conodont (U-Th)/He thermochronology: Initial results, potential, and problems: Earth and Planetary Science Letters, v. 258, p. 569-580.

Pierce, W.G., 1957, Heart Mountain and south Fork detachment thrusts of Wyoming: AAPG Bulletin, v. 41, no. 4, p. 591-626.

Pierce, W.G., 1975, Principal features of the Heart Mountain fault and the mechanism problem: Geology and Mineral Resources of the Bighorn Basin; 27th Annual Field Conference Guidebook, p. 139-148.

Pietzner, H., 1968, The chemical composition and micromorphology of conodonts: Palaeontographica, v. 128, p. 115-148.

Powell, J., Schneider, D., Flowers, R., Metcalf, J., and Stockli, D., 2014, Thermal evolution of the Anticosti Basin, eastern Canada: an empirical calibration of the conodont (U-Th)/He thermochronometer: Geological Society of America Annual Meeting Paper No. 230-15.

Quigley, M.C., Karlstrom, K.E., Kelley, S., and Heizler, M., 2010, Timing and mechanisms of basement uplift and exhumation in the Colorado Plateau-Basin and Range transition zone, Virgin Mountain anticline, Nevada-Arizona: The Geological Society of America Special Paper 463, p. 311-329.

Quinton, P.C., Leslie, S.A., Herrmann, A.D., and MacLeod, K.G., 2016, Effects of extraction protocols on the oxygen isotope composition of conodont elements: Chemical Geology, v. 431, p. 36-43.

Reiners, P.W., and Farley, K.A., 1999, Helium diffusion and (U-Th)/He thermochronometry of titanite: Geochimica et Cosmochimica Acta, v. 63, No. 22, p. 3845-3859.

Reiners, P.W., and Farley, K.A., 2001, Influence of crystal size on apatite (U-Th)/He thermochronology: an example from the Bighorn Mountains, Wyoming: Earth and Planetary Science Letters, v. 188, p. 413-420.

Reiners, P.W., Brady, R., Farley, K.A., Fryxell, J.E., Wernicke, B., and Lux, D., 2000, Helium and argon thermochronometry of the Gold Butte block, south Virgin Mountains, Nevada: Earth and Planetary Science Letters, v. 178, p. 315-326.

Reiners, P.W., 2005, Zircon (U-Th)/He thermochronometry: Reviews in Mineralogy and Geochemistry, v. 58, no. 1, p. 151-179.

Rejebian, V.A., Epstein, A.G., and Huebner, J.S., 1987, Conodont color and textural alteration: An index to regional metamorphism, contact metamorphism, and hydrothermal alteration: The Geological Society of America Bulletin, v. 99, p. 471-479.

Sachs, H.M., Denkinger, M., Bennett, C.L., and Harris, A.G., 1980, Radiometric dating of sediments using fission tracks in conodonts: Nature, v. 288, p. 359-361.

Sanz-Lopez, J., and Blanco-Ferrera, S., 2012, Overgrowths of large authigenic apatite crystals on the surface of conodonts from Cantabrian limestones (Spain): Facies, v. 58, p. 707-726.

Schneider, C. A., Rasband, W. S., and Eliceiri, K. W., 2012, NIH Image to ImageJ: 25 years of image analysis: Nature Methods, v. 9, no. 7, p. 671-675.

Shaw, H.F., and Wasserberg, G.J., 1985, Sm-Nd in marine carbonates and phosphates: Implications for Nd isotopes in seawater and crustal ages: Geochimica et Cosmochimica Acta, v. 49, p. 503-518.

Shuster, D.L., Flowers, R.M., and Farley, K.A, 2006, The influence of artificial radiation damage and thermal annealing on helium diffusion kinetics in apatite: Earth and Planetary Science Letters, v. 249, p. 148-161.

Söderlund, P., Juez-Larré, J., Page, L.M., and Dunai, T.J., 2005, Extending the time range of apatite (U-Th)/He thermochronometry in slowly cooled terrances: Palaeozoic to Cenozoic exhumation history of southeast Sweden: Earth and Planetary Science Letters, v. 239, p. 266-275.

Spotila, J.A., Farley, K.A., and Sieh, K., 1998, Uplift and erosion of the San Bernardino Mountains associated with transpression along the San Andreas fault, California, as constrained by radiogenic helium thermochronometry: Tectonics, v. 17, no. 3, p. 360-378.

Stock, G.M., Ehlers, T.A., and Farley, K.A., 2006, Where does sediment come from? Quantifying catchment erosion with detrital apatite (U-Th)/He thermochronometry: GEOLOGY, v. 34, no. 9, p. 725-728.

Stockli, D.F., 1999, Regional timing and spatial distribution of Miocene extension in the northern Basin and Range province [Ph.D. thesis]: Stanford, California, Stanford University, p. 1-239.

Stockli, D.F., 2005, Application of low-temperature thermochronometry to extensional tectonic settings, *in* Reiners, P.W., and Ehlers, T.A., eds., Low-temperature thermochronology: Reviews in Mineralogy and Geochemistry, v. 58, p. 411–448.

Stockli, D.F., Farley, K.A., and Dumitru, T.A., 2000, Calibration of the apatite (U-Th)/He thermochronometer on an exhumed fault block, White Mountains, California: GEOLOGY, v. 28, no. 11, p. 983-986.

Stockli, D.F., Linn, J.K., Walker, J.D., and Dumitru, T.A., 2001, Miocene unroofing of the Canyon Range during extension along the Sevier Desert Detachment, west central Utah: American Geophysical Union: Tectonics, v. 20, No. 3, p. 289-307.

Stockli, D.F., Surpless, B.E., Dumitru, T.A., and Farley, K.A., 2002, Thermochronological constraints on the timing and magnitude of Miocene and Pliocene extension in the central Wassuk Range, western Nevada: Tectonics, v. 21, p. 10-1–10-19.

Swanson, E.M., and Wernicke, B.P., 2015, Chapter 3: Geologic map of the east-central Meadow Valley Mountains, and implications for reconstruction of the Mormon Peak detachment fault, Nevada, *in* Structural and clumped-isotope constraints on the mechanisms of displacement along low-angle detachments, Dissertation (Ph.D.): California Institute of Technology, p. 48-102.

Sweet, W.C., Ethington, R.L., and Barnes, C.R., 1970, North American Middle and Upper Ordovician conodont faunas: The Geological Society of America Memoirs, v. 127, p. 163-194.

Trotter, J.A., and Eggins, S.M., 2006, Chemical systematics of conodont apatite determined by laser ablation ICPMS: Chemical Geology, v. 233, p. 196–216.

Trotter, J.A., Fitzgerald, J.D., Kokkonen, H., and Barnes, C.R., 2007, New insights into the ultrastructure, permeability, and integrity of conodont apatite determined by transmission electron microscopy: Lethaia, no. 24, p. 1-14.

Trotter, J.A., Williams, I.S., Barnes, C.R., Lécuyer, C., and Nicoll, R.S., 2008, Did cooling oceans trigger Ordovician biodiversification? Evidence from conodont thermochronometry: Science, v. 321, p. 550-554.

Trueman, C.N., and Tuross, N., 2002, Trace elements of recent and fossil bone apatite. In: Kohn, M.J., Rakovan, J., Hughes, J.M. (Eds.), Phosphates-Geochemical, Geobiological, and Materials Importance. Reviews in Mineralogical Geochemistry, v. 48, p. 489-521.

Turekian, K.K., and Kharkar, D.P., 1970, An evaluation of the uranium-helium method of dating fossil bones: Earth and Planetary Science Letters, v. 7, p. 420-424.

Turner-Walker, G., and Syversen, U., 2002, Quantifying histological changes in archaeological bones using BSE-SEM image analysis: Archaeometry, v. 3, p. 461-468.

Ueki, S., and Sano, Y., 2001, In situ ion microprobe Th-Pb dating of Silurian conodonts: Geochemical Journal, v. 35, p. 307-314.

Walker, J.D., Greissman, J.W., Bowring, S.A., and Babcock, L.E., 2013, The Geological Society of America Geologic Time Scale: GSA Bulletin, v. 125, no. 3/4, p. 259-272.

Wenzel, B., Lécuyer, C., and Joachimski, M.M., 2000, Comparing the oxygen isotope records of Silurian calcite and phosphate - $\delta^{18}O$ compositions of brachiopods and conodonts: Geochimica et Cosmochimica Acta, v. 64, p. 1859-1872.

Wernicke, B.P., 1982, Processes of extensional tectonics [Ph.D. thesis]: Cambridge, Massachusetts, Massachusetts Institute of Technology, p 1-171.

Wernicke, B., Spencer, J.E., Burchfiel, B.C., and Guth, P.L., 1982, Magnitude of crustal extension in the southern Great Basin: GEOLOGY, v. 10, p. 499-502.

Wernicke, B., and Axen, G.J., 1988, On the role of isostasy in the evolution of normal fault systems: Geology, v. 16, p. 848–851.

Wernicke, B., Guth, P.L., and Axen, G.J., 1984, Tertiary extensional tectonics in the Sevier thrust belt of southern Nevada: Western Geological Excursions, v. 4, p. 473-510.

Wernicke, B.P., Walker, J.D., and Beaufait, M.S., 1985, Structural discordance between Neogene detachments and frontal Sevier thrusts, central Mormon Mountains, southern Nevada: Tectonics, v. 4, p. 213–246.

Wheeley, J.R., Smith, M.P., and Boomer, I., 2012, Oxygen isotope variability in conodonts: implications for reconstructing Palaeozoic palaeoclimates and palaeoceanography: Journal of the Geological Society, London, v. 169, p. 239–250.

Wolf, R.A., Farley, K.A., and Silver, L.T., 1996, Helium diffusion and low temperature thermochronometry of apatite: Geochimica et Cosmochimica Acta, v. 60, p. 4231-4240.

Wolf, R.A., Farley, K.A., and Kass, D.M., 1998, Modeling the temperature sensitivity of the apatite (U-Th)/He thermochronometer: Chemical Geology, v. 148, p. 104-114.

Wright, J., Seymour, R.S., and Shaw, H.F., 1984, REE and Nd isotopes in conodont apatite: Variations with geological age and depositional environment: Geological Society of America Special Paper 196, p. 325-340.

Wright, J., 1990, Conodont apatite: structure and geochemistry: Skeletal Biomineralization: Patterns, Processes, and Evolutionary Trends, v. 1, p. 445-460.

Zhao, L., Chen, Z., Algeo, T.J., Chen, J., Chen, Y, Tong, J., Gao, S., Zhou, L., Hu, and Z., Liu, Y., 2013, Rare-earth element patterns in conodont albid crowns, Evidence for massive imputs of vocanic ash during the latest Permian biocrisis?: Global and Planetary Change, v. 105, p. 135-151.

Ziegler, W., Lindström, M., and McTavish, R., 1971, Monochloracetic acids and conodonts – a warning: Nature, v. 230, p. 584-585.

FIGURES

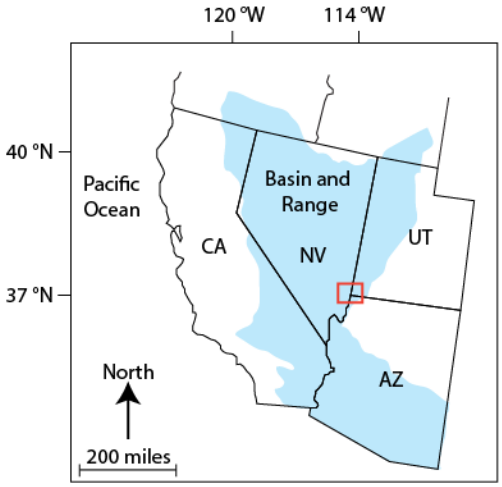

Figure 1. Map of western U.S. showing location of study area. Red box highlights the Mormon Mountains, Tule Spring Hills, and Beaver Dam Mountains study area location along the southern Nevada – Utah border. Blue shaded region defines the spatial extent of the Basin and Range province. AZ – Arizona; CA – California; NV – Nevada; UT – Utah.

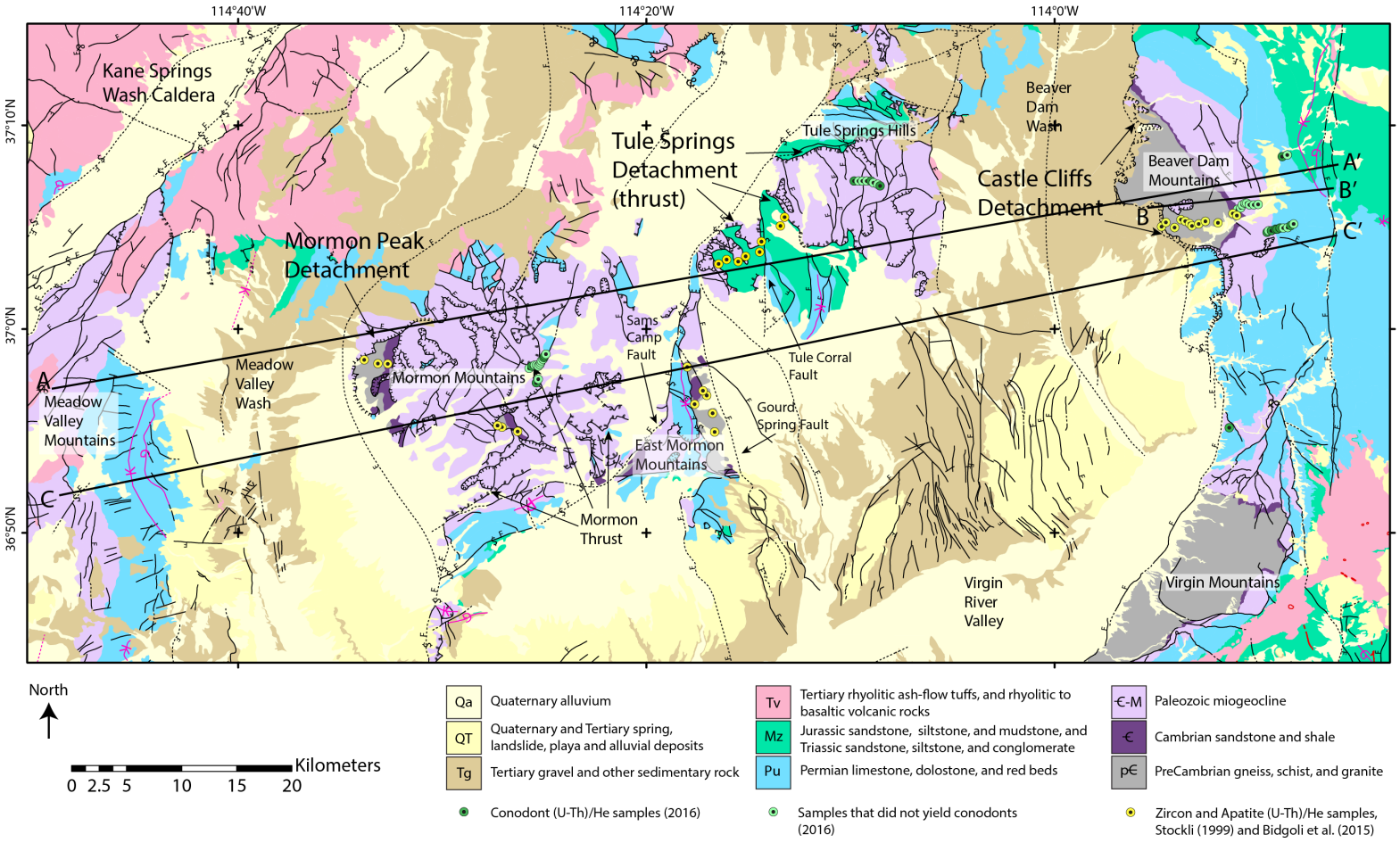
114°40'W
114°20'W
114°0'W
37°10'N
37°0'N
36°50'N
Kane Springs Wash Caldera
Tule Springs Detachment (thrust)
Tule Springs Hills
Beaver Dam Wash
Beaver Dam Mountains
Castle Cliffs Detachment
Mormon Peak Detachment
A
A′
B
B′
C
C′
Meadow Valley Wash
Meadow Valley Mountains
Mormon Mountains
Sams Camp Fault
Tule Corral Fault
Gourd Spring Fault
East Mormon Mountains
Mormon Thrust
Virgin River Valley
Virgin Mountains
North
0 2.5 5 10 15 20
Kilometers
Qa Quaternary alluvium
QT Quaternary and Tertiary spring, landslide, playa and alluvial deposits
Tg Tertiary gravel and other sedimentary rock
Tv Tertiary rhyolitic ash-flow tuffs, and rhyolitic to basaltic volcanic rocks
Mz Jurassic sandstone, siltstone, and mudstone, and Triassic sandstone, siltstone, and conglomerate
Pu Permian limestone, dolostone, and red beds
Є-M Paleozoic miogeocline
Є Cambrian sandstone and shale
pЄ PreCambrian gneiss, schist, and granite
Conodont (U-Th)/He samples (2016)
Samples that did not yield conodonts (2016)
Zircon and Apatite (U-Th)/He samples, Stockli (1999) and Bidgoli et al. (2015)

Figure 2. Geologic map of the Mormon Mountains – Tule Spring Hills – Beaver Dam Mountains study area, with sample locations from this study (green dots) and earlier studies (yellow dots). A total of 43 carbonate samples were collected, but only 15 samples yielded conodonts. Line A-A' shows the location of the cross section in Figure 3. Lines B-B' and C-C' show the locations of cross sections that are restored to their preextensional configurations in Figure 4. Geologic map data are simplified from the compilation of Felger and Beard (2010). Figure is modified from Bidgoli et al. (2015).

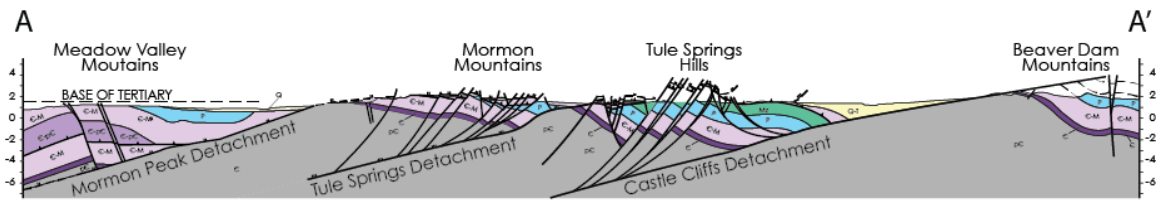

Figure 3. Geologic cross-section A-A' showing the relative positions of the Castle Cliffs, Tule Springs, and Mormon Peak detachments. Cross section location shown in Figure 2. Cross section is modified from Axen et al. (1990) and Bidgoli et al. (2015).

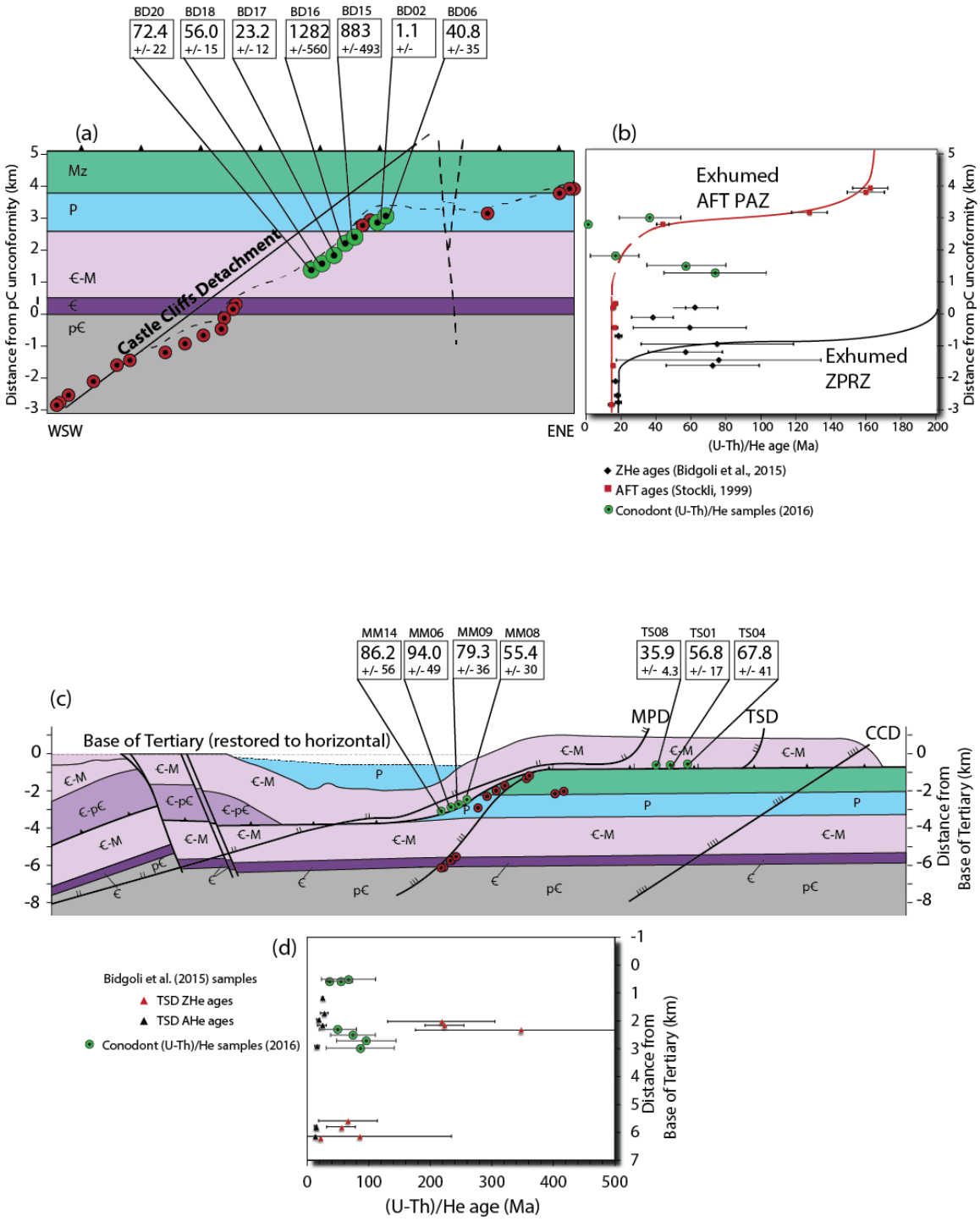

Figure 4. Paleodepth reconstructions and (U-Th)/He age vs. paleodepth plots (modified from Axen et al., 1990 and Bidgoli et al., 2015). Conodont (U-Th)/He samples from this study are shown with green dots. Apatite and zircon (U-Th)/He from Bidgoli et al. (2015) and apatite fission track data

from Stockli (1999) are also shown (red dots). Error bars are 1σ standard deviations. Cross section locations are shown in Figure 2. (A) Restored state cross section B-B' across the Beaver Dam Mountains showing the preextensional configuration of our conodont (U-Th)/He samples. (B) Plot of mean (U-Th)/He age versus distance from nonconformity above the Precambrian basement with previously determing AFT PAZ and ZPRZ. (C) Restored state cross section C-C' across the Tule Spring Hills and Mormon Mountains showing paleodepth positions of samples prior to extension. (D) Plot of mean (U-Th)/He age versus distance from base of Tertiary.

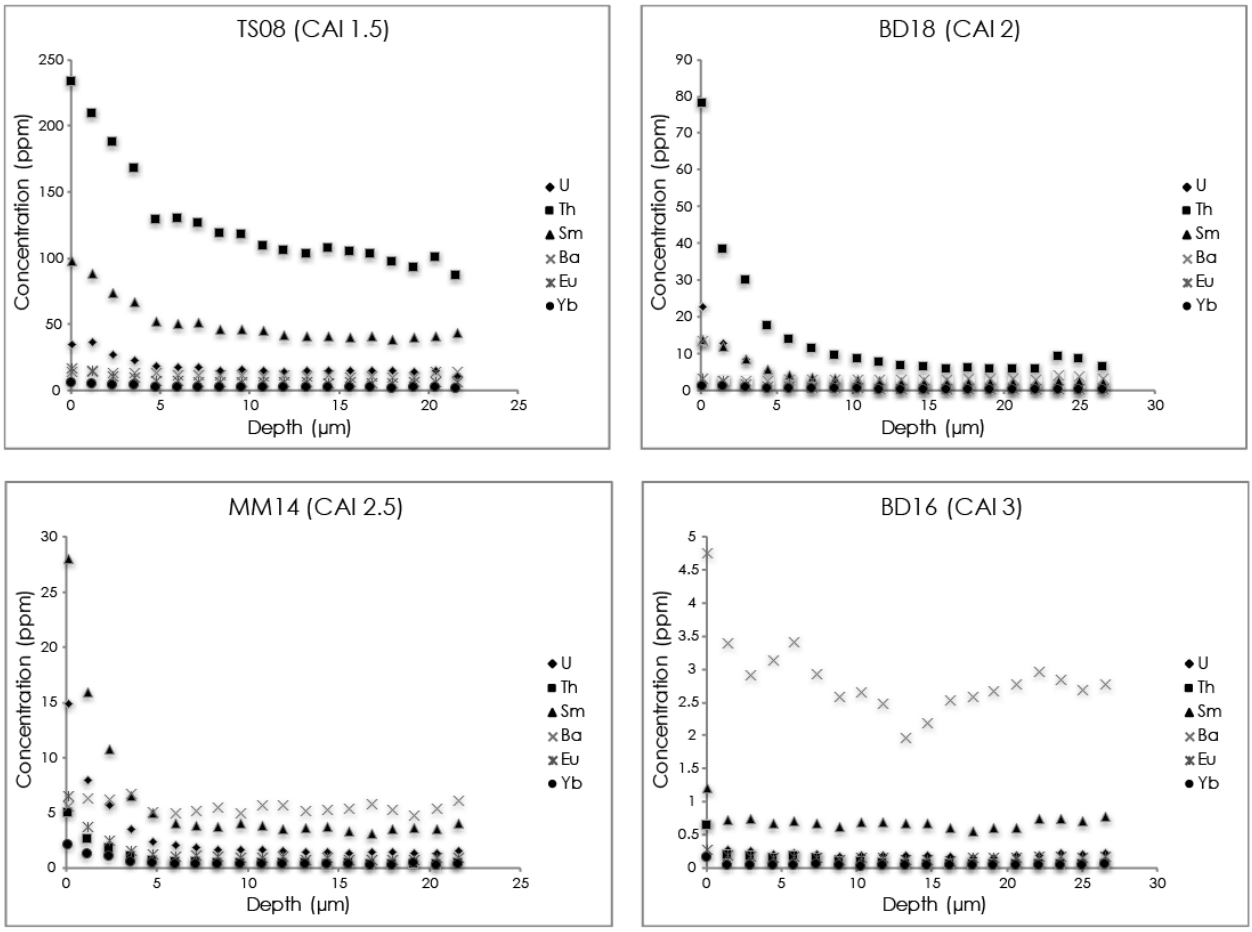

Figure 5. Representative LA-ICPMS depth profile data showing concentrations (ppm) of trace and REEs versus depth (μm) for conodonts with a range of CAIs. Scatter plot data includes the parent U, Th, and Sm as well as trace and trace and REE Ba, Eu, and Yb. Note high rim enrichments (5x-10x) at the margins of the conodonts relative to depth concentrations. LREE Ba typically shows higher concentrations than MREE Eu and HREE Yb. With increasing CAI, all trace and REE concentrations tend to drop both at the margins and at depth. Concentrations also tend to decrease with increasing CAI. TS08 and BD18 display high Th concentrations, which may be influenced by apatite tissue type and lower CAI.

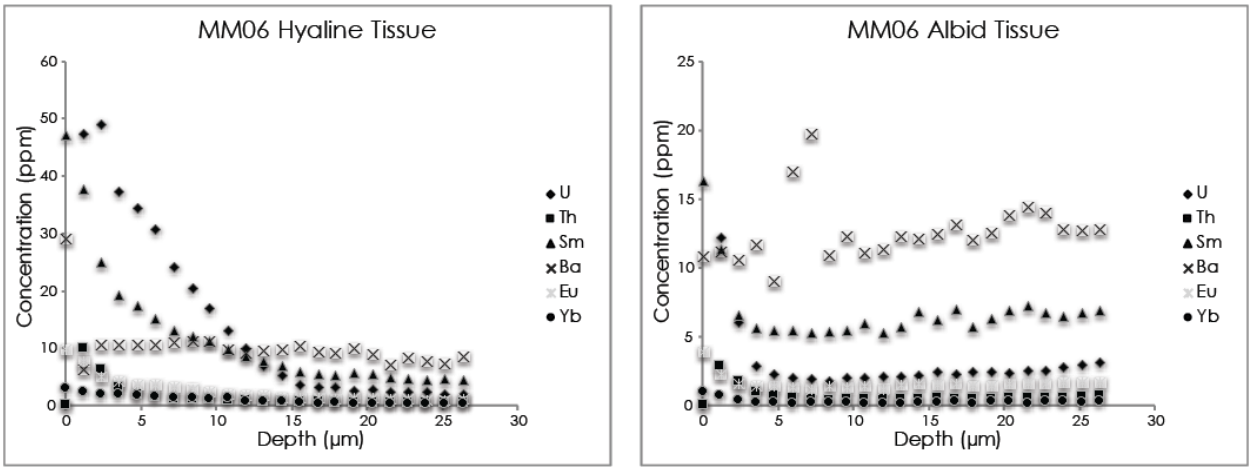

Figure 6. Plot of representative LA-ICPMS depth profiles showing differences between hyaline and albid apatite tissue from sample MM06. Scatter plot data includes the parent U, Th, and Sm as well as trace and REE Ba, Eu, and Yb. Note higher concentrations in hyaline tissue than albid tissue, and more gradual depletion pattern in parent U, Th, and Sm in hyaline tissue. Parent isotope concentrations moderately increase with depth in albid tissue.

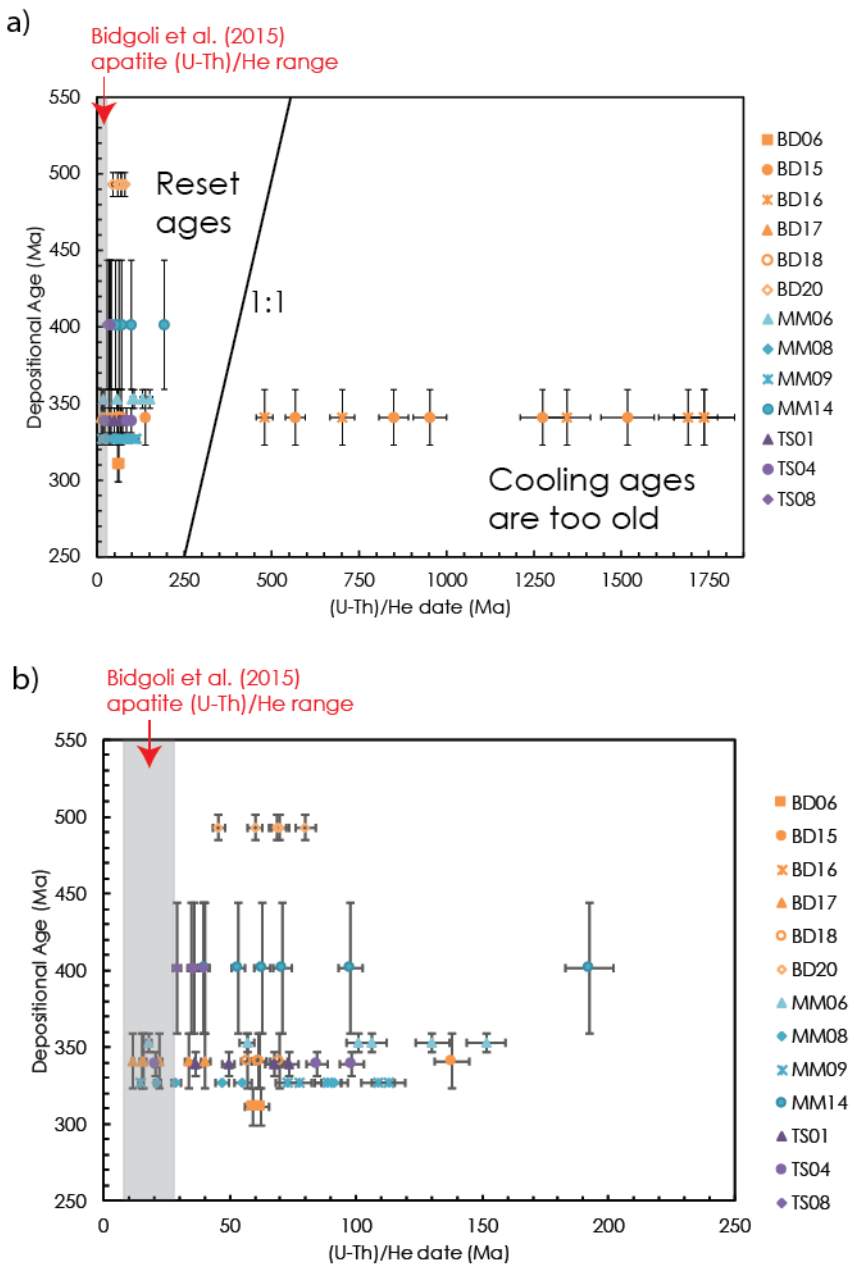

Figure 7. (A) Depositional age versus conodont (U-Th)/He date. Horizontal error bars are standard (U-Th)/He errors (6%). Vertical error bars show potential range in depositional age. Most dates are younger than the approximate depositional age of the samples, but two samples (BD15 and BD16) produced (U-Th)/He dates that are much too old given the known geology. (B) Same data rescale to show conodont dates <200 Ma.

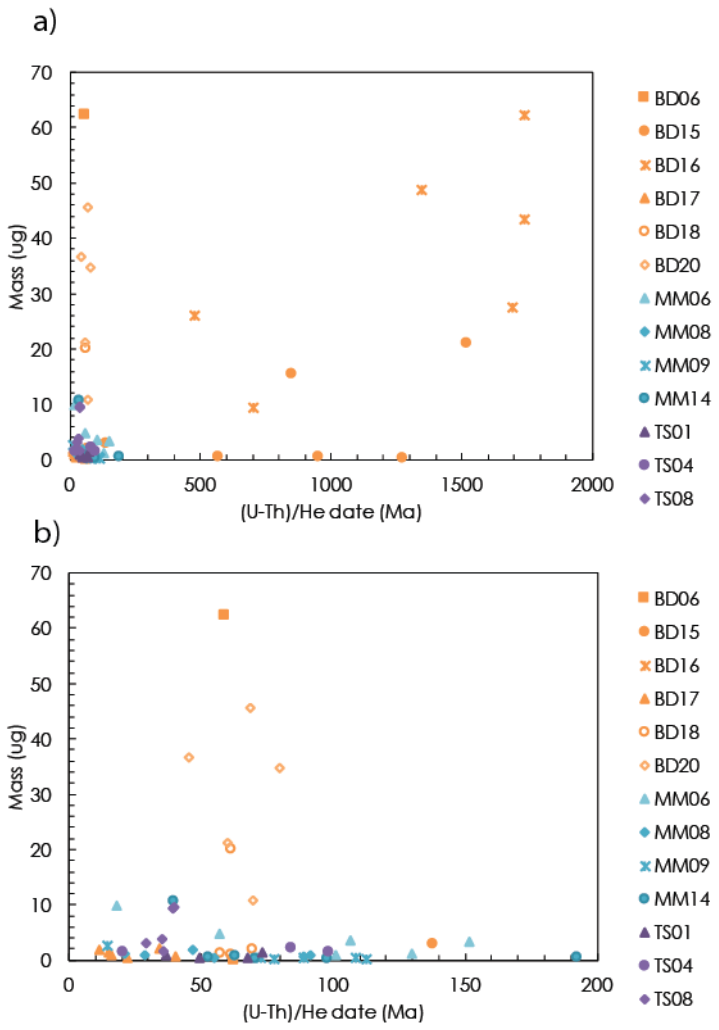

Figure 8. (A) Mass versus (U-Th)/He date of conodonts analyzed in this study. No relationship is seen between the two. (B) Same figure rescaled to show only conodont dates younger than 200 Ma.

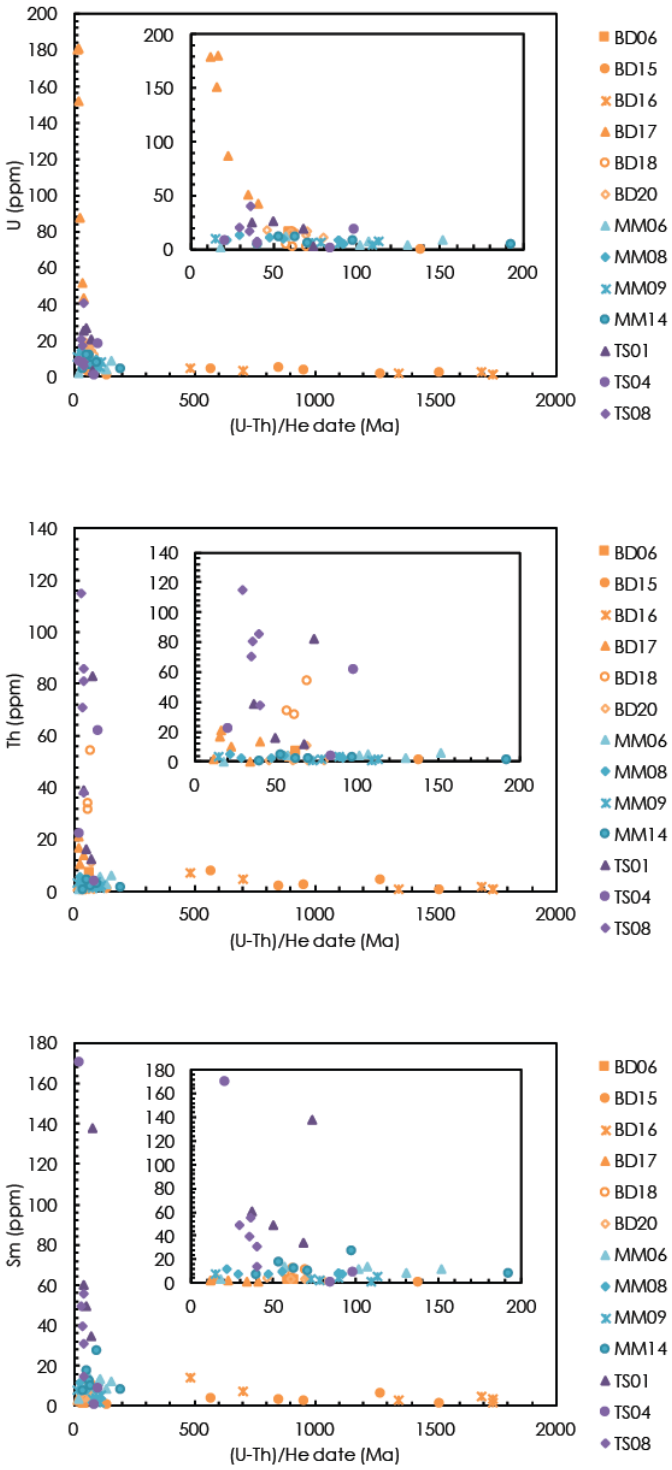

Figure 9. Relationship between parent isotope (U, Th, Sm) concentrations and conodont (U-Th)/He dates. Inset plot shows the same data rescaled to only show dates <200 Ma.

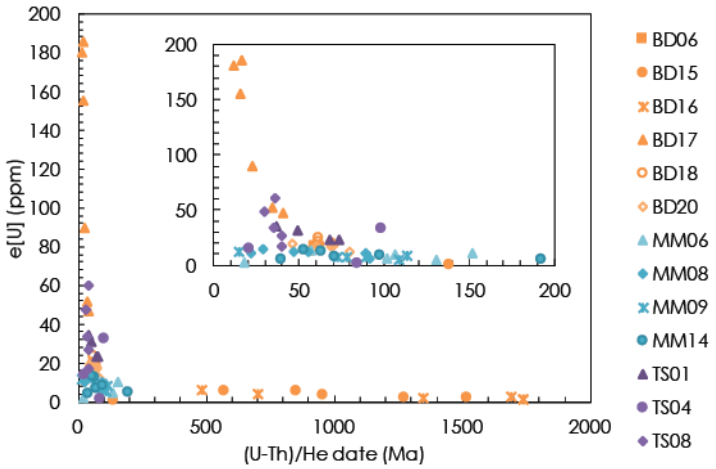

Figure 10. Plot of e[U] versus (U-Th)/He date for conodonts from this study. The data show a strong inverse relationship between the two. BD17 conodonts have the highest e[U] of all samples. Inset plot shows the same data rescaled to only show conodont dates <200 Ma.

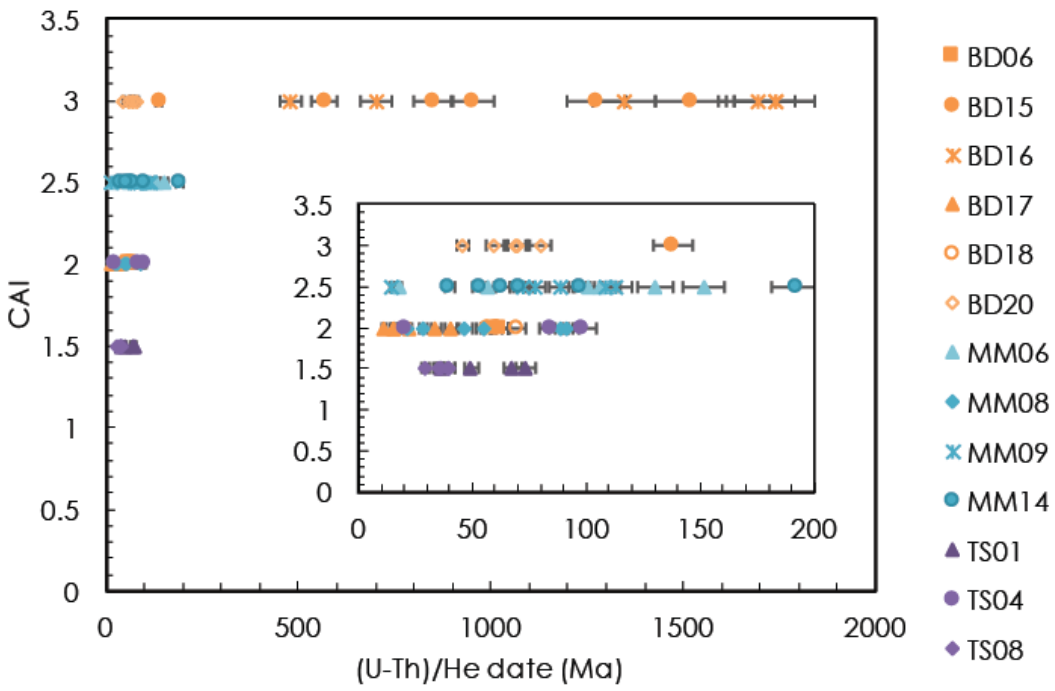

Figure 11. Plot of CAI versus (U-Th)/He date for conodonts analyzed in this study. In general, higher CAI conodonts produce older and more scattered (U-Th)/He dates.

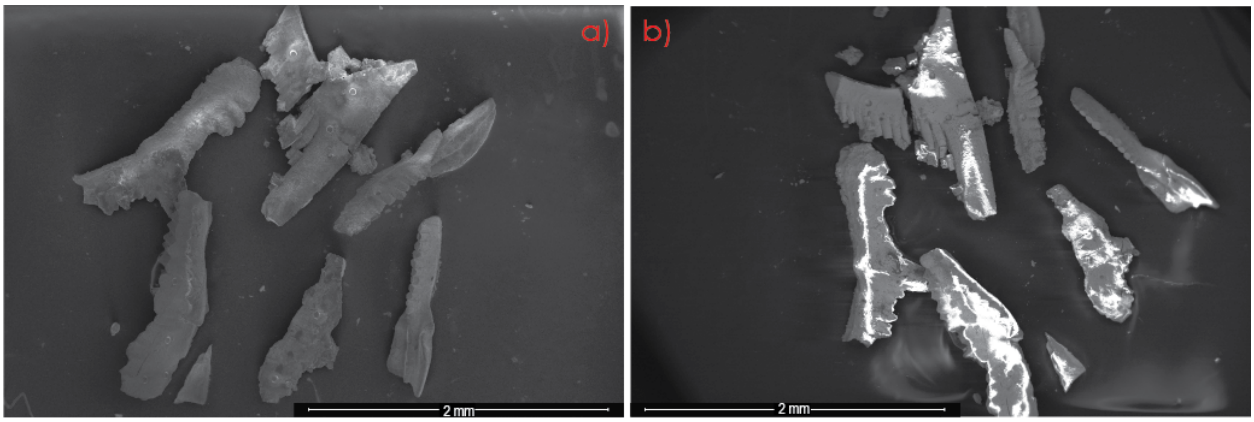

Figure 12. Comparison of SEM images between secondary electron (SE) and backscattered electron (BSE) techniques. Figure 12a. SE image of large MM08 conodonts, CAI 2. Figure 12b. BSE image of large MM08 conodonts, CAI 2.

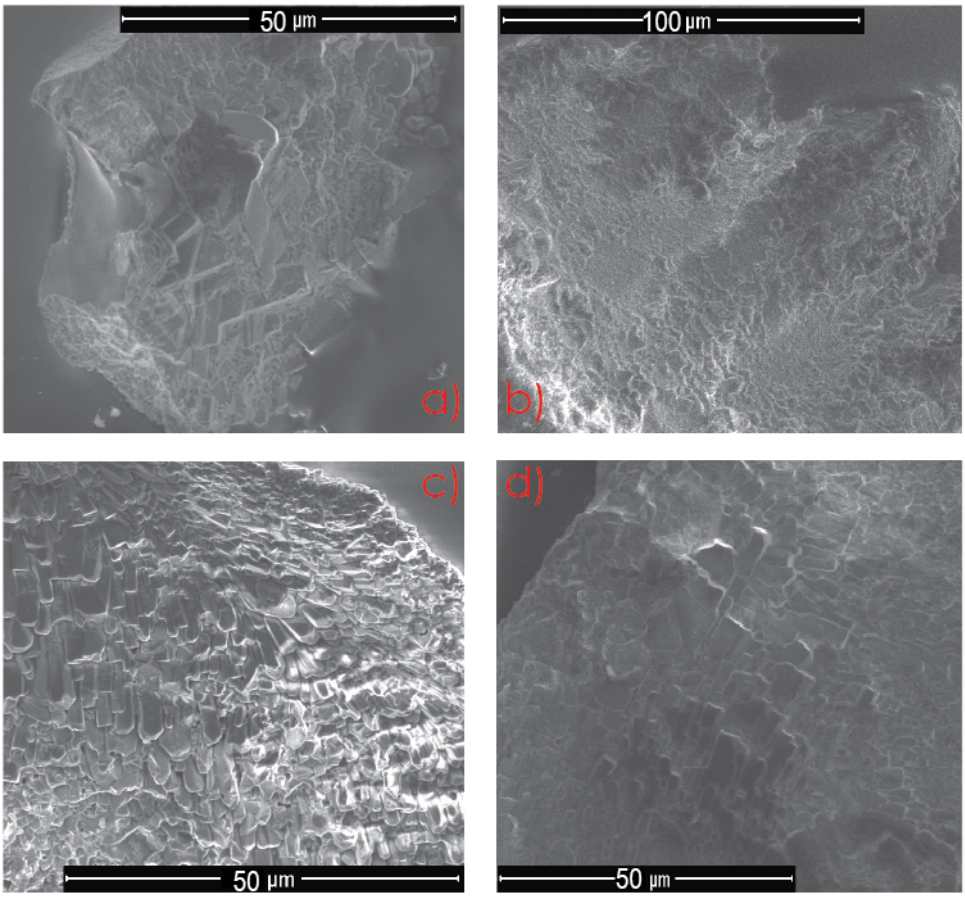

Figure 13. SE images displaying microstructural differences in conodont surfaces between CAI 1.5, 2, 2.5, and 3 blade conodont elements. (A) CAI 1.5 conodont element from sample TS08 showing microcrystals oriented perpendicular to the conodont surface. Microcrystal size is widely variable. (B) CAI 2 conodont from sample MM08. Note random overgrowth pattern. (C) CAI 2.5 conodont from sample MM06 showing microcrystals oriented roughly 45 degrees to the principal axis of the conodont. (D) CAI 3 conodont from sample BD20 with microcrystals oriented near parallel to the major axis of the conodont.

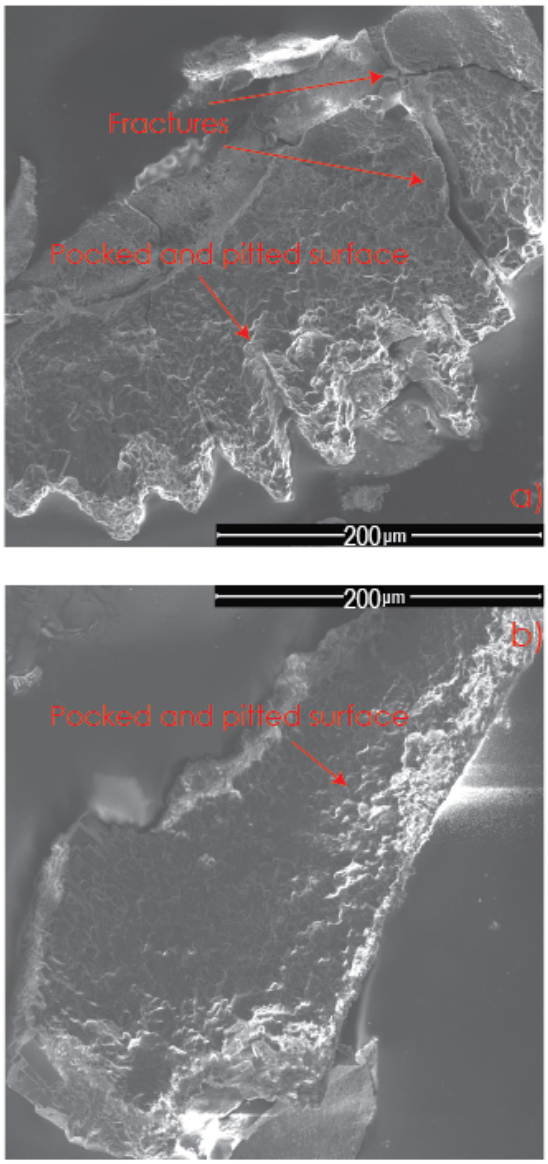

Figure 14. SE images displaying corrosion alterations to conodonts. Figure 12a: SEM image of MM06 conodont (CAI 2.5) with pocked and pitted texture consistent with surface corrosion. Also note small fractures in the upper-right corner. Figure 12b: SEM image of BD20 conodont (CAI 3) with pocked and pitted texture consistent with surface corrosion.

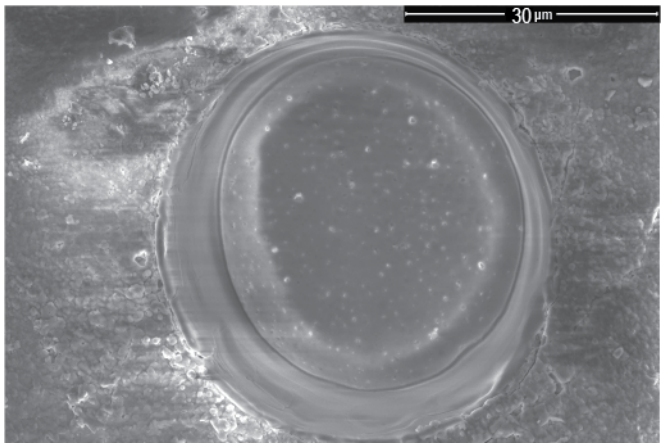

Figure 15. SE image of laser ablation spot in MM08 conodont. Note the darker color at the rim and darker irregularities in the sidewalls of the ablation pit. These features are evident in tilted images, indicating they are not imaging artifacts.

TABLES

Table 1. Laser Ablation and ICPMS Operating Parameters

	Trotter & Eggins, Chemical Geology 2006	This study 11/17/2015	This study 11/24/2015
Laboratory & Sample Preparation			
Laboratory name	ANU, Canberra	KU Isotope Geochemistry Laboratories	KU Isotope Geochemistry Laboratories
Sample type/mineral	Apatite, Conodonts	Apatite, Conodonts	Apatite, Conodonts
Sample preparation		tape mount	tape mount
Laser ablation system			
Make, Model & type	Arf excimer 193 nm, Lambda Physik LPX120i	Arf excimer 193 nm, Photon Machines Analyte G2, ATL	Arf excimer 193 nm, Photon Machines Analyte G2, ATL
Ablation cell & volume		Helex 2, two-volume cell	Helex 2, two-volume cell
Laser wavelength (nm)	193	193	193
Pulse width (ns)	?	5	5
Fluence ($J.cm^2$)	8	2.5	2.5
Repetition rate (Hz)	5	10	10
Spot size (um)	40, 48, 65	50	35
Carrier gas	5cm3/s He, 20cm3/s Ar	He, 1.01 l/min, Ar, 1.1 l/min	He, 1.01 l/min, Ar, 1.1 l/min
Ablation duration (secs)	30secs	30	30
Cell carrier gas flow (l/min)		Ar, 1.1 l/min	Ar, 1.1 l/min
ICP-MS Instrument			
Make, Model & type	Agilent 7500s quadrupole	Thermo Element2 magnetic sector field ICP-MS	Thermo Element2 magnetic sector field ICP-MS
RF power (W)	1200	1100	1100
Make-up gas flow (l/min)	20cm3/sec Ar	Ar, 1.1 l/min	Ar, 1.1 l/min
sampling depth	6.5	3.6	3.6
Detection system	single detector, counting & analog	single detector, counting & analog	single detector, counting & analog
Masses measured	see below, Table in paper	see below	see below
Integration time per peak (ms)	20-30ms	5-10 ms	5-10 ms
Total integration time per reading (secs)	1		
Total method time	150-200	50	50
IC Dead time (ns)		4	4
ThO+/Th+ (%)	<0.5	U/UO <0.2	U/UO <0.2
238+/232Th+	>0.9 for NIST 612	0.95	0.95
Data Processing			
Gas blank (s)		23	23
Calibration strategy		NIST 612	NIST 612
Reference Material info	NIST 612 (Pearce et al. 1997)	NIST 612 (Pearce et al. 1997)	NIST 612 (Pearce et al. 1997)
		in-house apatite Mud Tank	in-house apatite Mud Tank
		Durango apatite	Durango apatite
Internal Standard	43Ca	43Ca	43Ca
Data processing package used / Correction for LIEF		IGOR PRO, Iolite 2.5	IGOR PRO, Iolite 2.5
Quality control / Validation		in-house apatite Mud Tank	in-house apatite Mud Tank
		Durango apatite	Durango apatite

Table 2. Isotopic concentrations of external standards measured by LA-ICPMS										
Measured Isotope	**Atomic Mass (amu)**	**NIST612 (Pearce et al., 1997) (ppm)**	**NIST612 (This study) (ppm)**	**NIST612 Deviation from Published Value**	**Durango LA-ICPMS (ppm)**	**Durango Standard Deviation (ppm)**	**Durango Detection Limit (ppm)**	**Fish Canyon Tuff LA-ICPMS (ppm)**	**Fish Canyon Tuff Standard Deviation (ppm)**	**Fish Canyon Tuff Detection Limit (ppm)**
Y	89	37.8	38	0.5%	426.9	9.60	0.0139	518.5	12.03	0.0164
Ba	137	38.5	39.7	3.0%	1.4	0.26	0.0327	4.7	2.91	0.0290
La	139	35.5	35.8	0.8%	2990.4	63.36	0.0239	2118.5	46.95	0.0229
Ce	140	38.2	38.7	1.3%	4009.7	82.80	0.0186	4108.0	92.36	0.0192
Pr	141	37.1	37.2	0.3%	321.2	7.02	0.0077	396.0	9.11	0.0076
Nd	146	35	35.8	2.2%	965.9	22.84	0.0336	1327.9	32.95	0.0322
Sm	147	36.4	38.1	4.5%	124.6	3.22	0.0190	177.5	5.40	0.0185
Eu	153	34.6	35	1.1%	14.4	0.39	0.0032	26.8	0.85	0.0027
Gd	158	37.1	36.7	1.1%	97.5	2.98	0.0488	126.6	5.09	0.0475
Dy	163	35.7	36	0.8%	65.1	1.84	0.0113	83.3	2.38	0.0112
Er	166	38	38	0.0%	34.1	0.99	0.0099	45.5	1.49	0.0092
Yb	172	-	39.2	-	25.0	0.71	0.0082	39.0	1.13	0.0071
Pb206	206	-	38.6	-	0.2	0.03	0.0069	3.1	0.40	0.0070
Pb207	207	-	38.6	-	0.1	0.06	0.0099	2.8	0.56	0.0103
Pb208	208	38.7	38.6	0.3%	0.4	0.06	0.0094	3.0	0.62	0.0088
Th	232	37.3	37.8	1.3%	145.4	5.66	0.0004	47.1	1.85	0.0004
U	238	36.9	37.4	1.3%	7.2	0.30	0.0001	12.0	0.49	0.0001

Table 3. Summary of Range of Parent Isotope Concentrations in LA-ICPMS Profiles (parts per million)						
Sample	**Minimum 238U**	**Maximum 238U**	**Minimum 232Th**	**Maximum 232Th**	**Minimum 147Sm**	**Maximum 147Sm**
BDM Margin	<1	345	<1	78	<1	72
BDM Depth	<1	25	<1	12	<1	46
MM Margin	1	109	<1	28	2	96
MM Depth	1	10	<1	3	1	8
TSH Margin	9	207	23	265	33	331
TSH Depth	4	41	18	85	2	83

Table 4. Conodont (U-Th)/He Sample Locations and Mean Dates					
Sample	**CAI**	**Latitude (UTM)**	**Longitude (UTM)**	**Mean Age, no Ft**	**Error, 2-sigma standard deviation**
Beaver Dam Mountains Samples					
BD02	2	783538.563	4110073.000	1.1	
BD06	2	782832.188	4115208.750	40.8	34.8
BD15	3	782757.188	4109797.000	883.2	493.4
BD16	3	782503.500	4109796.000	1281.9	559.7
BD17	2	782293.625	4109730.250	23.2	11.6
BD18	2	782818.375	4109638.500	56.0	15.2
BD20	3	781910.563	4109491.250	72.4	21.7
Mormon Mountains Samples					
MM06	2.5	728868.075	4094060.729	94.0	49.0
MM08	2	729939.810	4095359.232	55.4	29.5
MM09	2.5	729831.934	4095241.549	79.3	35.5
MM14	2.5	728471.217	4093376.276	86.2	55.6
Tule Spring Hills Samples					
TS01	1.5	751907.528	4110736.381	56.8	16.9
TS04	2	752391.438	4110630.811	67.8	41.4
TS08	1.5	751175.595	4110666.494	35.9	4.3

Table 5. Conodont (U-Th)/He Data												
Sample	**CAI**	**Age, no Ft**	**Analytical Error, Ma**	**Age, 3D Ft**	**3DFt**	**U (ppm)**	**Th (ppm)**	**Sm (ppm)**	**e[U]**	**Th/U**	**He (nmol/g)**	**mass (ug)**
Beaver Dam Mountains Samples												
BD02-01	2	**1.1**	0.01	**1.2**	0.910	41.7	27.8	128.7	48.8	0.67	0.3	0.09
BD06-01	2	**0.7**	0.01	**0.8**	0.825	11	10.3	1.6	13.4	0.94	0.05	0.07
BD06-02	2	**62.5**	0.63	**77.6**	0.806	13.7	7.4	1.9	15.4	0.54	5.26	0.02
BD06-100	2	**59.2**	0.44	**75.9**	0.780	15.58	2.66	1.96	16.2	0.17	5.24	62.3
BD15-04	3	**952.2**	2.85	**1351.0**	0.705	3	2.2	2.4	3.5	0.73	20.46	0.46
BD15-05	3	**567.2**	8.14	**767.6**	0.739	3.6	7.6	3.2	5.4	2.14	17.42	0.52
BD15-08	3	**1274.6**	21.41			1	4.2	5.6	2	4.41	15.36	0.28
BD15-100	3	**138.1**	5.82	**227.6**	0.607	0.05	0.85	0.24	0.2	17.27	0.19	3
BD15-16	3	**1518.1**	4.38	**1881.1**	0.807	1.42	0.67	1.14	1.6	0.47	17.93	20.9
BD15-22	3	**848.8**	4.69	**1163.3**	0.730	4.51	1.7	2.81	4.9	0.38	25.39	15.5
BD16-01	3	**1737.2**	0.12	**2054.9**	0.845	0.96	1.01	3.09	1.2	1.05	17.82	62.3
BD16-05	3	**479.5**	0.94	**602.2**	0.796	4.33	7.1	14.14	6.1	1.64	16.63	25.9
BD16-100	3	**701.7**	3.85	**910.7**	0.771	2.75	4.93	7.04	3.9	1.79	16.15	9.3
BD16-18	3	**1344.6**	5.18	**1642.3**	0.819	1.7	1.07	2.74	2	0.63	17.92	48.8
BD16-23	3	**1737.3**	3.01	**2202.7**	0.789	0.79	0.91	1.54	1	1.15	16.42	43.5
BD16-36	3	**1691.1**	0.14	**2166.5**	0.781	2.34	1.98	4.51	2.8	0.85	40.48	27.4
BD17-02	2	**22.4**	0.2	**32.3**	0.694	87	10.7	2.3	89.6	0.12	10.89	0.38
BD17-04	2	**40.4**	0.31	**56.9**	0.710	43.1	14.2	1.5	46.4	0.33	10.22	0.58
BD17-06	2	**15.9**	0.06	**25.4**	0.627	180.8	21.2	4.9	185.8	0.12	16.1	0.92
BD17-07	2	**15.1**	0.1	**24.5**	0.618	151.3	16.8	3.1	155.3	0.11	12.79	1.33
BD17-08	2	**34.1**	0.23	**49.9**	0.683	51.17	0.79	1.72	51.4	0.02	9.54	2
BD17-100	2	**11.5**	0.06	**19.2**	0.598	179.48	1.7	2.46	179.9	0.01	11.22	2
BD18-02	2	**61.6**	0.57	**91.4**	0.674	16	31.6	12.1	23.5	1.97	7.91	0.95
BD18-08	2	**30.1**	2.87	**51.3**	0.587	0.1	8.6	0	2.1	93.22	0.35	1.96
BD18-09	2	**57.3**	0.48	**113.2**	0.506	4.4	33.6	7.3	12.3	7.67	3.85	1.13
BD18-100	2	**61.6**	0.24	**76.5**	0.806	19.83	1.09	3.62	20.1	0.05	6.77	20.1
BD18-11	2	**69.6**	0.71	**181.1**	0.384	5.7	54.2	10.6	18.5	9.46	7.04	1.9
BD20-02	3	**68.9**	0.34	**81.2**	0.849	14.15	11.14	3.25	16.8	0.79	6.32	45.7
BD20-03	3	**110.0**	0.75	**125.3**	0.878	11.32	0.62	2.24	11.5	0.05	6.95	62.5
BD20-04	3	**79.9**	0.41	**98.7**	0.810	11.9	0.87	2.81	12.1	0.07	5.31	34.7
BD20-100	3	**69.9**	0.28	**95.4**	0.733	17.44	1.37	4.46	17.8	0.08	6.81	10.7
BD20-20	3	**45.6**	0.2	**56.5**	0.807	18.56	1.2	4.19	18.9	0.06	4.7	36.8
BD20-41	3	**60.0**	0.33	**78.4**	0.765	16.07	1.09	3.08	16.3	0.07	5.36	21.1

Table 5 (continued). Conodont (U-Th)/He Data												
Sample	**CAI**	**Age, no Ft**	**Analytical Error, Ma**	**Age, 3D Ft**	**3DFt**	**U (ppm)**	**Th (ppm)**	**Sm (ppm)**	**e[U]**	**Th/U**	**He (nmol/g)**	**mass (ug)**
Mormon Mountains Samples												
MM06-01	2.5	**130.2**	1.03	**159.6**	0.816	3.8	2.8	8.4	4.5	0.73	3.27	1.18
MM06-02	2.5	**101.2**	0.4	**134.2**	0.754	4.7	4.6	11.9	5.9	0.98	3.27	0.92
MM06-03	2.5	**106.5**	0.45	**142.5**	0.747	8.2	5.6	13.5	9.6	0.68	5.62	3.67
MM06-04	2.5	**56.9**	0.29	**71.2**	0.799	12	4.4	14.3	13.1	0.37	4.09	4.67
MM06-100	2.5	**17.9**	0.1	**23.7**	0.756	1.92	0.74	3.07	2.1	0.38	0.21	9.8
MM06-14	2.5	**151.5**	1.13	**222.0**	0.683	8.5	6.2	12.1	10	0.73	8.37	3.32
MM08-03	2	**91.5**	0.67	**112.4**	0.814	5.6	2.6	8	6.3	0.45	3.15	0.92
MM08-04	2	**28.8**	0.18	**34.9**	0.825	13.9	3.2	7.6	14.7	0.23	2.31	0.92
MM08-100	2	**21.3**	0.09	**29.9**	0.713	8.8	5.6	11.4	10.2	0.64	1.18	1.11
MM08-13	2	**47**	0.16	**59.0**	0.797	11.1	3	7.4	11.9	0.27	3.05	1.91
MM08-19	2	**88.9**	0.35	**105.9**	0.839	9.5	3.4	8.8	10.4	0.35	5.06	0.64
MM08-21	2	**55.2**	0.39	**74.3**	0.743	10.7	4.7	9.8	11.8	0.44	3.57	0.41
MM09-01	2.5	**108.7**	0.65	**153.2**	0.710	4.8	1.3	1.6	5.1	0.26	3.05	0.4
MM09-03	2.5	**77.7**	0.45	**110.6**	0.703	7	1.8	2.8	7.4	0.25	3.17	0.13
MM09-05	2.5	**88.9**	0.31	**117.6**	0.756	6.1	3.9	4.3	7	0.64	3.41	0.33
MM09-06	2.5	**112.9**	0.47	**143.0**	0.790	7.8	2.1	5.5	8.3	0.28	5.15	0.27
MM09-09	2.5	**72.8**	0.56	**92.6**	0.786	6.9	1.5	3.2	7.3	0.22	2.92	0.5
MM09-100	2.5	**14.8**	0.14	**27.5**	0.539	10.69	3.46	7.8	11.5	0.32	0.93	2.7
MM14-02	2.5	**192.4**	0.79	**241.3**	0.797	4	1.6	7.4	4.4	0.41	4.69	0.4
MM14-03	2.5	**62.9**	0.52	**83.4**	0.754	11.5	2.2	12	12.1	0.19	4.17	0.66
MM14-04	2.5	**70.7**	0.6	**89.9**	0.787	5.9	1.9	9.5	6.4	0.33	2.49	0.2
MM14-05	2.5	**97.8**	0.72	**136.6**	0.716	7.4	3	26.9	8.3	0.4	4.49	0.26
MM14-100	2.5	**40**	0.33	**52.4**	0.764	3.87	0.44	6.88	4	0.11	0.88	10.7
MM14-11	2.5	**53.2**	0.73	**82.6**	0.644	11.5	4.4	17	12.6	0.38	3.68	0.34

Table 5 (continued). Conodont (U-Th)/He Data												
Sample	**CAI**	**Age, no Ft**	**Analytical Error, Ma**	**Age, 3D Ft**	**3DFt**	**U (ppm)**	**Th (ppm)**	**Sm (ppm)**	**e[U]**	**Th/U**	**He (nmol/g)**	**mass (ug)**
Tule Spring Hills Samples												
TS01-01	1.5	**67.6**	0.43	**108.6**	0.622	20	12.5	34.2	23.1	0.63	8.57	0.41
TS01-02	1.5	**73.5**	0.52	**123.5**	0.595	2.8	83	137.9	23	29.75	9.39	1.34
TS01-03	1.5	**49.4**	0.19	**81.3**	0.607	26.8	16.5	49.4	30.9	0.62	8.38	0.46
TS01-04	1.5	**36.6**	0.43	**95.4**	0.384	25.1	39	60.2	34.6	1.55	6.93	0.81
TS04-01	2	**98.4**	0.9	**173.7**	0.566	17.9	61.7	8.6	32.4	3.46	17.45	1.37
TS04-02	2	**20.7**	0.33	**45.7**	0.453	7.7	22.1	169.9	13.7	2.89	1.61	1.3
TS04-03	2	**84.3**	46.75	**339.8**	0.248	0.5	3.7	0.3	1.4	6.95	0.64	2.15
TS08-02	1.5	**39.6**	0.19	**55.6**	0.712	6.03	85.94	30.67	26.4	14.26	5.71	9.5
TS08-03	1.5	**39.8**	0.22	**55.0**	0.724	7.97	38.26	14.47	17	4.8	3.71	9.6
TS08-08	1.5	**35.1**	0.18	**64.9**	0.541	16.63	71	39.13	33.5	4.27	6.43	3.8
TS08-09	1.5	**35.9**	0.12	**65.6**	0.548	40.64	81.1	55.4	60	2	11.75	1.6
TS08-11	1.5	**29.2**	0.15	**47.2**	0.619	20.32	115.14	49.21	47.6	5.67	7.59	3

APPENDIX A

Naming Acronym: Mountain Range and Sample Number – LA-ICPMS Spot Number

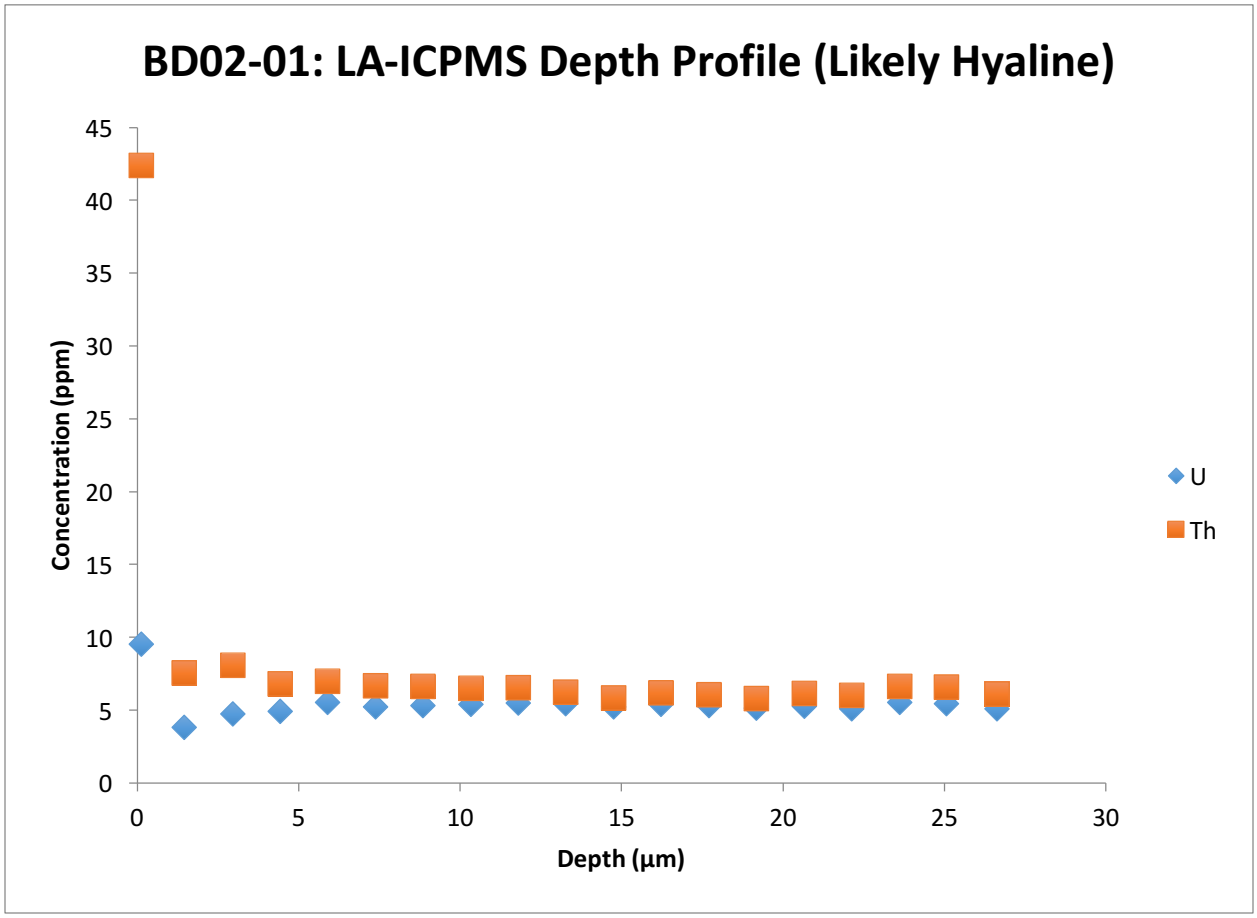

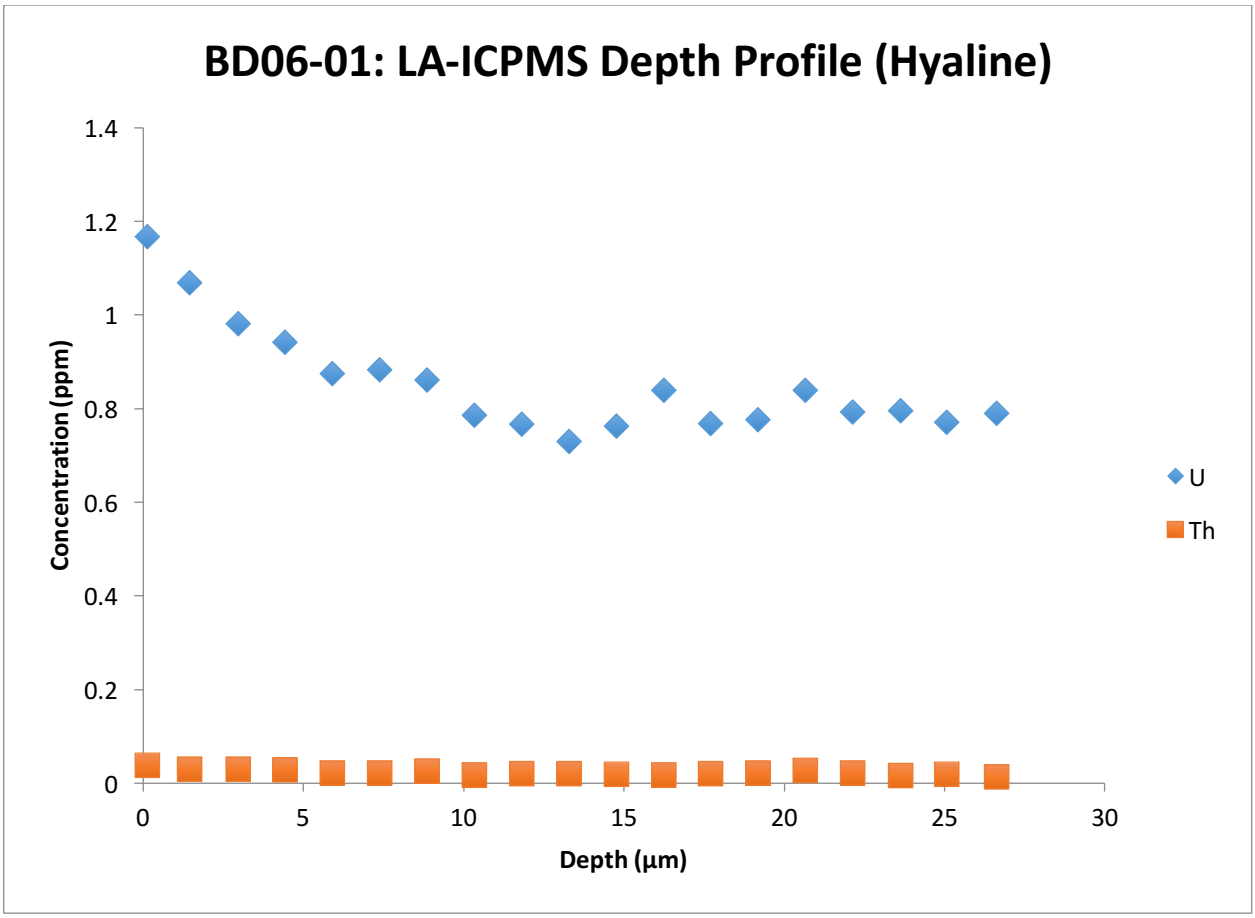
BD06-01: LA-ICPMS Depth Profile (Hyaline)
Concentration (ppm)
1.4
1.2
1
0.8
0.6
0.4
0.2
0
0
5
10
15
20
25
30
Depth (µm)
U
Th

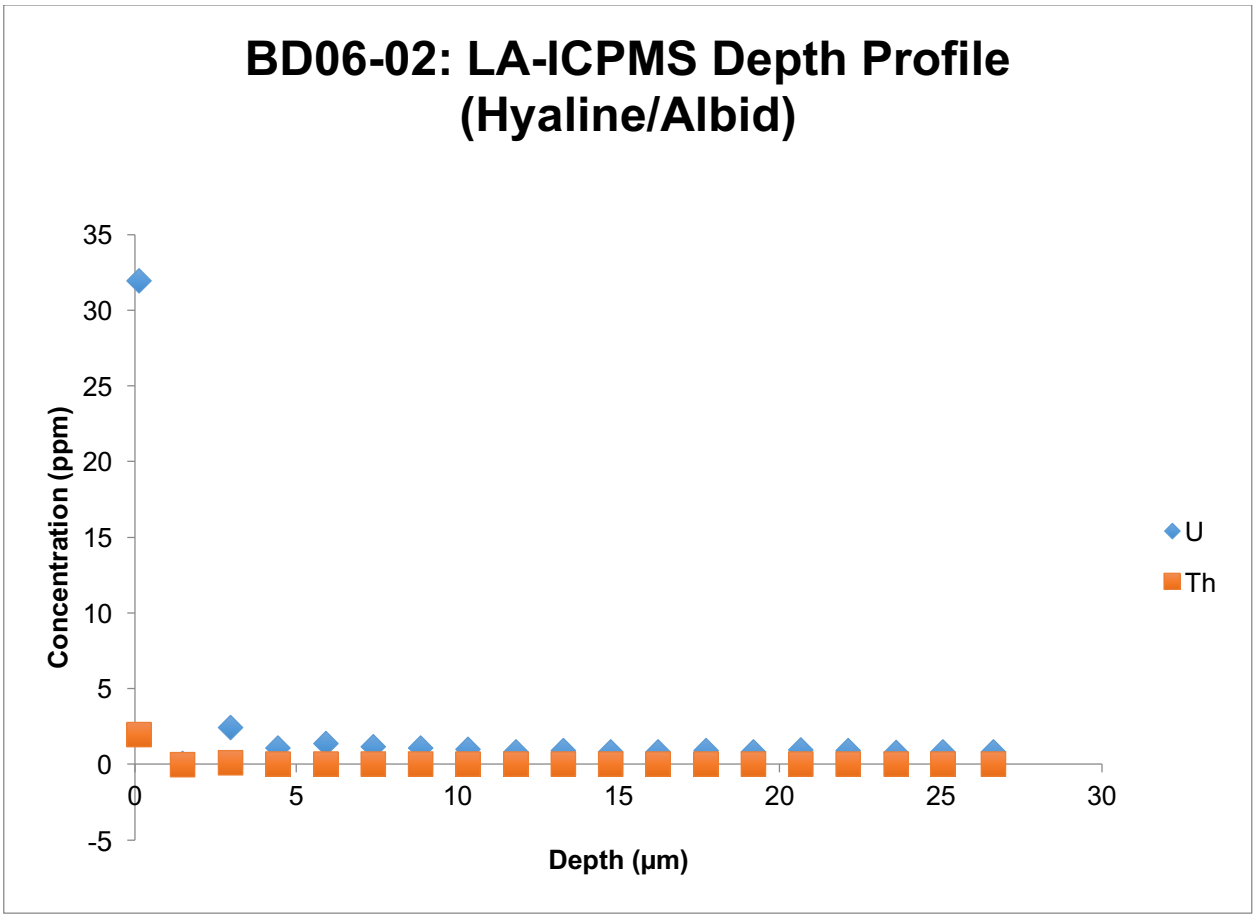
BD06-02: LA-ICPMS Depth Profile
(Hyaline/Albid)
Concentration (ppm)
35
30
25
20
15
10
5
0
-5
0
5
10
15
20
25
30
Depth (µm)
U
Th

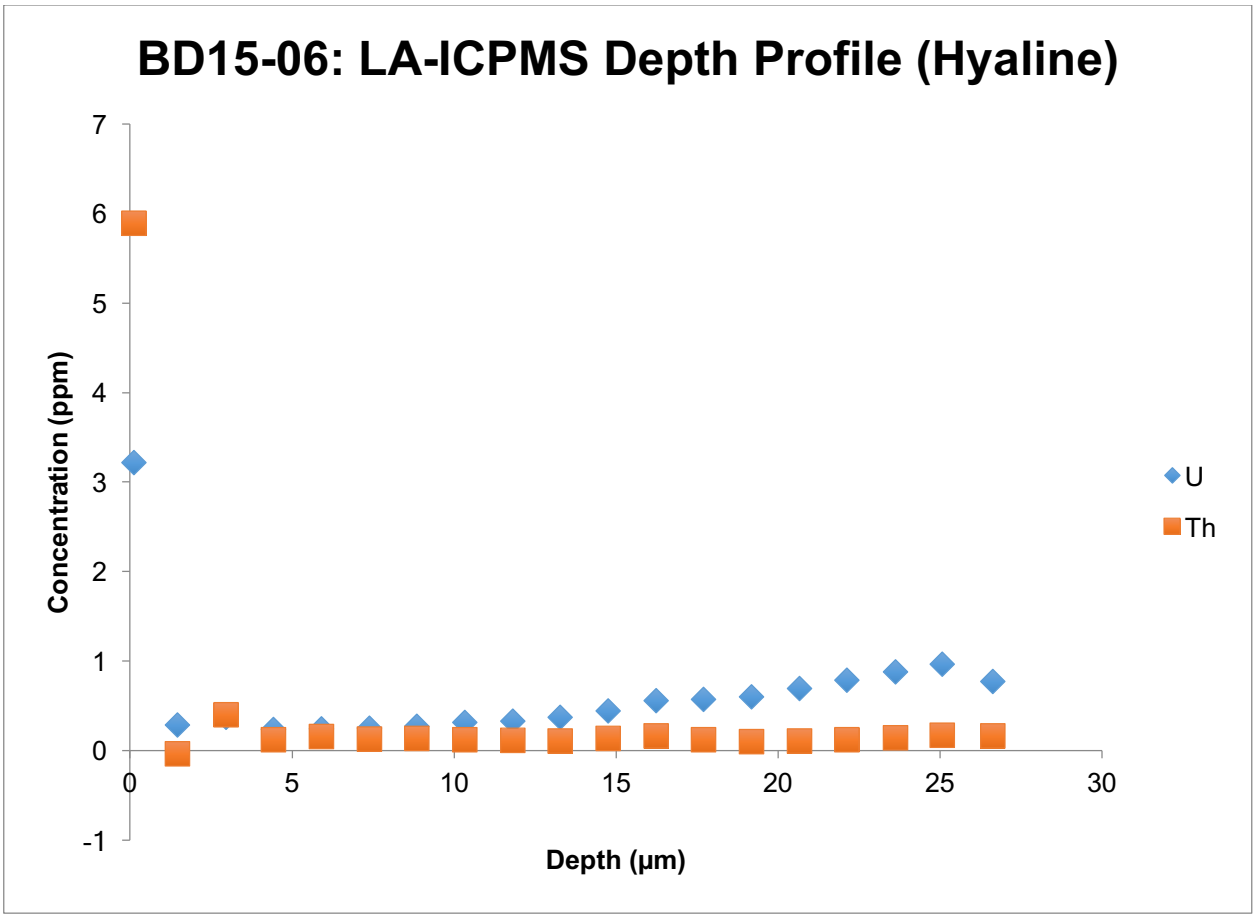
BD15-06: LA-ICPMS Depth Profile (Hyaline)
Concentration (ppm)
7
6
5
4
3
2
1
0
-1
0
5
10
15
20
25
30
Depth (µm)
U
Th

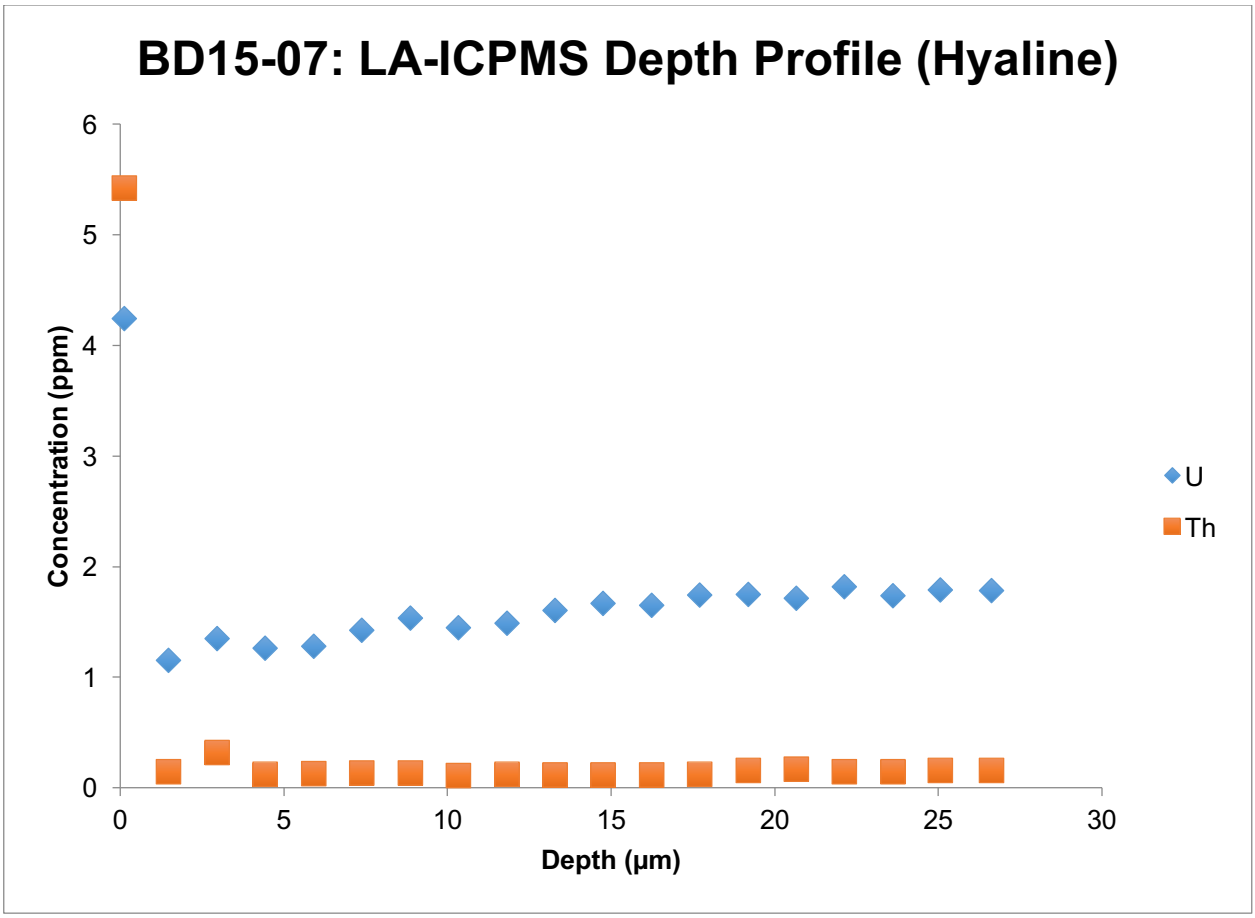
BD15-07: LA-ICPMS Depth Profile (Hyaline)
Concentration (ppm)
Depth (µm)
U
Th
0
1
2
3
4
5
6
0
5
10
15
20
25
30

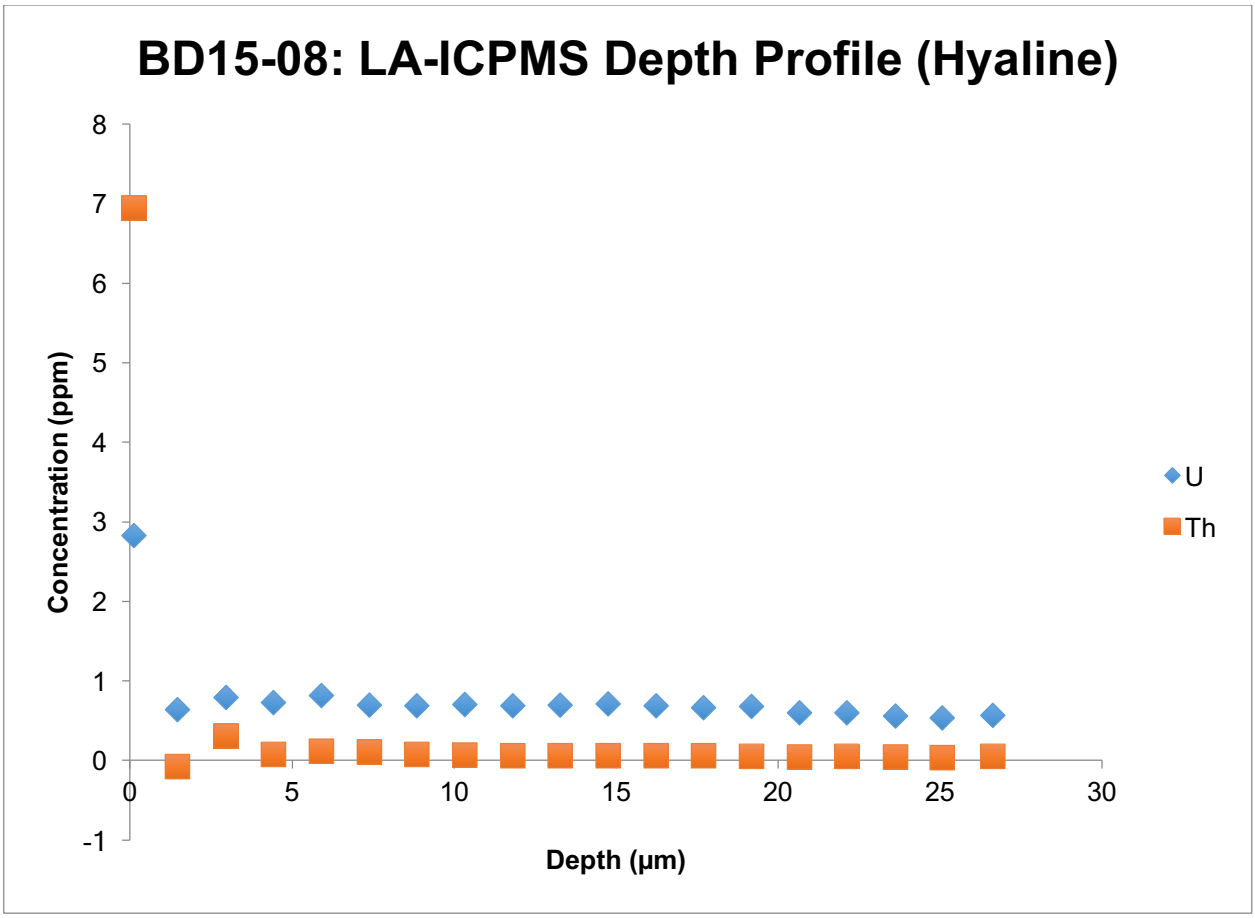
BD15-08: LA-ICPMS Depth Profile (Hyaline)
Concentration (ppm)
8
7
6
5
4
3
2
1
0
-1
0
5
10
15
20
25
30
Depth (µm)
U
Th

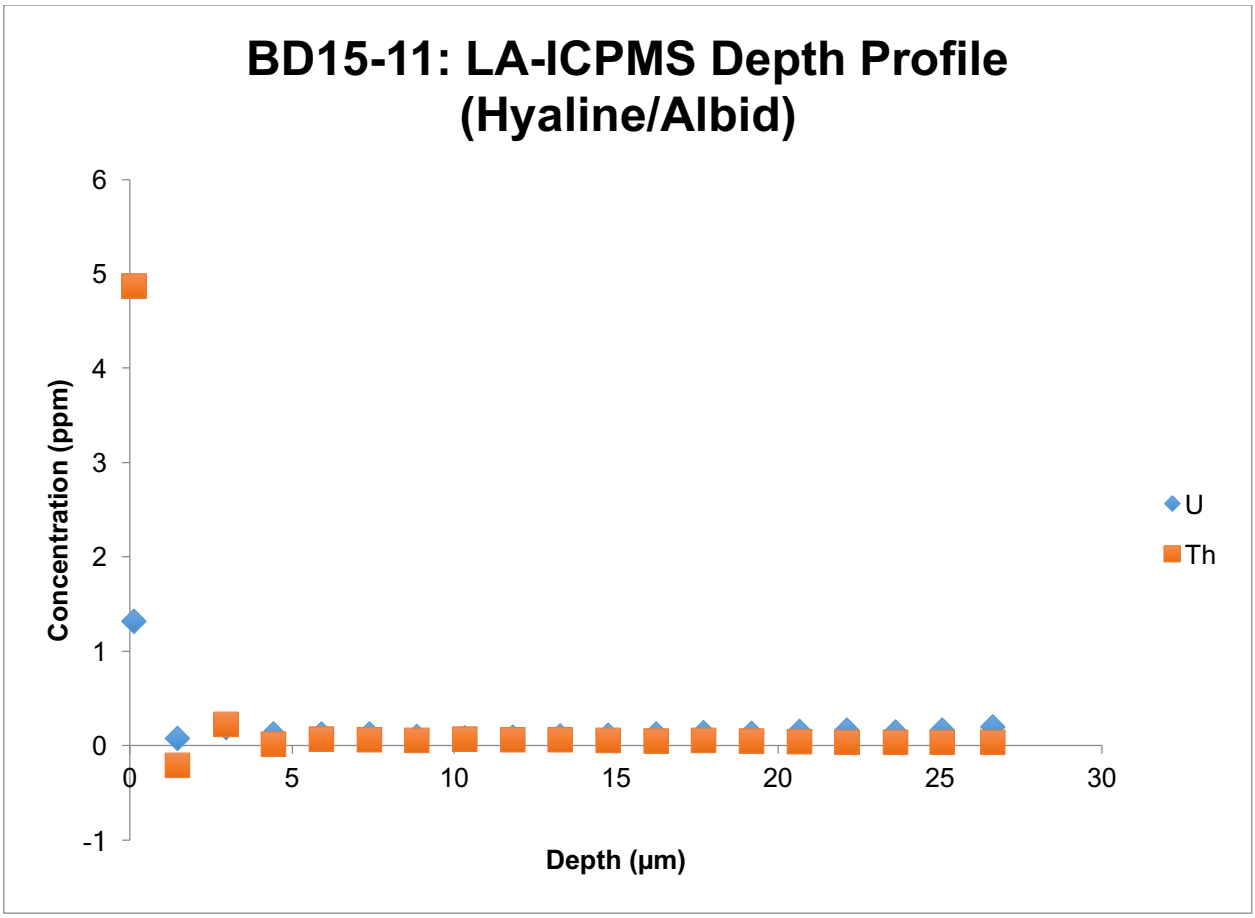
BD15-11: LA-ICPMS Depth Profile
(Hyaline/Albid)
Concentration (ppm)
6
5
4
3
2
1
0
-1
0
5
10
15
20
25
30
Depth (µm)
U
Th

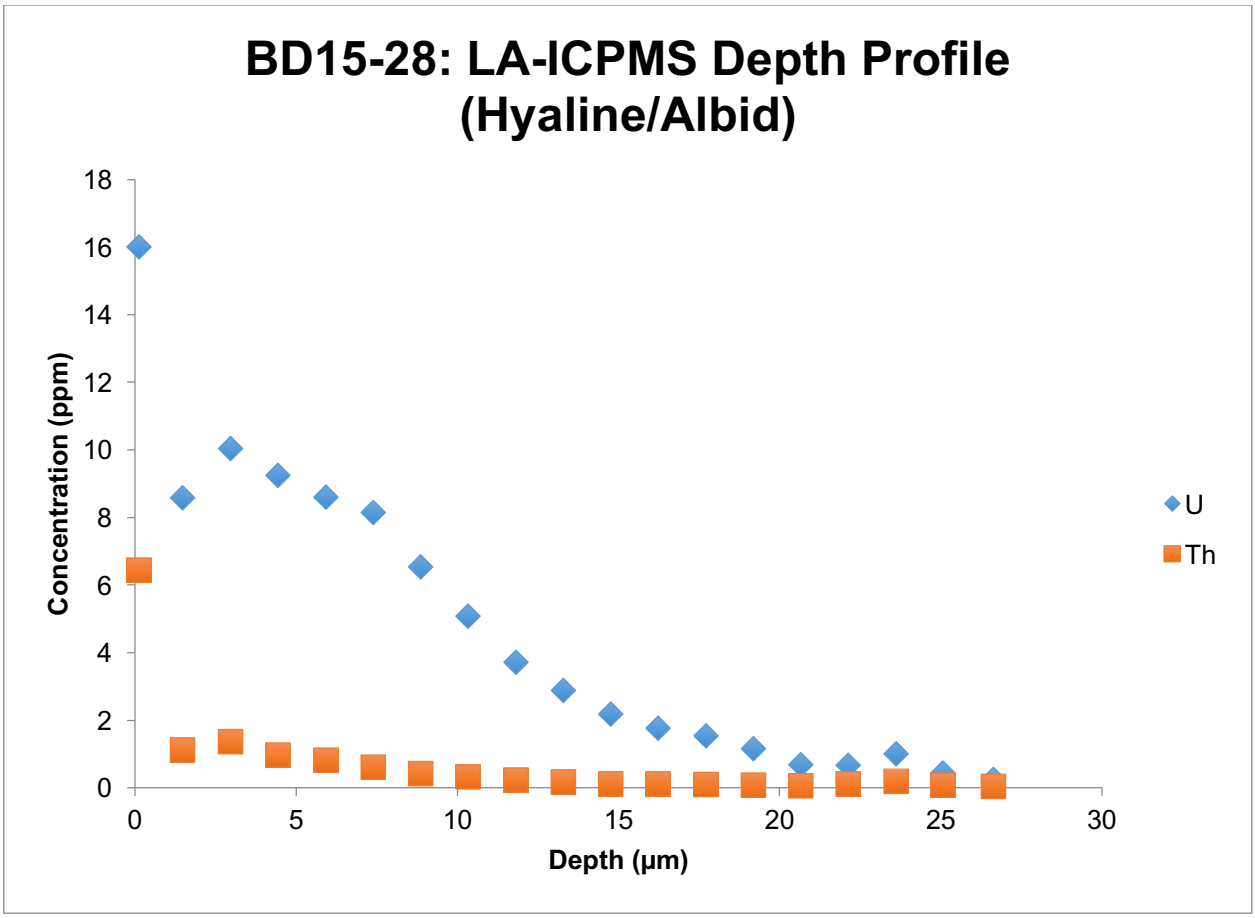
BD15-28: LA-ICPMS Depth Profile
(Hyaline/Albid)
Concentration (ppm)
18
16
14
12
10
8
6
4
2
0
0
5
10
15
20
25
30
Depth (µm)
U
Th

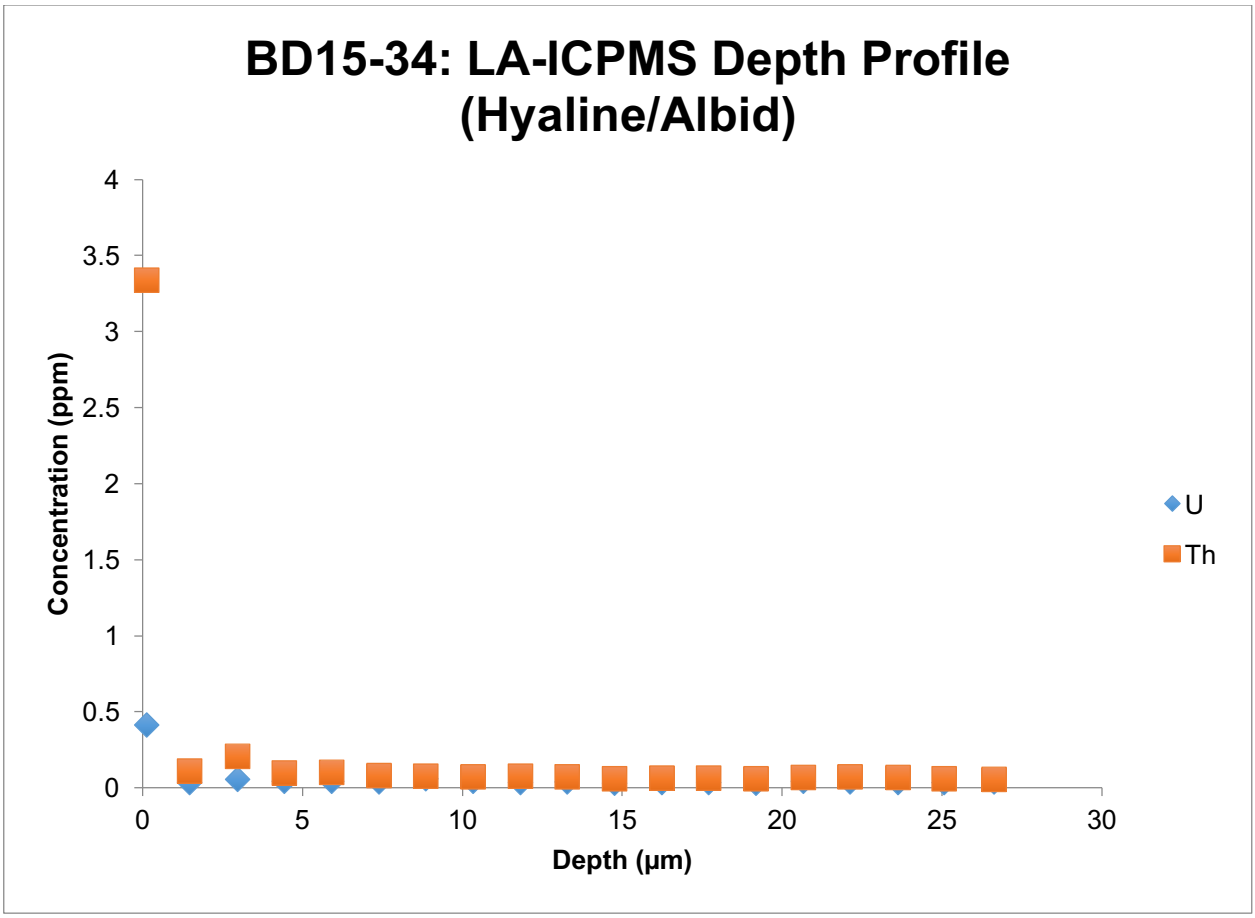
BD15-34: LA-ICPMS Depth Profile
(Hyaline/Albid)
Concentration (ppm)
4
3.5
3
2.5
2
1.5
1
0.5
0
0
5
10
15
20
25
30
Depth (µm)
U
Th

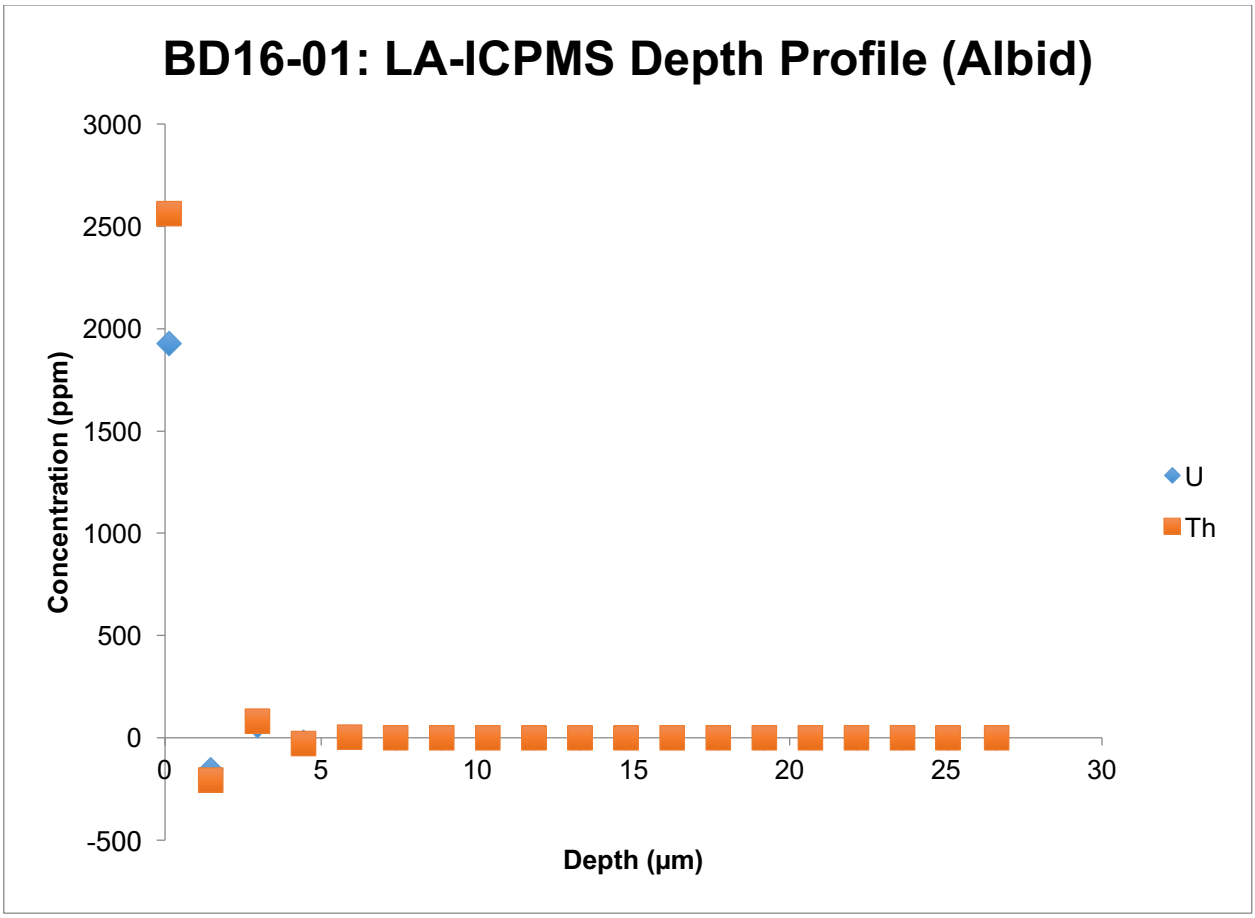
BD16-01: LA-ICPMS Depth Profile (Albid)
Concentration (ppm)
3000
2500
2000
1500
1000
500
0
-500
0
5
10
15
20
25
30
Depth (µm)
U
Th

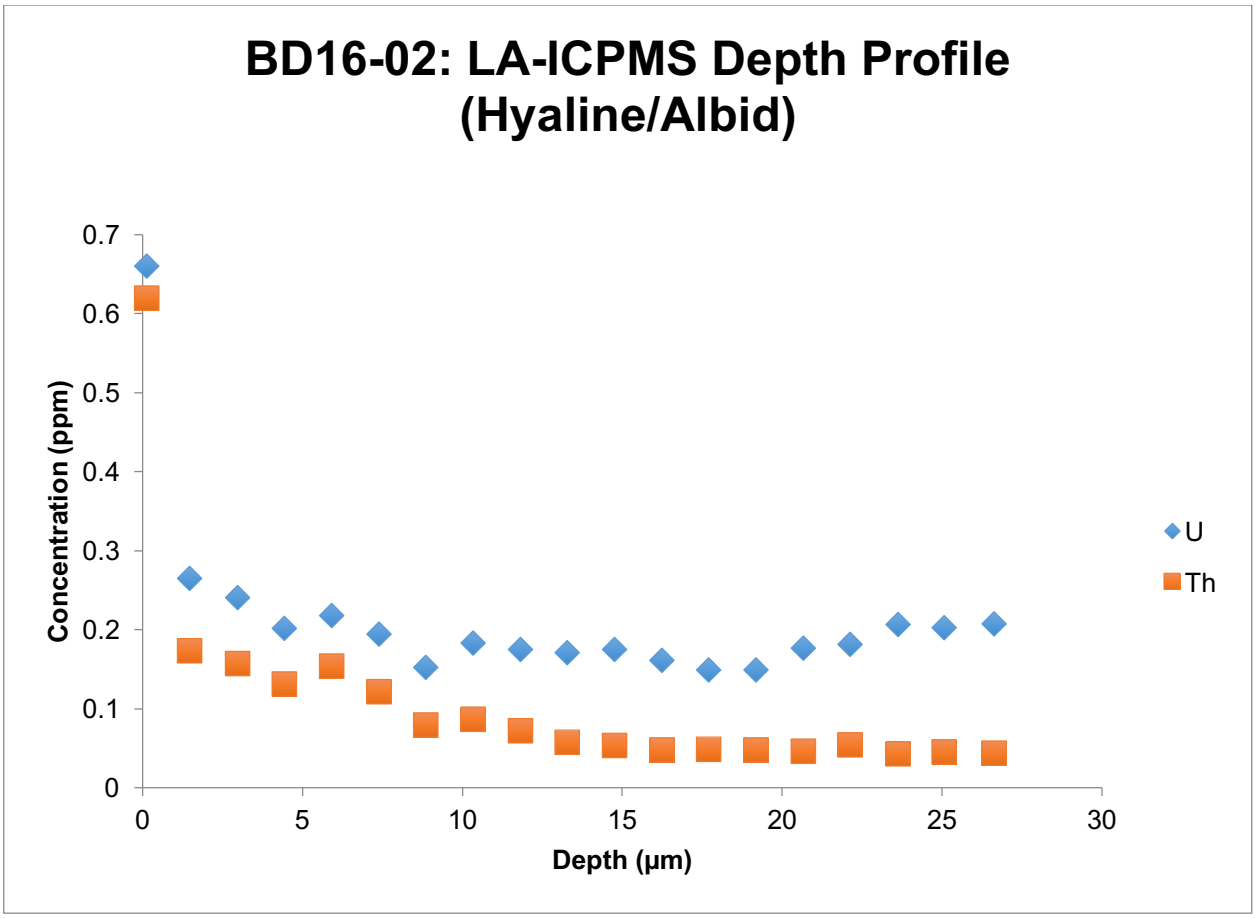
BD16-02: LA-ICPMS Depth Profile
(Hyaline/Albid)
Concentration (ppm)
0.7
0.6
0.5
0.4
0.3
0.2
0.1
0
0
5
10
15
20
25
30
Depth (µm)
U
Th

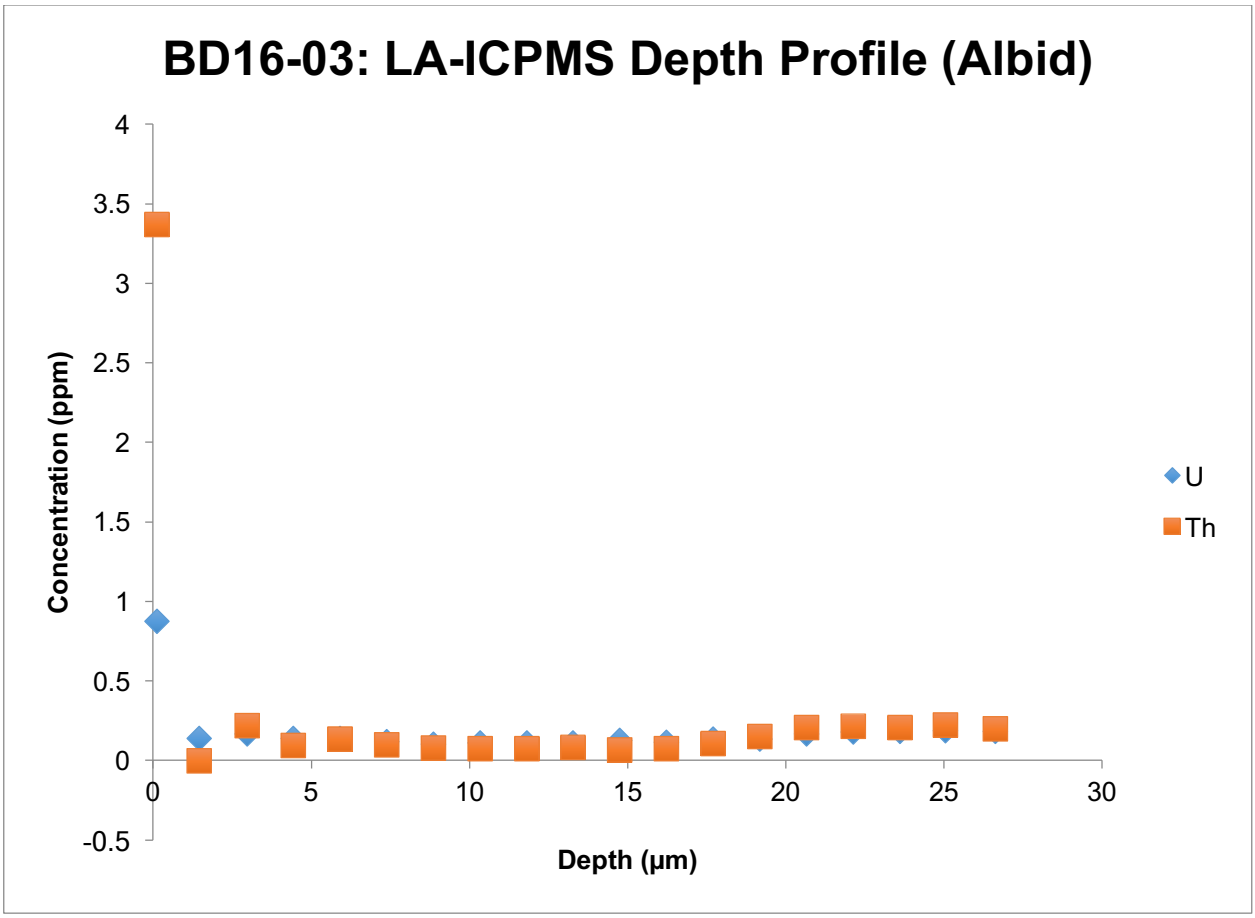
BD16-03: LA-ICPMS Depth Profile (Albid)
Concentration (ppm)
4
3.5
3
2.5
2
1.5
1
0.5
0
-0.5
0
5
10
15
20
25
30
Depth (µm)
U
Th

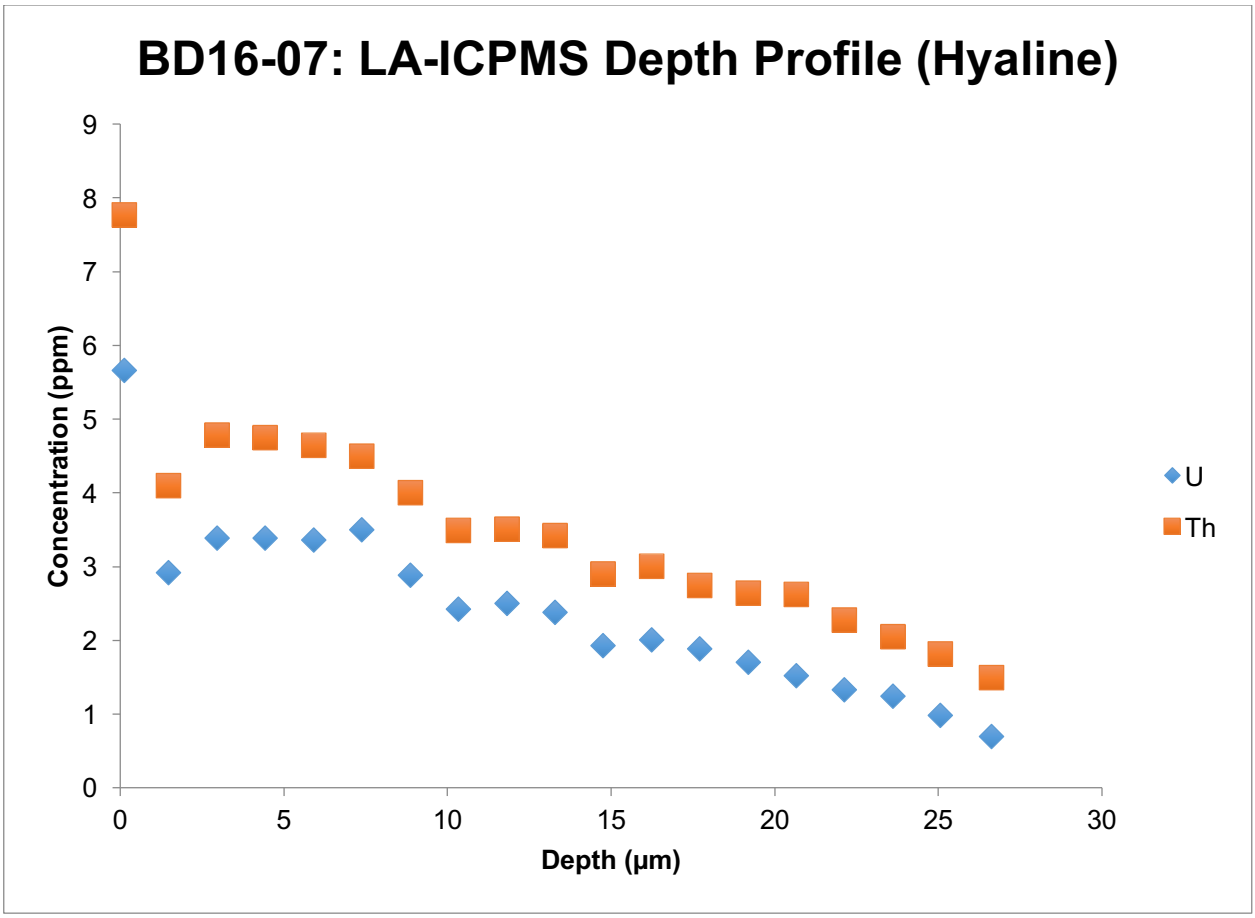
BD16-07: LA-ICPMS Depth Profile (Hyaline)
Concentration (ppm)
Depth (µm)
0
1
2
3
4
5
6
7
8
9
0
5
10
15
20
25
30
U
Th

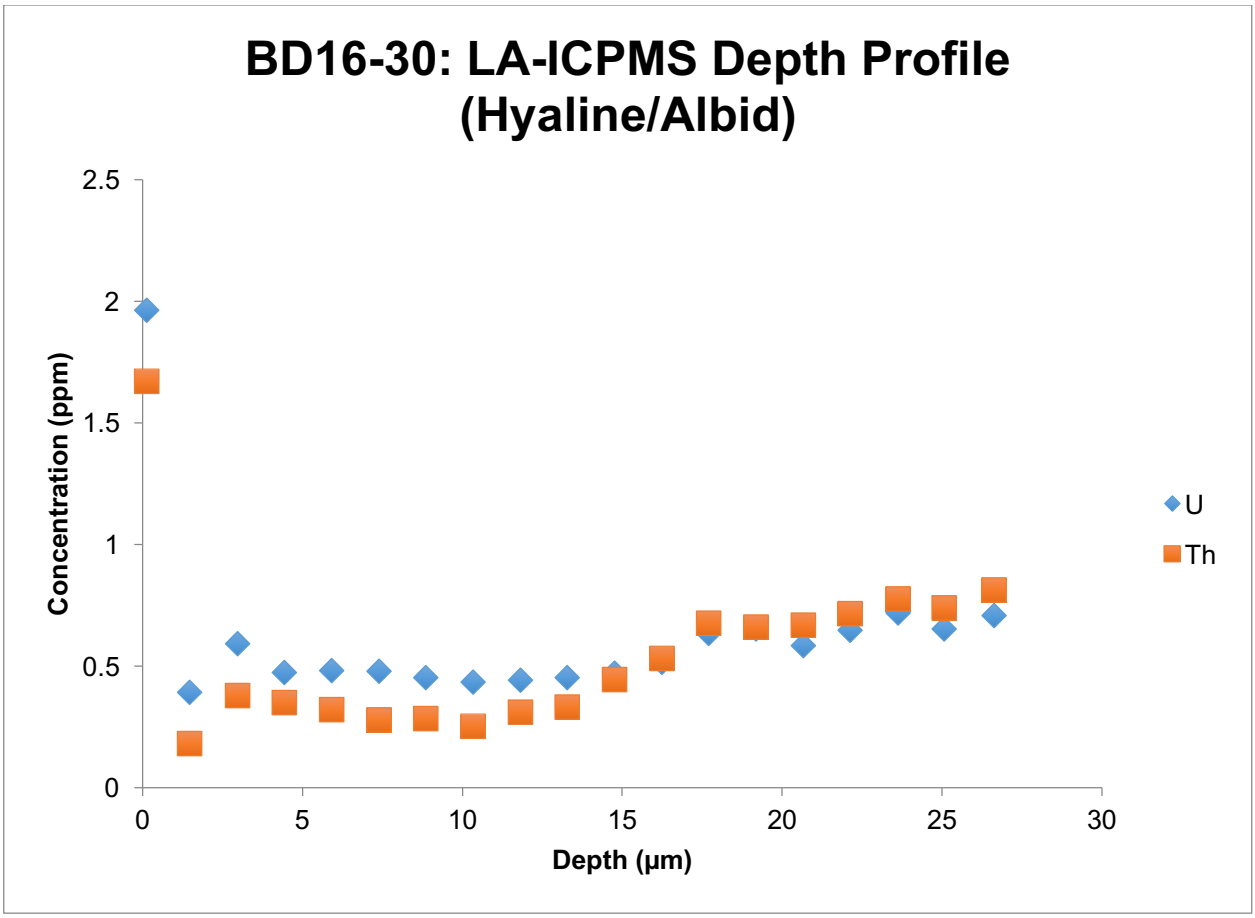
BD16-30: LA-ICPMS Depth Profile
(Hyaline/Albid)
Concentration (ppm)
2.5
2
1.5
1
0.5
0
0
5
10
15
20
25
30
Depth (µm)
U
Th

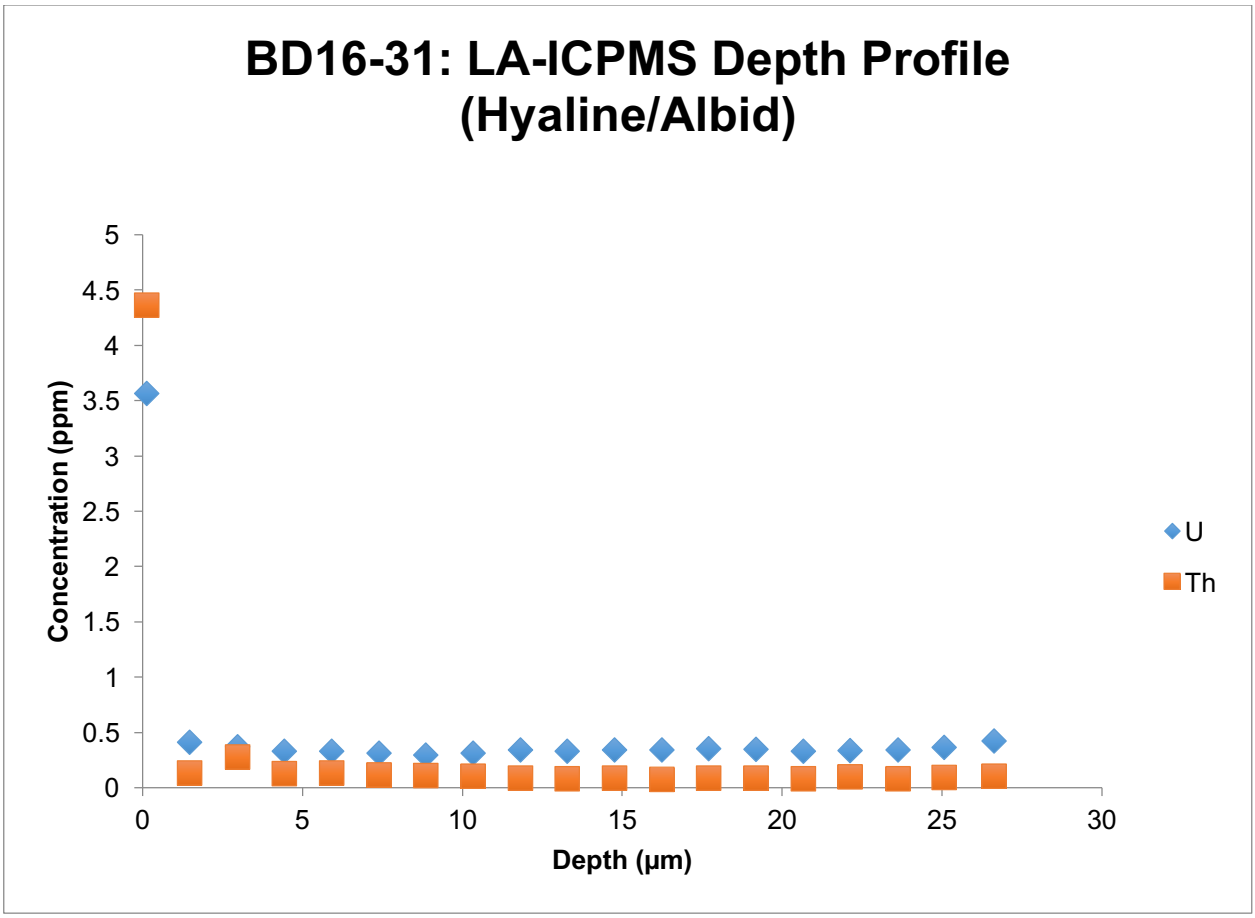
BD16-31: LA-ICPMS Depth Profile
(Hyaline/Albid)
Concentration (ppm)
5
4.5
4
3.5
3
2.5
2
1.5
1
0.5
0
0
5
10
15
20
25
30
Depth (µm)
U
Th

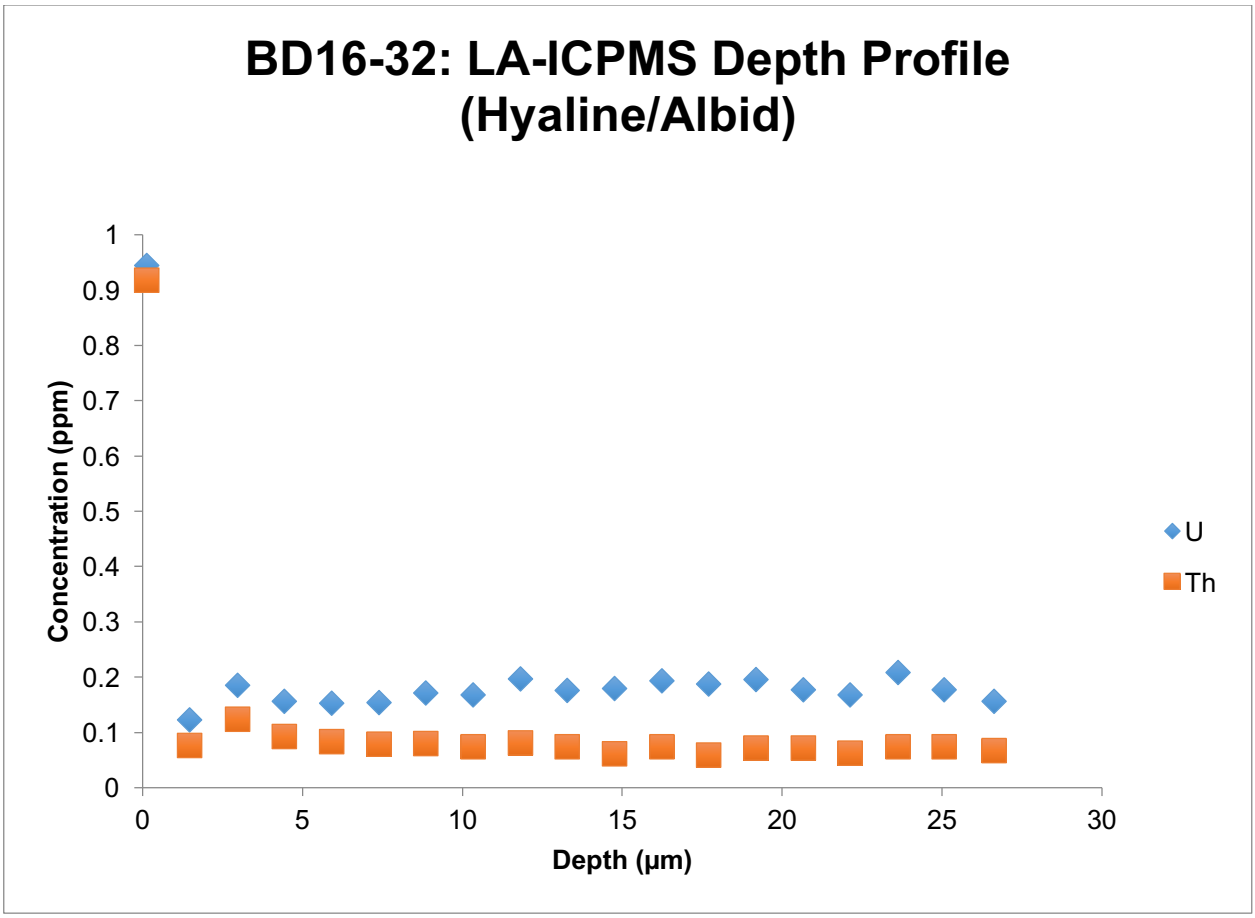
BD16-32: LA-ICPMS Depth Profile
(Hyaline/Albid)
Concentration (ppm)
1
0.9
0.8
0.7
0.6
0.5
0.4
0.3
0.2
0.1
0
0
5
10
15
20
25
30
Depth (µm)
U
Th

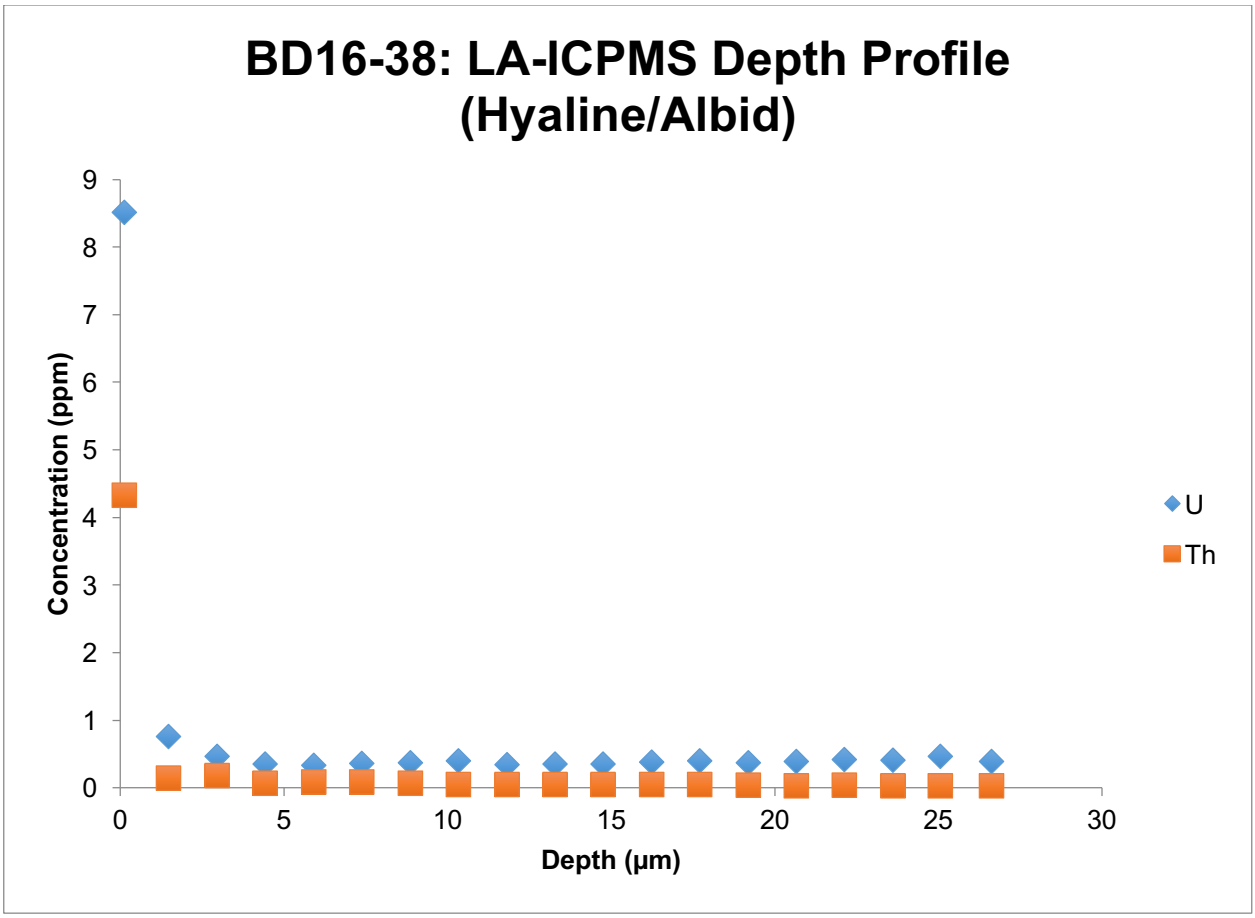
BD16-38: LA-ICPMS Depth Profile
(Hyaline/Albid)
Concentration (ppm)
Depth (µm)
U
Th
0
1
2
3
4
5
6
7
8
9
0
5
10
15
20
25
30

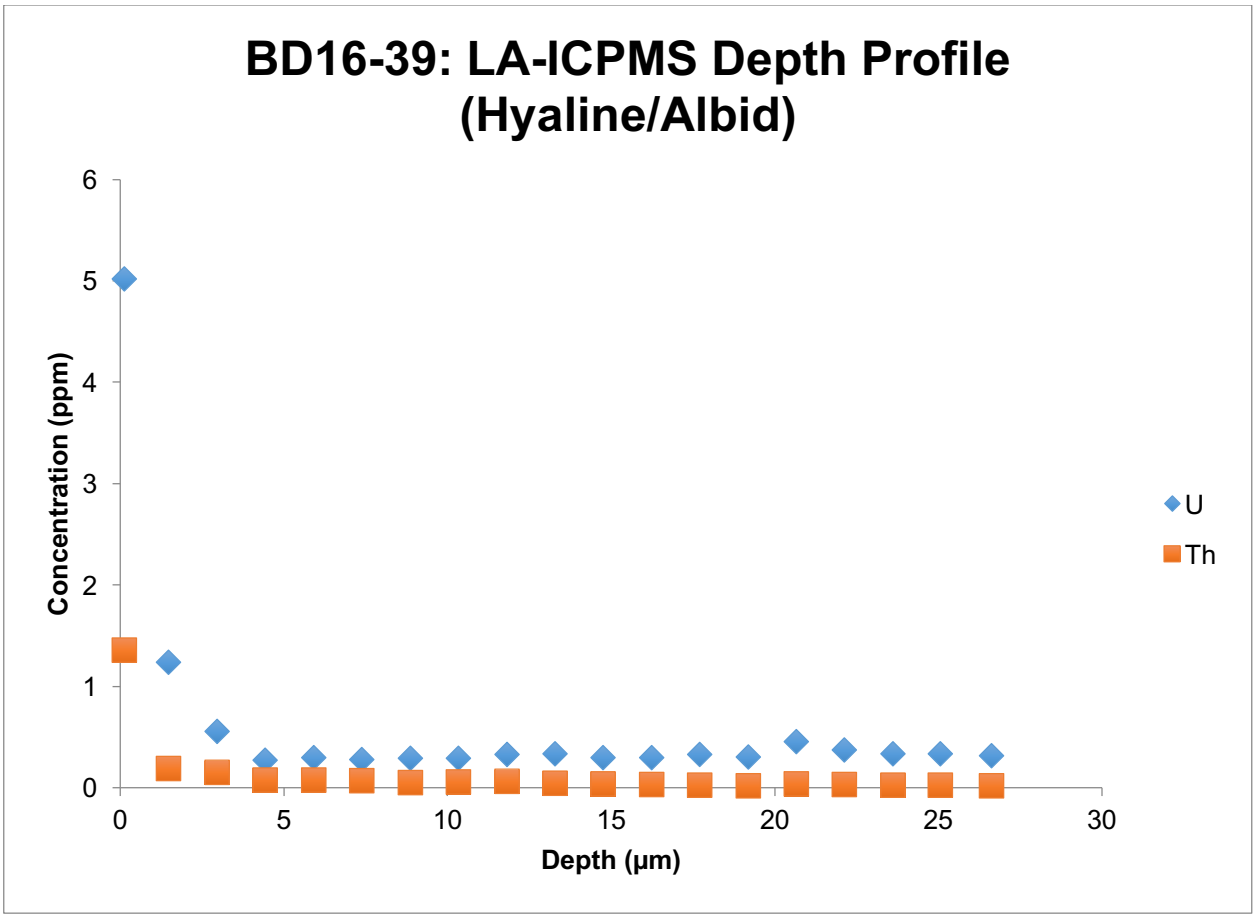
BD16-39: LA-ICPMS Depth Profile
(Hyaline/Albid)
Concentration (ppm)
0
1
2
3
4
5
6
0
5
10
15
20
25
30
Depth (µm)
U
Th

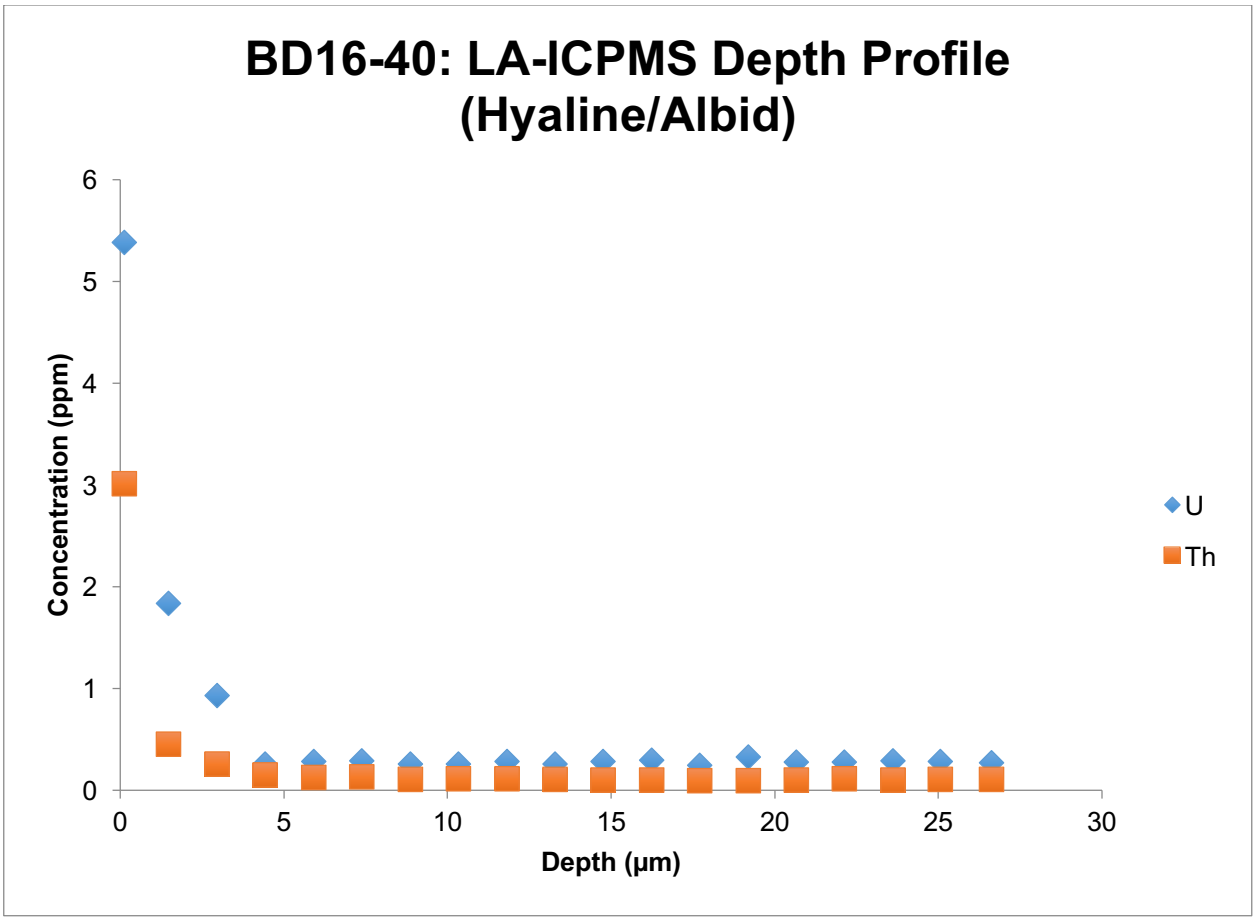
BD16-40: LA-ICPMS Depth Profile
(Hyaline/Albid)
Concentration (ppm)
0
1
2
3
4
5
6
0
5
10
15
20
25
30
Depth (µm)
U
Th

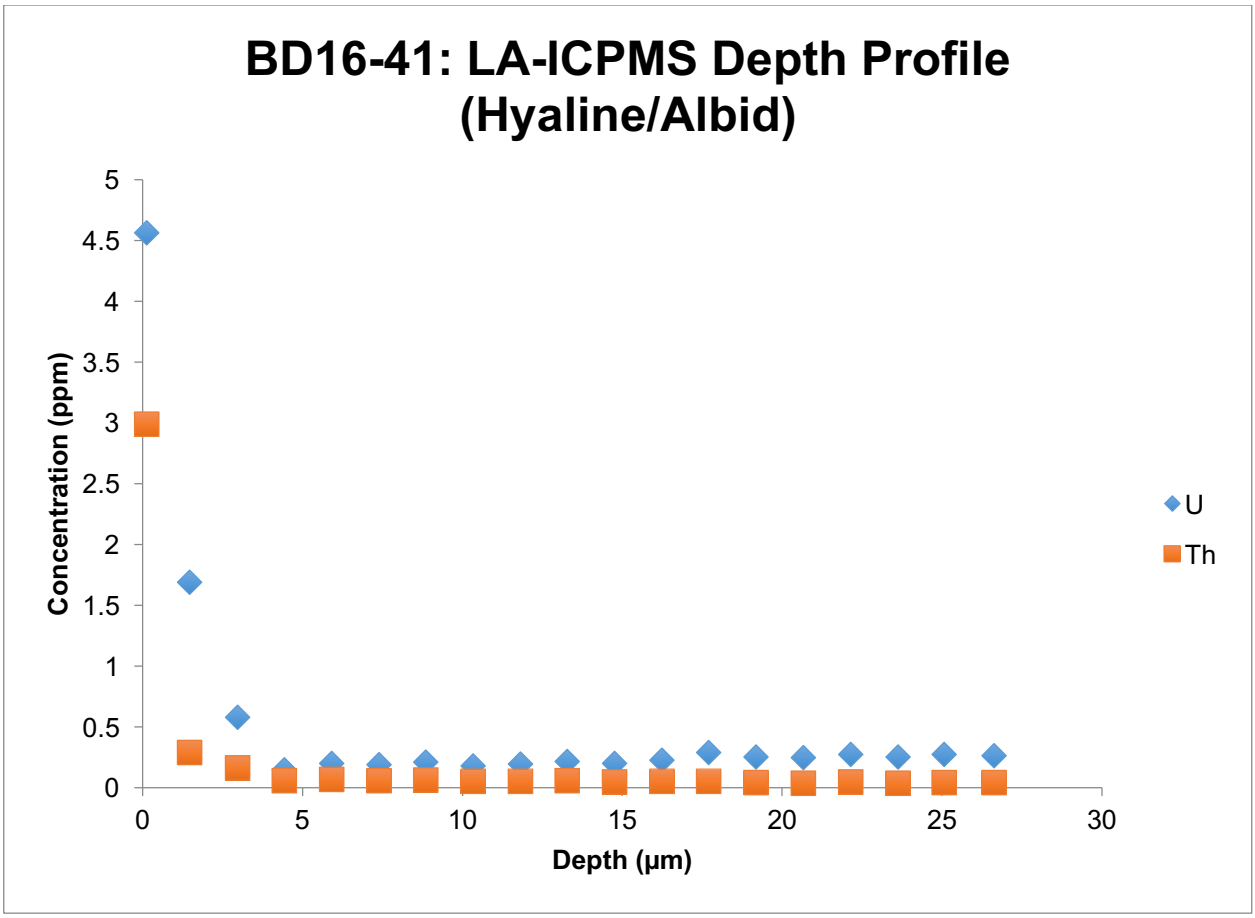
BD16-41: LA-ICPMS Depth Profile
(Hyaline/Albid)
Concentration (ppm)
5
4.5
4
3.5
3
2.5
2
1.5
1
0.5
0
0
5
10
15
20
25
30
Depth (µm)
U
Th

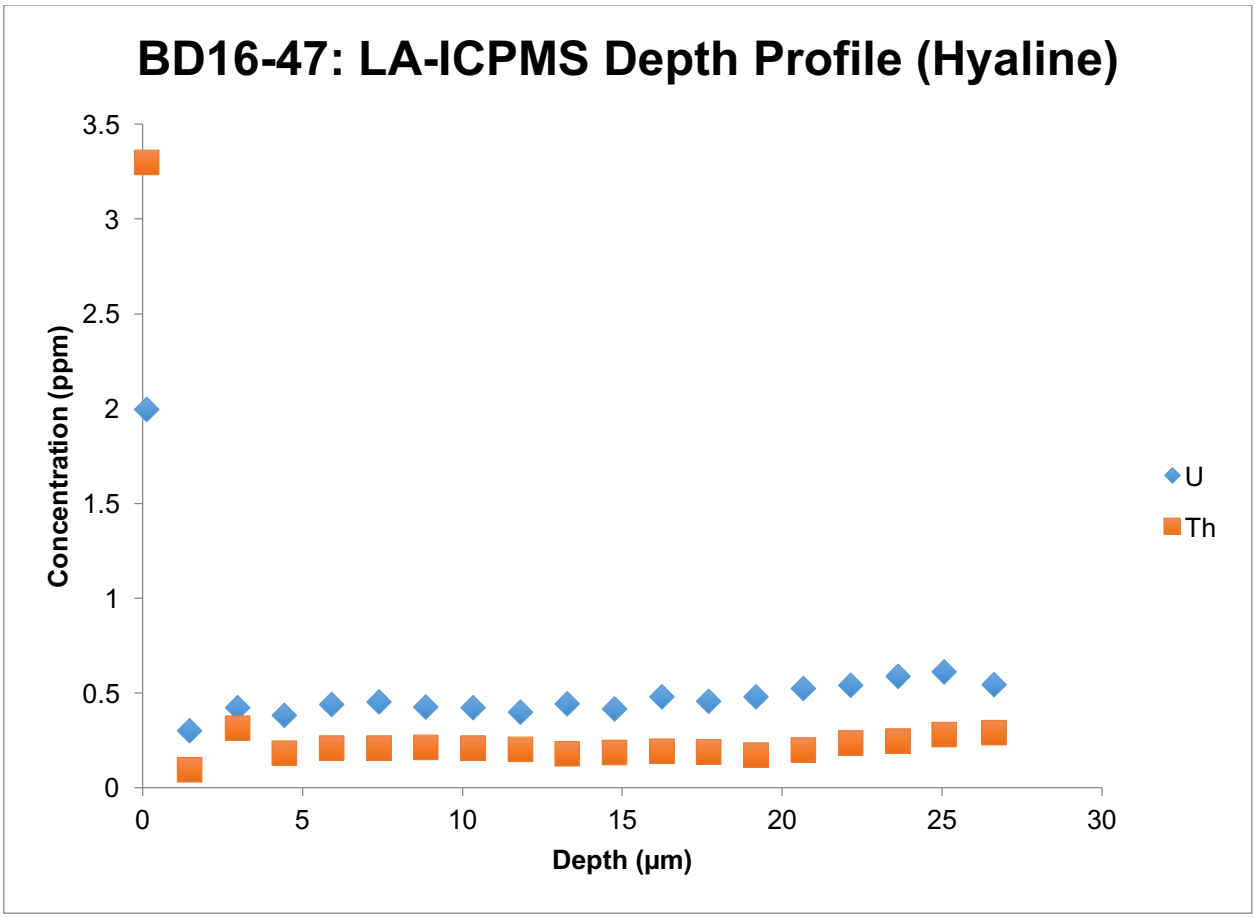
BD16-47: LA-ICPMS Depth Profile (Hyaline)
Concentration (ppm)
3.5
3
2.5
2
1.5
1
0.5
0
0
5
10
15
20
25
30
Depth (µm)
U
Th

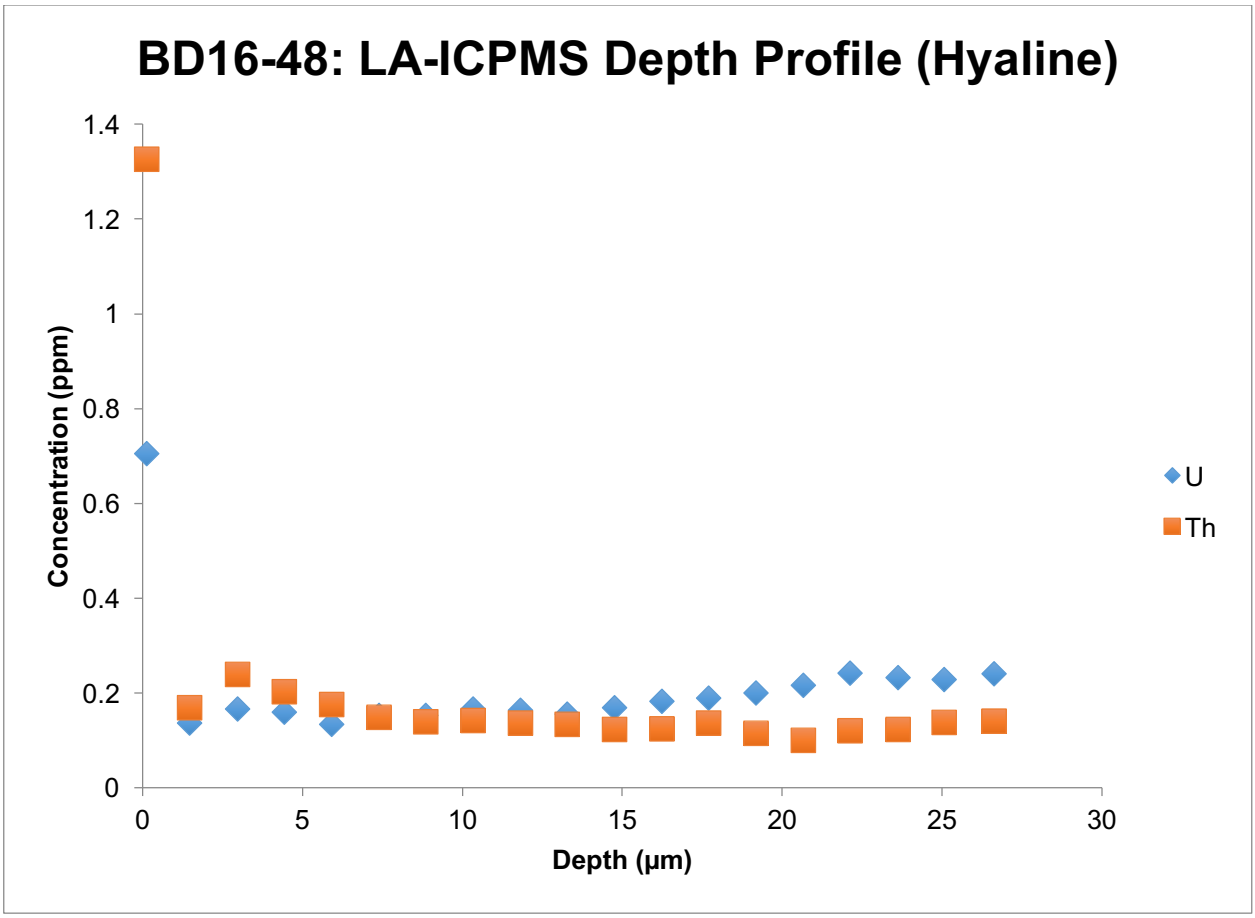
BD16-48: LA-ICPMS Depth Profile (Hyaline)
Concentration (ppm)
1.4
1.2
1
0.8
0.6
0.4
0.2
0
0
5
10
15
20
25
30
Depth (µm)
U
Th

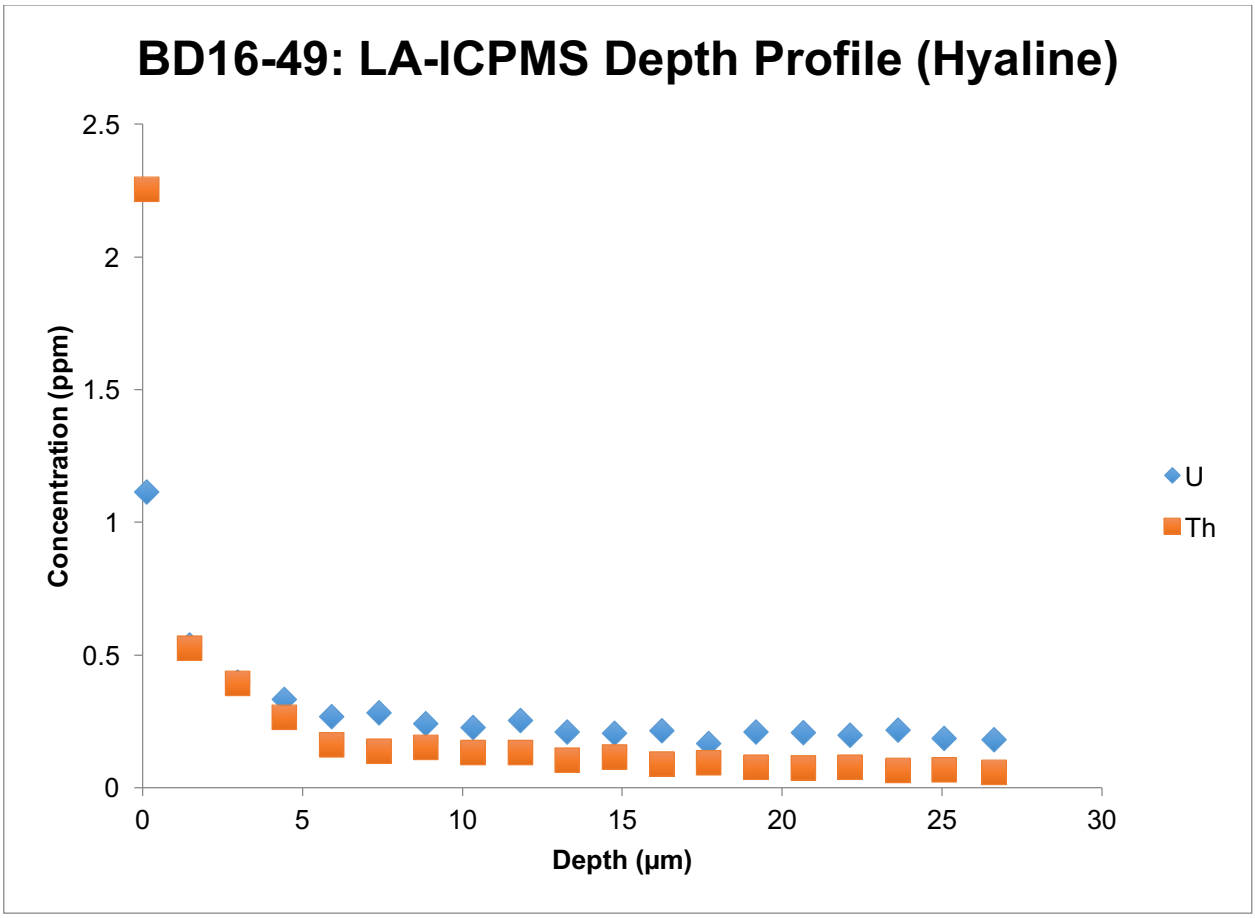
BD16-49: LA-ICPMS Depth Profile (Hyaline)
Concentration (ppm)
2.5
2
1.5
1
0.5
0
0
5
10
15
20
25
30
Depth (µm)
U
Th

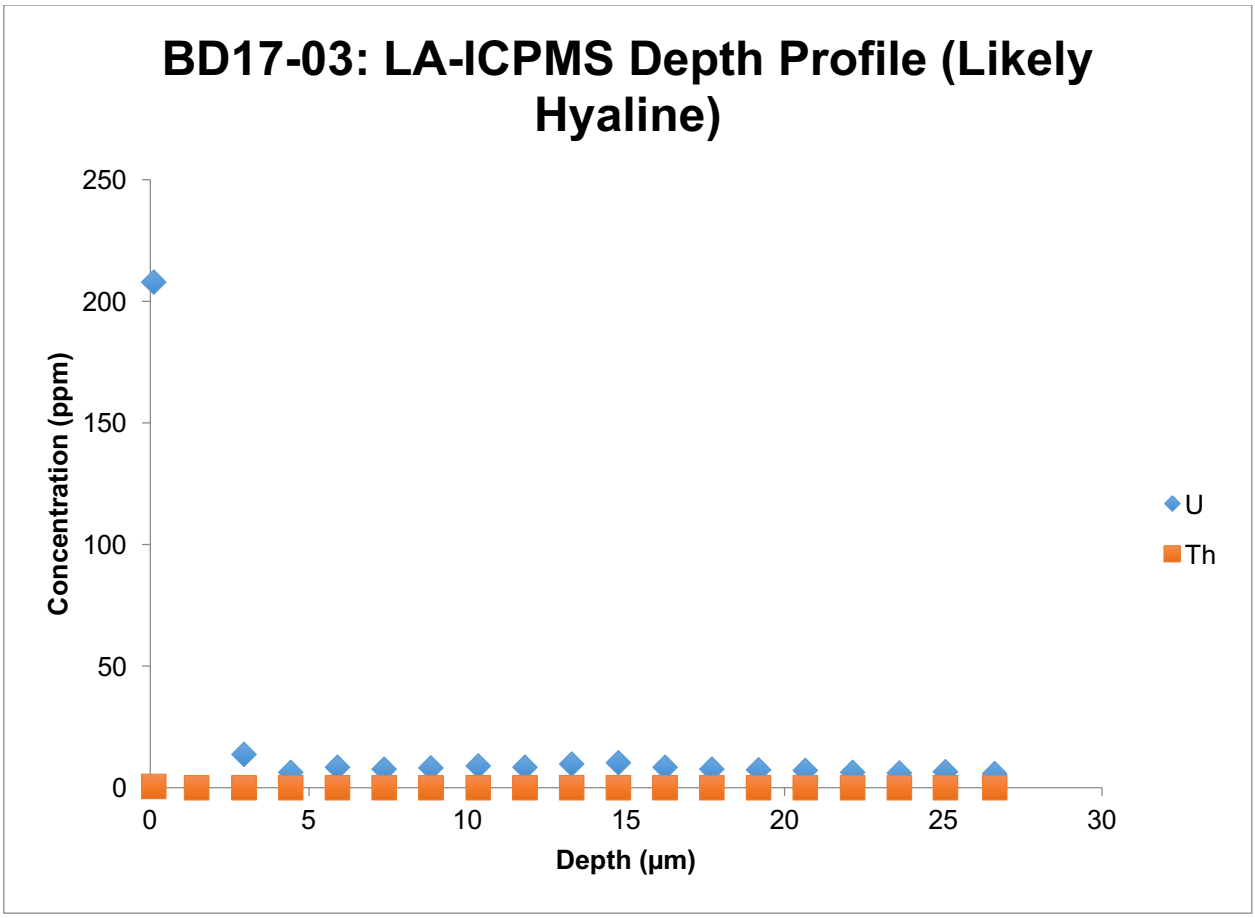
BD17-03: LA-ICPMS Depth Profile (Likely Hyaline)
Concentration (ppm)
250
200
150
100
50
0
0
5
10
15
20
25
30
Depth (µm)
U
Th

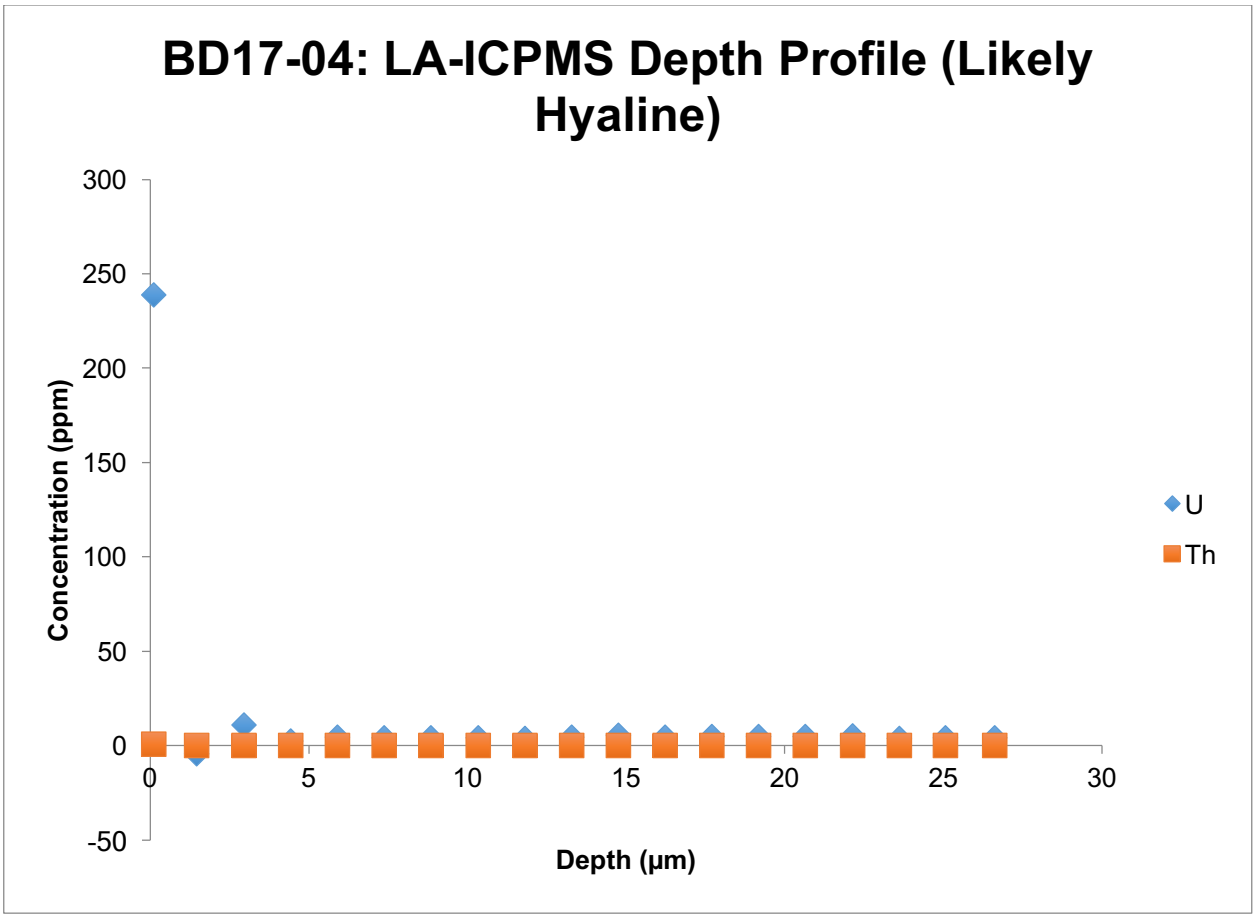
BD17-04: LA-ICPMS Depth Profile (Likely Hyaline)
300
250
200
150
100
50
0
-50
Concentration (ppm)
0
5
10
15
20
25
30
Depth (µm)
U
Th

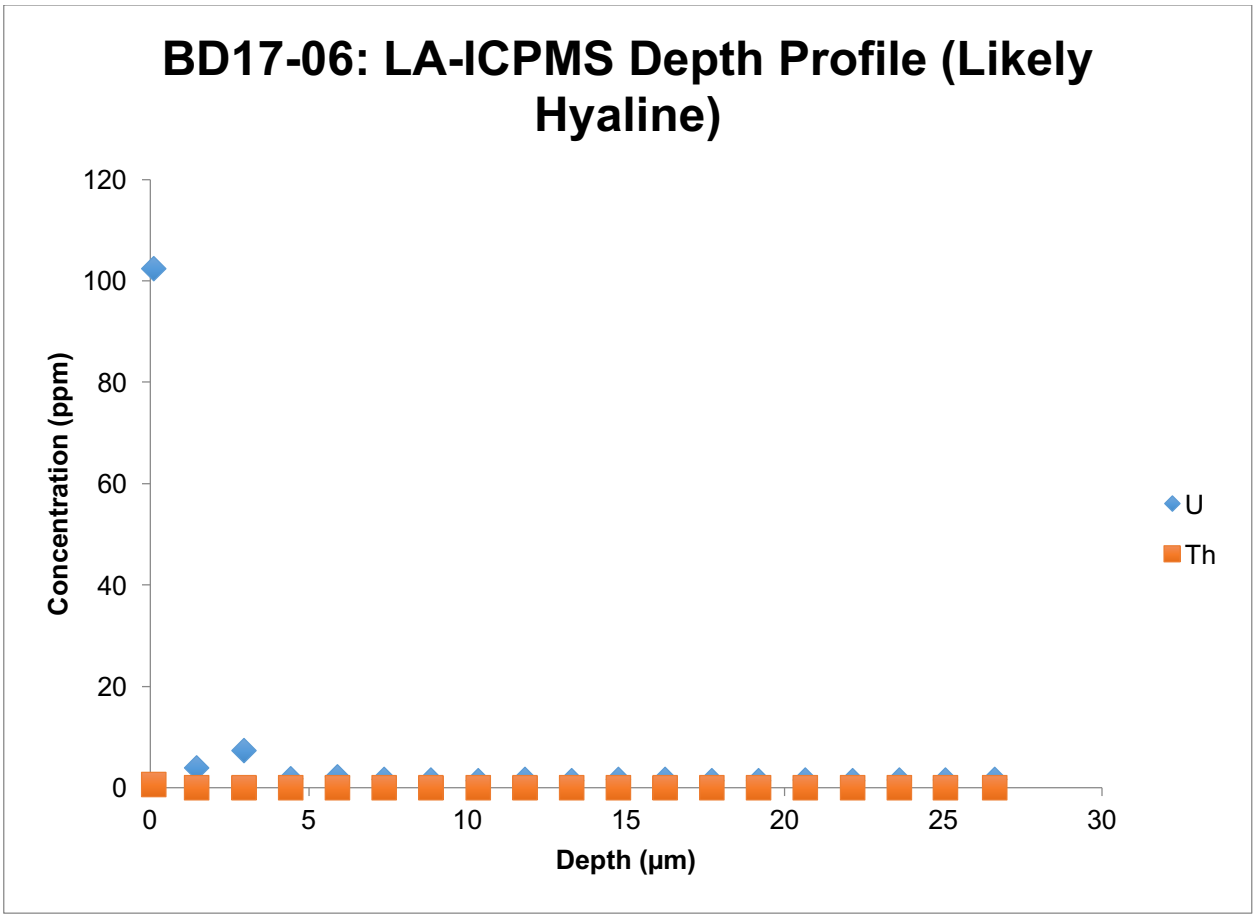
BD17-06: LA-ICPMS Depth Profile (Likely Hyaline)
Concentration (ppm)
120
100
80
60
40
20
0
0
5
10
15
20
25
30
Depth (µm)
U
Th

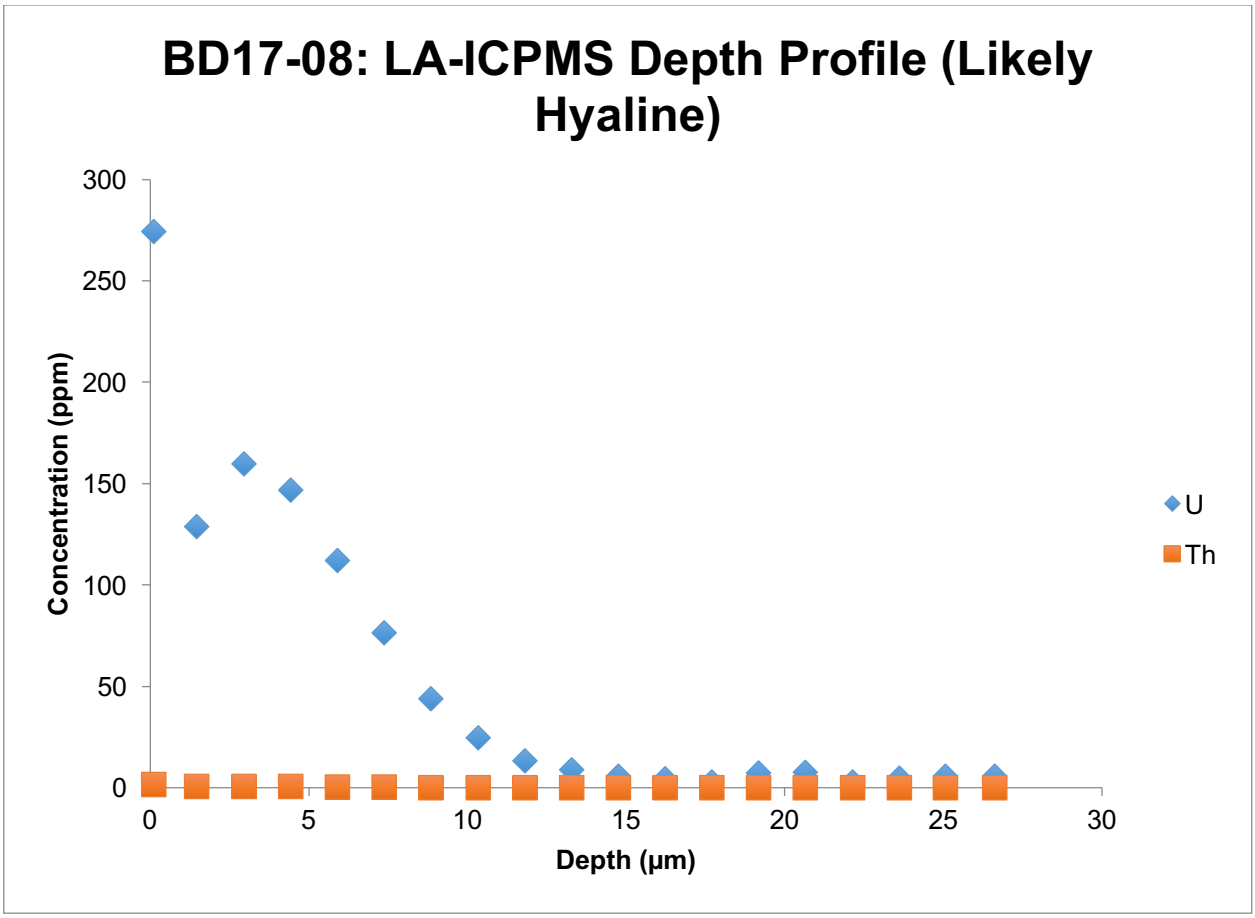
BD17-08: LA-ICPMS Depth Profile (Likely Hyaline)
Concentration (ppm)
300
250
200
150
100
50
0
0
5
10
15
20
25
30
Depth (µm)
U
Th

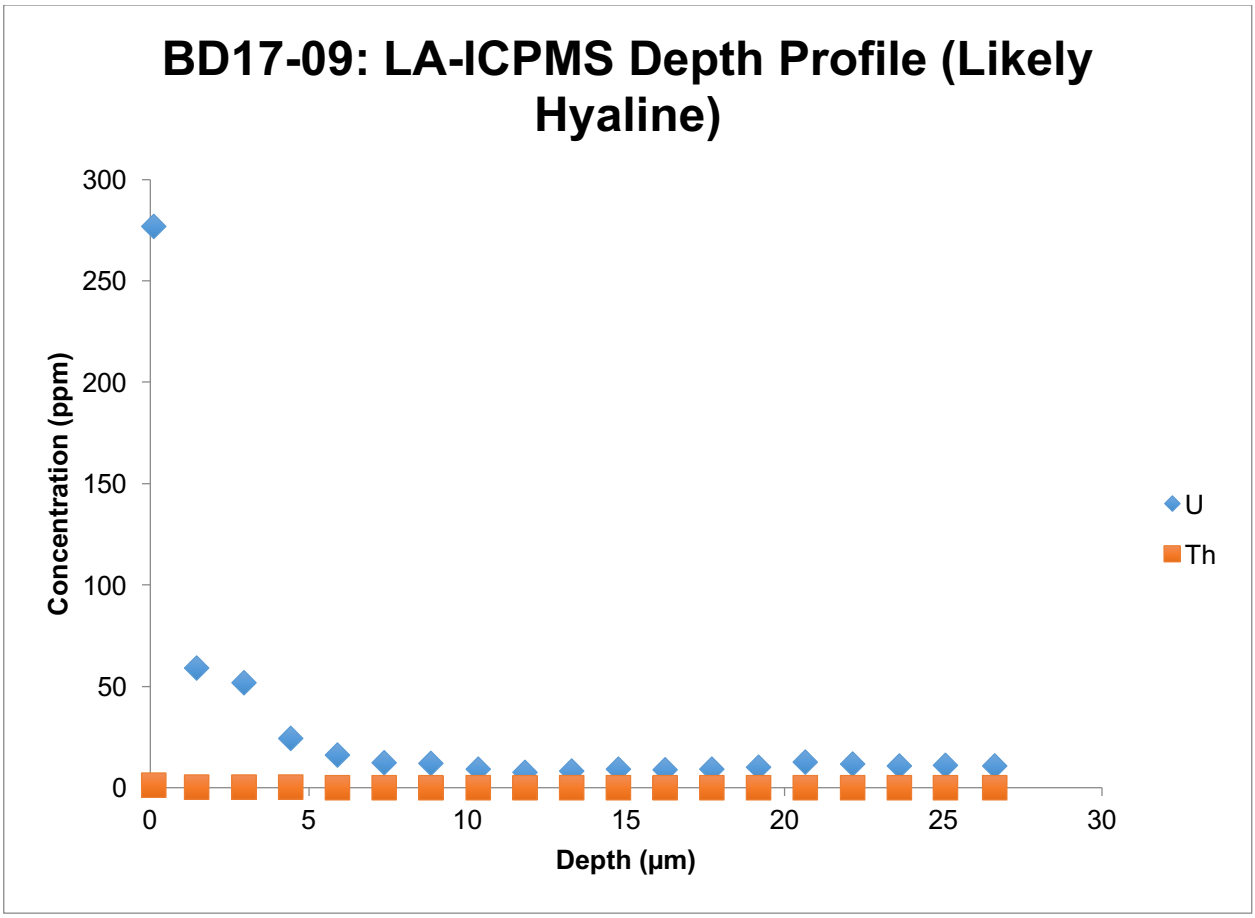
BD17-09: LA-ICPMS Depth Profile (Likely Hyaline)
Concentration (ppm)
300
250
200
150
100
50
0
0
5
10
15
20
25
30
Depth (µm)
U
Th

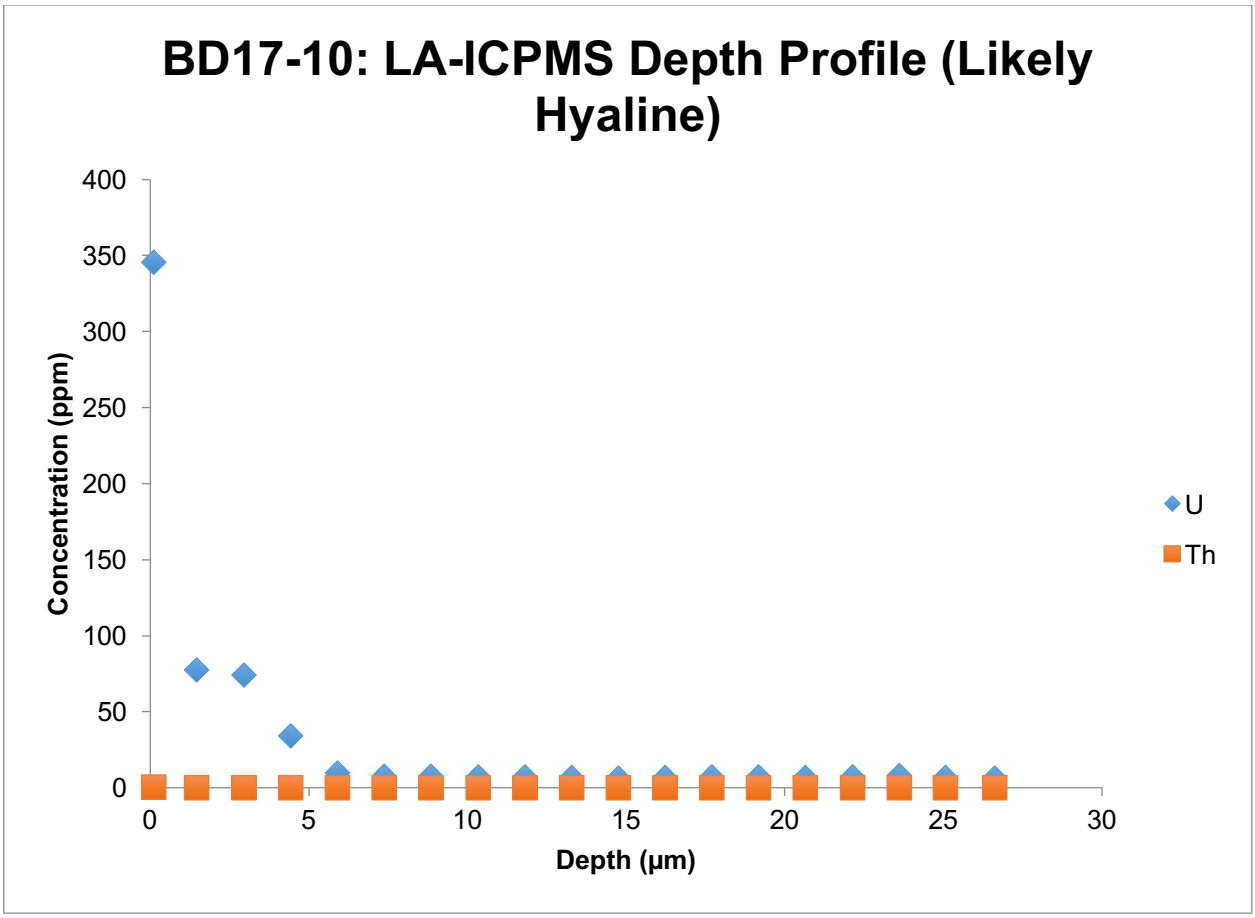
BD17-10: LA-ICPMS Depth Profile (Likely Hyaline)
Concentration (ppm)
400
350
300
250
200
150
100
50
0
0
5
10
15
20
25
30
Depth (µm)
U
Th

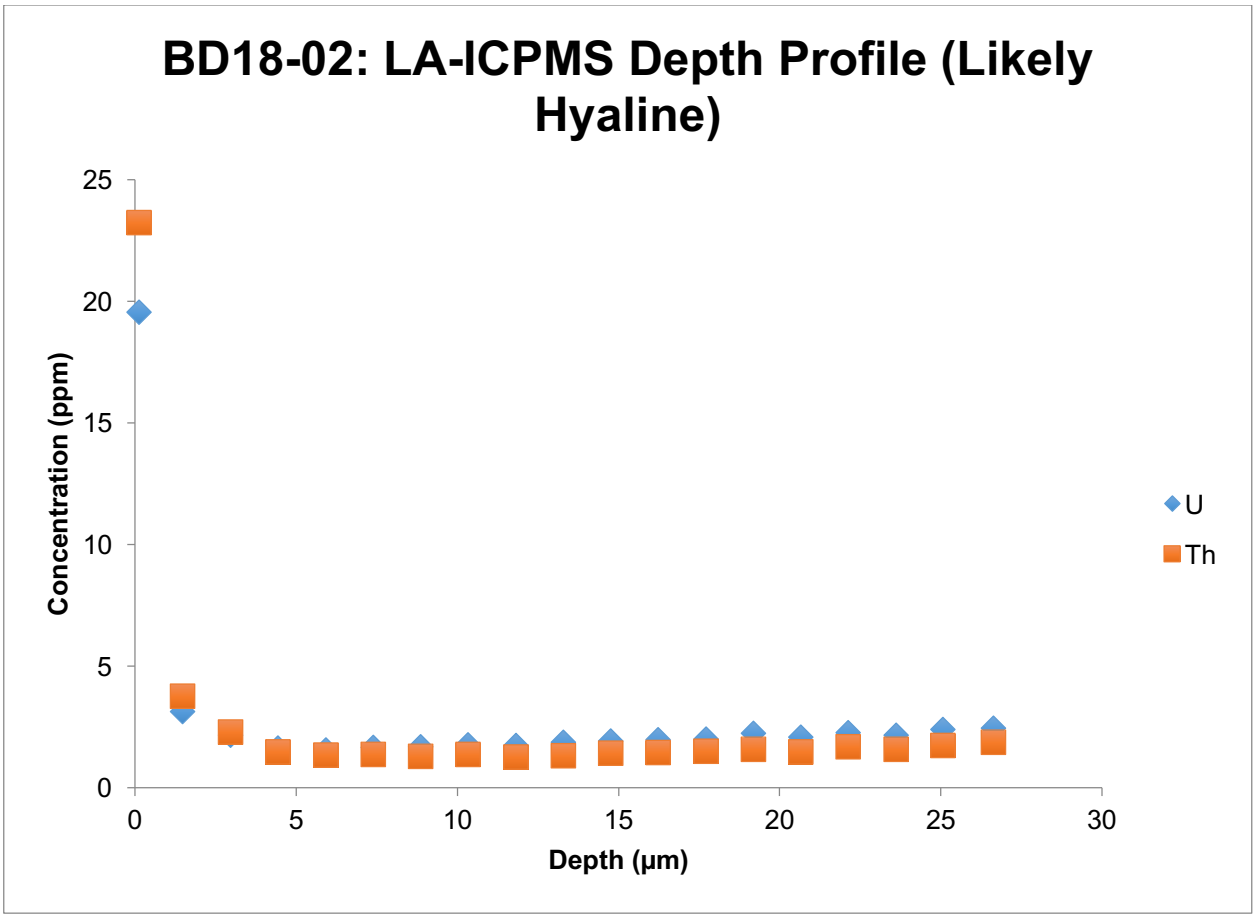
BD18-02: LA-ICPMS Depth Profile (Likely Hyaline)
Concentration (ppm)
25
20
15
10
5
0
0
5
10
15
20
25
30
Depth (µm)
U
Th

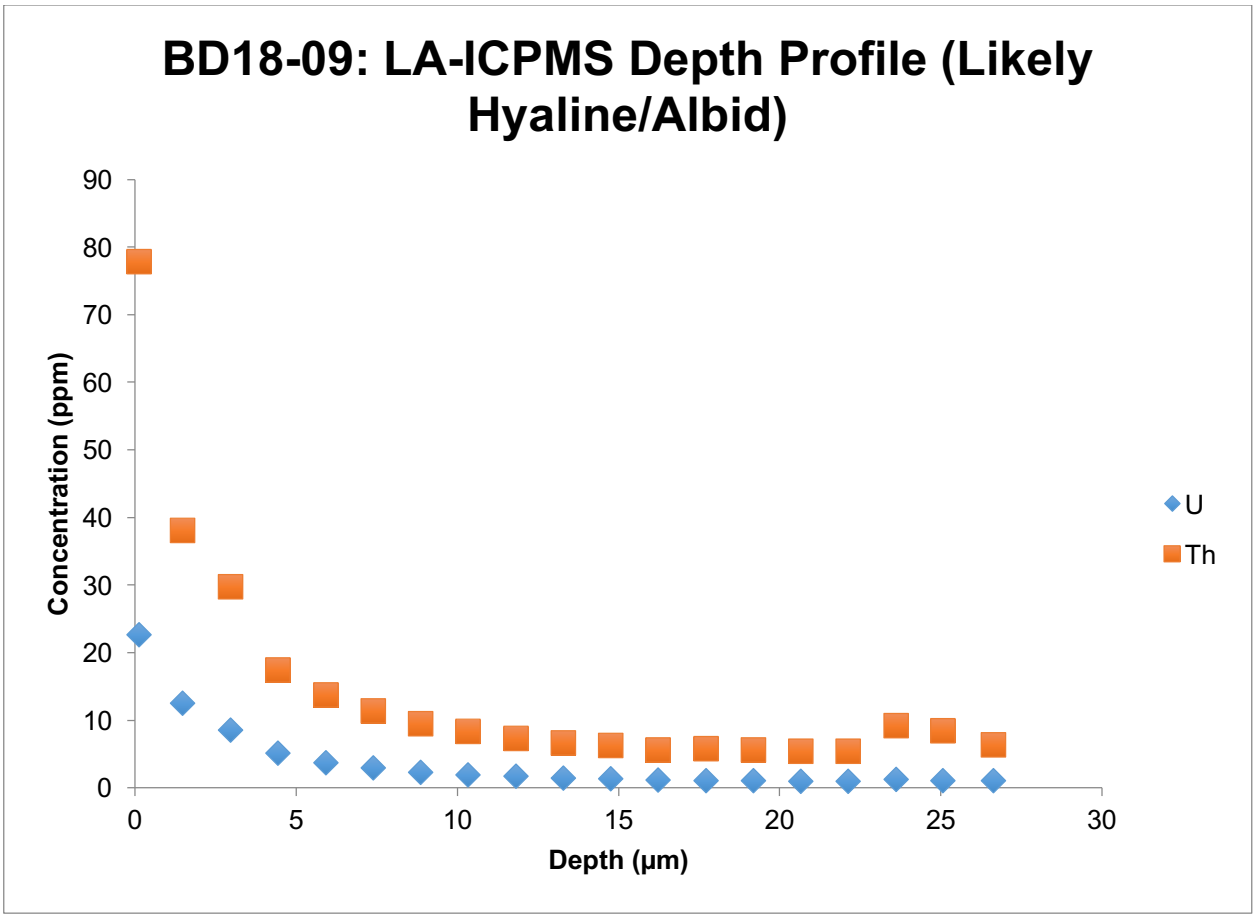
BD18-09: LA-ICPMS Depth Profile (Likely Hyaline/Albid)
Concentration (ppm)
90
80
70
60
50
40
30
20
10
0
0
5
10
15
20
25
30
Depth (µm)
U
Th

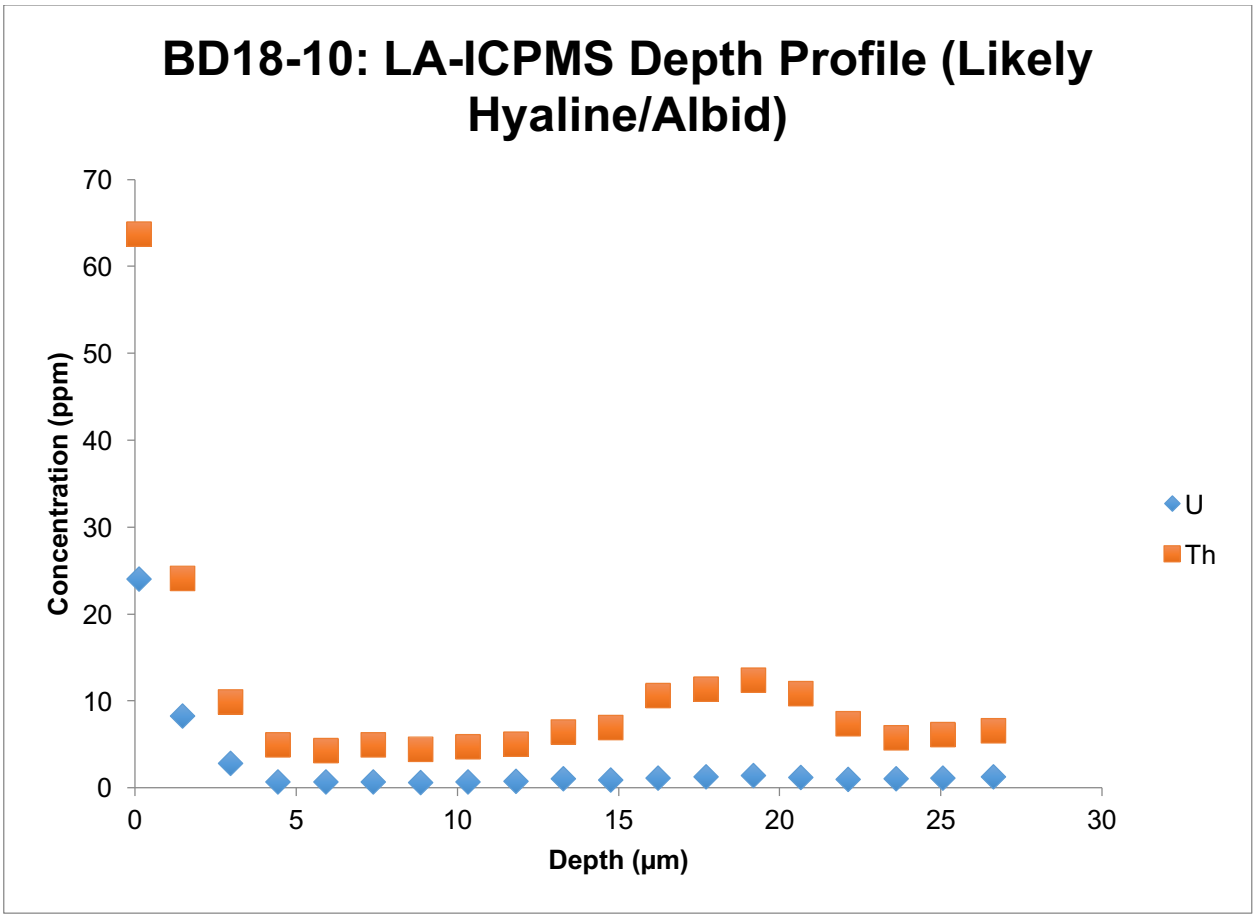
BD18-10: LA-ICPMS Depth Profile (Likely Hyaline/Albid)
Concentration (ppm)
70
60
50
40
30
20
10
0
0
5
10
15
20
25
30
Depth (µm)
U
Th

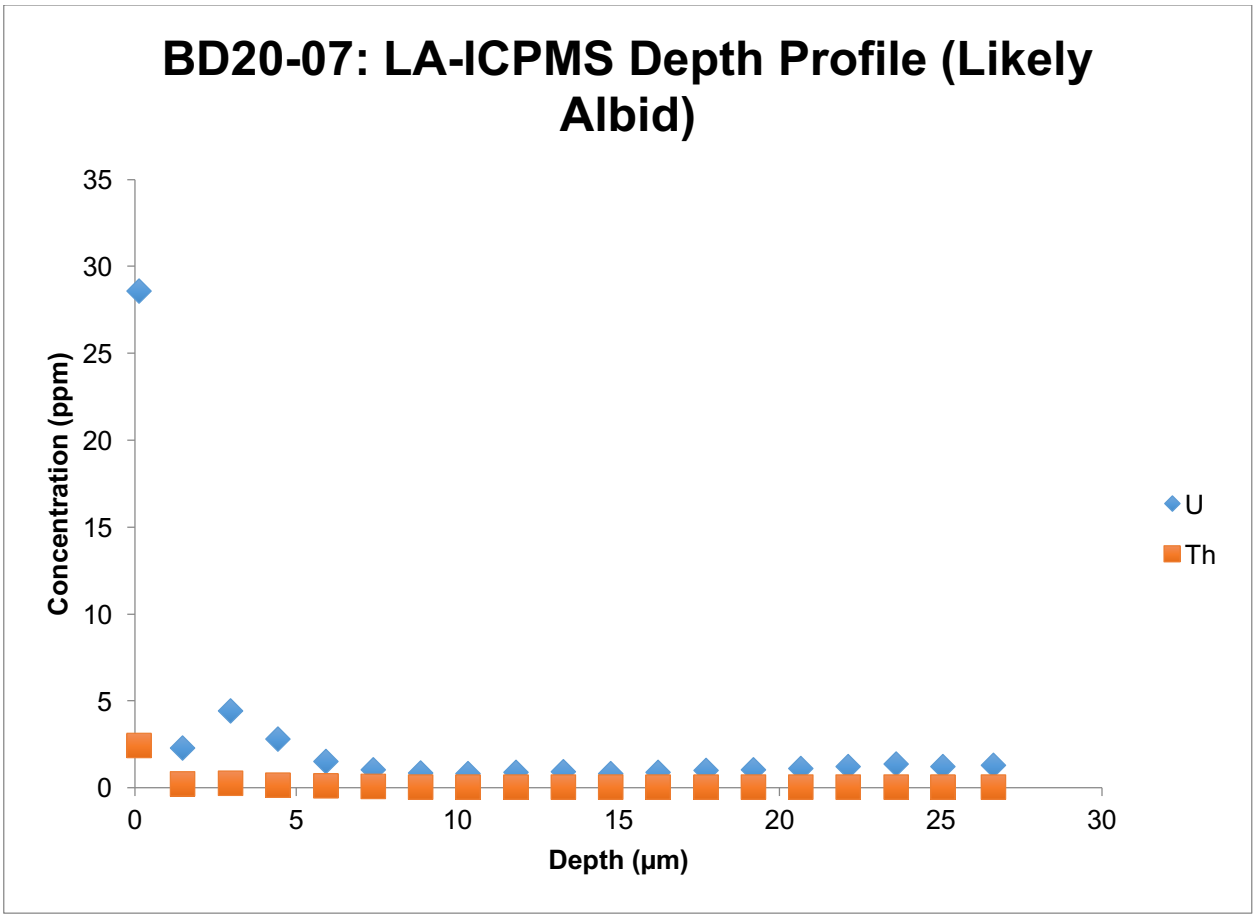
BD20-07: LA-ICPMS Depth Profile (Likely Albid)
Concentration (ppm)
35
30
25
20
15
10
5
0
0
5
10
15
20
25
30
Depth (µm)
U
Th

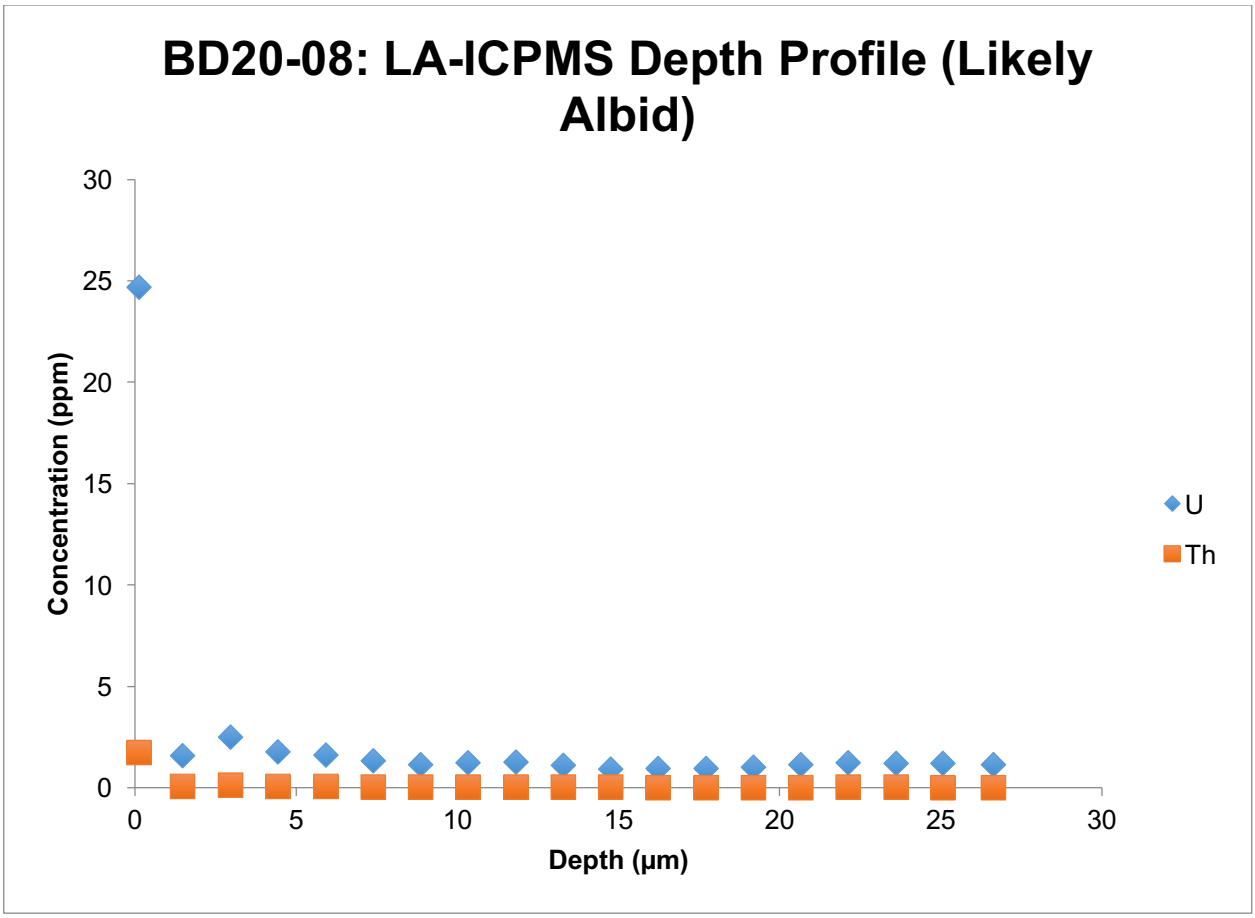
BD20-08: LA-ICPMS Depth Profile (Likely Albid)
Concentration (ppm)
30
25
20
15
10
5
0
0
5
10
15
20
25
30
Depth (µm)
U
Th

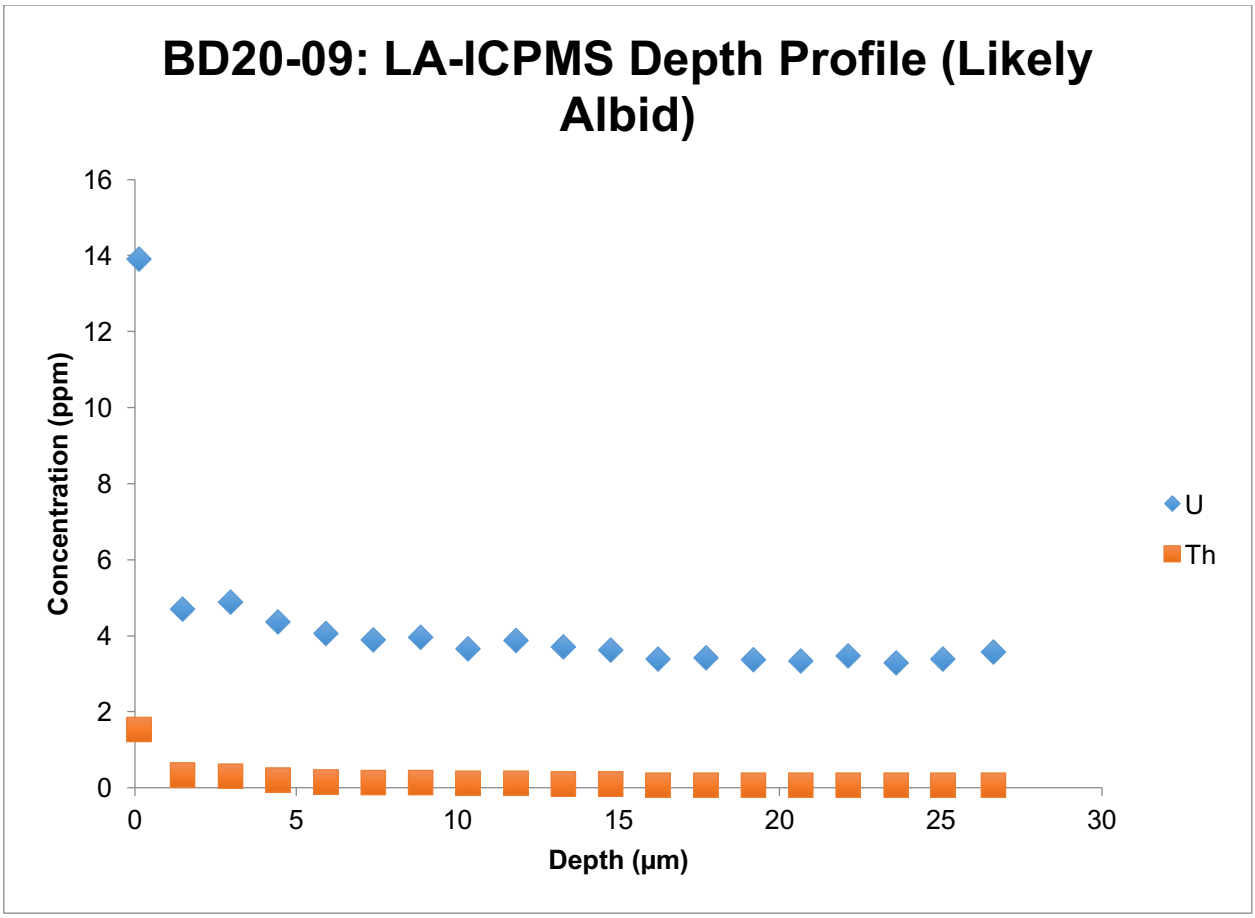
BD20-09: LA-ICPMS Depth Profile (Likely Albid)
Concentration (ppm)
16
14
12
10
8
6
4
2
0
0
5
10
15
20
25
30
Depth (µm)
U
Th

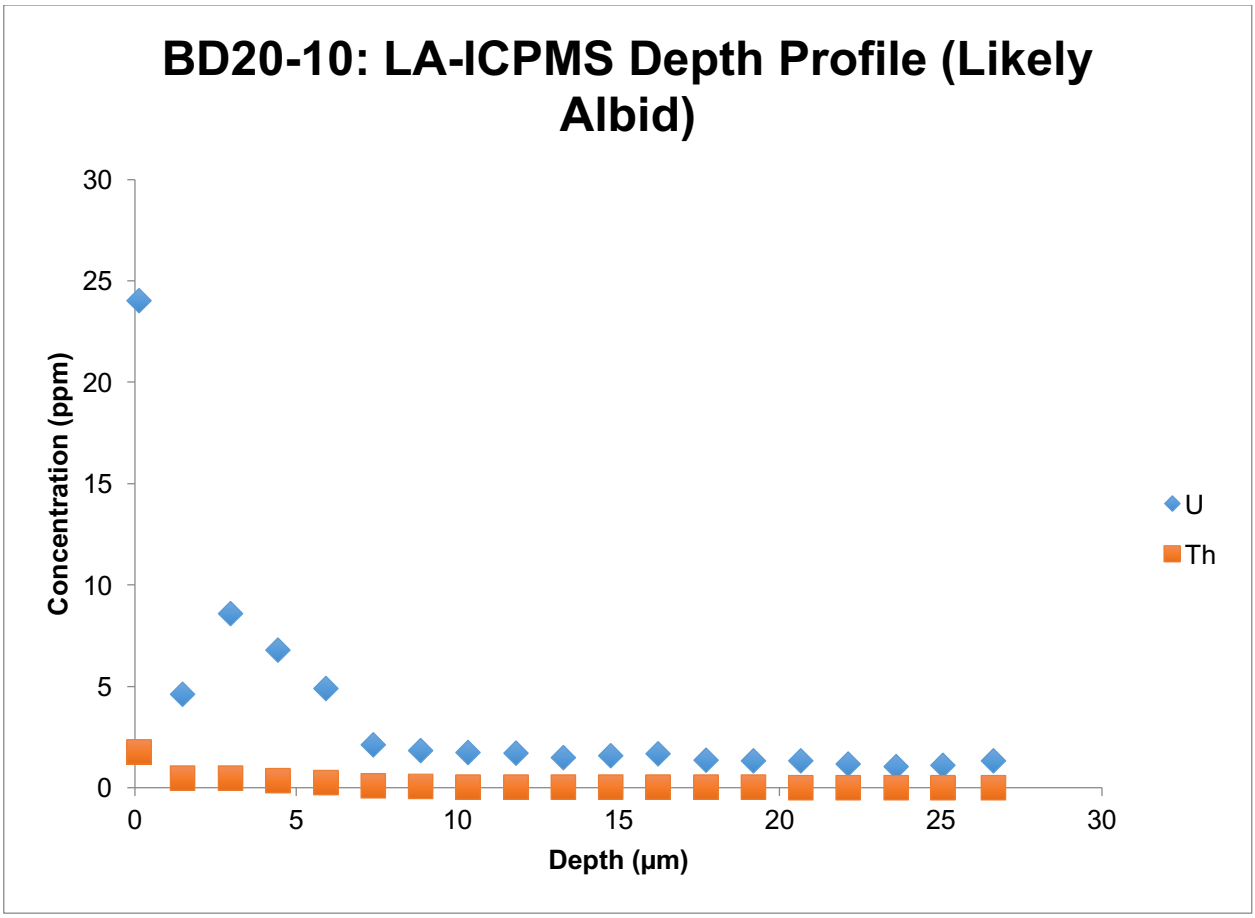
BD20-10: LA-ICPMS Depth Profile (Likely Albid)
Concentration (ppm)
30
25
20
15
10
5
0
0
5
10
15
20
25
30
Depth (µm)
U
Th

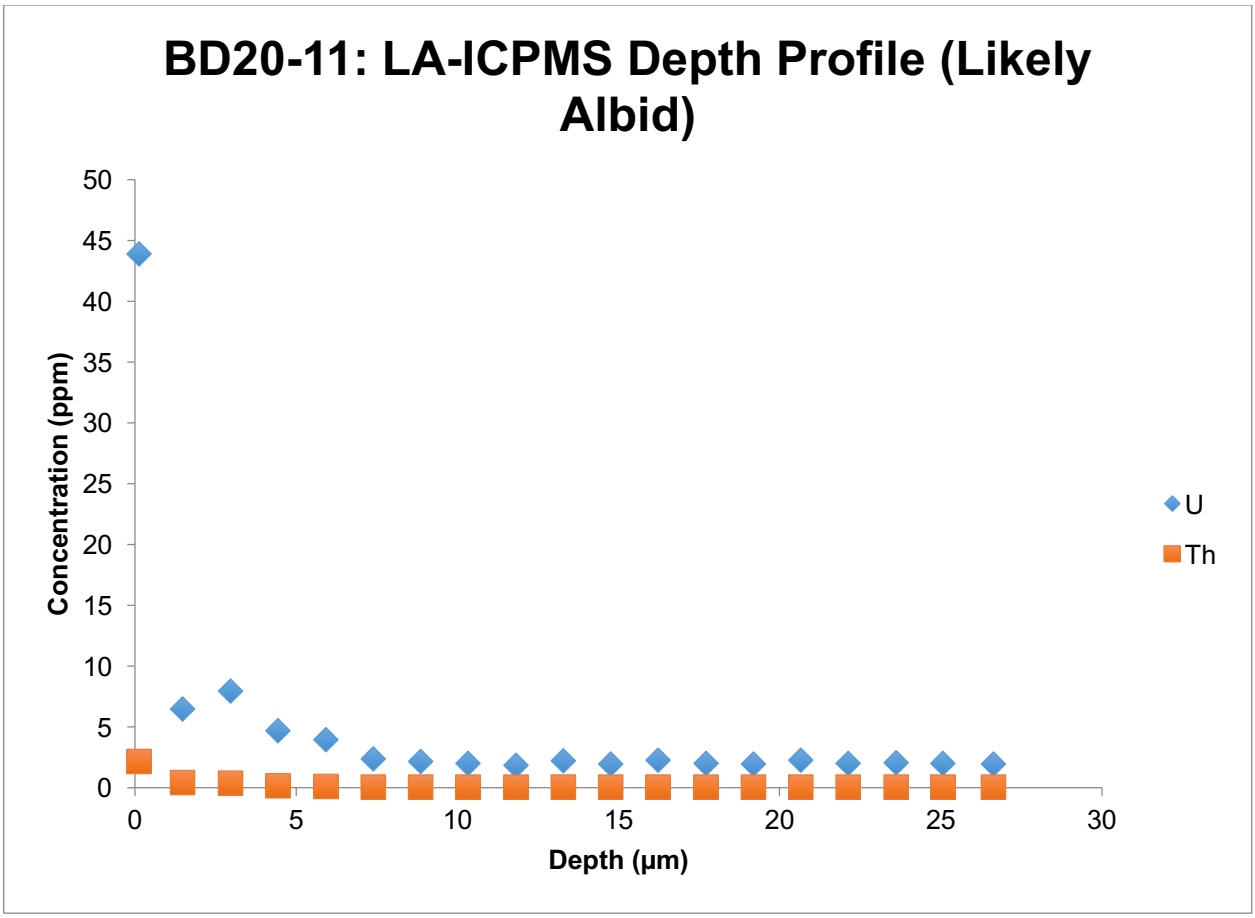
BD20-11: LA-ICPMS Depth Profile (Likely Albid)
Concentration (ppm)
50
45
40
35
30
25
20
15
10
5
0
0
5
10
15
20
25
30
Depth (µm)
U
Th

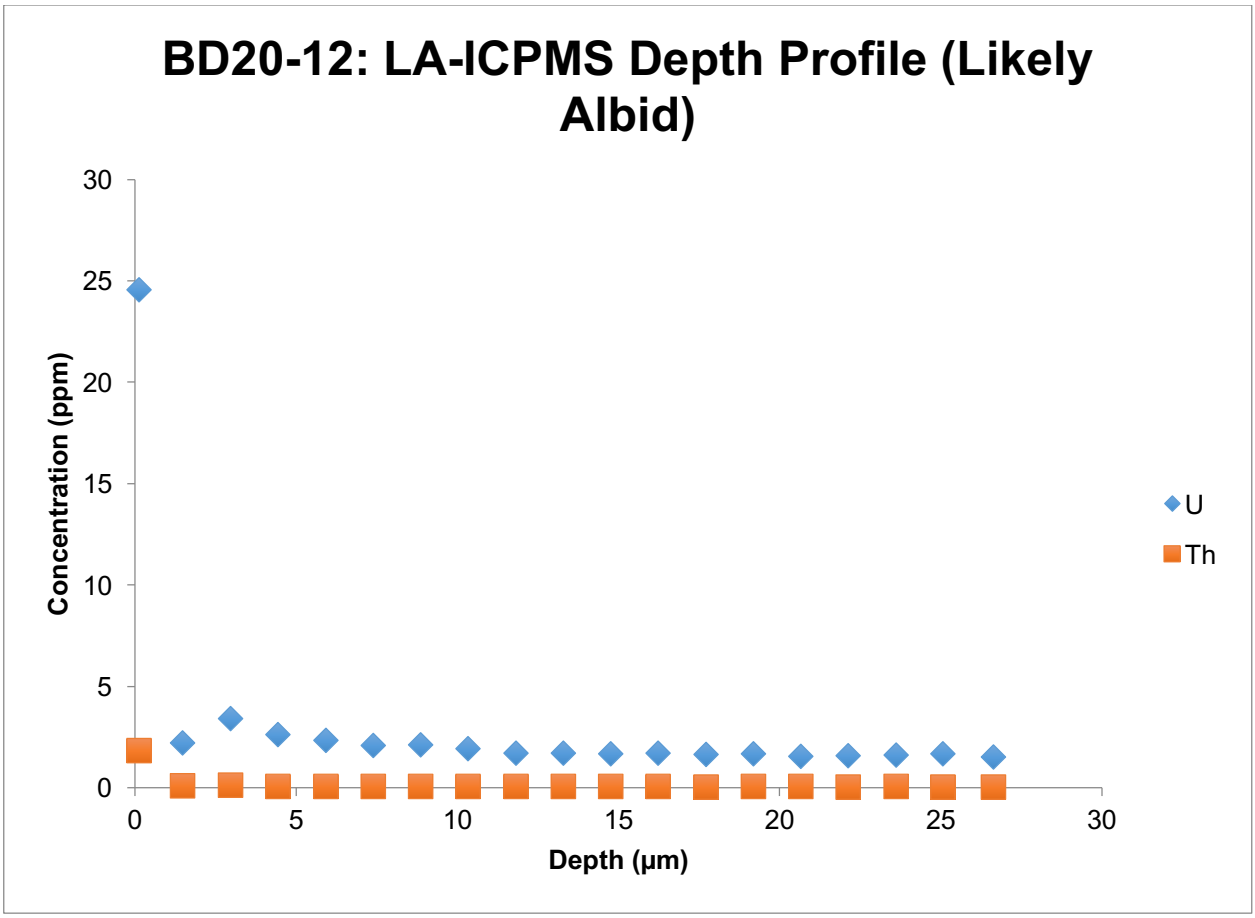
BD20-12: LA-ICPMS Depth Profile (Likely Albid)
Concentration (ppm)
30
25
20
15
10
5
0
0
5
10
15
20
25
30
Depth (µm)
U
Th

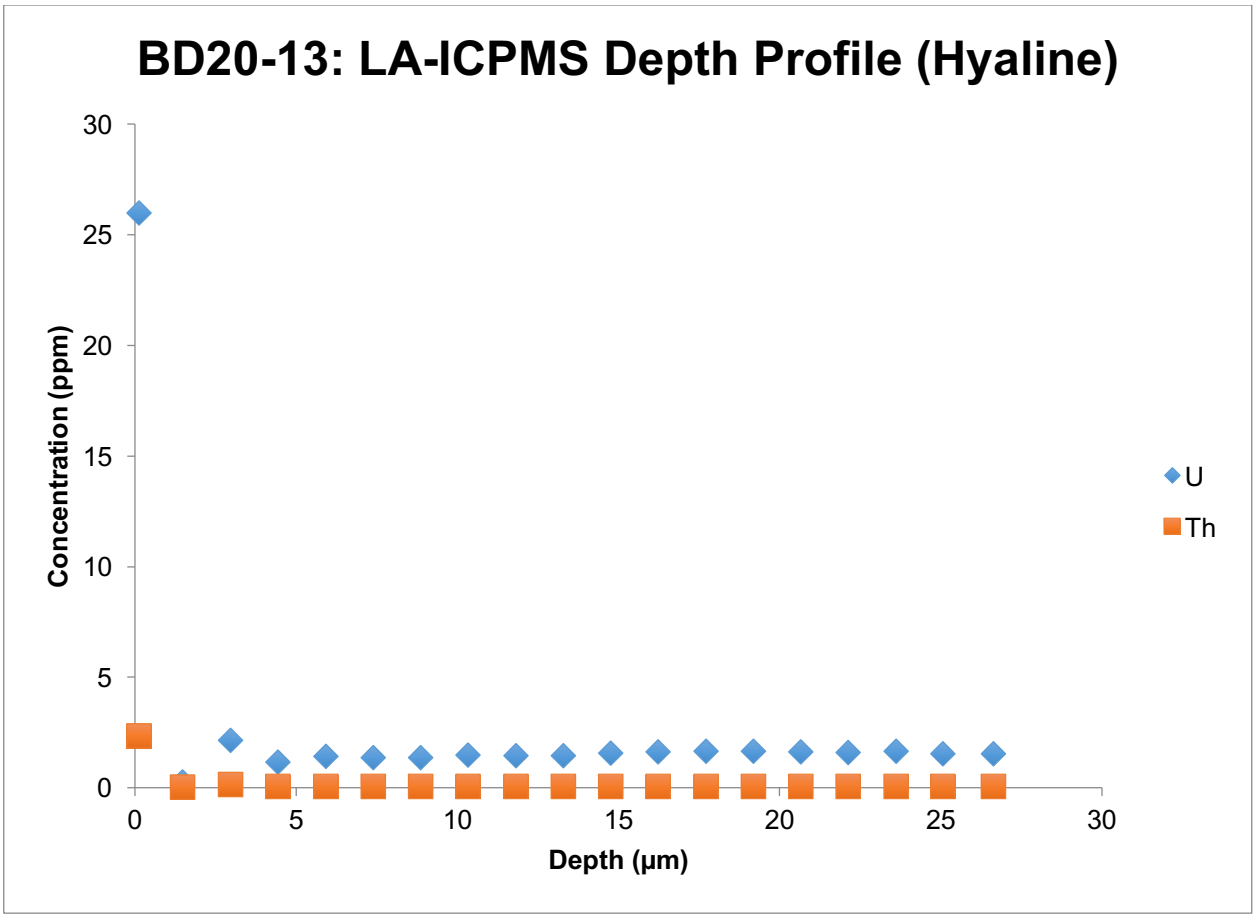
BD20-13: LA-ICPMS Depth Profile (Hyaline)
Concentration (ppm)
30
25
20
15
10
5
0
0
5
10
15
20
25
30
Depth (µm)
U
Th

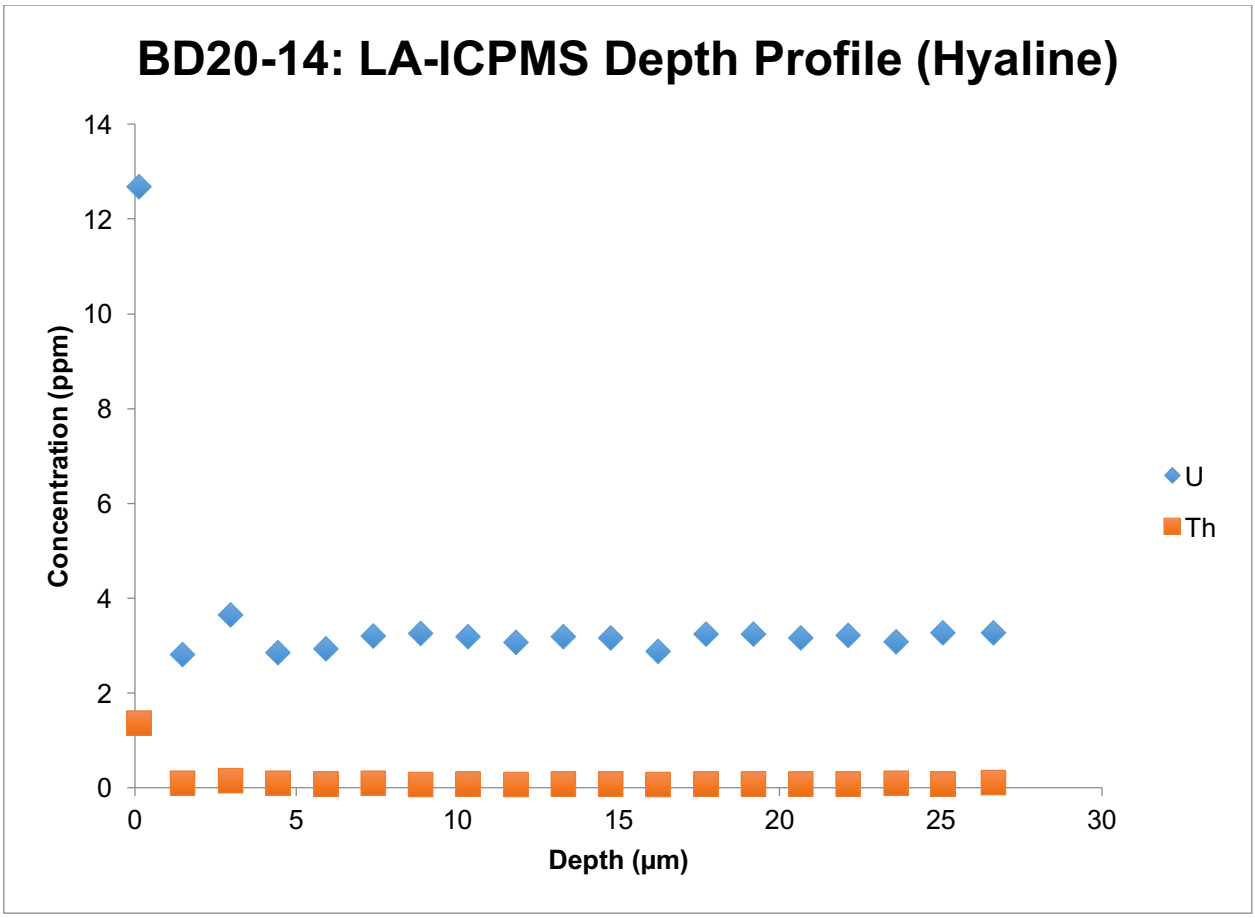
BD20-14: LA-ICPMS Depth Profile (Hyaline)
Concentration (ppm)
14
12
10
8
6
4
2
0
0
5
10
15
20
25
30
Depth (µm)
U
Th

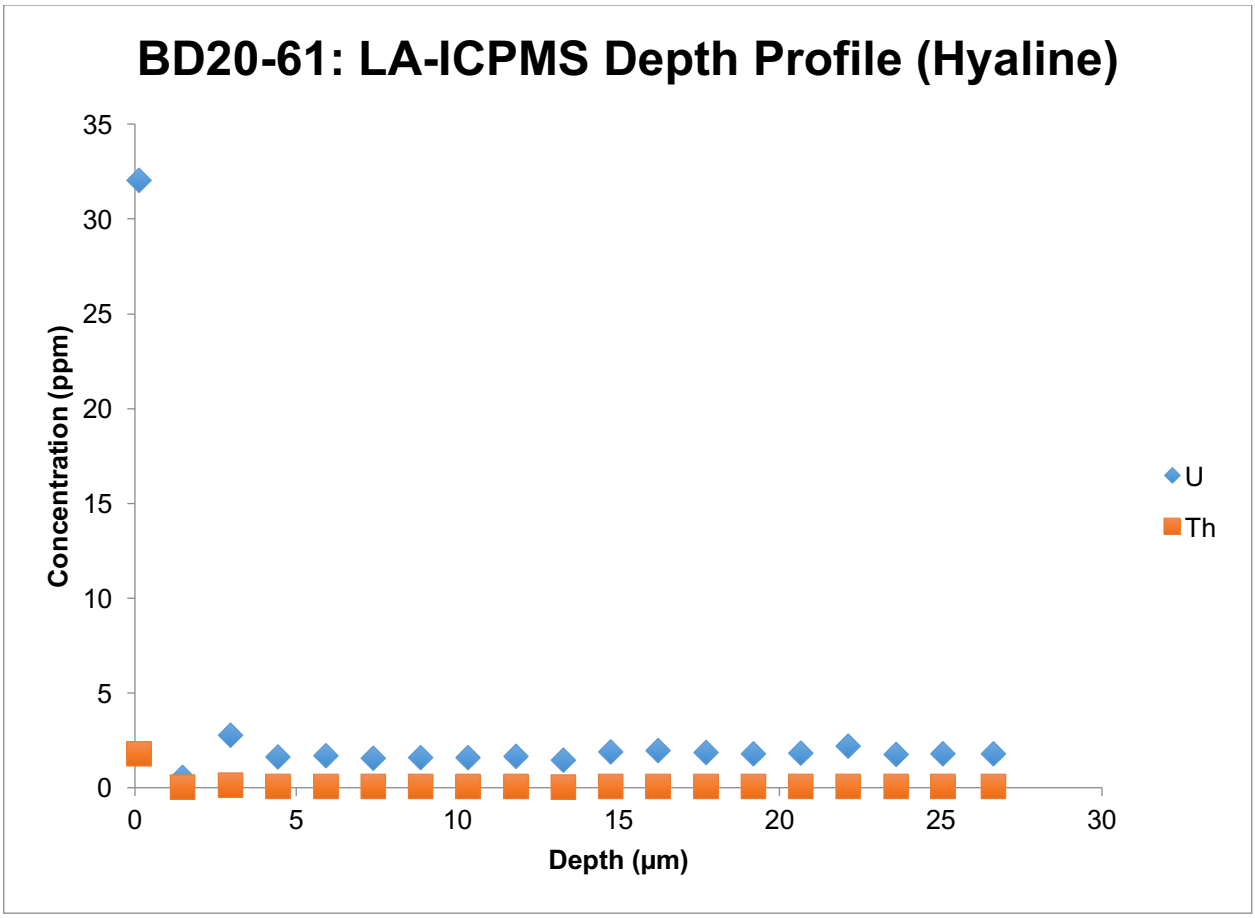
BD20-61: LA-ICPMS Depth Profile (Hyaline)
Concentration (ppm)
35
30
25
20
15
10
5
0
0
5
10
15
20
25
30
Depth (µm)
U
Th

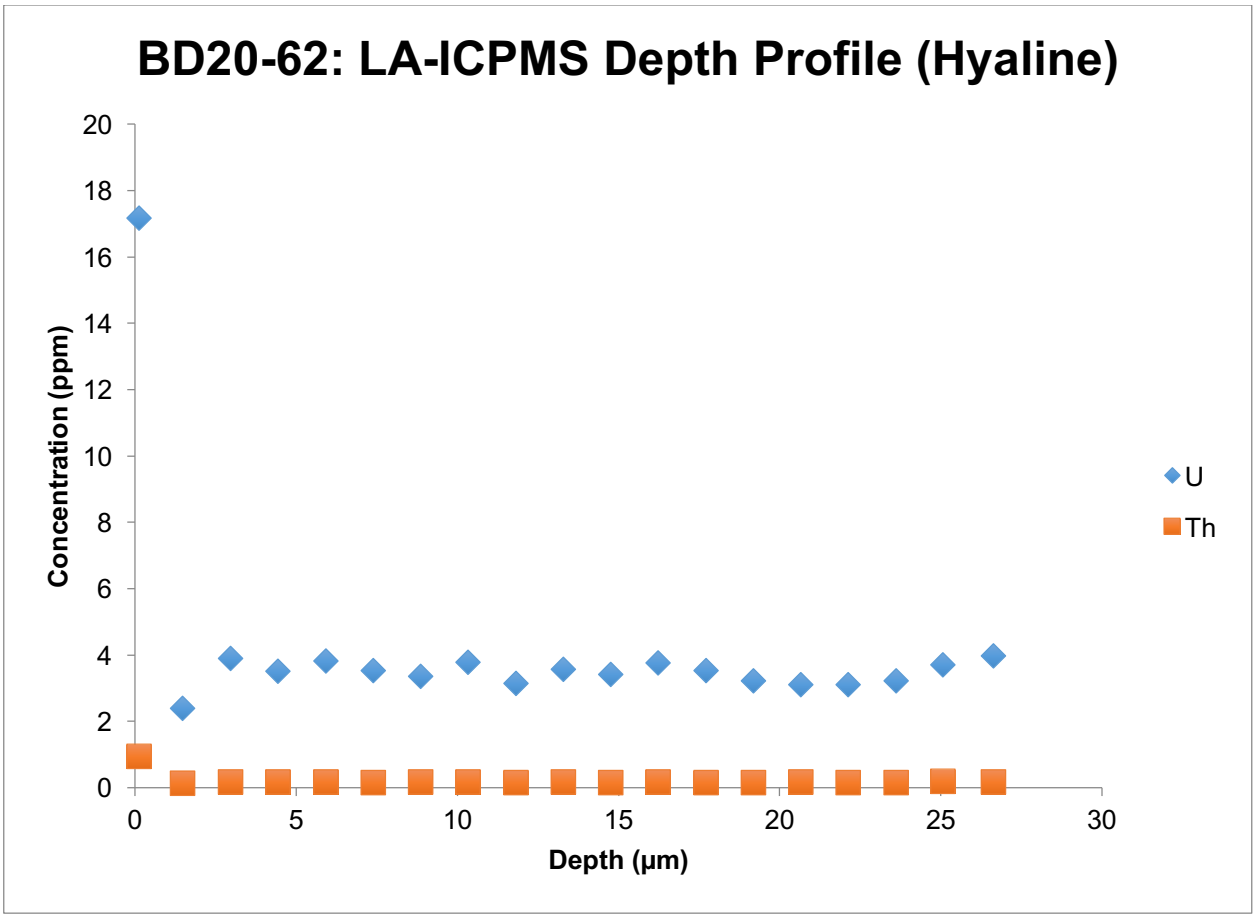
BD20-62: LA-ICPMS Depth Profile (Hyaline)
Concentration (ppm)
20
18
16
14
12
10
8
6
4
2
0
0
5
10
15
20
25
30
Depth (µm)
U
Th

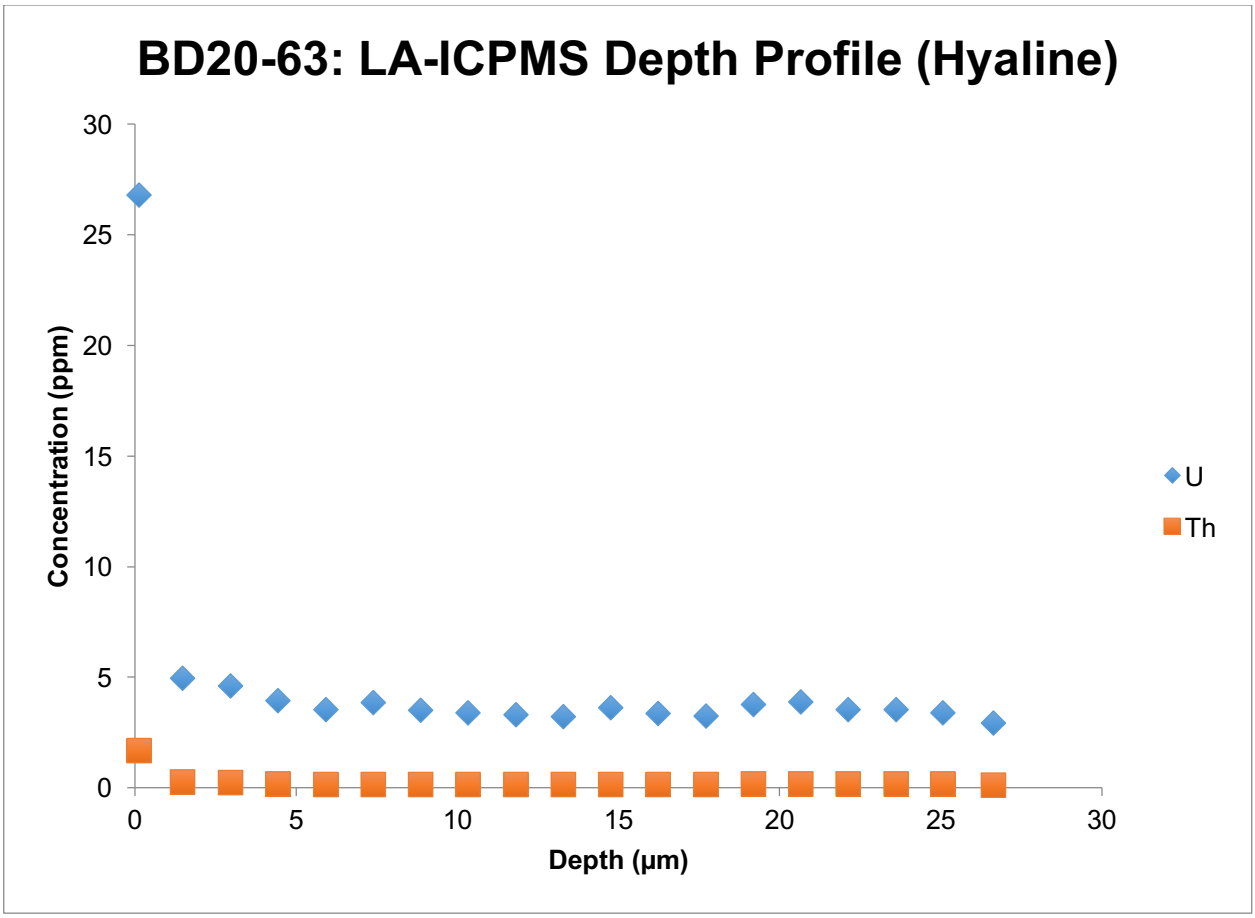
BD20-63: LA-ICPMS Depth Profile (Hyaline)
Concentration (ppm)
30
25
20
15
10
5
0
0
5
10
15
20
25
30
Depth (µm)
U
Th

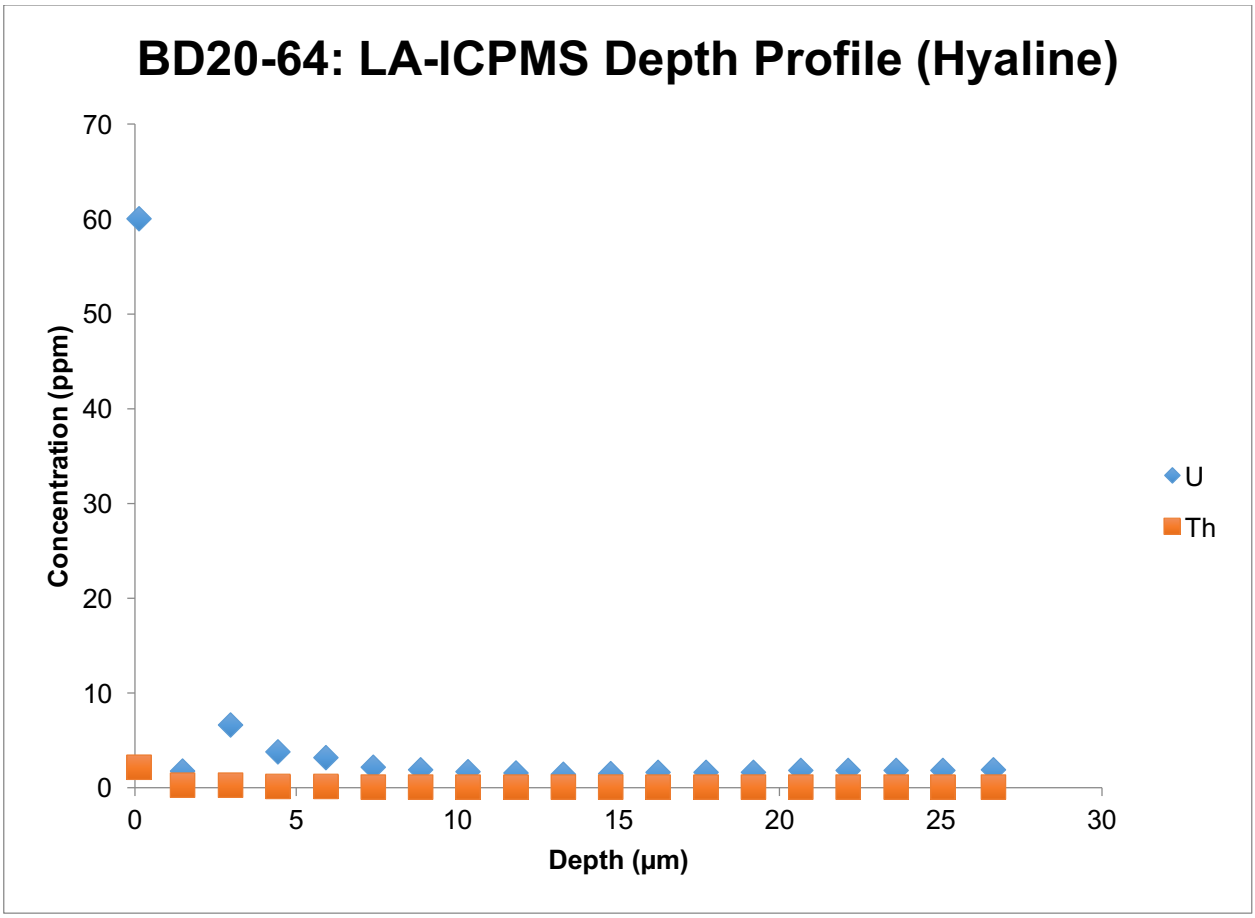
BD20-64: LA-ICPMS Depth Profile (Hyaline)
Concentration (ppm)
70
60
50
40
30
20
10
0
0
5
10
15
20
25
30
Depth (µm)
U
Th

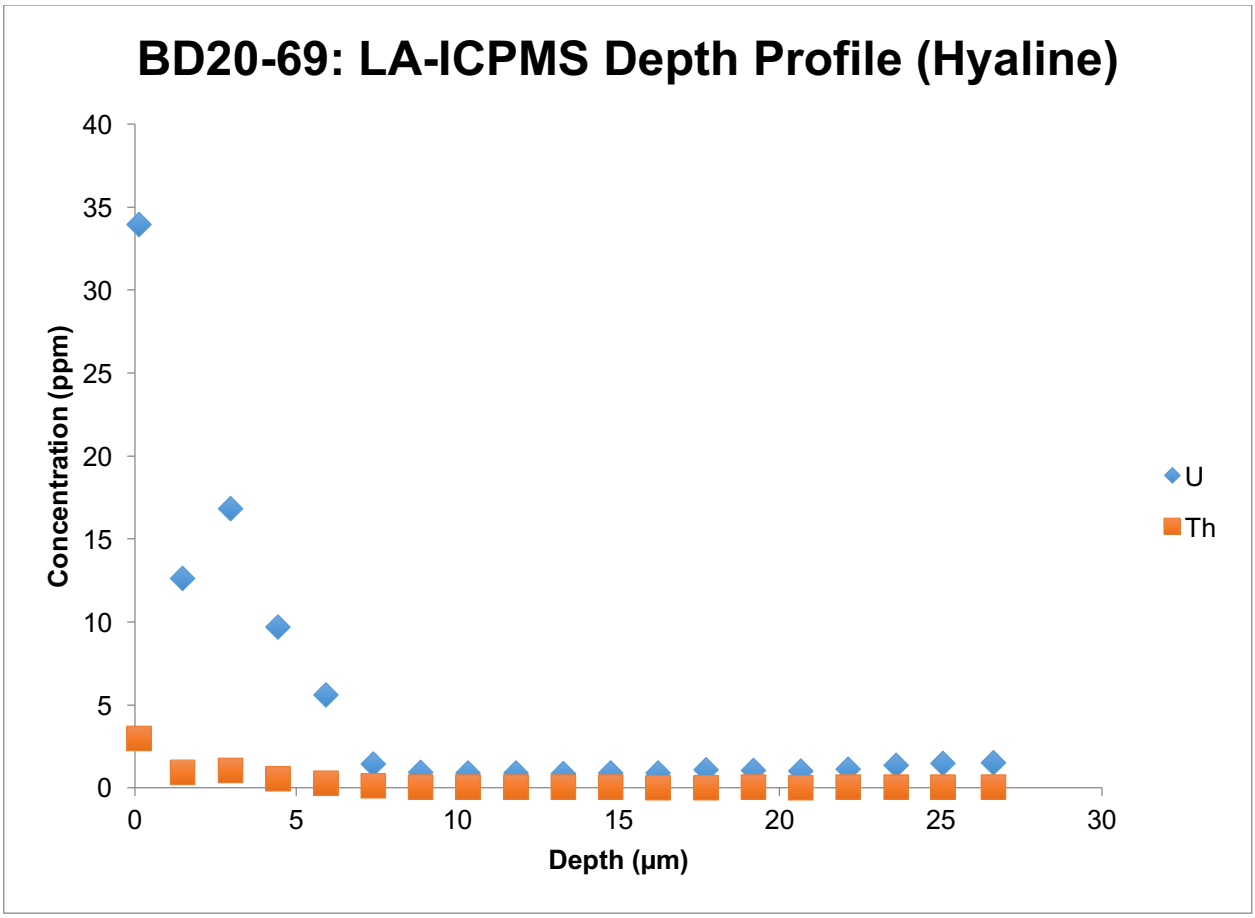
BD20-69: LA-ICPMS Depth Profile (Hyaline)
Concentration (ppm)
40
35
30
25
20
15
10
5
0
0
5
10
15
20
25
30
Depth (µm)
U
Th

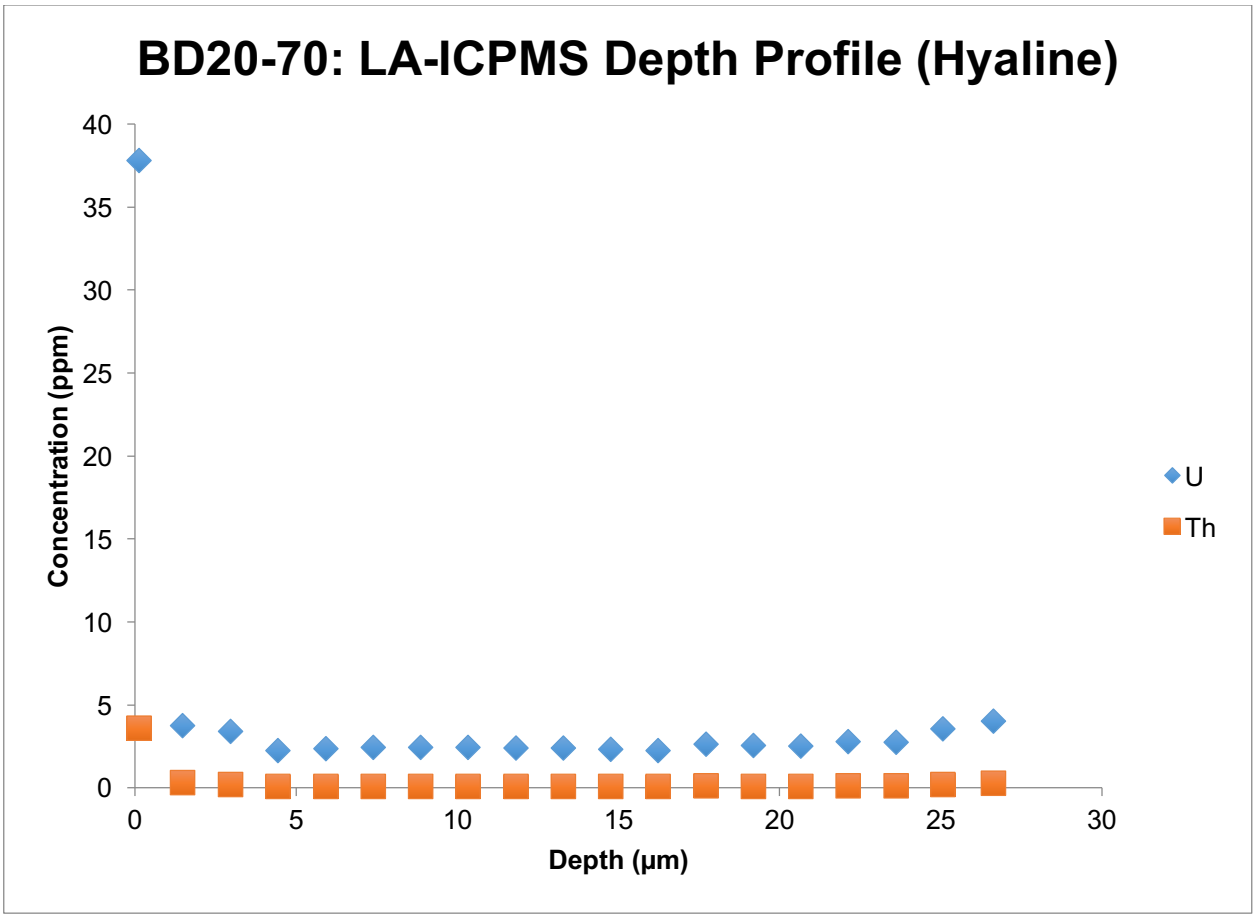
BD20-70: LA-ICPMS Depth Profile (Hyaline)
Concentration (ppm)
40
35
30
25
20
15
10
5
0
0
5
10
15
20
25
30
Depth (µm)
U
Th

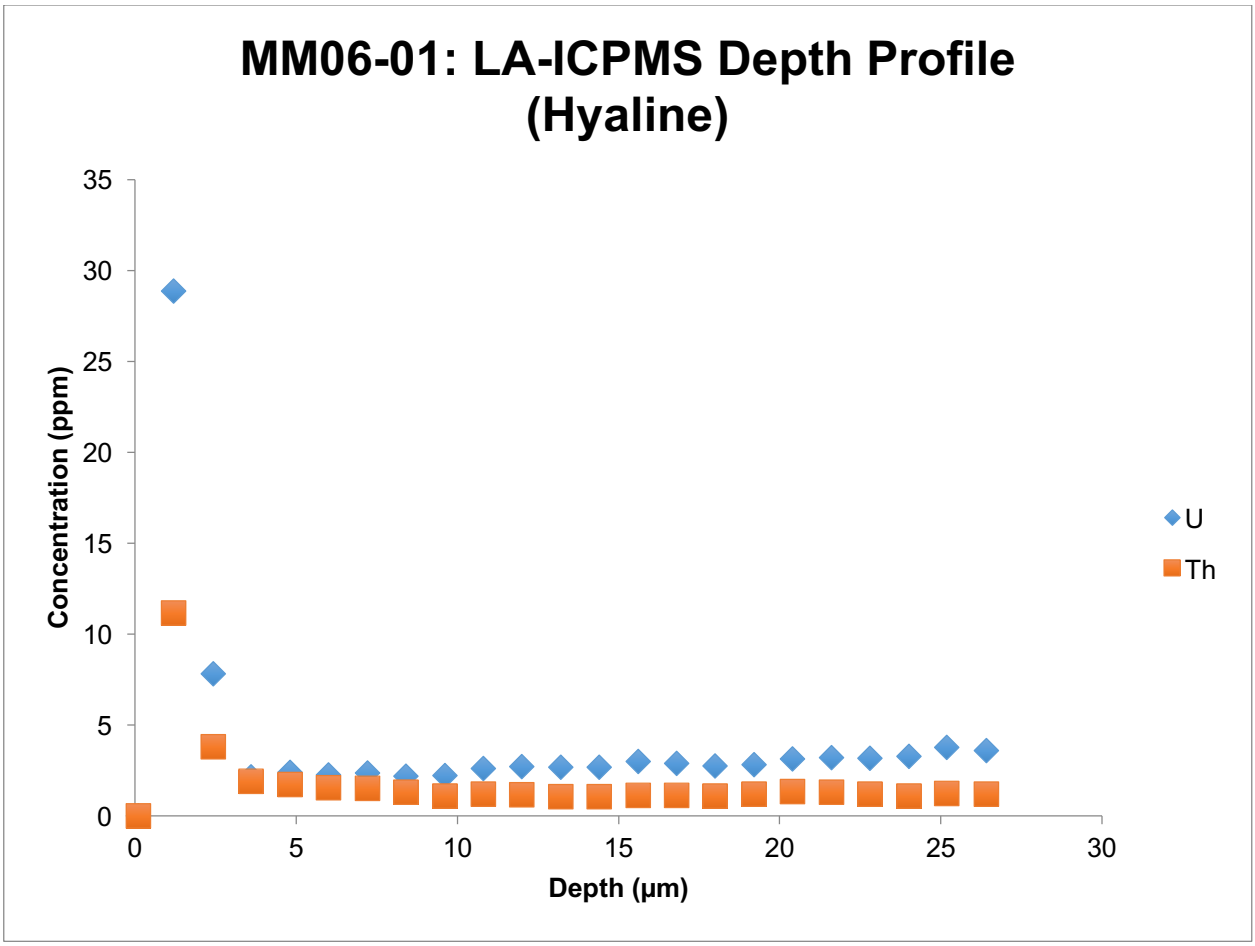
MM06-01: LA-ICPMS Depth Profile (Hyaline)
Concentration (ppm)
35
30
25
20
15
10
5
0
0
5
10
15
20
25
30
Depth (µm)
U
Th

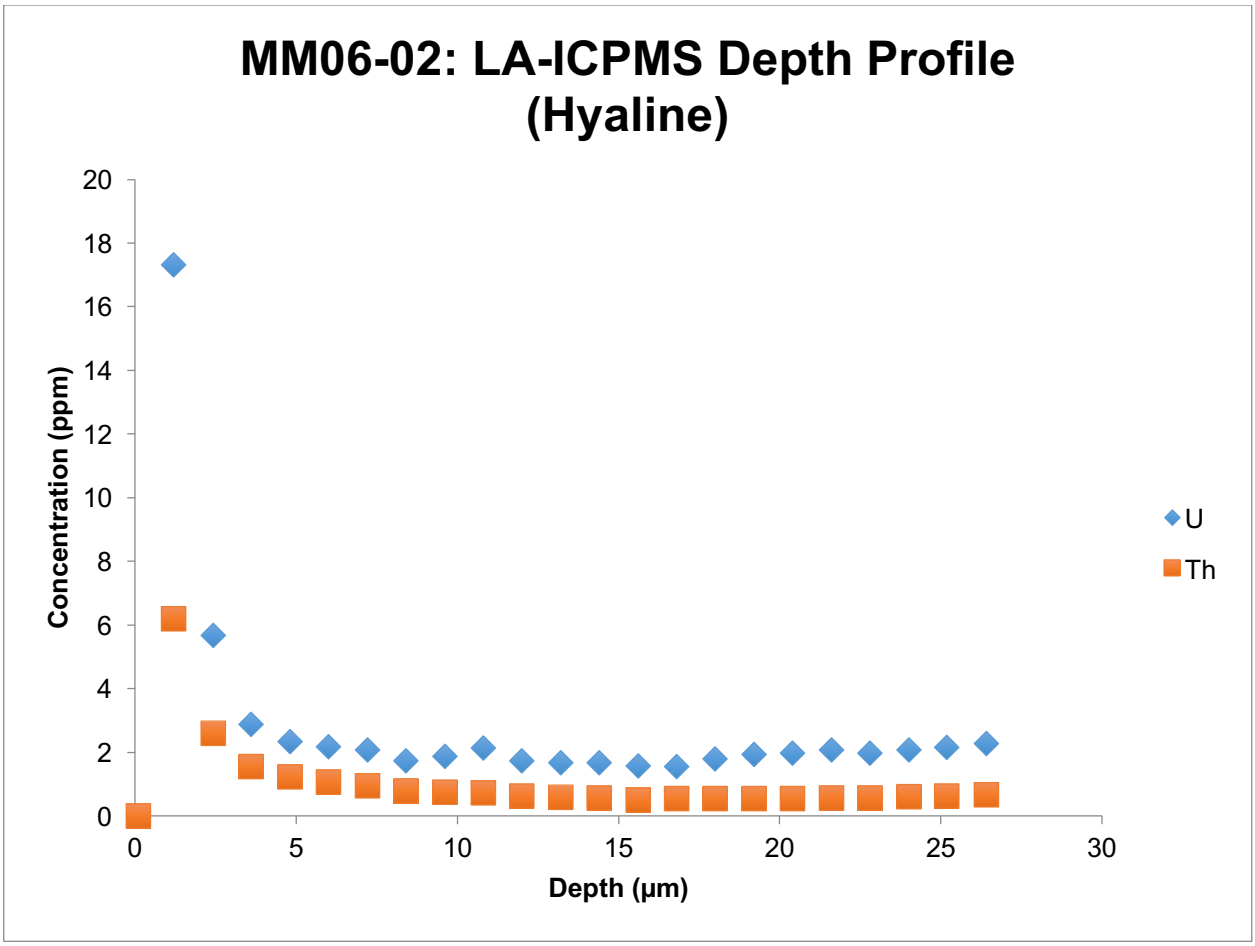
MM06-02: LA-ICPMS Depth Profile (Hyaline)
Concentration (ppm)
0
2
4
6
8
10
12
14
16
18
20
0
5
10
15
20
25
30
Depth (µm)
U
Th

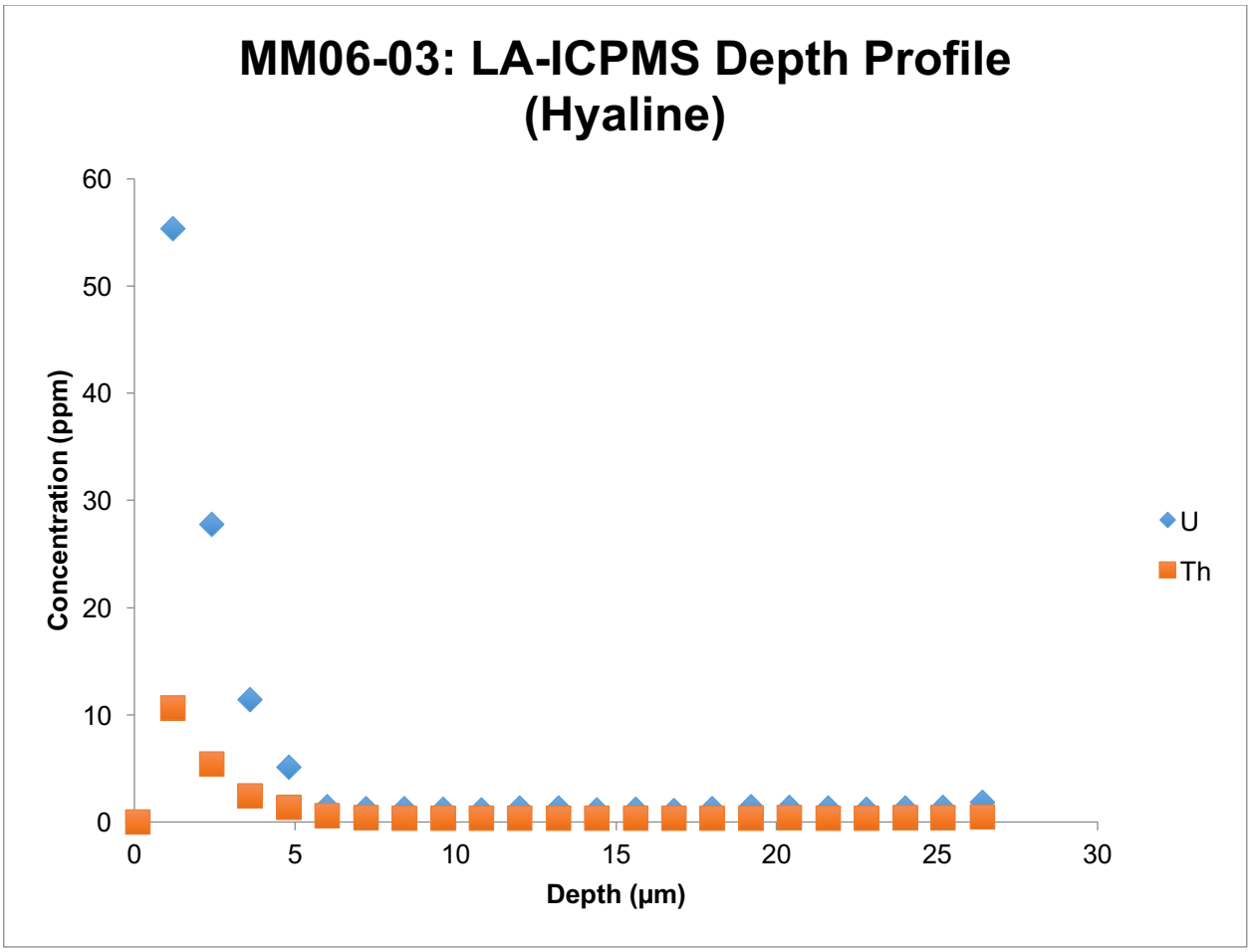
MM06-03: LA-ICPMS Depth Profile (Hyaline)
Concentration (ppm)
60
50
40
30
20
10
0
0
5
10
15
20
25
30
Depth (µm)
U
Th

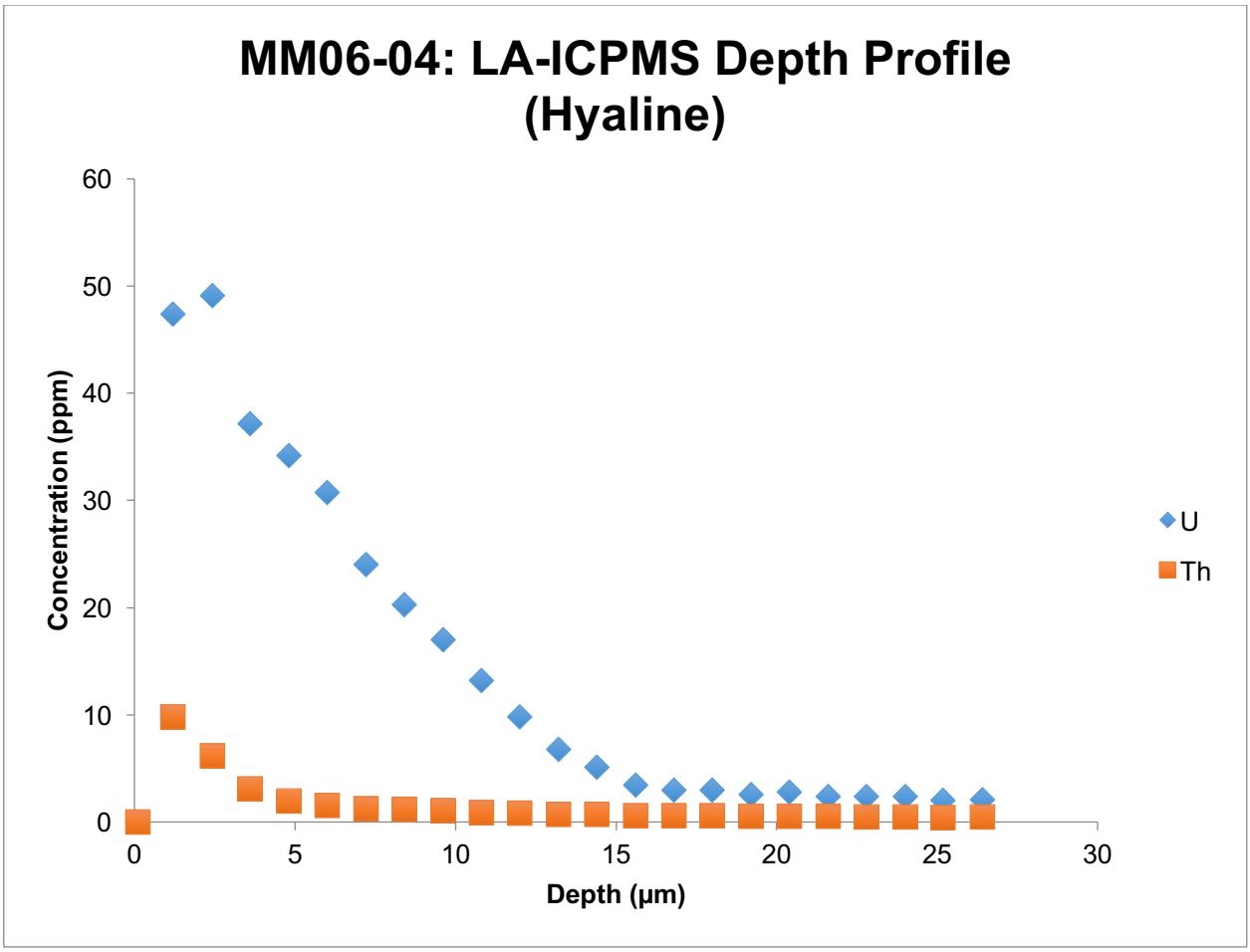
MM06-04: LA-ICPMS Depth Profile (Hyaline)
Concentration (ppm)
60
50
40
30
20
10
0
0
5
10
15
20
25
30
Depth (µm)
U
Th

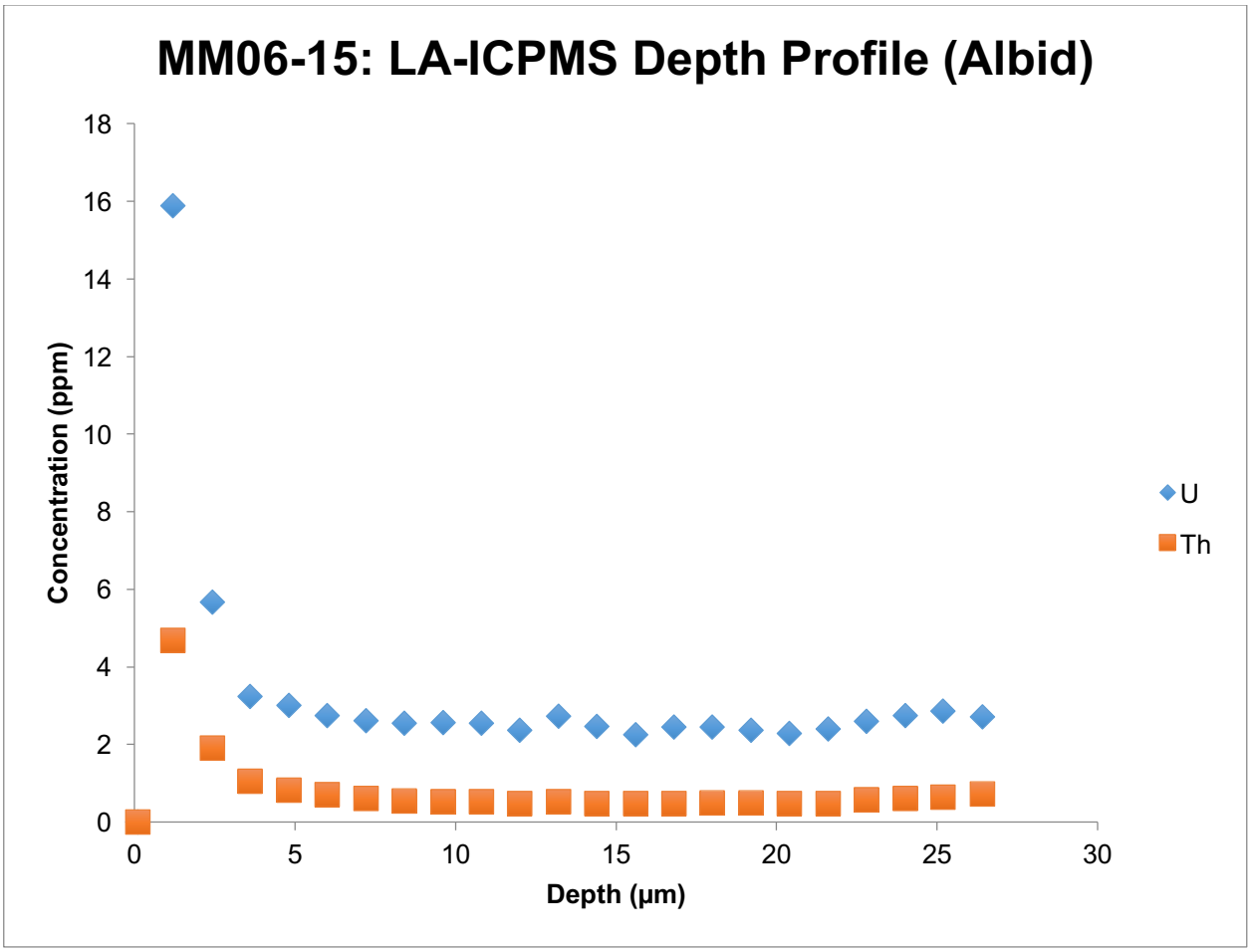
MM06-15: LA-ICPMS Depth Profile (Albid)
Concentration (ppm)
18
16
14
12
10
8
6
4
2
0
0
5
10
15
20
25
30
Depth (μm)
U
Th

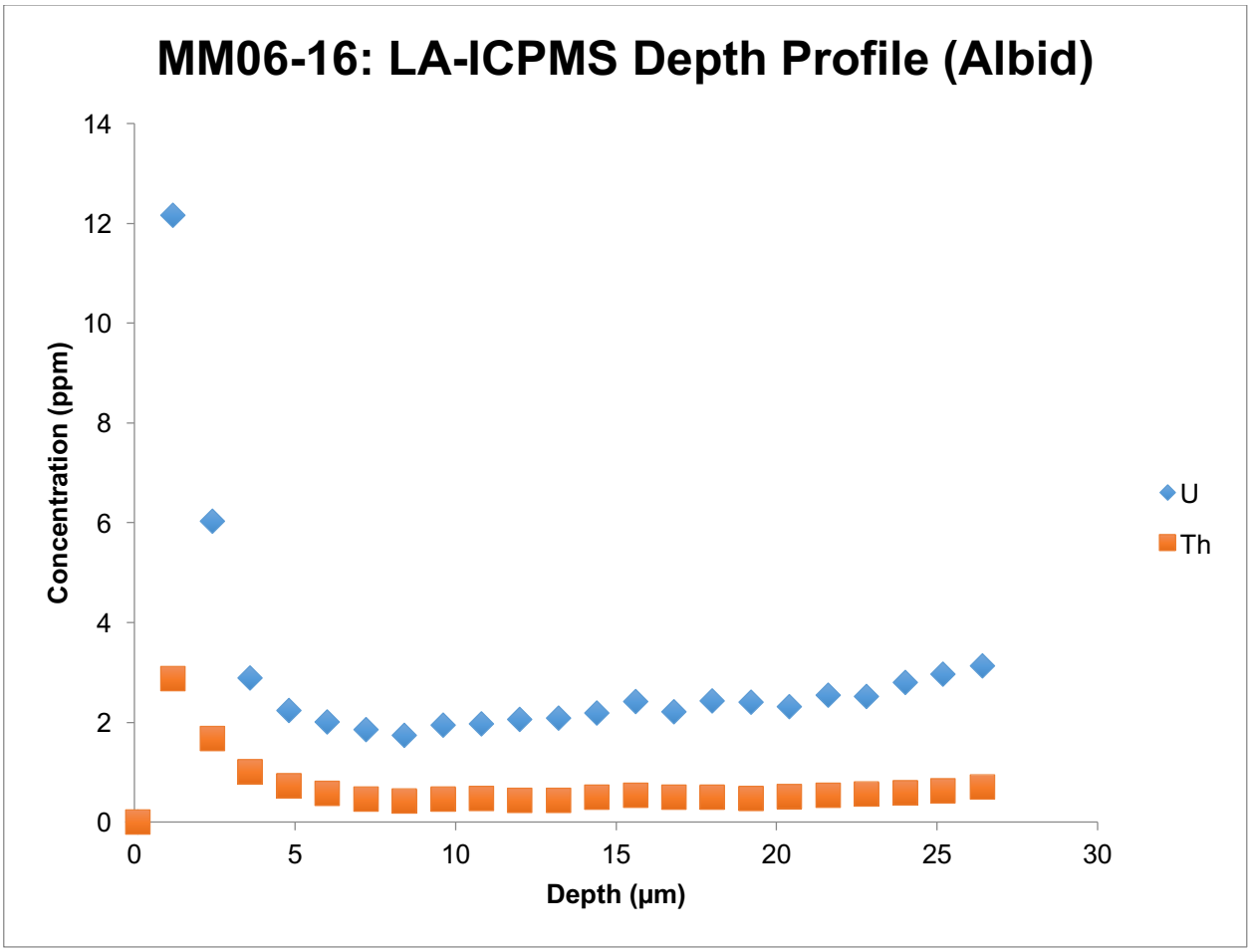
MM06-16: LA-ICPMS Depth Profile (Albid)
Concentration (ppm)
14
12
10
8
6
4
2
0
0
5
10
15
20
25
30
Depth (µm)
U
Th

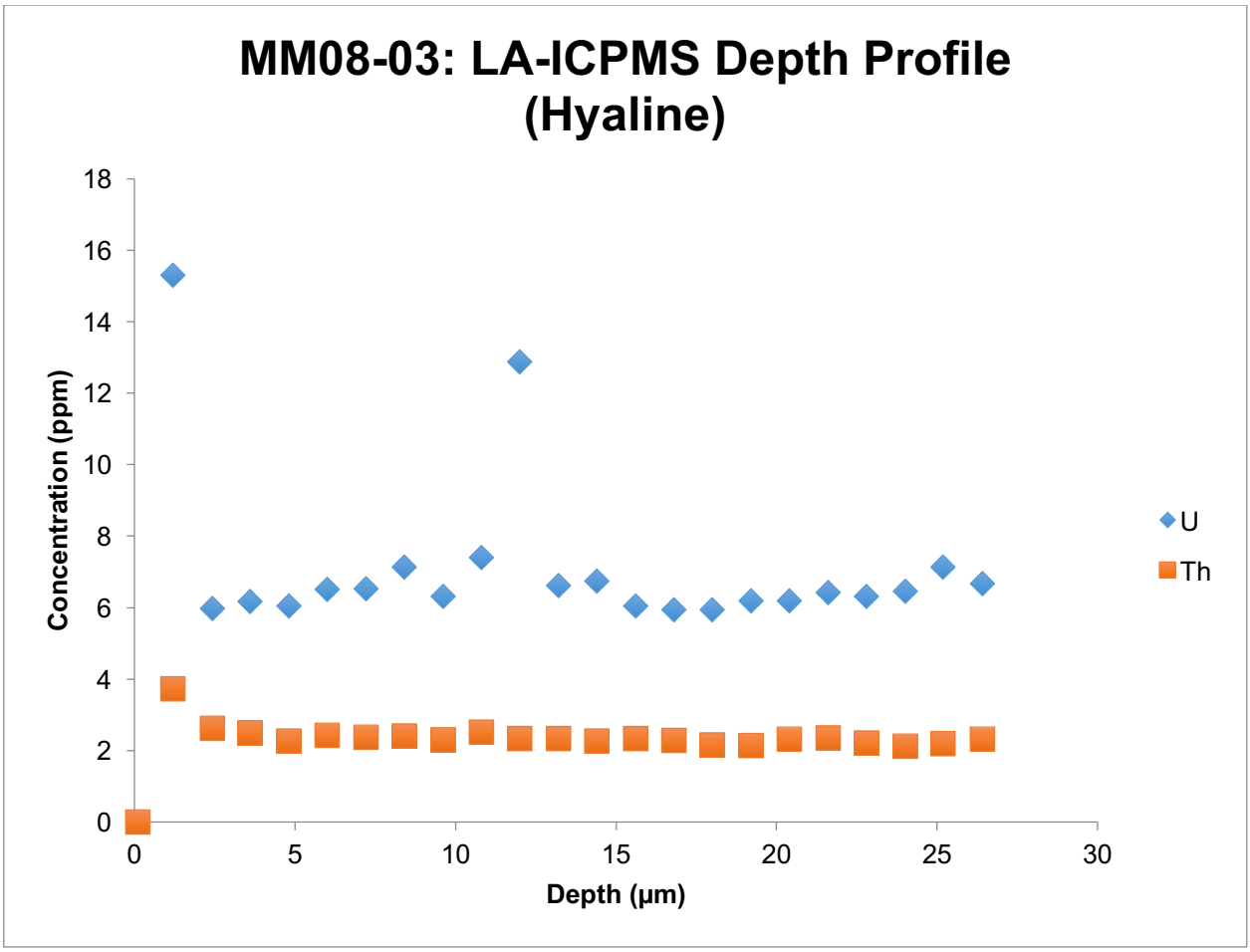
MM08-03: LA-ICPMS Depth Profile (Hyaline)
Concentration (ppm)
18
16
14
12
10
8
6
4
2
0
0
5
10
15
20
25
30
Depth (µm)
U
Th

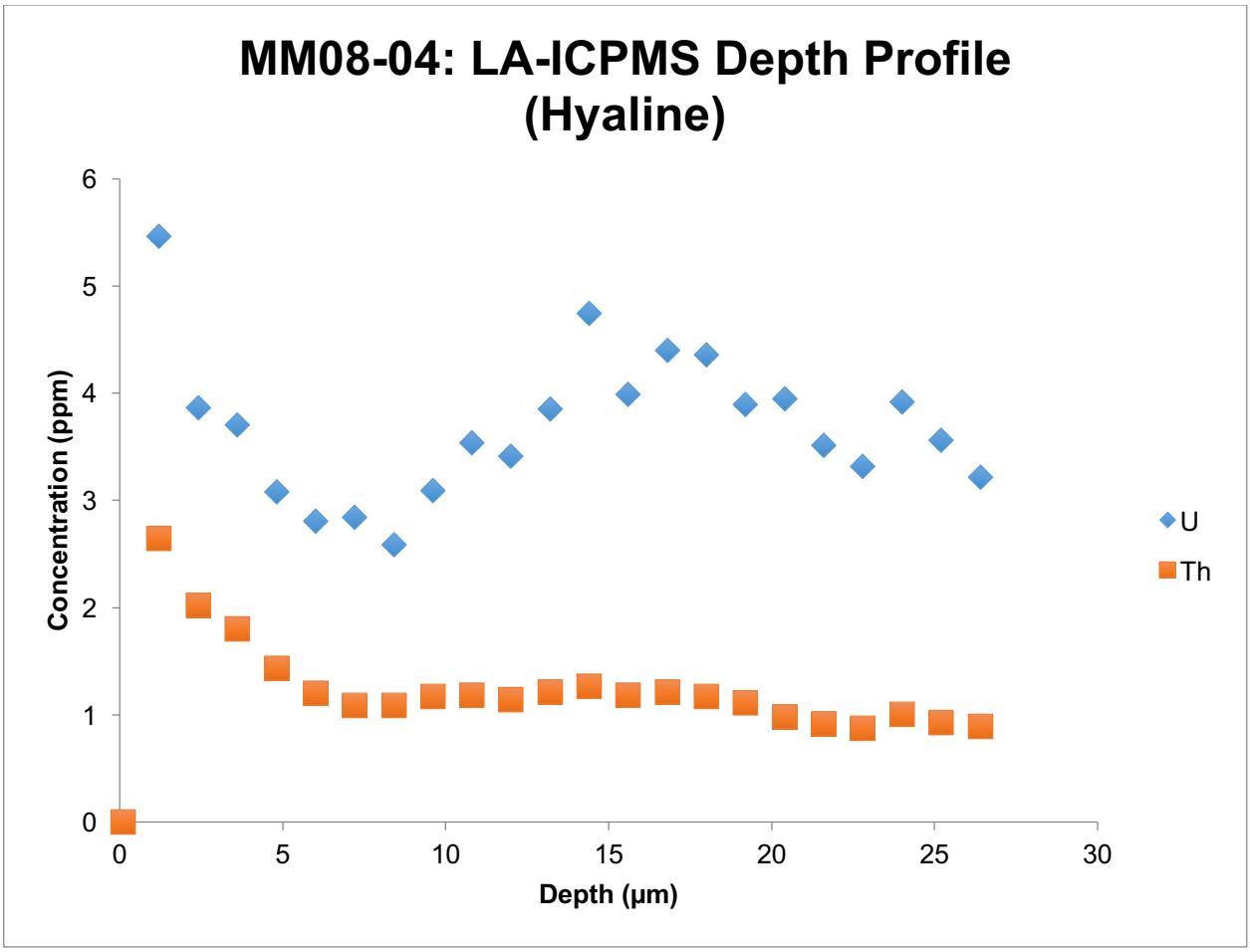
MM08-04: LA-ICPMS Depth Profile (Hyaline)
Concentration (ppm)
Depth (µm)
0
1
2
3
4
5
6
0
5
10
15
20
25
30
U
Th

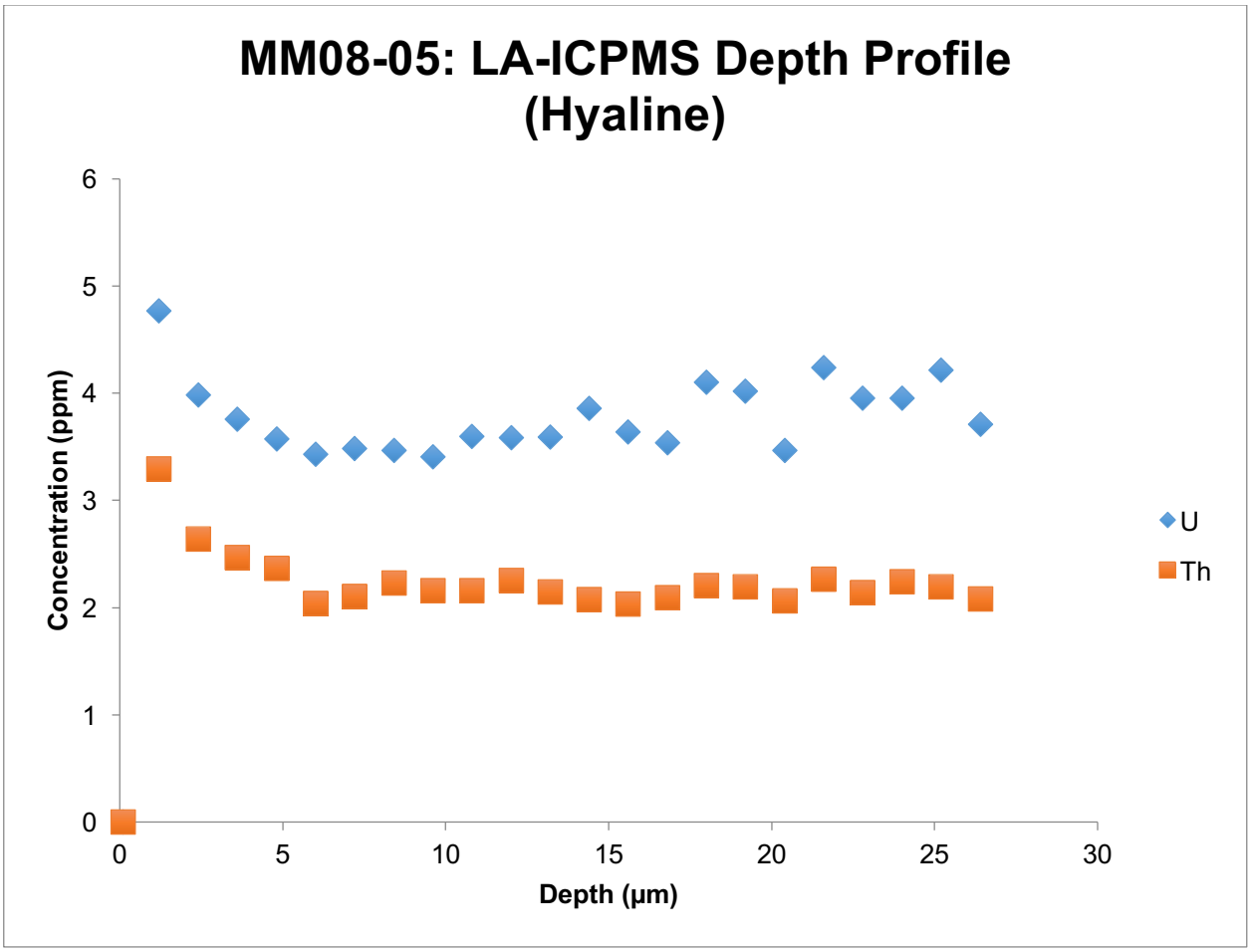
MM08-05: LA-ICPMS Depth Profile (Hyaline)
Concentration (ppm)
0
1
2
3
4
5
6
0
5
10
15
20
25
30
Depth (µm)
U
Th

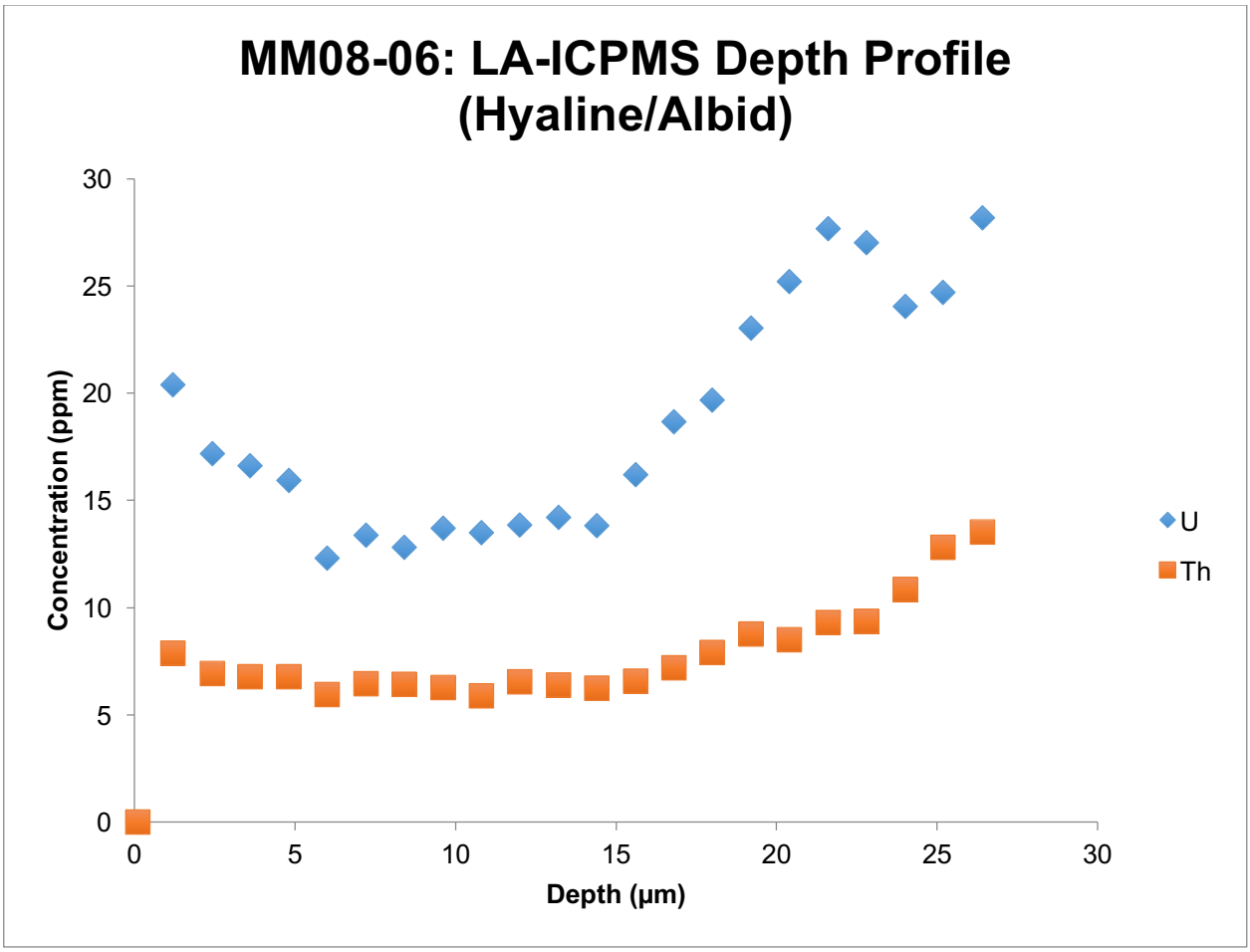
MM08-06: LA-ICPMS Depth Profile
(Hyaline/Albid)
Concentration (ppm)
30
25
20
15
10
5
0
0
5
10
15
20
25
30
Depth (µm)
U
Th

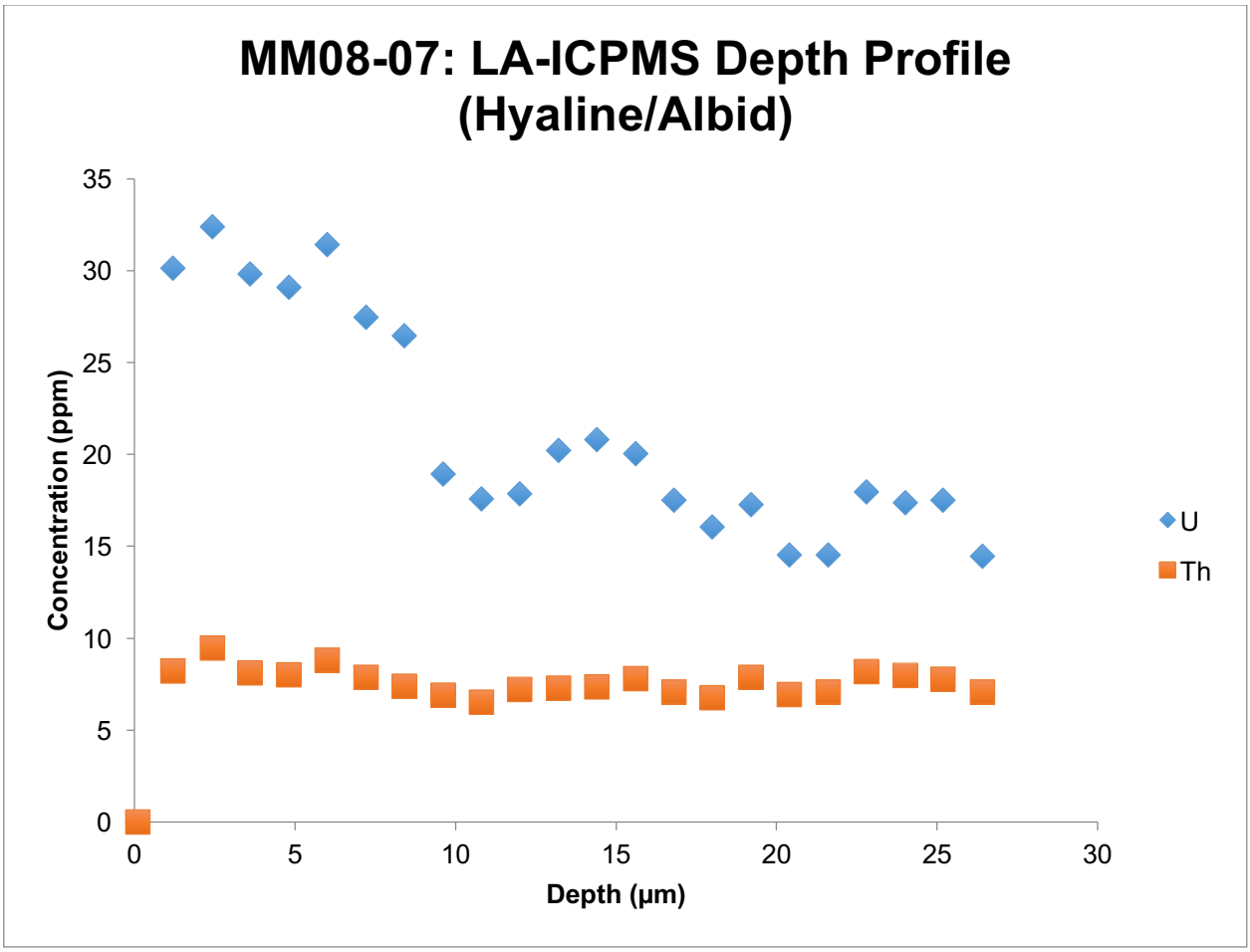
MM08-07: LA-ICPMS Depth Profile
(Hyaline/Albid)
Concentration (ppm)
35
30
25
20
15
10
5
0
0
5
10
15
20
25
30
Depth (µm)
U
Th

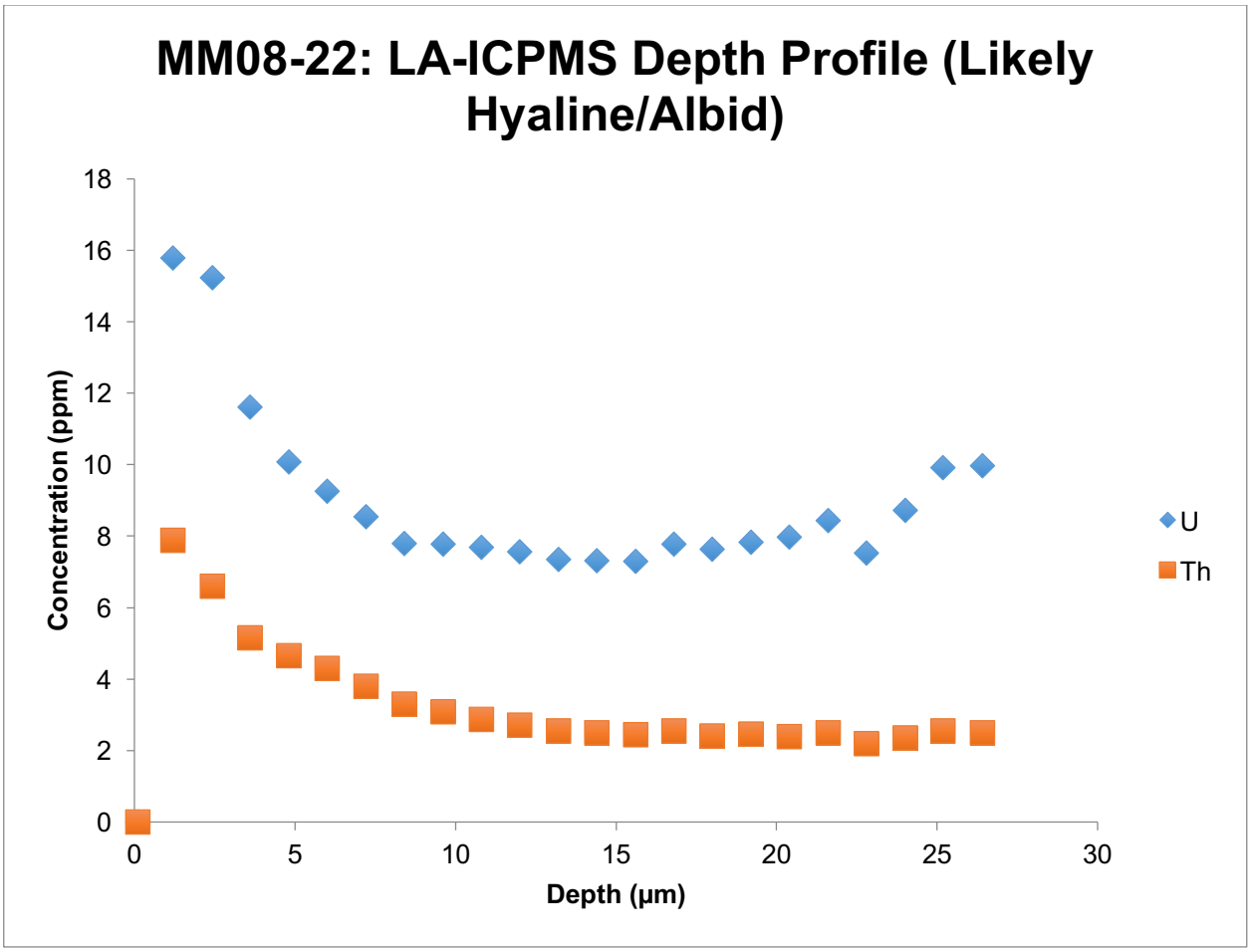
MM08-22: LA-ICPMS Depth Profile (Likely Hyaline/Albid)
Concentration (ppm)
18
16
14
12
10
8
6
4
2
0
0
5
10
15
20
25
30
Depth (µm)
U
Th

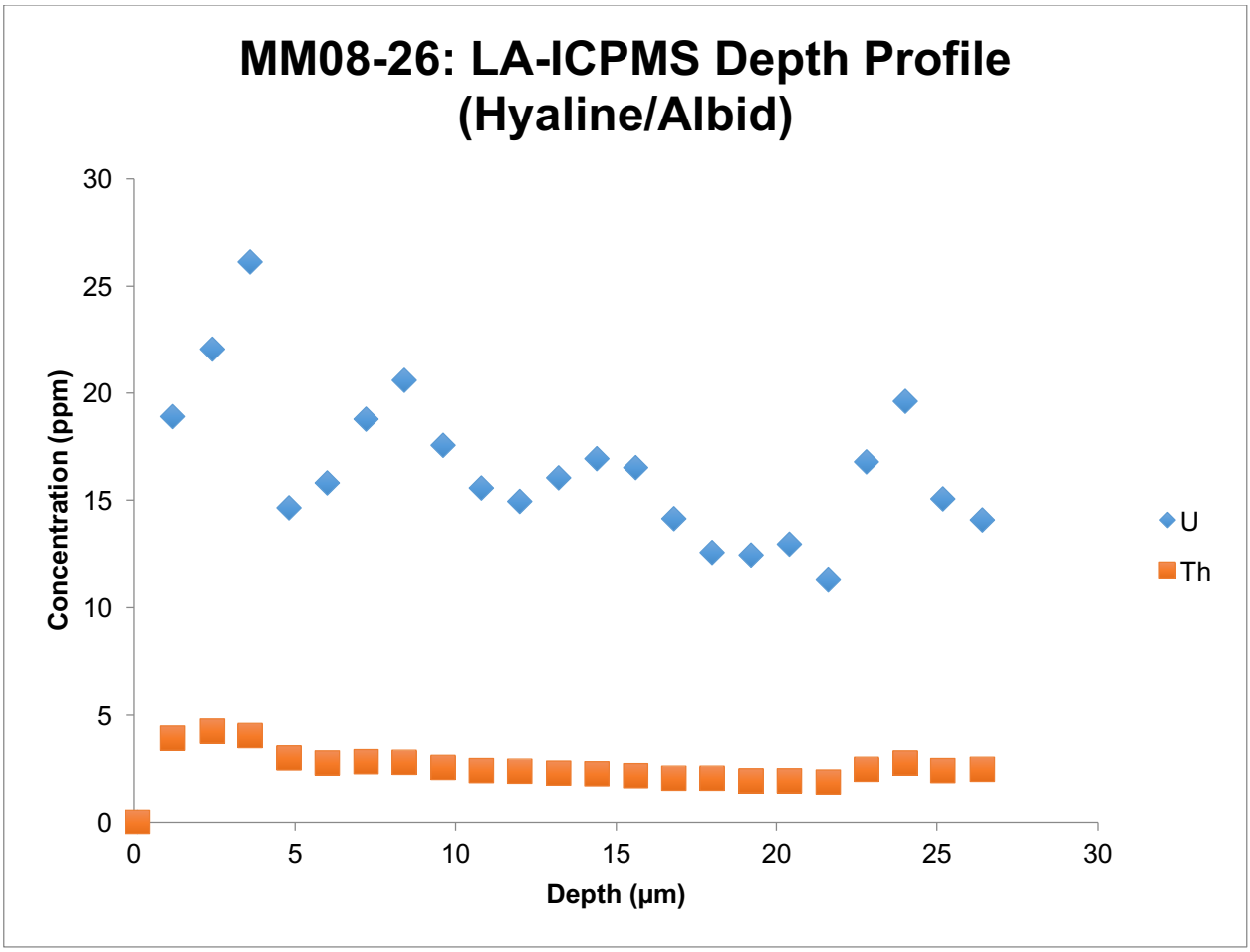
MM08-26: LA-ICPMS Depth Profile
(Hyaline/Albid)
Concentration (ppm)
30
25
20
15
10
5
0
0
5
10
15
20
25
30
Depth (μm)
U
Th

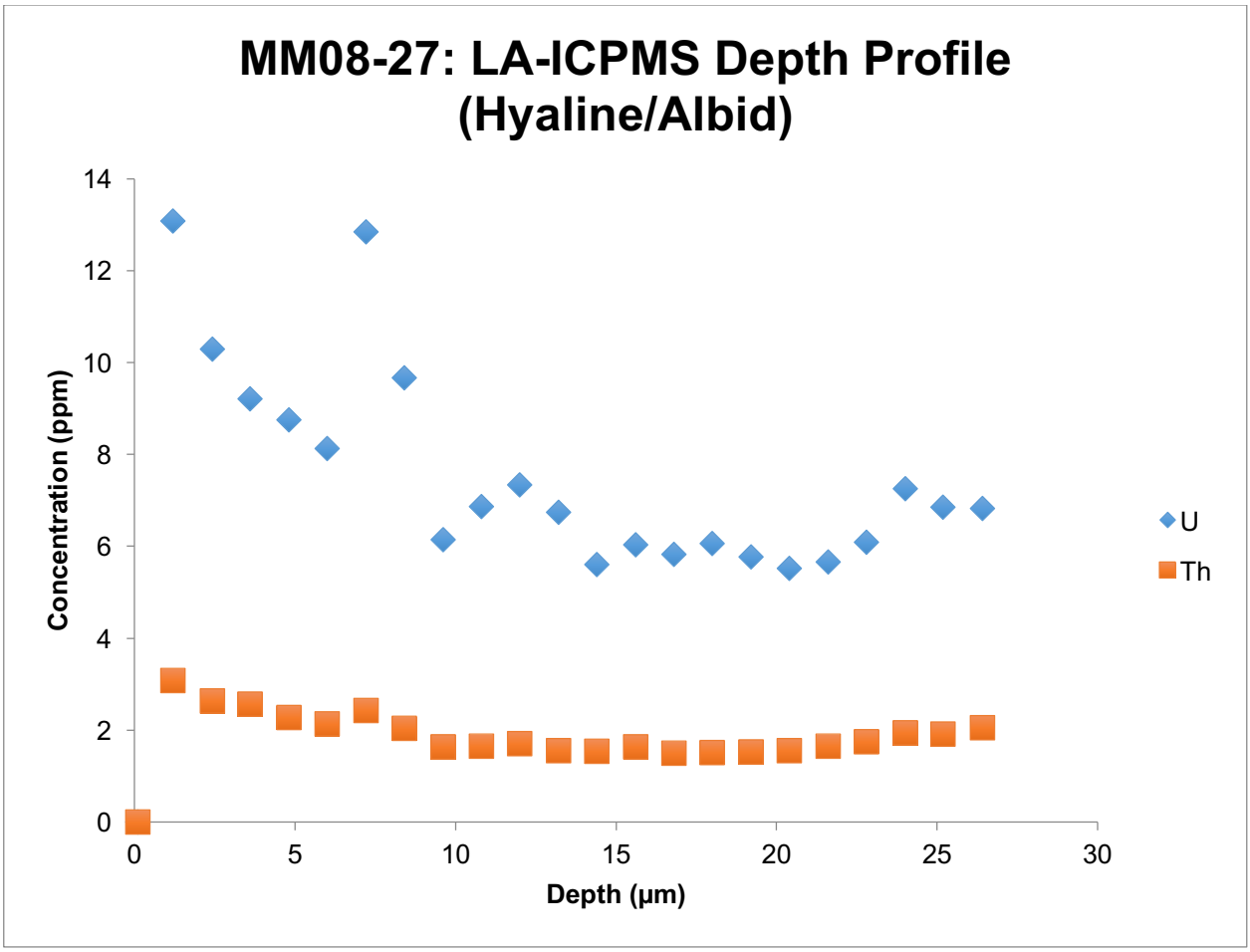
MM08-27: LA-ICPMS Depth Profile
(Hyaline/Albid)
Concentration (ppm)
14
12
10
8
6
4
2
0
0
5
10
15
20
25
30
Depth (µm)
U
Th

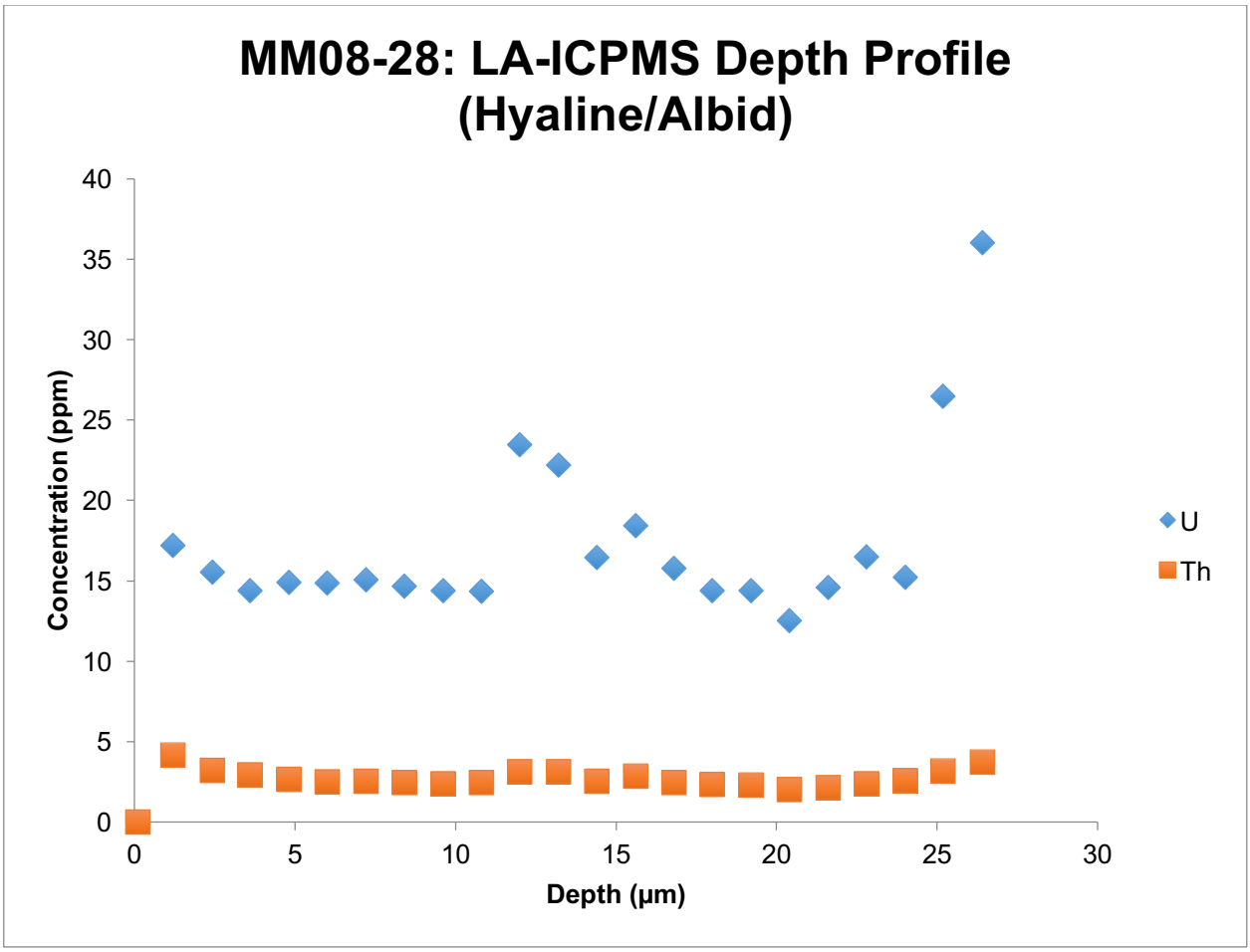
MM08-28: LA-ICPMS Depth Profile
(Hyaline/Albid)
Concentration (ppm)
40
35
30
25
20
15
10
5
0
0
5
10
15
20
25
30
Depth (µm)
U
Th

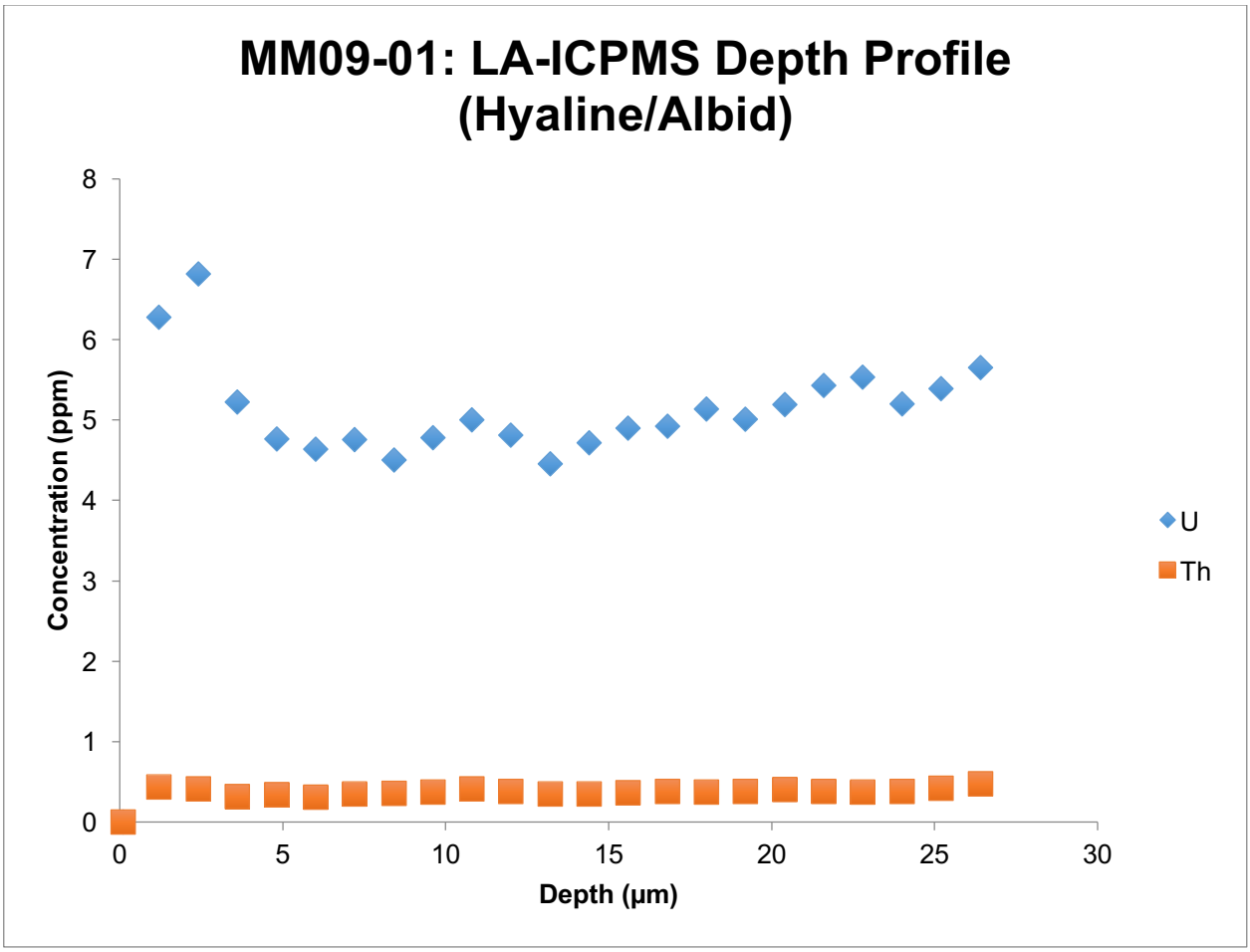
MM09-01: LA-ICPMS Depth Profile
(Hyaline/Albid)
Concentration (ppm)
0
1
2
3
4
5
6
7
8
0
5
10
15
20
25
30
Depth (µm)
U
Th

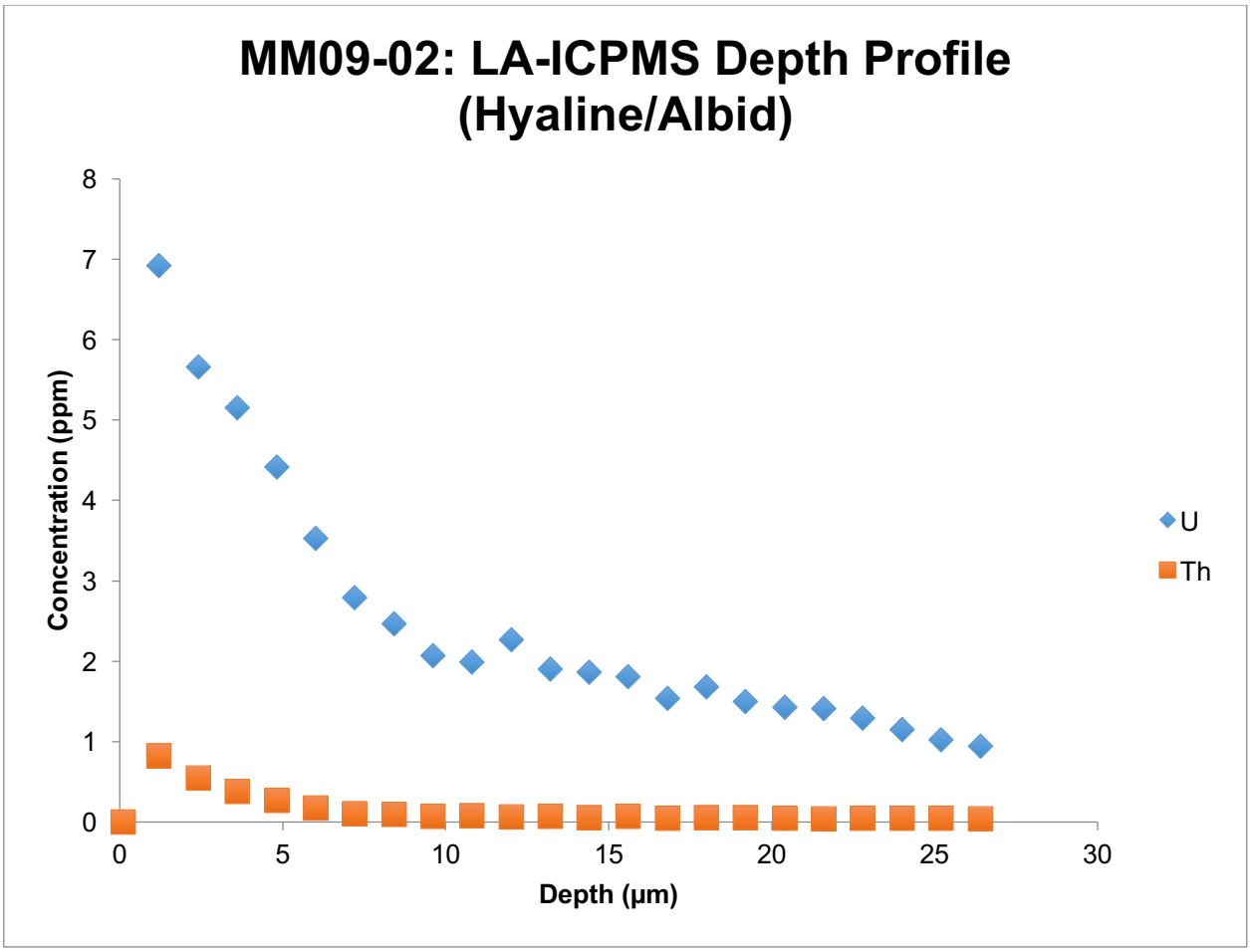
MM09-02: LA-ICPMS Depth Profile
(Hyaline/Albid)
Concentration (ppm)
Depth (µm)
0
1
2
3
4
5
6
7
8
0
5
10
15
20
25
30
U
Th

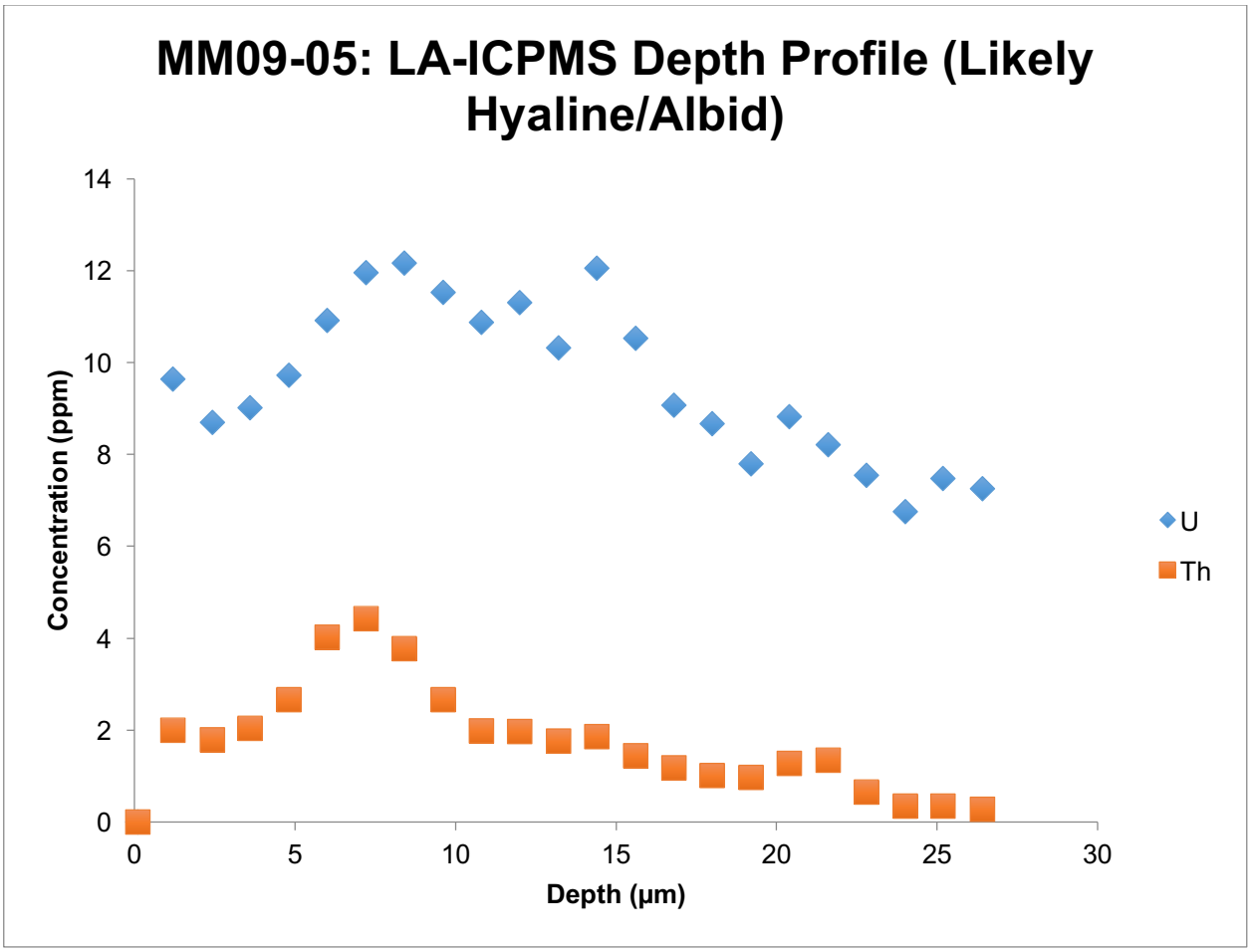
MM09-05: LA-ICPMS Depth Profile (Likely Hyaline/Albid)
Concentration (ppm)
0
2
4
6
8
10
12
14
0
5
10
15
20
25
30
Depth (µm)
U
Th

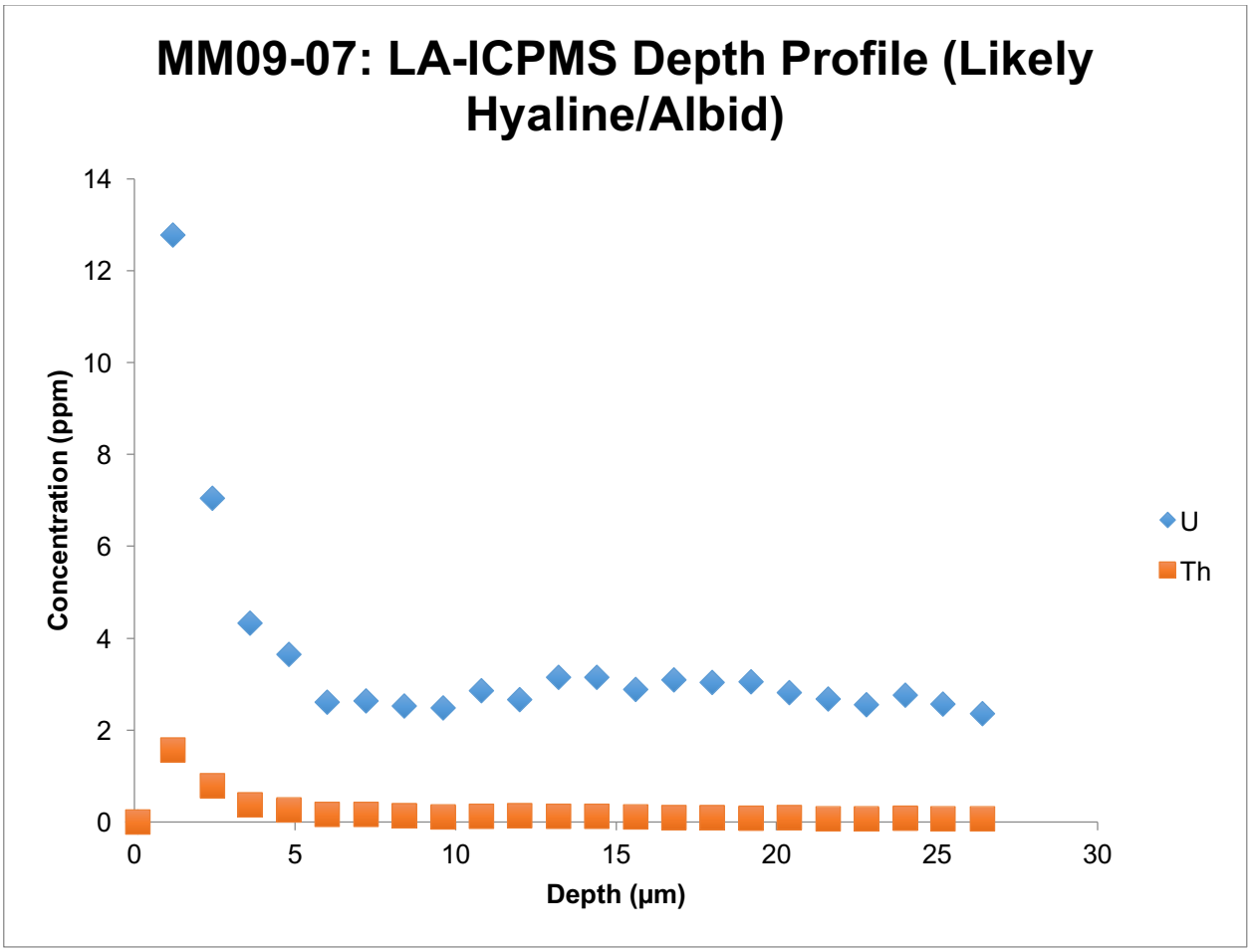
MM09-07: LA-ICPMS Depth Profile (Likely Hyaline/Albid)
Concentration (ppm)
14
12
10
8
6
4
2
0
0
5
10
15
20
25
30
Depth (µm)
U
Th

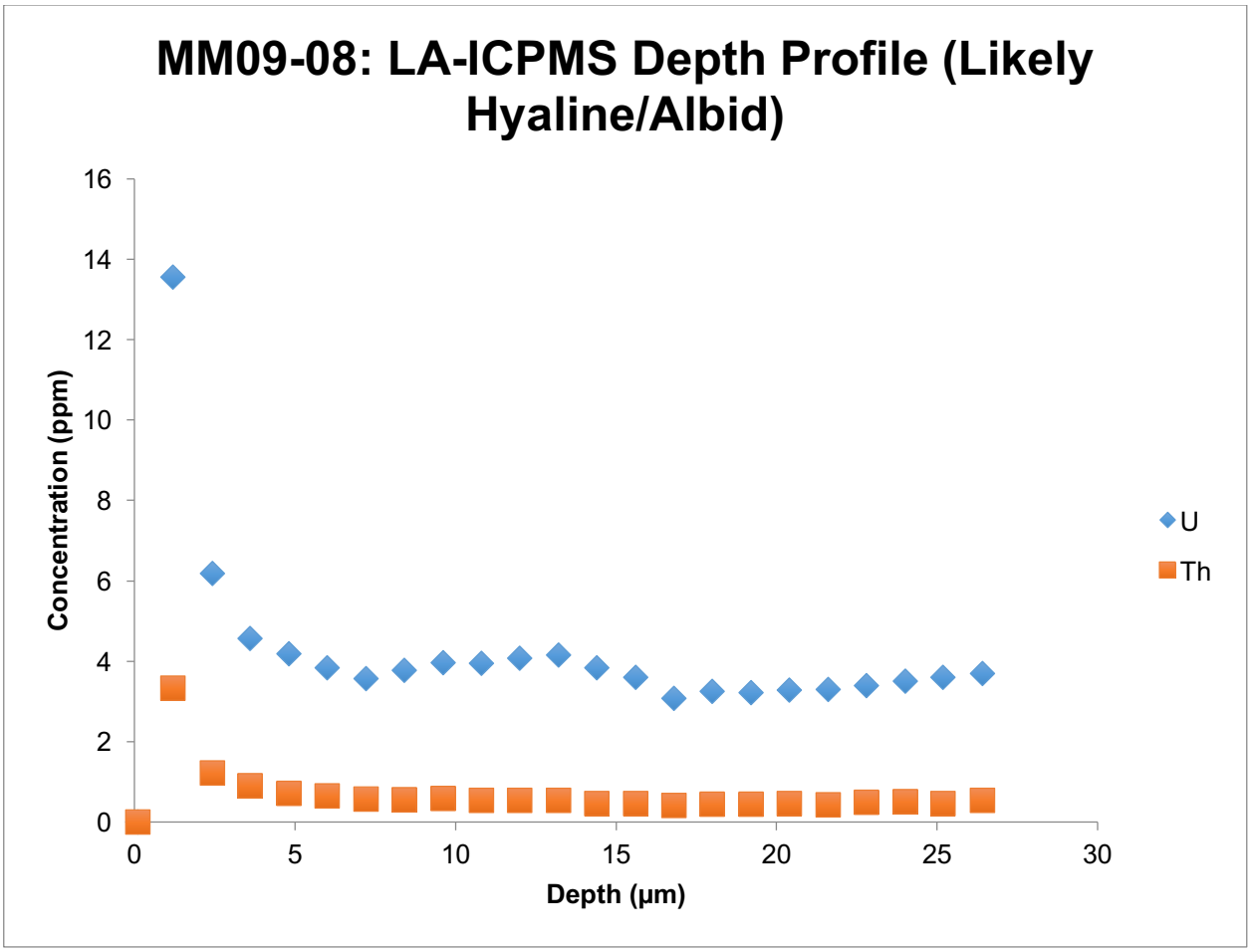
MM09-08: LA-ICPMS Depth Profile (Likely Hyaline/Albid)
Concentration (ppm)
16
14
12
10
8
6
4
2
0
0
5
10
15
20
25
30
Depth (µm)
U
Th

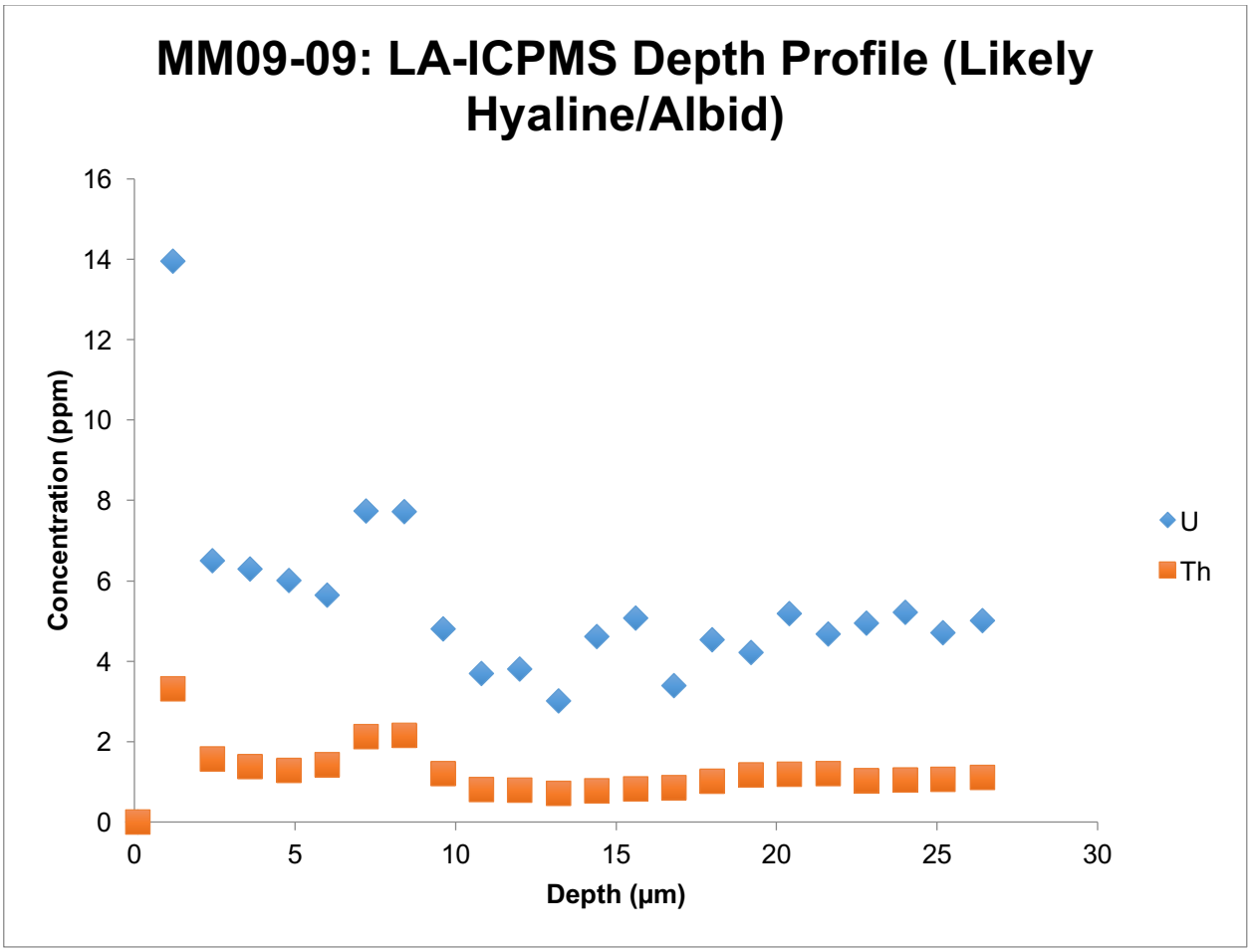
MM09-09: LA-ICPMS Depth Profile (Likely Hyaline/Albid)
Concentration (ppm)
16
14
12
10
8
6
4
2
0
0
5
10
15
20
25
30
Depth (µm)
U
Th

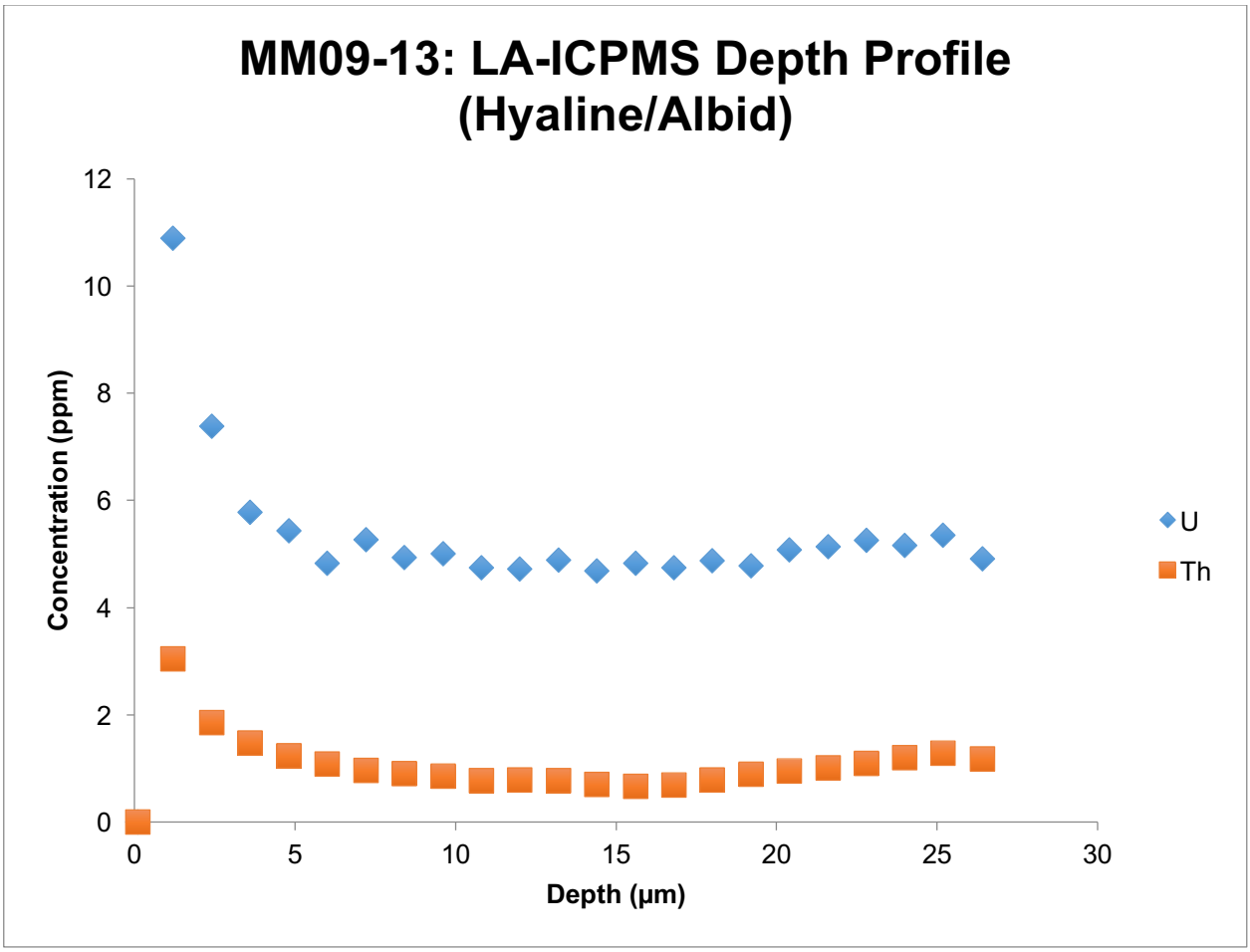
MM09-13: LA-ICPMS Depth Profile
(Hyaline/Albid)
Concentration (ppm)
12
10
8
6
4
2
0
0
5
10
15
20
25
30
Depth (μm)
U
Th

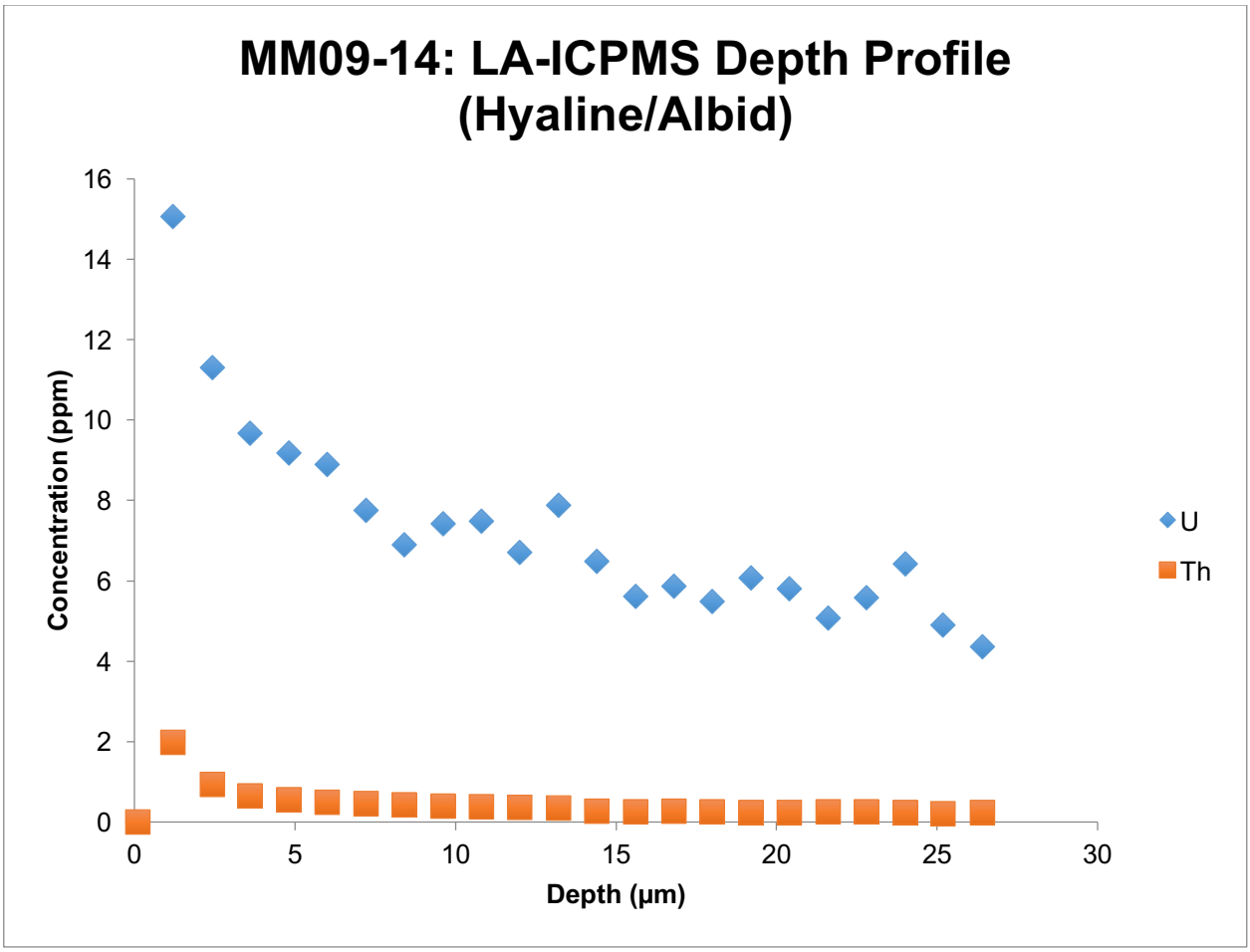
MM09-14: LA-ICPMS Depth Profile
(Hyaline/Albid)
Concentration (ppm)
16
14
12
10
8
6
4
2
0
0
5
10
15
20
25
30
Depth (μm)
U
Th

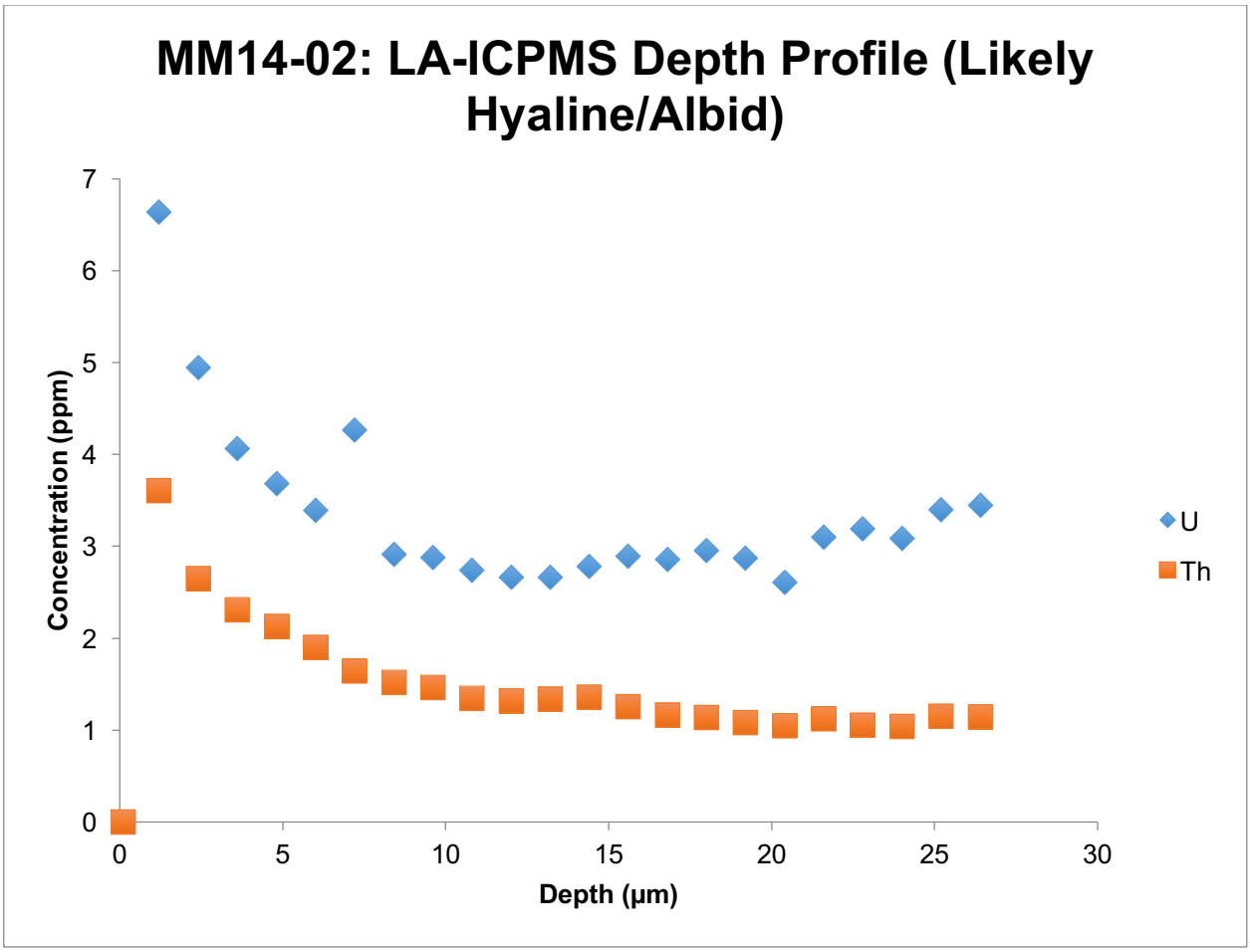
MM14-02: LA-ICPMS Depth Profile (Likely Hyaline/Albid)
Concentration (ppm)
0
1
2
3
4
5
6
7
0
5
10
15
20
25
30
Depth (µm)
U
Th

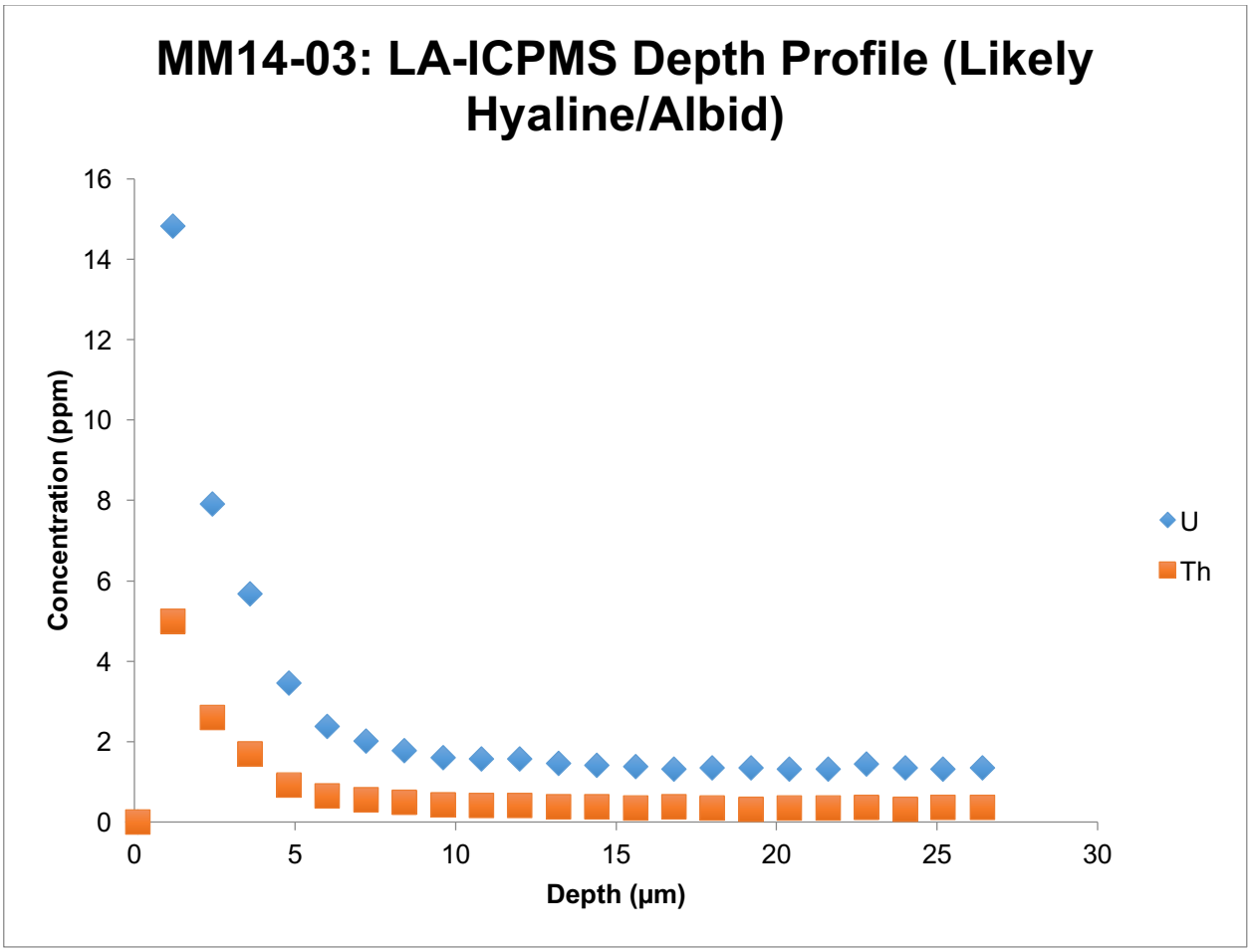
MM14-03: LA-ICPMS Depth Profile (Likely Hyaline/Albid)
Concentration (ppm)
16
14
12
10
8
6
4
2
0
0
5
10
15
20
25
30
Depth (µm)
U
Th

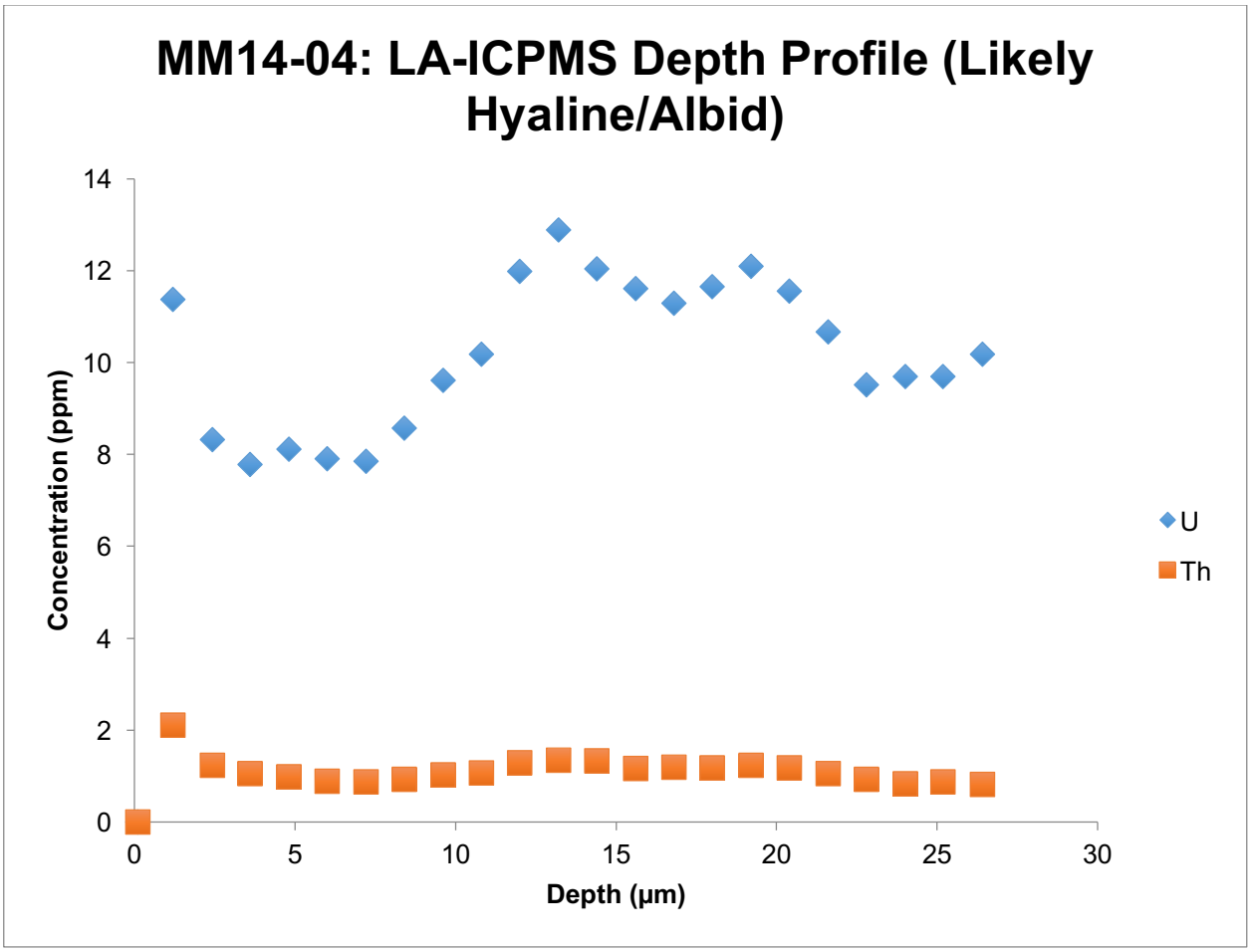
MM14-04: LA-ICPMS Depth Profile (Likely Hyaline/Albid)
Concentration (ppm)
14
12
10
8
6
4
2
0
0
5
10
15
20
25
30
Depth (µm)
U
Th

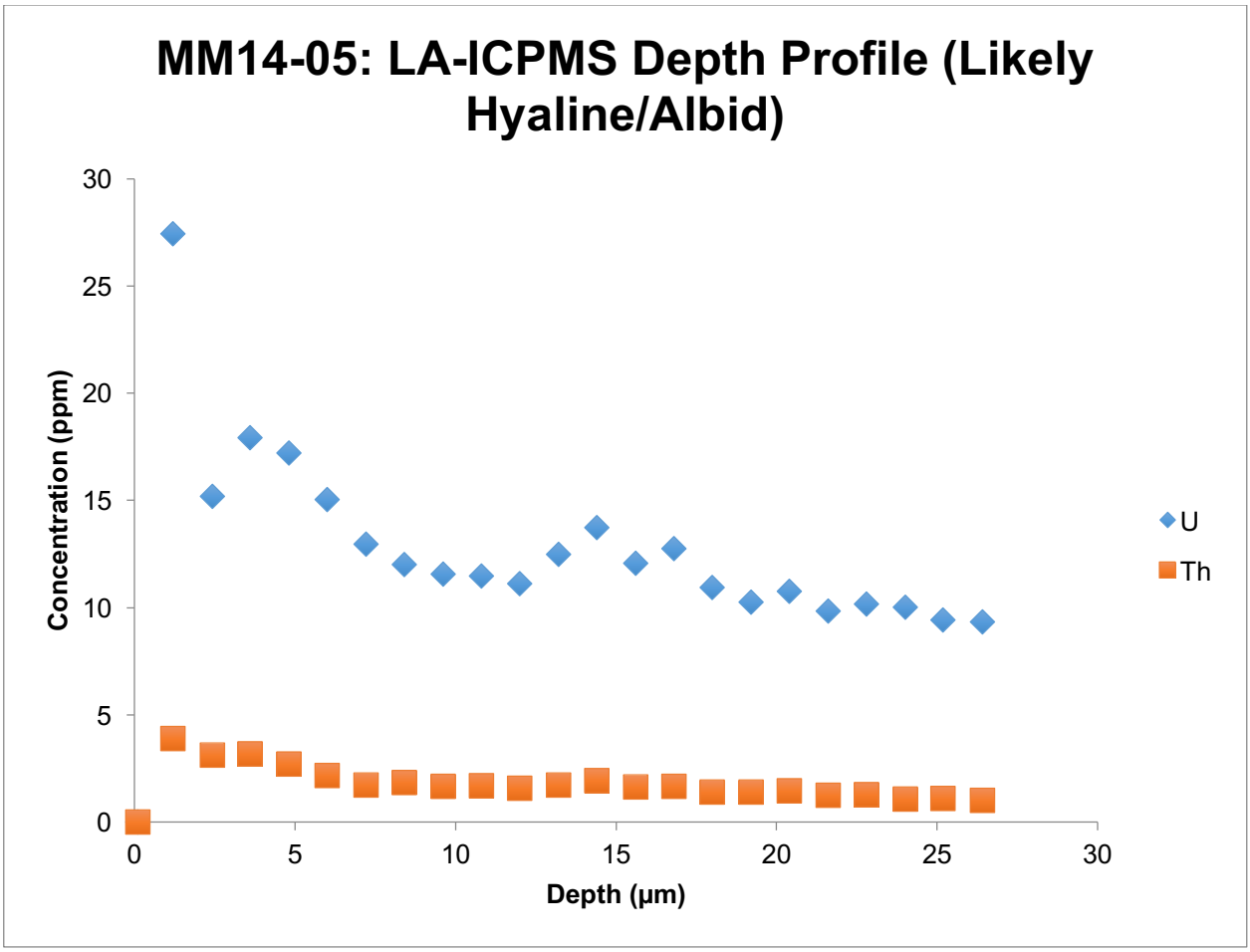
MM14-05: LA-ICPMS Depth Profile (Likely Hyaline/Albid)
Concentration (ppm)
30
25
20
15
10
5
0
0
5
10
15
20
25
30
Depth (µm)
U
Th

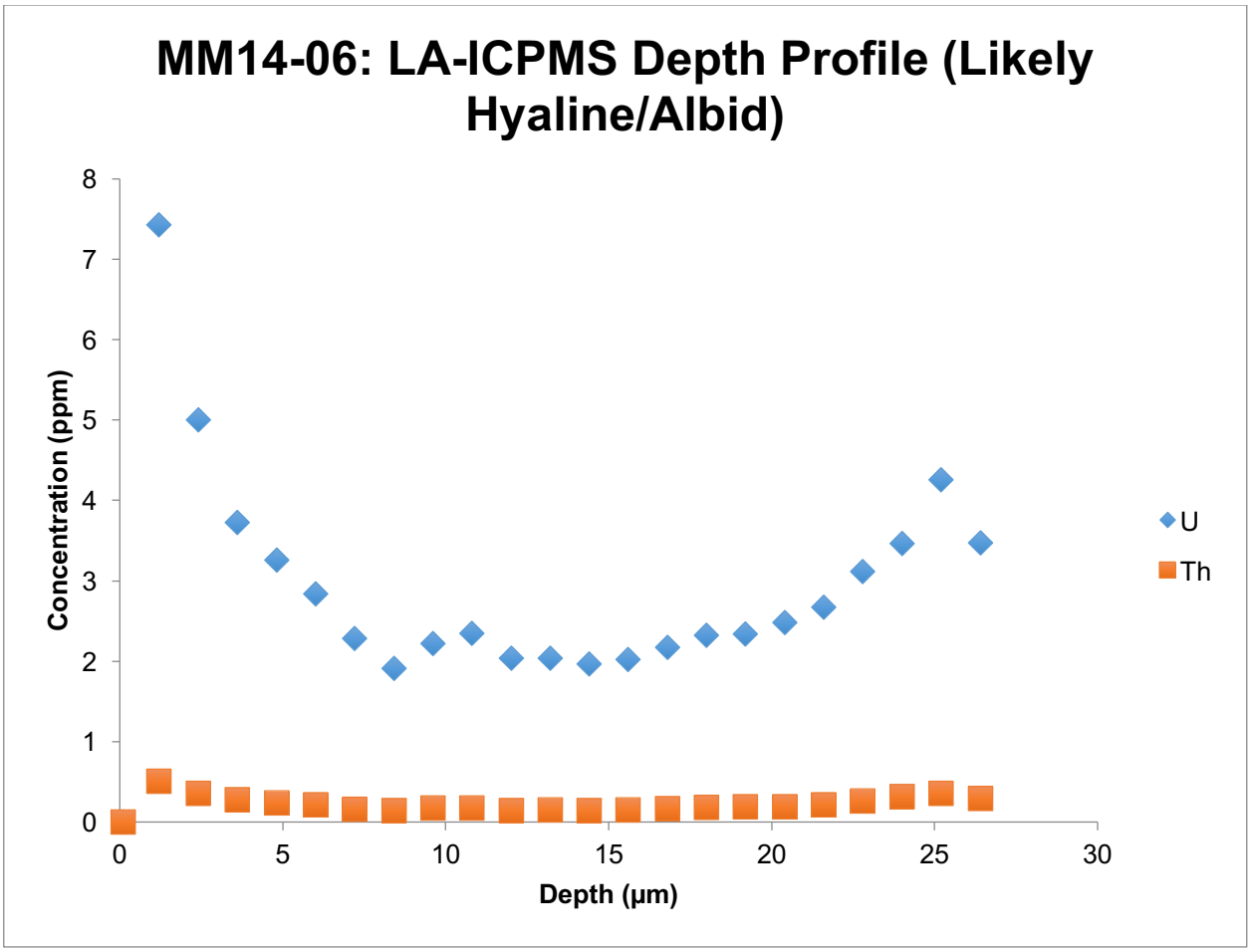
MM14-06: LA-ICPMS Depth Profile (Likely Hyaline/Albid)
Concentration (ppm)
Depth (µm)
0
1
2
3
4
5
6
7
8
0
5
10
15
20
25
30
U
Th

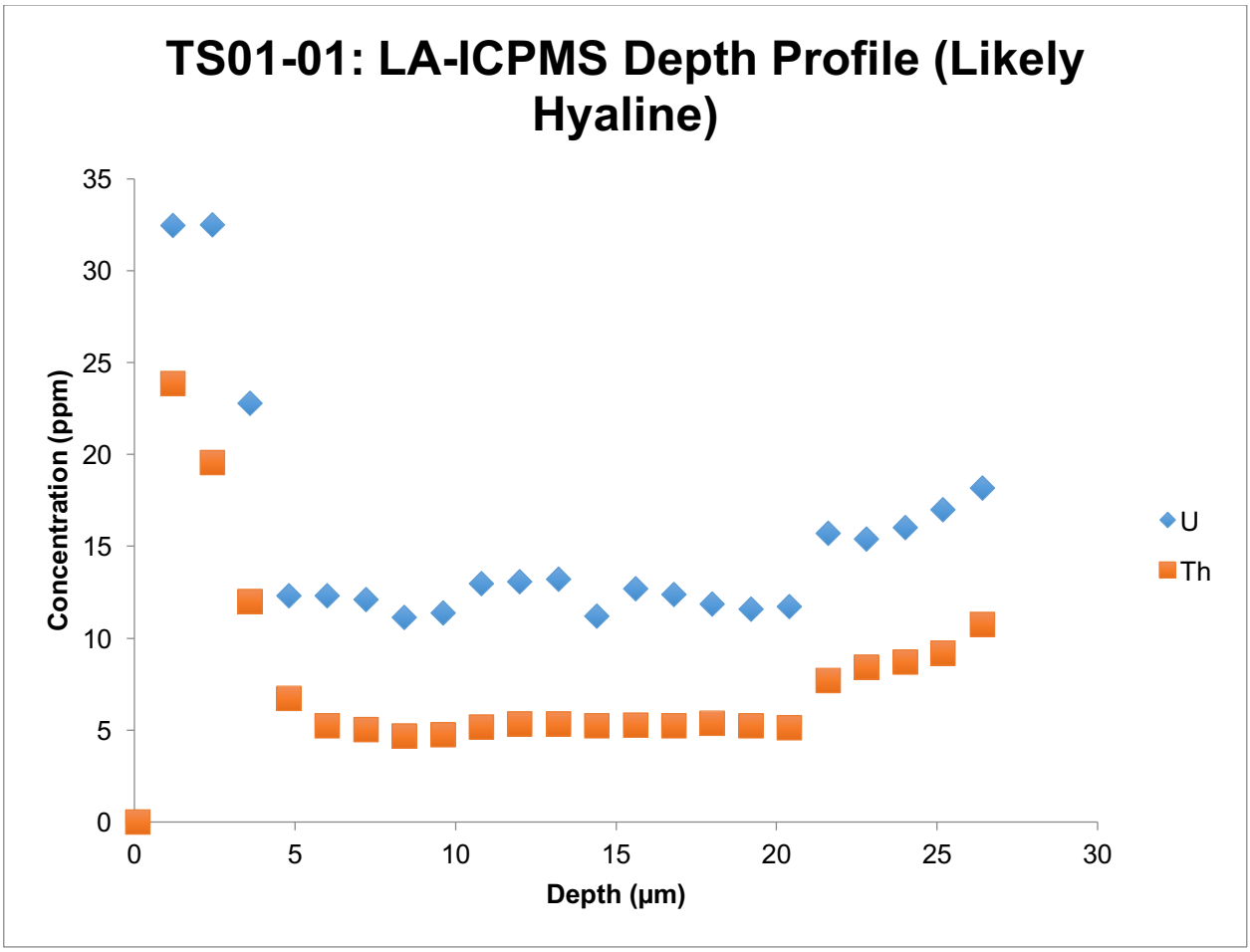
TS01-01: LA-ICPMS Depth Profile (Likely Hyaline)
Concentration (ppm)
35
30
25
20
15
10
5
0
0
5
10
15
20
25
30
Depth (µm)
U
Th

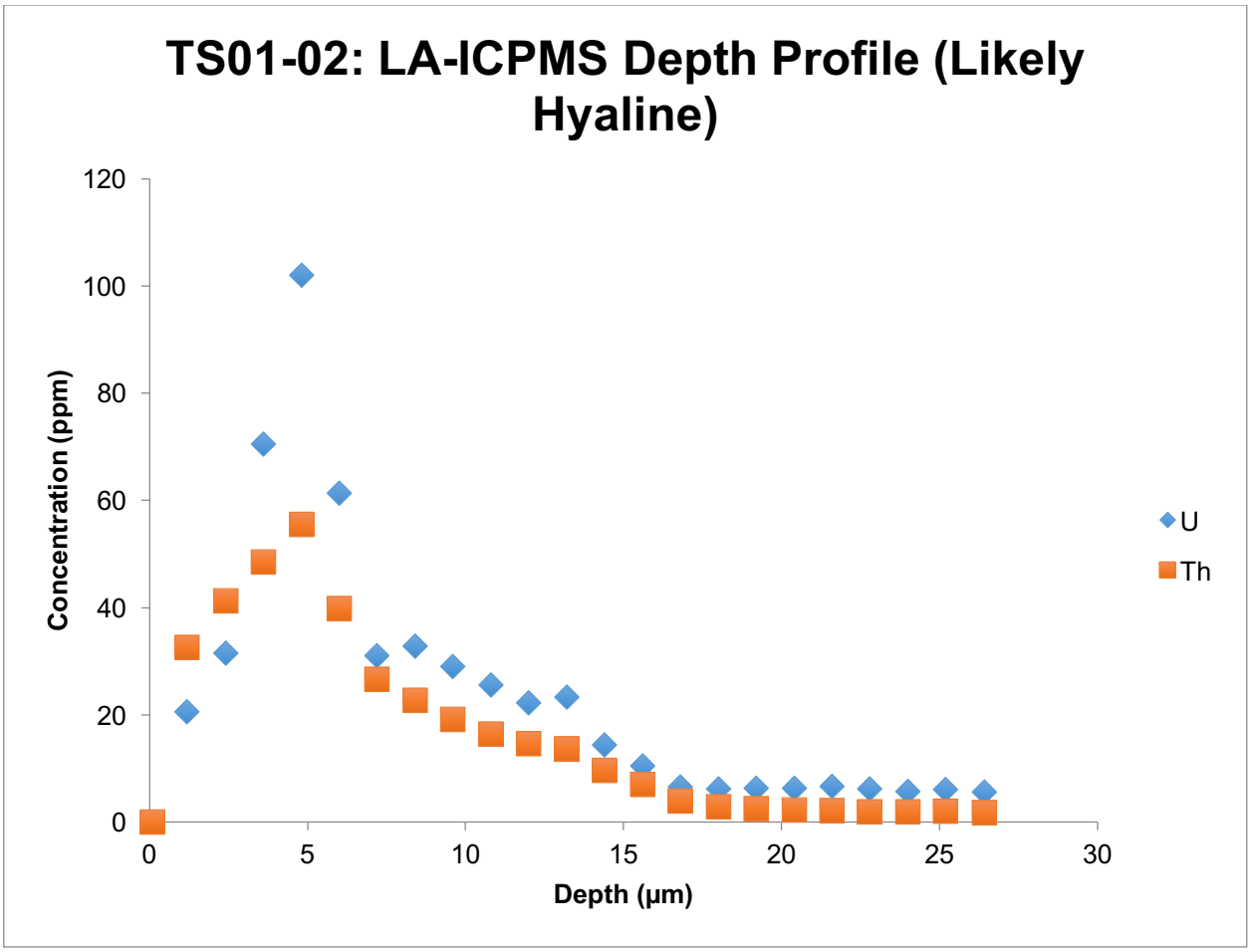
TS01-02: LA-ICPMS Depth Profile (Likely Hyaline)
Concentration (ppm)
120
100
80
60
40
20
0
0
5
10
15
20
25
30
Depth (µm)
U
Th

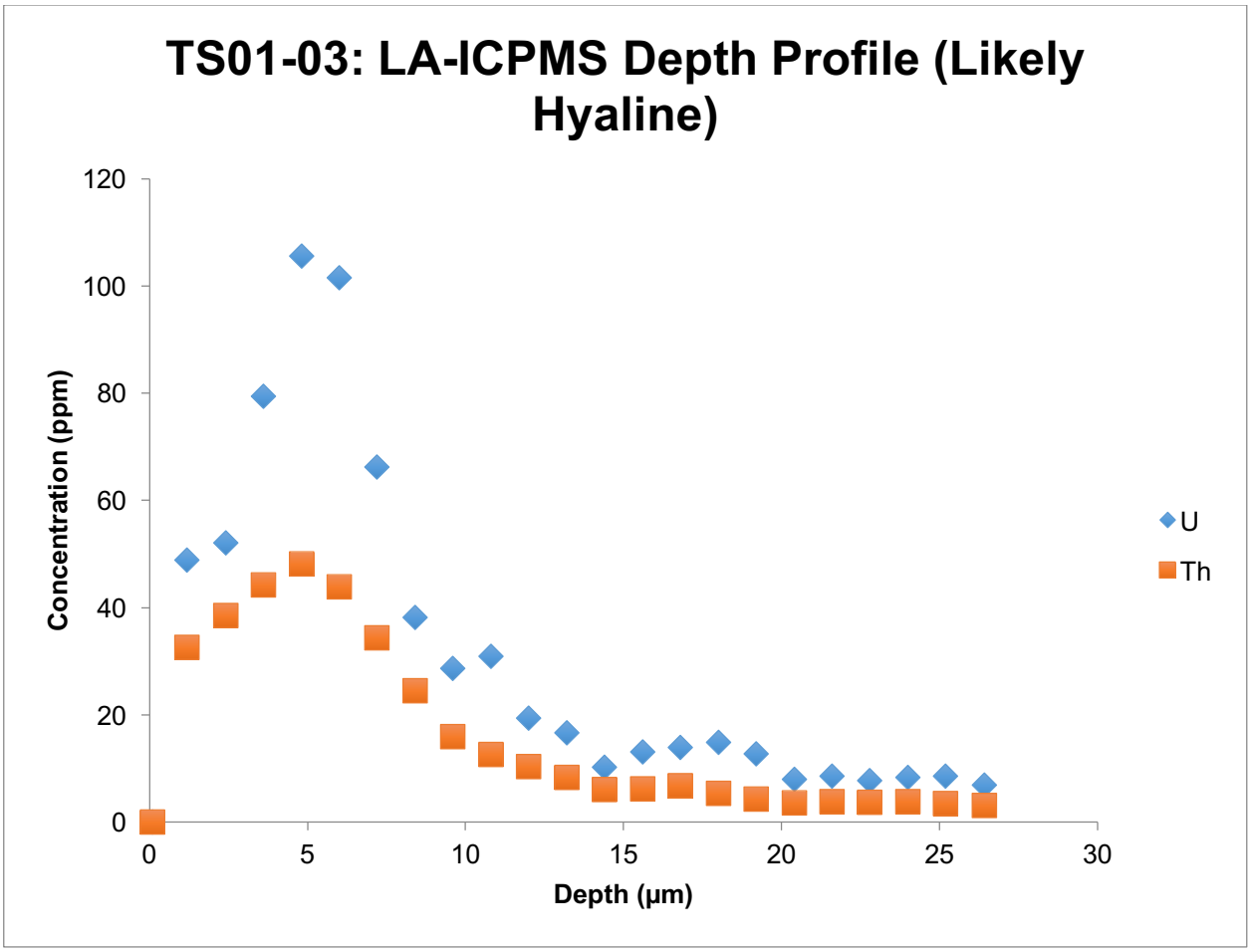
TS01-03: LA-ICPMS Depth Profile (Likely Hyaline)
Concentration (ppm)
120
100
80
60
40
20
0
0
5
10
15
20
25
30
Depth (µm)
U
Th

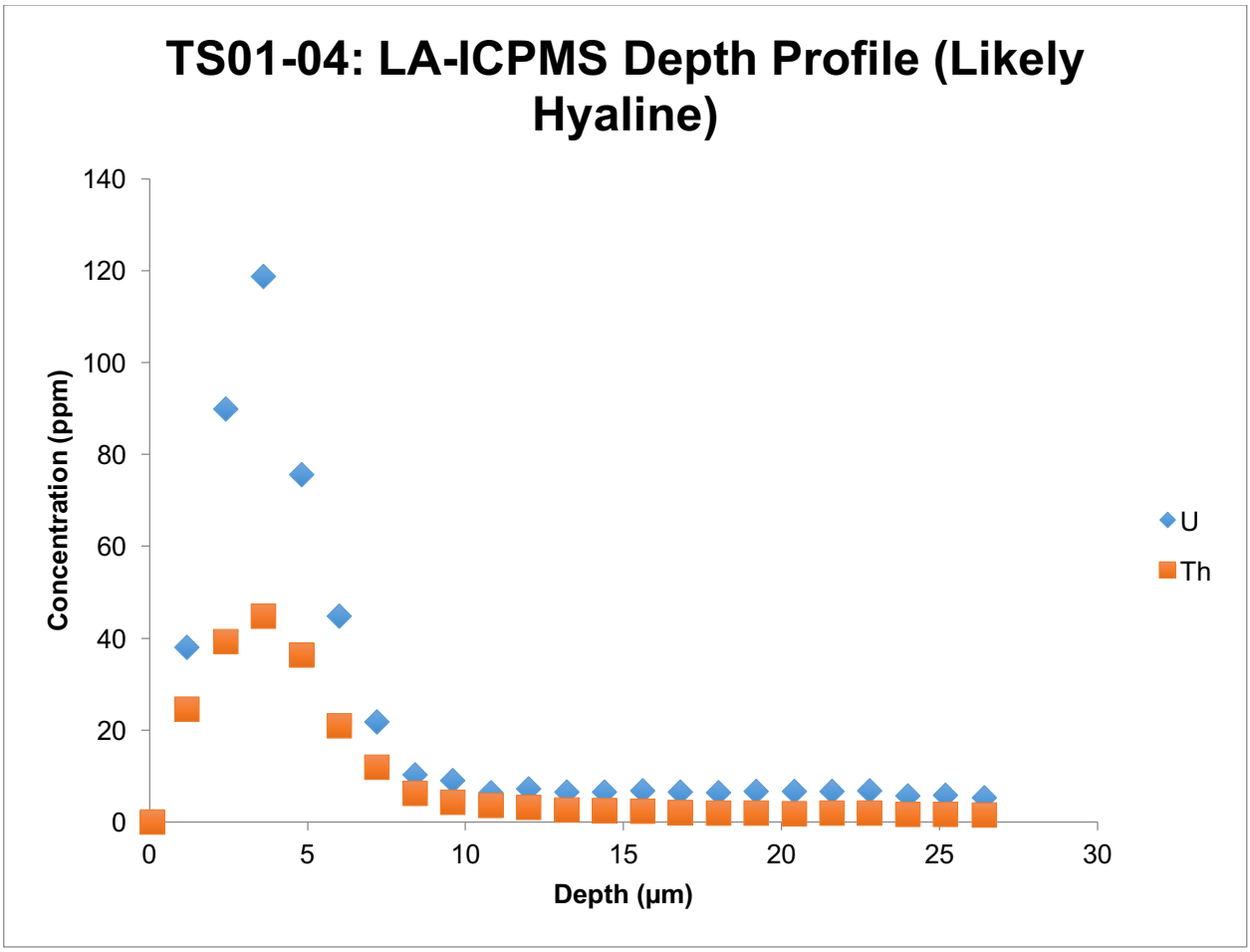
TS01-04: LA-ICPMS Depth Profile (Likely Hyaline)
Concentration (ppm)
140
120
100
80
60
40
20
0
0
5
10
15
20
25
30
Depth (µm)
U
Th

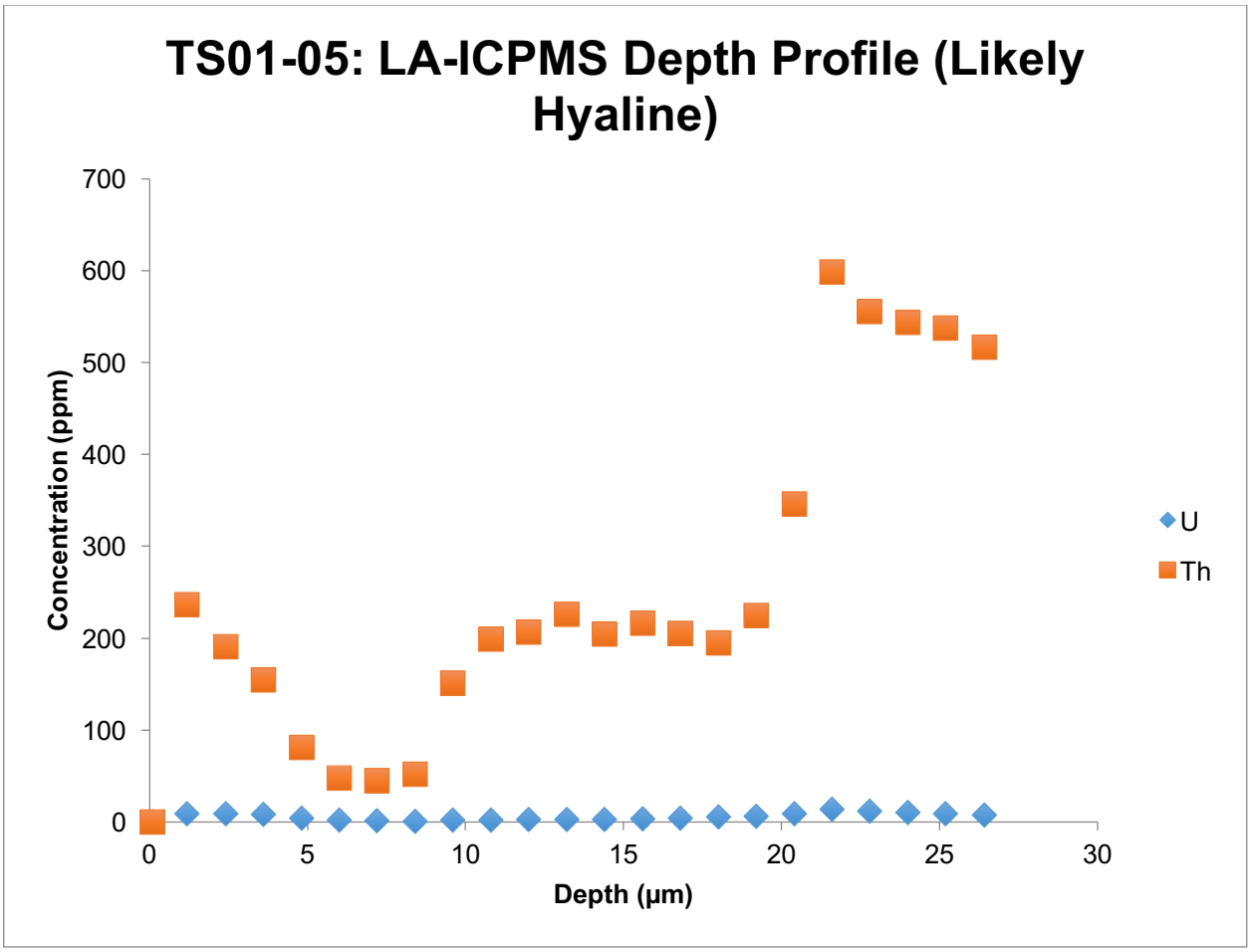
TS01-05: LA-ICPMS Depth Profile (Likely Hyaline)
Concentration (ppm)
700
600
500
400
300
200
100
0
0
5
10
15
20
25
30
Depth (µm)
U
Th

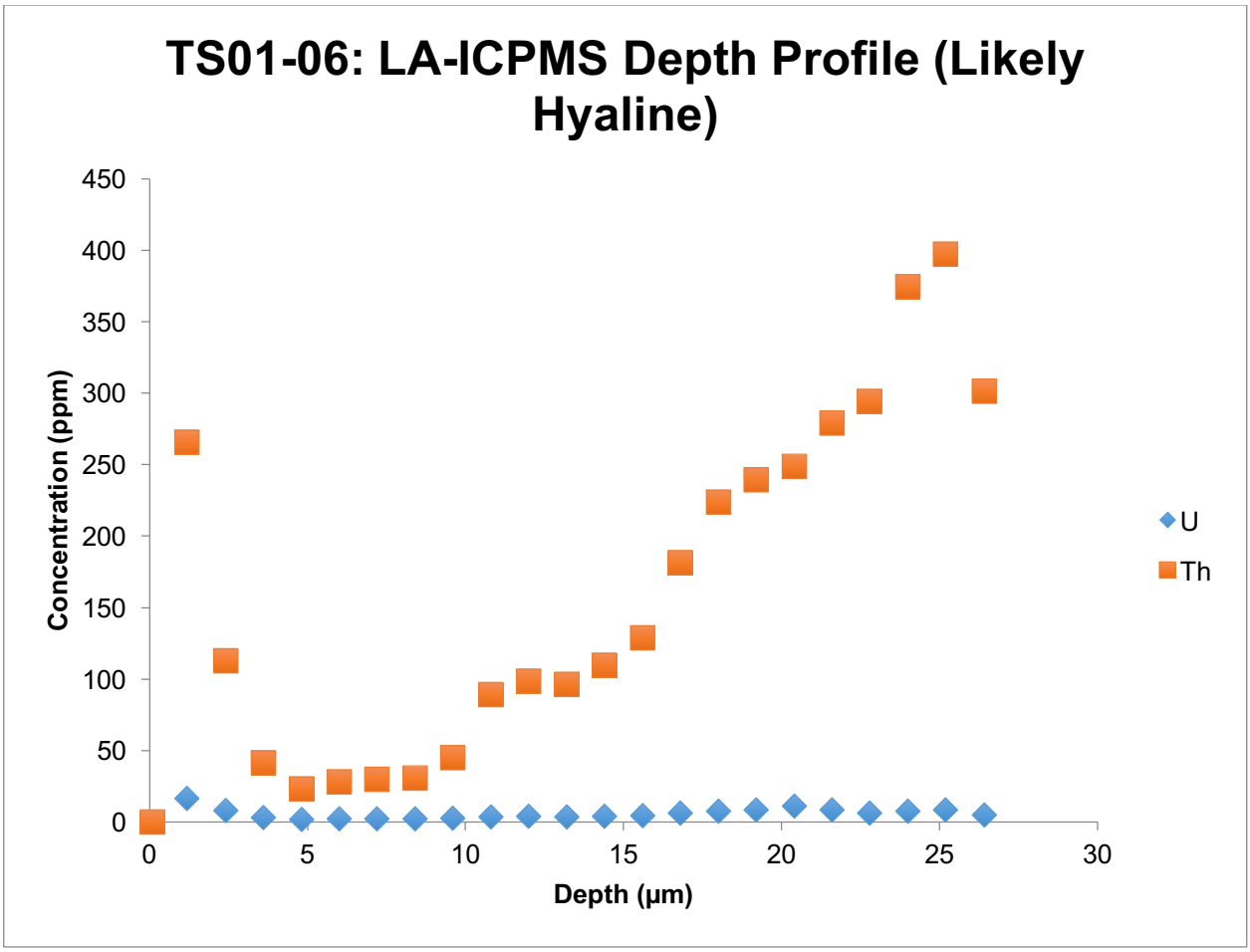
TS01-06: LA-ICPMS Depth Profile (Likely Hyaline)
Concentration (ppm)
450
400
350
300
250
200
150
100
50
0
0
5
10
15
20
25
30
Depth (µm)
U
Th

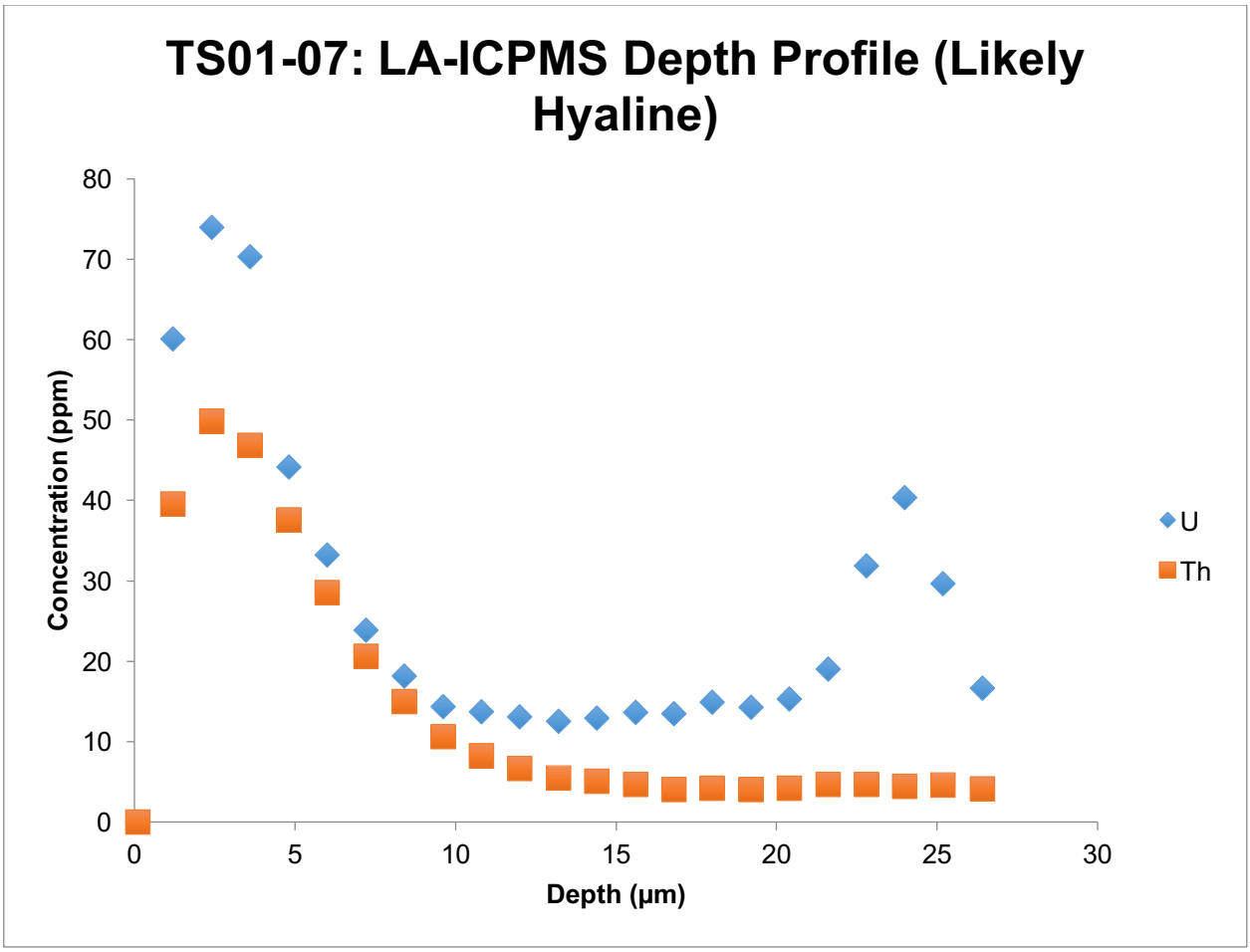
TS01-07: LA-ICPMS Depth Profile (Likely Hyaline)
Concentration (ppm)
80
70
60
50
40
30
20
10
0
0
5
10
15
20
25
30
Depth (µm)
U
Th

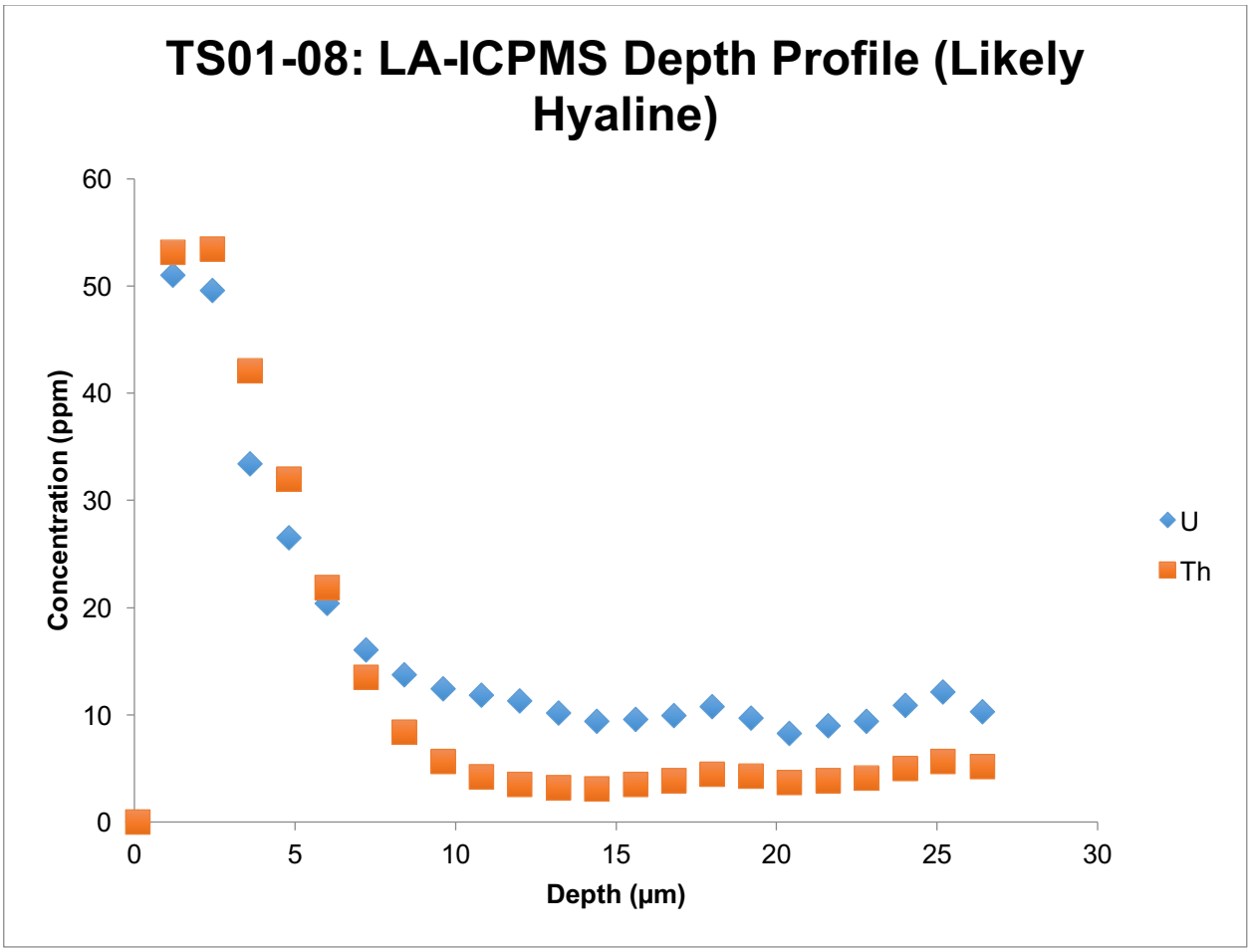
TS01-08: LA-ICPMS Depth Profile (Likely Hyaline)
Concentration (ppm)
60
50
40
30
20
10
0
0
5
10
15
20
25
30
Depth (µm)
U
Th

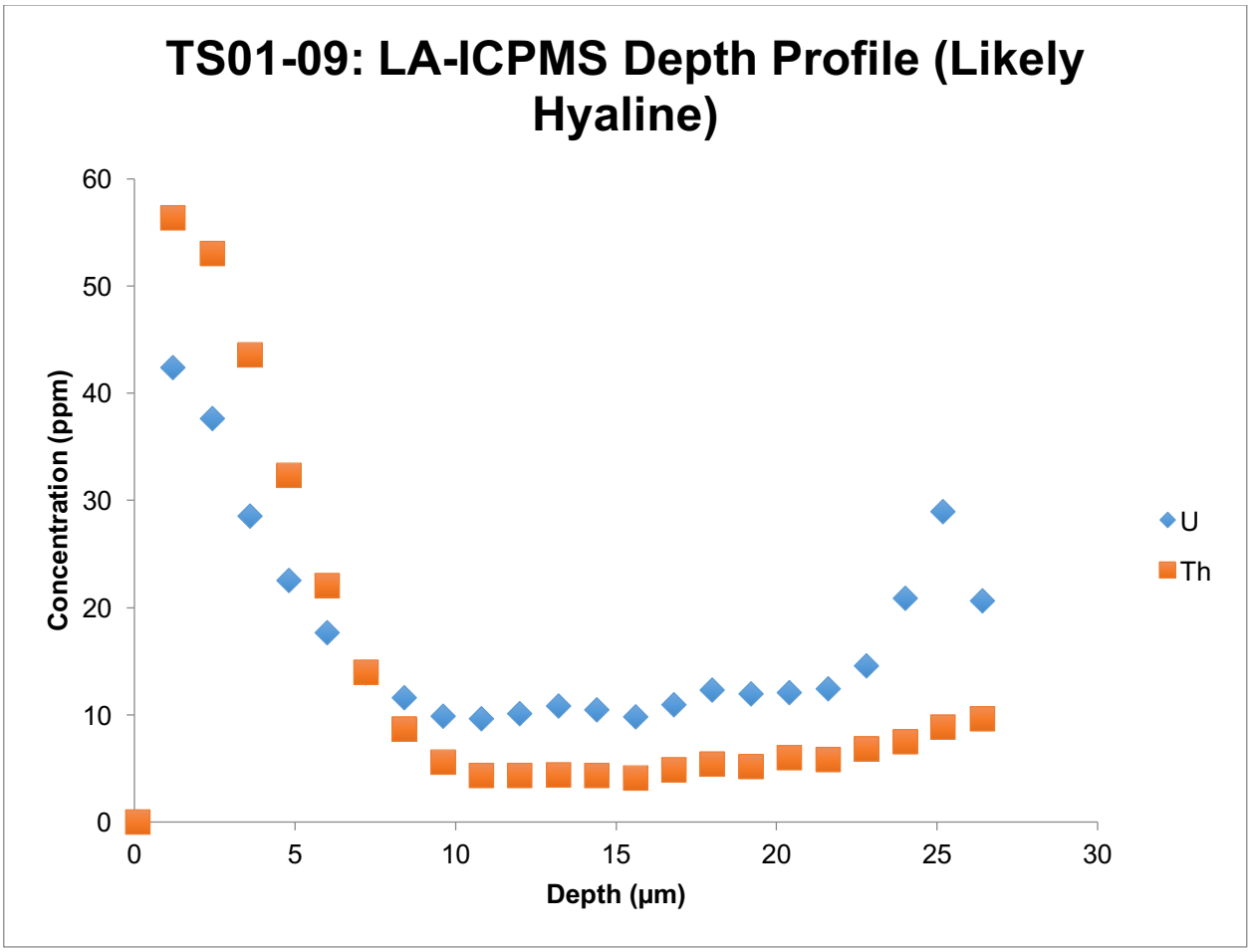
TS01-09: LA-ICPMS Depth Profile (Likely Hyaline)
Concentration (ppm)
60
50
40
30
20
10
0
0
5
10
15
20
25
30
Depth (µm)
U
Th

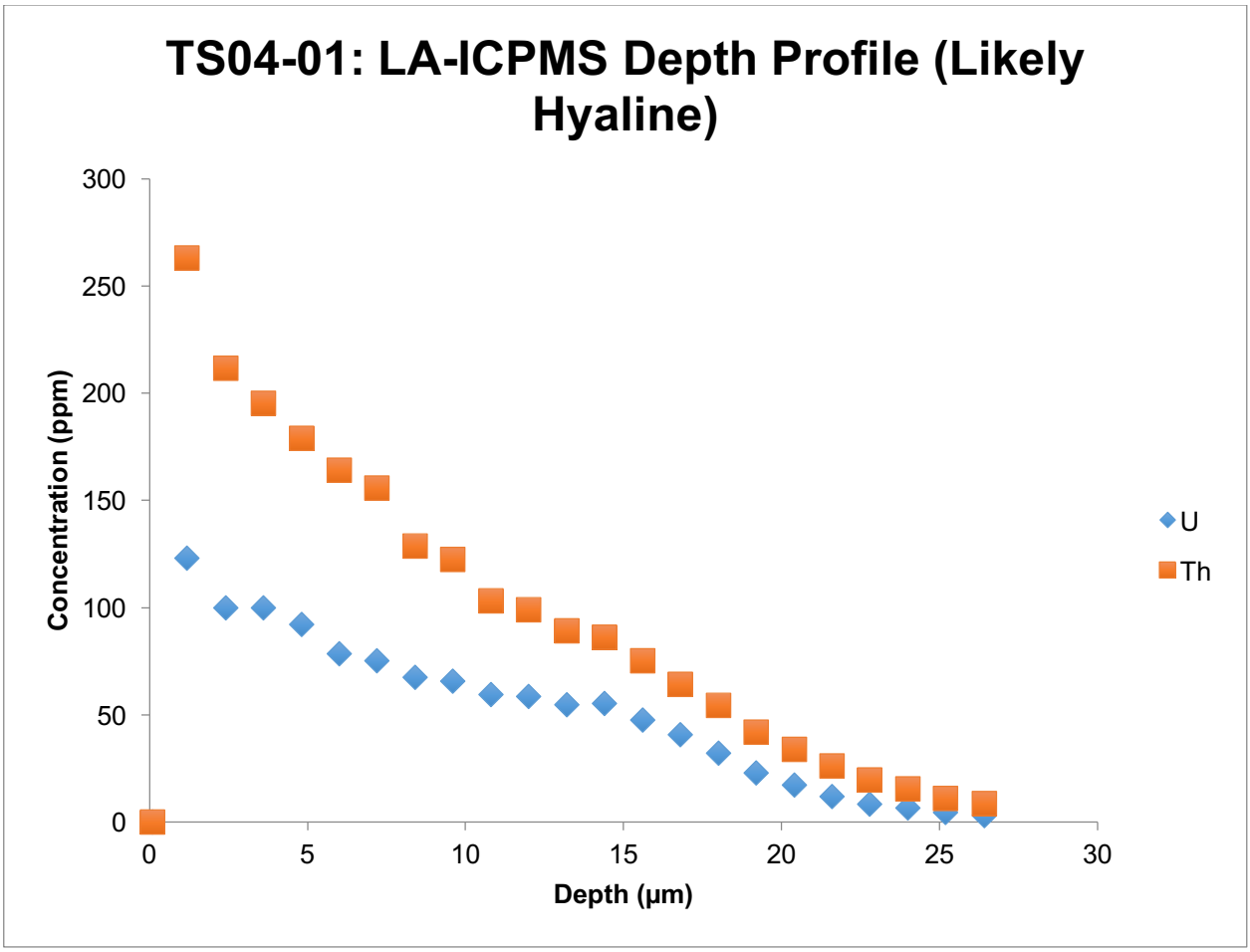
TS04-01: LA-ICPMS Depth Profile (Likely Hyaline)
Concentration (ppm)
300
250
200
150
100
50
0
0
5
10
15
20
25
30
Depth (µm)
U
Th

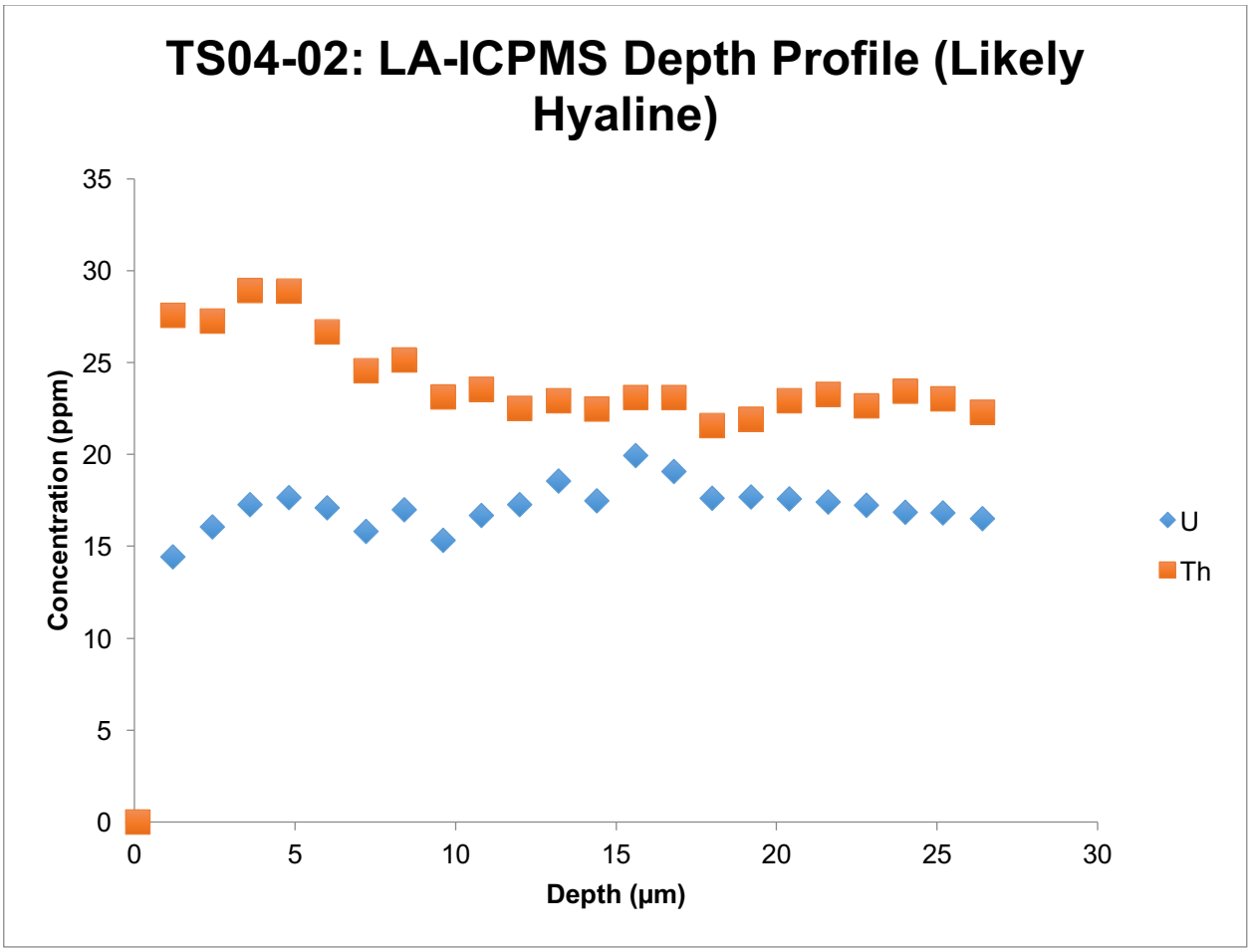
TS04-02: LA-ICPMS Depth Profile (Likely Hyaline)
Concentration (ppm)
35
30
25
20
15
10
5
0
0
5
10
15
20
25
30
Depth (µm)
U
Th

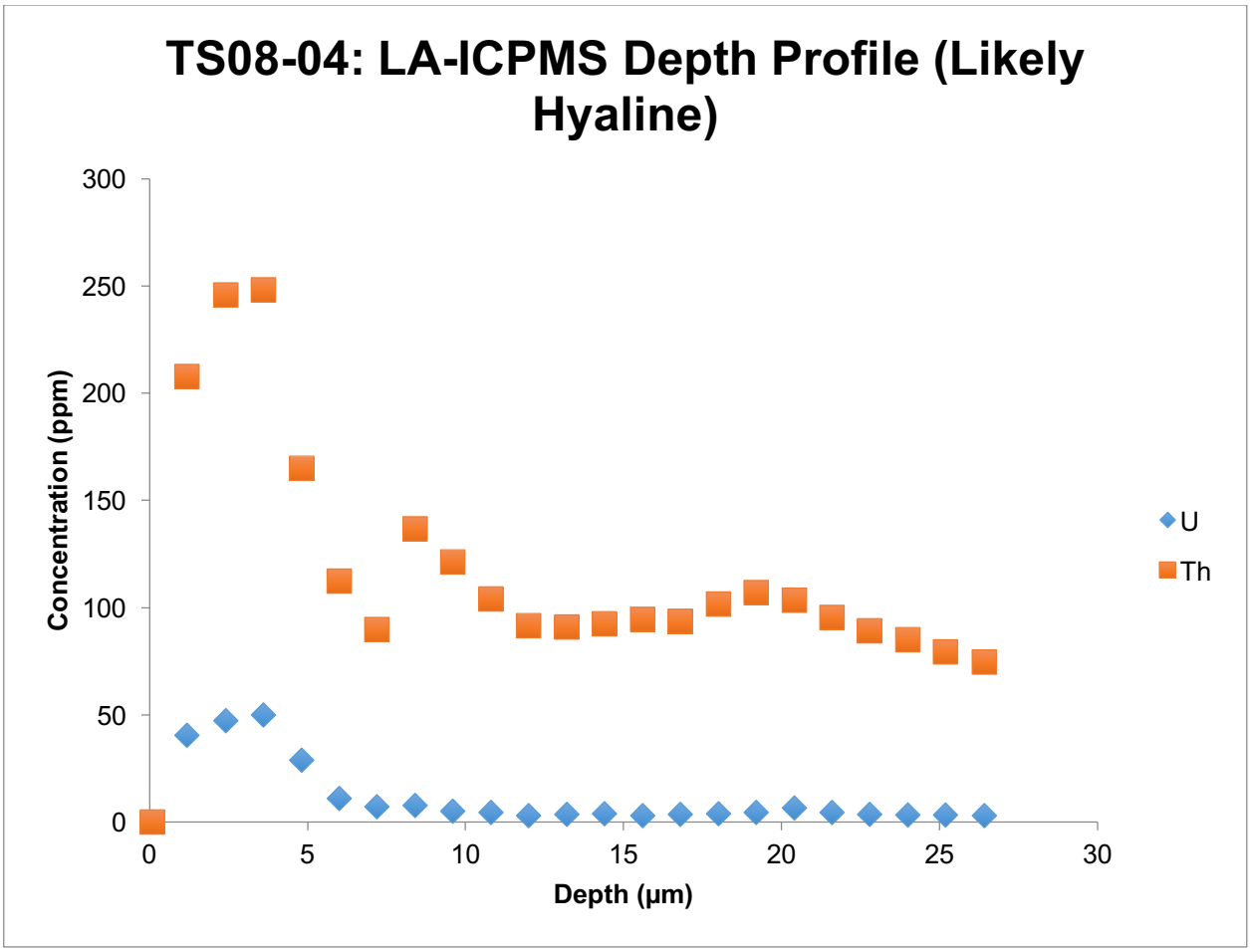
TS08-04: LA-ICPMS Depth Profile (Likely Hyaline)
Concentration (ppm)
300
250
200
150
100
50
0
0
5
10
15
20
25
30
Depth (µm)
U
Th

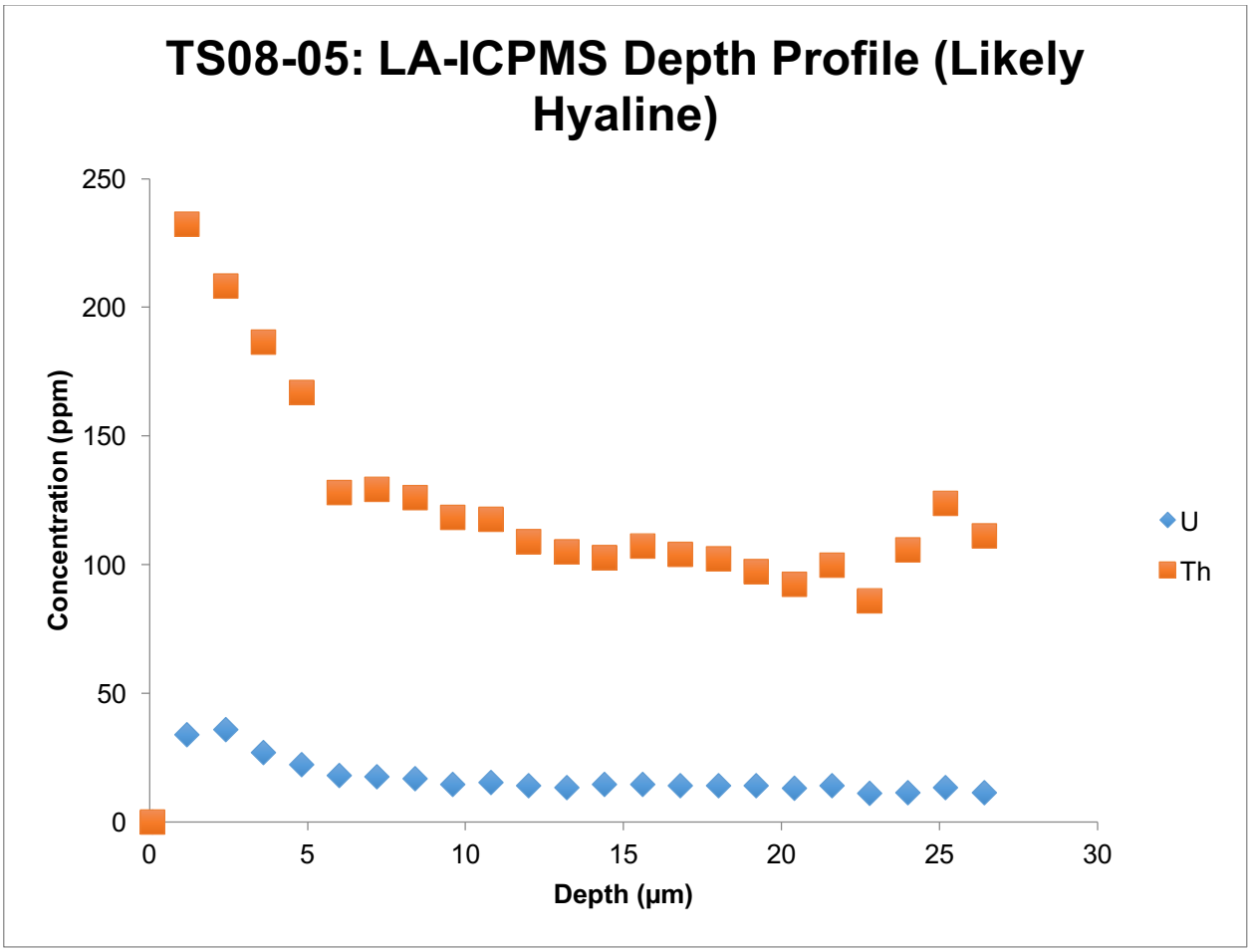
TS08-05: LA-ICPMS Depth Profile (Likely Hyaline)
Concentration (ppm)
250
200
150
100
50
0
0
5
10
15
20
25
30
Depth (µm)
U
Th

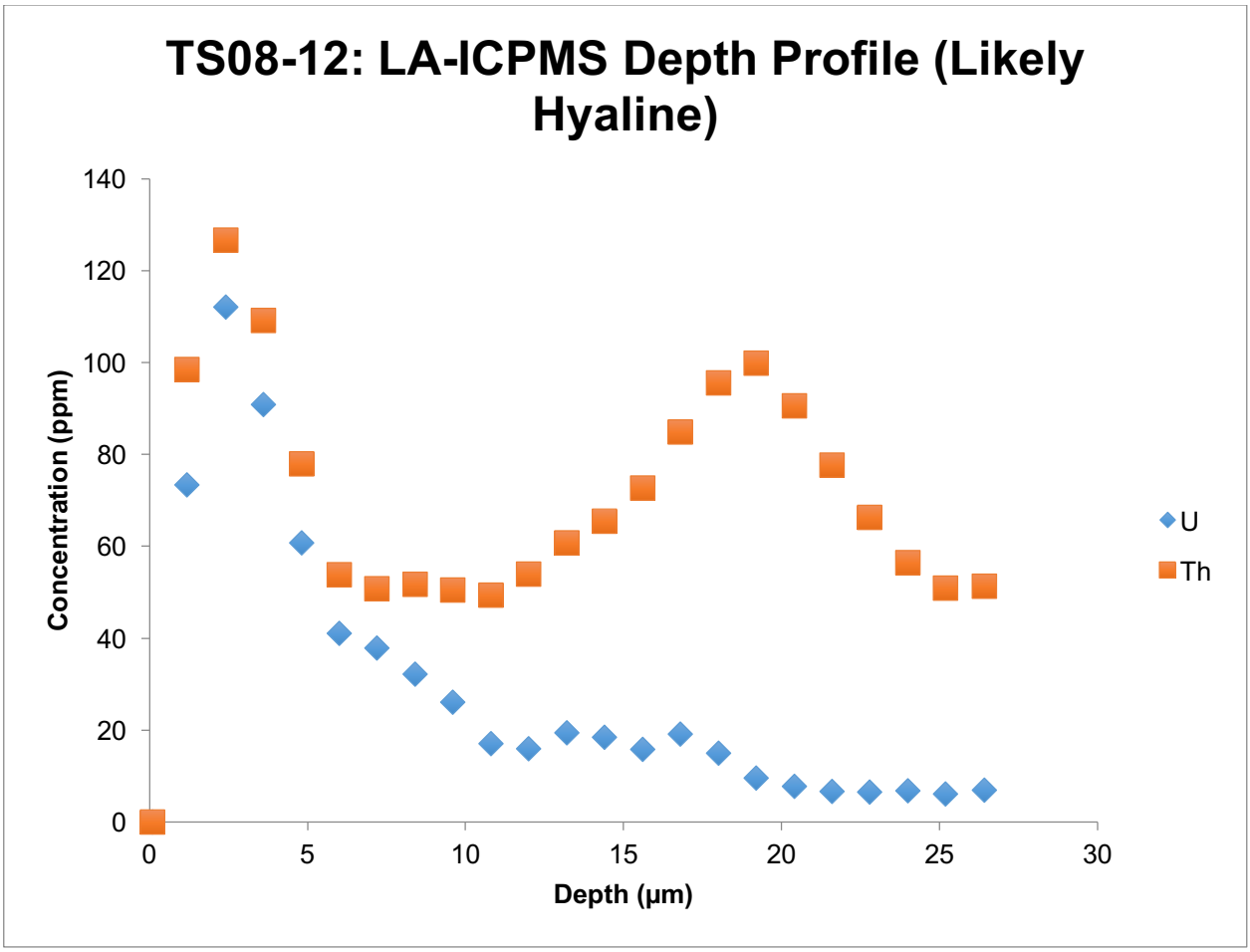
TS08-12: LA-ICPMS Depth Profile (Likely Hyaline)
Concentration (ppm)
140
120
100
80
60
40
20
0
0
5
10
15
20
25
30
Depth (µm)
U
Th

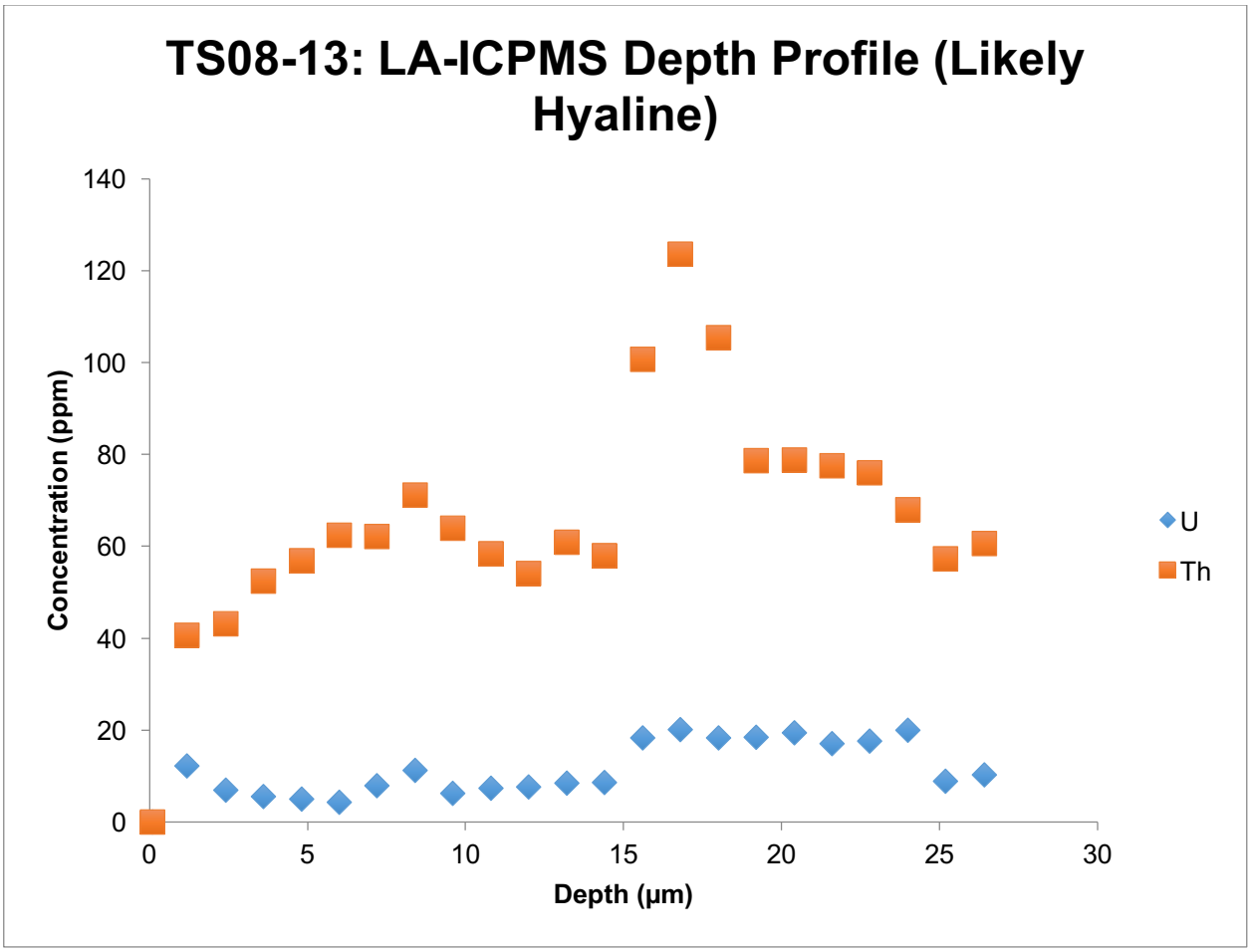
TS08-13: LA-ICPMS Depth Profile (Likely Hyaline)
Concentration (ppm)
140
120
100
80
60
40
20
0
0
5
10
15
20
25
30
Depth (µm)
U
Th